Republic of Iraq
Ministry of Higher Education &
Scientific Research
University of Diyala
College of Science
Department of Physics

Synthesis of Some Ternary Metal Oxides and Sulphides Nanostructures Thin Films For Photovoltaic Applications

A thesis
Submitted to the Council of the College of Science
University of Diyala in Partial Fulfillment of Requirements
for the Degree of Doctor of Philosophy in Physics sicences

By

Layth Ali Saleh

B.Sc. in Physics, 2003
M.Sc. in Physics, 2016

Supervised By

Prof. Dr.
Ziad T. Khodair

2022 A.D. 1444 A.H.

بسم الله الرحمن الرحيم

هُو الَّذِي جَعَلَ الشَّمْسَ ضِيَاءً وَالْقَمَرَ نُورًا
وَقَدَّرَهُ مَنَازِلَ لِتَعْلَمُوا عَدَدَ السِّنِينَ
وَالْحِسَابَ مَا خَلَقَ اللَّهُ ذَلِكَ إِلَّا بِالْحَقِّ
يُفَصِّلُ الْآيَاتِ لِقَوْمٍ يَعْلَمُونَ ﴿5﴾

صدق الله العظيم

سورة يونس : الآية-5-

Supervisors Certification

We certify that this thesis entitled "*Synthesis of Some Ternary Metal Oxides and sulphides Nanostructures Thin Films for Photovoltaic Applications*" for the student (Layth Ali Saleh), was prepared under our supervisions at the Department of Physics, College of Science, University of Diyala in partial fulfillment of requirements needed to award the degree of *Doctor of Philosophy (Ph.D.) of Science in Physics.*

Signature:

Name: Dr. Ziad Tariq Khodair

Title: Professor

Address: College of Science,

University of Diyala

Date: / / 2022

Head of the Physics Department

In view of available recommendation, I forward this thesis for debate by the examining committee.

Signature:

Name: Dr. Ammar Ayesh Habeeb

Title: Assistant Professor

Head of the Physics Department

Address: College of Science, University of Diyala

Date: / / 2022

Scientific Amendment

I certify that the thesis entitled " ***Synthesis of Some Ternary Metal Oxides and sulphides Nanostructures Thin Films for Photovoltaic Applications*** **" presented by student (Layth Ali Saleh) has been evaluated scientifically, therefore, it is suitable for debate by examining committee.**

Signature

Name: Widad H . Abbas

Title: Assistant Professor

Address: Al-Mustansiriyah University, College of Basic Education, Science Department

Data: / / 2022

Scientific Amendment

I certify that the thesis entitled " ***Synthesis of Some Ternary Metal Oxides and sulphides Nanostructures Thin Films for Photovoltaic Applications*** **" presented by student (Layth Ali Saleh) has been evaluated scientifically, therefore, it is suitable for debate by examining committee.**

Signature

Name: Dr. Isam M. Ibrahim

Title: Professor

Address: University of Baghdad, College of science, department of Physics

Data: / / 2022

Linguistic Amendment

I certify that the thesis entitled " ***Synthesis of Some Ternary Metal Oxides and sulphides Nanostructures Thin Films for Photovoltaic Applications*** **" presented by (Layth Ali Saleh) has been corrected linguistically; therefore, it is suitable for debate by examining committee.**

Signature

Name: Esam H. Hameed

Title: Assistant Professor

Address: University of Diyala, College of science

Data: / / 2022

Examination Committee Certificate

We certify that we have read this thesis entitled " *Synthesis of Some Ternary Metal Oxides and sulphides Nanostructures Thin Films for Photovoltaic Applications* " and, as an examining committee, we examined the student (Layth Ali Saleh) on its content, and in what is related to it, and that in our opinion it meets the standard of a thesis for the degree of *Doctor of Philosophy of Science in Physics.*

(Chairman)
Signature
Name: **Dr. Tahseen H. Mubarak**
Title: Professor
Address: College of Science, University of Diyala
Date: / / 2022

(Member)
Signature
Name: **Dr. Nabeel A. Bakr**
Title: Professor
Address: College of Science,
University of Diyala
Date: / / 2022

(Member)
Signature
Name: **Dr. Suad.H. Aleabi**
Title: Professor
Address: College of Eduction (Ibn Al-Haitham),University of Baghdad
Date: / / 2022

(Member)
Signature
Name: **Dr. Muslim A . Abid**
Title: Assistant Professor
Address: College of Science,
Al-Mustansiriyah University
Date: / / 2022

(Member)
Signature
Name: **Dr. Jasim M. Mansoor**
Title: Assistant Professor
Address: College of Science,
University of Diyala
Date: / / 2022

(Member / supervisor)
Signature
Name: **Dr. Ziad Tariq Khodair**
Title: professor
Address: College of Science,
University of Diyala
Date: / / 2022

Approved by the Council of the College of Science
(**The dean**) Signature: Date: / / 2022
Name: **Dr. Tahseen H. Mubarak** Title: professor

Dedications

To

The first teacher who gave me the strength and patience and diligence.

(My father)

To

My way candle that lit up my life and stayed up nights to my care.

(My late Mother)

To:

The lights of my life

My wife and my children

To:
The lights of my eyes
Brothers and sisters
To:
My beloved country Iraq
The martyrs of Iraq with all the love and appreciation

Acknowledgments

First of all, I would like to thank ***Allah***, for his generosity and mercy in giving the strength and the ability to complete my studies.

I would like to express my deep gratitude and appreciation to my supervisor **Prof. Dr. Ziad Tariq Khodair** for suggesting the topic of the thesis and for his continuous advice and guidance during this work.

I would like to express my profound gratitude to **prof. Dr. Nabeel Ali Bakr** for his kind cooperation and constant support and **Prof. Dr. Sabah Anwer Salman**, for his constant encouragement throughout my studies for helping me. study in the Department of Physics,College of Science, University of Diyala.

Special thanks are extended to the University of Diyala, College of Science,Special thanks to the Dean of the College of Science, University of Diyala **Prof. Dr. Tahseen H. Mubarak** and the head of the Physics Department, **Assist .Prof. Dr. Ammar A. Habeeb** and all the Staff of the Department of Physics for their assistance.

Finally, I thank all my classmates and I wish them success and I would also express my deep sense of gratitude to **Omar Ahmad, Shahlaa Munther and Marwa Rashid.**

Abstract

In this study, thin films of prepared materials (Cd_2SnO_4 and Zn_2SnO_4) were deposited via spray pyrolysis at temperatures (450, 500, and 550 ℃), while thin films of prepared materials (Cu_2SnS_3 and CuZnS) were deposited using spin coating at temperatures (2000, 250, and 300 ℃). The materials NPs (Cd_2SnO_4 and Zn_2SnO_4) were prepared at temperatures of (550 ℃) while the materials (Cu_2SnS_3 and CuZnS) were prepared at temperatures of (300 ℃) using the autocombostion sol-gel method.

The structural, optical, and electrical (Hall effect) properties of the obtained thin films were investigated. X-ray diffraction (XRD) results demonstrated that the films prepared by spray pyrolysis method Cd_2SnO_4 and $Zn_2SnO_4$are polycrystalline with a cubic structure (Spinel), whereas the films prepared by spin coating Cu_2SnS_3 are polycrystalline with a tetragonal structure and a hexagonal structure of CuZnS, and that an increase in substrate temperature increased the crystal size. Using the Scherer formula, the crystal sizes of (Cd_2SnO_4, Zn_2SnO_4, Cu_2SnS_3, and CuZnS) were determined to be 43.8 nm, 22.0 nm, 22.5 nm, and 37.2 nm, respectively. The X-ray diffraction results further revealed that all sol-gel-prepared films of Cd_2SnO_4, Zn_2SnO_4, Cu_2SnS_3, and CuZnS are polycrystalline with a cubic structure. The FTIR spectra indicated the formation of the materials and the presence of broad vibration peaks (O-H) via spray pyrolysis and spin coating methods.

The existence of nanostructures in the thin films prepared with (XRD, AFM and FE-SEM) techniques was confirmed as the results of atomic force

microscopy (AFM) measurements demonstrated a clear temperature dependence in the values of grain size, surface roughness, and the square root of the mean roughness with the substrate. Through the use of thermal evaporation and spin coating methods . The optical characteristics were investigated by recording the spectrum absorbance and transmittance over a range of wavelengths (300-900 nm).

Thin films of Cd_2SnO_4 and Zn_2SnO_4 demonstrated a decrease in absorption with rising transmittance values and an increase in wavelength. The results also demonstrated an increase in the values of the absorption coefficient with an increase in the substrate temperature, an increase in the absorption of the films with a decrease in the transmittance values, and an increase in the wavelength of Cu_2SnS_3 and CuZnS. For the films prepared by spin coating method. It showed that the energy gap values increase with the increase in the substrate temperature of the films prepared by spray pyrolysis method Cd_2SnO_4 and Zn_2SnO_4 their energy gap values were 2.75 eV and 3.30 eV at 550 ^oC, respectively. The energy gap of each of Cu_2SnS_3.and.CuZnS was.also measured, and it was found to be equal to eV1.65 and eV1.80, respectively, at a temperature of 300 ^oC, which was prepared by spin coating method.

The Hall effect results demonstrated that increasing the substrate temperature improves the electrical properties of all films, with Cu_2SnS_3 having the highest electrical conductivity at 1.001×10^6 $(\Omega .cm)^{-1}$, which was offset by an increase in the concentration of charge carriers of 1.23×10^{23} $(cm)^{-3}$ and a decrease in electrical resistivity of 9.987×10^{-7} $(\Omega .cm)$.

Cd_2SnO_4 and Zn_2SnO_4 were subsequently deposited on porous silicon by the spray pyrolysis method, while Cu_2SnS_3 and CuZnS were deposited via the spin coating method. And Cd_2SnO_4, Zn_2SnO_4, Cu_2SnS_3, and CuZnS were deposited using the drop-casting method (1µm thick porous silicon). Then, using spray pyrolysis, aluminum was deposited as a conducting electrode on the back face of the silicon cell. The features of the solar cell and photodetector were subsequently evaluated. The parameters of the photovoltaic current density (I-V) curves of manufactured solar cells were measured under 100mW/m^2 of simulated solar light. The parameters (open-circuit voltage V_{OC}), (closed-circuit current I_{SC}), (fill factor FF %), and (solar cell efficiency η %) were determined.

The thin films that were deposited by spin coating method offered the maximum performance, and its value was (4.7%).For heterogeneous junctions (CuZnS)/PSi/n-Si/Al, and the results indicated that the drop-casting approach had a major role in enhancing the performance of the solar cell. The heterojunctions (Cu_2SnS_3)/PSi/n-Si/Al produced the greatest efficiency value (7.80 %). The spectral response measurements of the prepared photodetectors revealed that they performed within the range of (400-900) nm, which is the maximum spectral response value for heterogeneous junction (CuZnS) PSi / n-Si / Al that can be employed for near-infrared photodetector applications. The red and visible spectrum, where the spectral response (Rλ) and specificity detection (D*) of CuZnS/PSi/n-Si/Al photodetectors are approximately (0.60A/W) and (9.2x10^{12} cm Hz1/2 W^{-1}) at λ~ 450 nm, respectively.

Table of Contents

Chapter Three: Experimental Part

List of Figures

List of Tables

List of Symbols

Symbol	Meaning	Units
λ	The wavelength of the incident X- ray	nm
θ	Bragg’s angle	degree
n	Integer number	-
D	crystallite size	nm
k	Shape factor	-
a ,b and c	Lattice constants	Å
hkl	Miller indices	-
d_{hkl}	Inter planar spacing	Å
β	Full width at half maximum	Degree
δ	Dislocation Density	cm^{-2}
$N_{\circ}$	Number of crystallites per unit area	cm^{-2}
T	Transmittance	-

I_o	Incident light intensity	mW/cm^2
I_T	Transmitted light intensity	mW /cm^2
R	Reflection	-
I_R	Reflectance light intensity	mW/cm^2
n	Refractive Index	-
A	Absorbance	-
ε	Micro strain	-
A' and B	Constant depending on properties of bands	-
h	Planck 's constant	J.s
$h\nu$	Photon energy	eV
E_g	Optical Energy Gap	eV
V.B	Valence band	eV
C.B	Conduction Band	eV
r	Exponential coefficient depends on the type of transition	-
α	Optical absorption coefficient	cm^{-1}
E_u	Urbach energy	meV
$\vec{k}$	Wave vector	cm^{-1}
E_{ph}	Phonon energy	eV
t	Film Thickness	nm
R_s	Series resistance	Ω
R_{Sh}	Shunt resistance	Ω
μ_H	Hall mobility	$m^2 /(V.s)$
n_H	Concentration of charge carriers	$(cm)^{-3}$
R_H	Hall coefficient	m^3/C
σ	Conductivity	$(\Omega.m)^{-1}$
V_H	Hall Voltage	V
B_Z	magnetic field strength	Tesla
V	Voltage	V

V_a	Applied Voltage	V
K_B	Boltzmann constant	J/K
q	Electron charge	C
I_{ph}	The light-generated current density	mA
I_L	Light induced current	mA
I_d	Dark current	mA
ǹ	The diode ideality factor	-
T	Temperature	K
I_o	The saturation current density	mA
I_E	Electric current	mA
I_{max}	Maximum current	mA
I_{sc}	Short circuit current	mA
I_{sh}	Shunt current	mA
V_{max}	Maximum voltage	V
V_{OC}	Open-circuit voltage	V
J_{max}	Current density at maximum power point	mA/cm^2
J_{sc}	Short- circuit current density	mA/cm^2
F.F	Fill Factor	-
ɳ	Efficiency	-
P_{in}	The incident power	mW/cm^2
p_{max}	Maximum power	mW/cm^2
R_λ	Responsivity	$A.W^{-1}$
$D_\lambda{}^*$	Spectral Detectivity	$cm.Hz^{1/2}.W^{-1}$
G	Photocurrent Gain	-
$\mathcal{A}$	The active surface area of the cell	cm^2

List of Abbreviations

Abbreviation	Definition
AFM	Atomic Force Microscope
FE-SEM	Field emission scanning electron microscopy
FTIR	Fourier Transform-Infrared Spectroscopy
FWHM	Full Width at Half Maximum
hkl	Miller Indices
I-V	Current-Voltage
J-V	Current density–Voltage
P	Porosity
PCE	Power Conversion Efficiency
PD	Photodetector
PL	Photoluminescence
PSi	Porous Silicon
PV	Photovoltaic
RMS	Root Mean Square
UV	Ultra violet
Vis	Visible
W-H	Williamson-Hall
XRD	X- ray Diffraction

Chapter One

Overview of Nanomaterials
and
Literature Review

1.1 Introduction

When a material's size is lowered to the nanoscale, its chemical and physical characteristics are radically altered. Nanoscience focuses on controlling the formation of nanostructures and morphology, whereas nanotechnology studies the link between matter's size and function [1]. Thin-film physics is a subfield of solid-state physics that will ultimately become a discipline. A layer with a thickness of tens of nanometers is referred to as a nanolayer (film). Thin film has a thickness of less than one micron, according to a published [2]. Because the film layer is so light, it is only placed on the specific type of substrates depending on the study's nature or scientific requirement necessity. Glass slides, silicon wafers, aluminum, quartz, and other substrates are among them. Properties of a thin film vary from bulk material depending on the kind of significant research. Thin films were produced for the first time in 1852 by (Busen & Grove) by a chemical reaction, and a thin metallic film was obtained in 1857 by the scientist (Farady) using thermal evaporation [3].Furthermore, various factors influence the characteristics of thin films, including the thickness and kind of film utilized, as well as the evaporation conditions employed to make the films. Thin films have a wide range of applications, including rectifiers then junction diodes, integrated circuits, optical communications as light-emitting diodes, semiconductor lasers and detectors, light filters, solar cells, and special-purpose mirrors [4]. In addition, they are used in a range of applications to protect thin-film-painted materials from corrosion, environmental contact, and surface deterioration [5]. The sensitive materials that are convenient for manufacture using a variety of electrical, optical, then optoelectronic possessions are required for a broad area of semiconductor applications. Rather than thinning down bulk material, thin films are generated by depositing ingredients onto a clean, supporting substrate to build up film thickness[6].

1.2 Thin Films Preparation Methods

Thin film properties are quietly sensitive to the preparation method. Different techniques have been developed to deposion thin film on alloys, polymers, superconductors, and metals on several kinds of substrate materials. Indeed, no technique can deposit thin films that cover all the desirable aspects like equipment cost, deposition conditions, substrate material nature, etc. The broad types of thin-film materials, their deposition methods, processing,spectroscopic characterization, fabrication technologies, optical characterization investigations, physical and chemical properties, and structure-property relationships are the main features of these devices and the basis of thin-film technologies. The achievement and economics of thin-film components are the industrialization techniques used to produce the devices.Several techniques are valuable and available to enhance nanostructure thin film in a wide range of potential applications. The production techniques of nanostructured thin film are usually classified into two categories, as shown in figure 1.1:

(i) Physical techniques, such as the evaporation or sputtering of the material from source and deposition on a substrate, etc. [7].

(ii) Chemical techniques like a chemical reaction between volatile/non-volatile compounds of the material and deposition on the various substrates etc. [8].

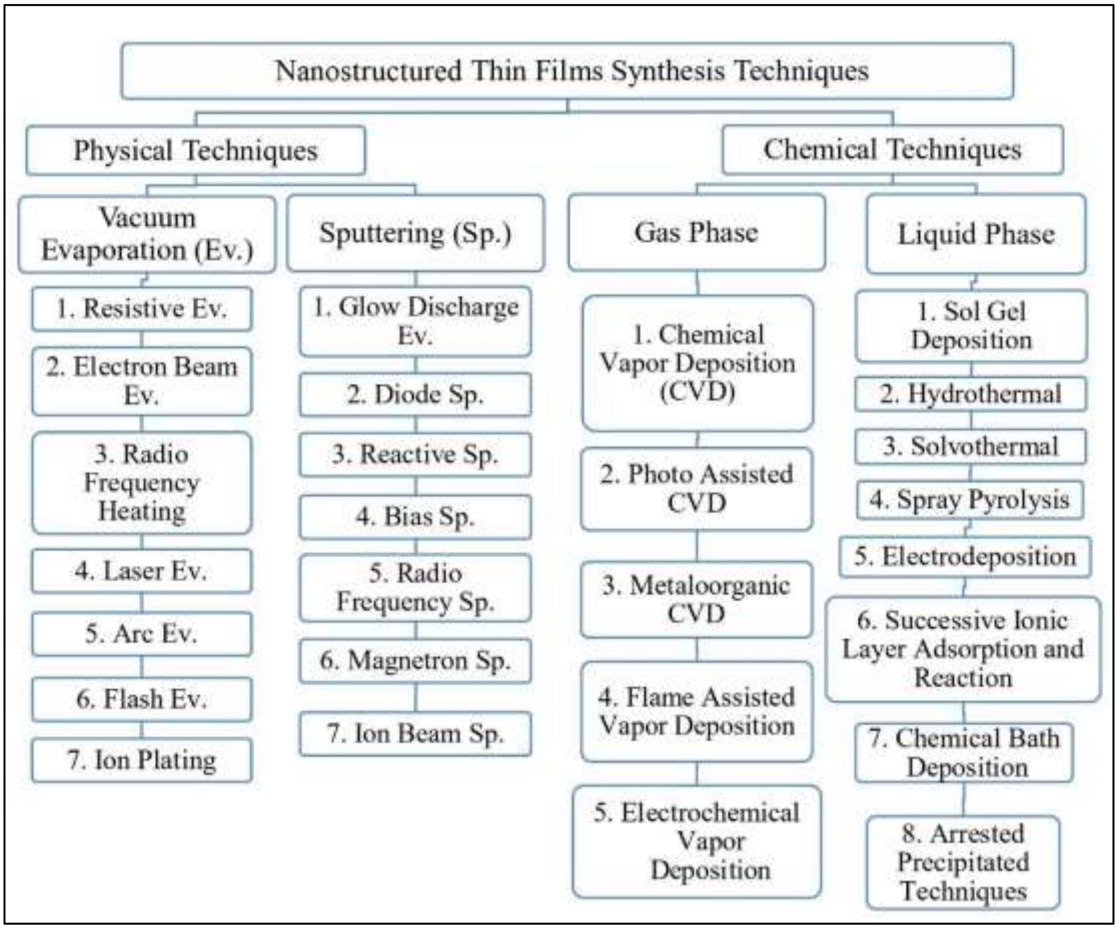

Figure **1.1.** Various nanostructured thin film syntheses techniques [9].

1.3 Spray pyrolysis Technique

One of the most common processes for generating big area homogeneous coatings is Chemical Pyrolysis by spraying. Chemical Pyrolysis by spraying. is particularly beneficial in the fabrication of conventional and thermal mirrors and very competent filters plus solar cells [10]. One of the most frequent depositings of .a wide-ranging of materials in thin-film form. It Chemical Pyrolysis by spraying . For manufacturing high-quality thin films, variables such as substrate temperature, spray rate, and solution concentration, among others, must be fine-tuned. Atomization pyrolysis have on the other hand, get a lot of interest [11]. Spray pyrolysis involves spraying an aqueous solution containing soluble salts of the constituent atoms of the desired compounds to the heated substrates onto a techniques like ultrasonic nebulization, better Pyrolysis by spraying. Coronas Pyrolysis by spraying., electronic Pyrolysis by spraying., and microprocessor-based spray pyrolysis have on the other hand, get a lot of interest [11]. Particles of the required chemicals are dissolved in water and then sprayed over heated surfaces that are held at high temperatures for spray pyrolysis. This is done in order to break down the compounds in question. When the sprayed droplets reach the hot substrate, they undergo pyrolysis breakdown and produce a single crystal or cluster of crystallites. In the vapor phase, various volatile byproducts and excess solvents escape [12]. Despite its flaws, this approach has numerous advantages [13, 14].

1- Safe low-cost and simple technique.
2- The necessary equipment cost and raw materials are inexpensive.
3 -Using high-quality targets and substrates is not essential.
4 -Spray settings can be adjusted to manage film thickness and uniformity.
5- It can be used in any type of weather.
6- It has the ability to manufacture thin film materials with a high melting point.
7- It has the ability to produce thin-film materials with excellent homogeneity and enormous dimensions.

1.4 Spin Coating Technique

A Spin coating is a fast and most commonly utilized chemical deposition method for producing thin and homogenous organic or inorganic sensing from solution. This method enables the creation of very repeatable and homogeneous films. Two forces act on the solution during spin coating: adhesive forces at the solution substrate contact and centrifugal forces induced by the high-speed spinning. These two opposing forces will cause a considerable shearing action at the interface, leading the solution to create a thin film of varying thickness, determined by rotating velocity, solution concentration, and a viscosity [15]. Several factors must be considered to generate homogeneous films, including solvent evaporation rate, fluid viscosity, solution concentration, angular velocity (rotation speed), and spinning time. The advantage of the spin coating technique is its high ability to provide thin films with thickness ranging from a few nanometers to a few microns in an easy, quick and economical way, the film thickness can be easily changed by changing spin speed, and it is considered a low-cost operating system [16].

1.5 Cadmium Stannate (Cd_2SnO_4) Properties

Cd_2SnO_4 films have a spinel cubic polycrystalline structure as shown in fig 1.2. The cations ratio of Cd and Sn has an essential role in achieving a homogeneous structure of thin-film without any secondary phases, and the lattice parameters have an approximate value of a=b=c=0.9174 nm [17, 18]. Cadmium tin oxide is a n-type semiconductor [17]. It has high carrier mobility, with n-type doping, The visible absorption edge goes to considerably higher energy [19]. Cadmium stannate has a low electrical resistivity, good transmittance in the visible light spectrum, and low reflection in the near IR range. Spray pyrolysis was used to make thin films of Cd_2SnO_4 with a 3eV energy bandgap [20]. Cd_2SnO_4 thin films were demonstrated. It has been several essential advantages of the CdTe/CdS-based solar cells. In contrast, they have the best adhesion to the CdTe/CdS solar cells with respect to tin oxide (SnO_2)[21].

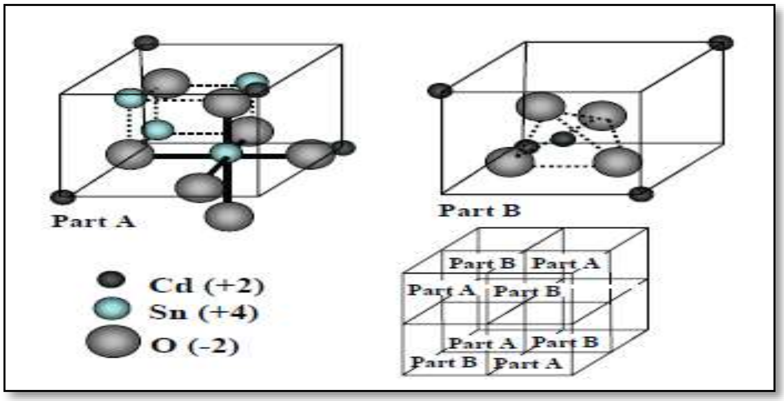

Figure **1.2.** Crystalline structures of Cd_2SnO_4(Cubic spinel) [17].

1.6 Zinc Stannate (Zn_2SnO_4) Properties

Because of their unique features in optics and electronics, ZnO and SnO_2 have gotten a lot of attention in recent years. However, ternary semiconductors Zn_2SnO_4 may have received better properties and are still less studied and investigated. As it has high-electron mobility, high-electrical conductivity, and significant optical properties, all of these properties make it to be appropriate for solar cell, dye sensitized solar cell, gas sensor Li-ion battery and photodtectors applications [22, 23]. Fig 1.3 Zn_2SnO_4 has a polycrystalline crystal structure (cubic spinel) [24], with the lattice parameters a=b=c= 8.657 nm [25]. has a lot of electron mobility . Pyrolysis by spraying was used to make thin film. Of high electrical, an n-type transparent conductive oxide with a conductivity of 3.7 e V and a large [24].

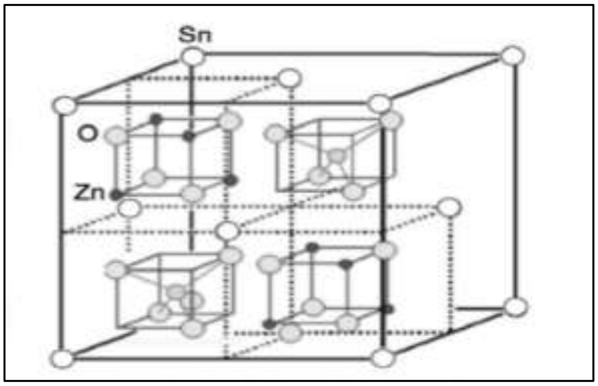

Figure **1.3.** The cubic spinel structure of Zn_2SnO_4 [24].

1.7 Copper-Tin-Sulphide(Cu_2SnS_3) Properties

Since 1960, the Cu–Sn–S system has been considered. Cu_2SnS_3, Cu_3SnS_4, and Cu_4SnS_4 are the three phases in this system Cu_2SnS_3 exhibits polymorphs such as monoclinic, cubic, tetragonal, and triclinic as shown in figure 1.4 structures in Additionally, Cu_2SnS_3 crystallizes in wurtzite and hexagonal nanocrystalline form . They've been discovered to be an important absorbent for solar cell use. The (Cu–Sn–S) system is part of the (I–IV–VI) group, and it contains non-toxic, abundant, and inexpensive elements. Due to its usefulness in a wide range of applications, the ternary Cu_2SnS_3 (CTS) semiconductor has recently gained a lot of attention. This system's optoelectronic features make it ideal for this application. As photovoltaic devices, the electrical conductivity of the p-type with band gap may be controlled in an optimal range from (1.0 to 1.5 eV). A high optical absorption value of $\sim 10^5$ cm^{-1} is also seen. CTS thin films have been tried as absorbers solar cells using thin films (TFSCs) by a variety from approaches such as evaporation, sputtering, electro-deposition, pulsed laser deposition and chemical bath deposition [26-28].

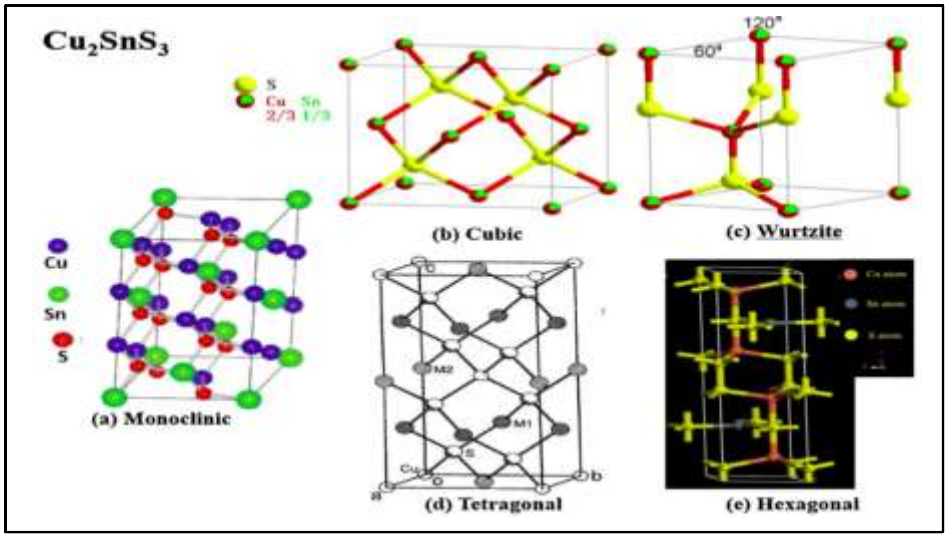

Figure **1.4.** Crystallographic structures of Cu_2SnS_3 (a) Monoclinic, (b) Cubic, (c) Wurtzite, (d) Tetragonal and (e) Hexagonal [27].

1.8 Coper-Zinc Sulphide (CuZnS) Properties

CuS is an essential semiconductor with unique electrical, chemical, and optical characteristics and a wide range of solar cell applications. CuS thin films have recently exposed ability in applications for example gas-sensor materials [29] .2.36 eV and 2.03 eV it direct bandgap has CuS with a hexagonal structure, according to structural and optical analysis [30] .The most significant rate of all (II–VI) composite semiconductors with n-type semiconductor and broad direct bandgep is (ZnS), which has on energy bandgep of (3.65 eV). It can therefore be utilized in optoelectronics and as an anti-reflective coating for heterojunction solar cells [31].

Nanocomposites thin films' structural, morphological, optical, and electrical properties have recently become an interesting topic due to their unique techniques. CuZnS ternary compounds are a promising nanostructured material for electroluminescent and photoconductor devices, as well as photovoltaic cells. The nano-composite films can also be used as a solar cell absorber. Improvements in the characterisation of copper-zinc sulphide (CZS) are of particular importance since these spectacular p-type inorganic materials have a large direct band gap and are crucial in solar cell applications [29].

1-9 Literature Review

Tiwari et al., (2013): Direct liquid coating (DLC) was used to precipitate thin films of tetragonal Cu_2SnS_3 (CTS) made of a metal-thiourea compound methanolic precursor solution. X-ray Diffraction confirms the formation of tetragonal Cu_2SnS_3. AFM and scanning electron microscopy demonstrated that the films are soft and uniform with a roughness (RMS) of 1–2 nm energy band gap (Eg) for Cu_2SnS_3 1.12 eV plus 10^5 cm^{-1} for absorption coefficient (α), according to optical measurements. The films are p-type, with a 0.5 s/cm electrical conductivity(s), rendering to hall measurements, The concentration and mobility of holes are around (10^{18} cm^{-3} and $1cm^2/V/s$), respectively. DLC developed non-toxic thin-film solar cells (TFSC) made from graphite/Cu_2SnS_3/ZnO/ITO/SLG with a power transformation efficiency PCE of 2.10 % and voltage in the open circuit., current in a short circuit, and the fill factor 0.816 V, 6.14mA/cm^2, pluse 0.42, respectively [32].

Sreejith et al., (2014): Chemical spray pyrolysis was used to make CuZnS thin films. Rendering to the findings, the material may be transformed of n-type to p-type with a 4-order improvement in electrical conductivity by just increasing the Cu content. In comparison, increasing Cu content causes the band-gap to decrease from 3.4 - 1.8 eV. High Cu concentration films are more absorbent, but low Cu concentration films can be employed as a buffer/window layer in solar cells. The absorber layer was CuZnS, and the buffer layer was In_2S_3. The J-V possessions from the cell were measured by Ag as the highest electrode. V_{oc} =0.451 V, J_{sc} =5.47 mA/cm^2, FF = 42.2 %, and η= 1.04% were the parameters obtained for the optimal doped cell [33].

Godines et al., (2014): On glass substrates, the researcher developed Cd_2SnO_4 polycrystalline thin films with cubic phase using the sol-gel process. Commencing with a combination of two simple CdO and SnO_2 precursor solutions and thin films formed at room temperature. In the precursor solution, the atomic concentrations of Sn (x) in relation to Cd (1-x) were x=16, 25, 29, 32, 35, and 40. After the annealing operations, Cd_2SnO_4 films retained their spinel-type crystalline structure. The Cd/Sn ratio of the Cd_2SnO_4 compounds was closest to that of the Cd_2SnO_4 compounds at x=29 at % without annealing. Cd_2SnO_4 films demonstrated good optical transmission ~85% in the 500 nm $<\lambda<$

1500 nm range, both with and without annealing. For Cd_2SnO_4 films (x=33 at%) annealed in a vacuum at 550 °C, a minimum resistivity of roughly 2×10^{-3} Ω cm was found, by a direct band gep energy of 3.55 eV [34].

Zhao et al., (2014): A method for producing high-quality, homogenous, and band-gap-adjustable Zn_2SnO_4 nanotubes has been published. By altering the heat treatment temperature, These nanotubes can be autologous-assemble inside a range from different nanofilms by changeable.Gaps in optical bands ranging of 3.54 to 3.18 eV. The Zn_2SnO_4 nanotube-nanofilm-based UV-light photo detectors have been successfully produced and show much greater photocurrent and a bigger photocurrent to dark current part than separate nanostructure-founded UV-light photodetectors. Top-showing photo detectors, solar cells, plus Li-ion battery electrode materials could all benefit from it [35].

Kanai et al., (2015): According to experts, Cu_2SnS_3 is a p-type semiconductor that has an coefficient of absorption of over 10^4 cm^{-1} and a bandgap energy of 0.92 to 1.77 eV. As a result, it has proven to be a highly absorbent layer to thin-film solar cells. According to this study, CTS thin films made via deposition and annealing of primary films made via co-evaporation of Cu,Sn,S. The photovoltaic properties of solar cells with CTS films as absorbent layers were then studied in relation to the annealing temperature. A solar cell with the voltage in an open circuit of 248 mV a 570°C annealed CTS thin film. A current density in a short circuit of 33.5 mA/cm^2, the factor of fill 0.439, and a transformation efficiency of 3.66% [36].

Dong et al., (2015): Cu_2SnS_3 Sulfurizing stacked metallic precursors yielded CTS thin sheets. and sputtering them by a radio frequency magnetron, according to this study. The synthetic, structural, morphological, optical, plus electrical characteristics of Cu_2SnS_3 thin films formed up soda-lime glass substrates are influenced by the sulfur temperature. The synthetic study reveals totally of the samples remain Sn- rich. Within increasing sulfurization temperatures, the Cu/Sn ratio approaches the stoichiometric composition of CTS. According to structural characterization, Cu_2SnS_3 thin films sulfurized by upper sulfur temperatures exhibit greater crystalline kind. At 550 °C for sulfurization, the CTS thin film has a greater amount of crystallization and a bigger average grain size. bandgap is roughly 1.0 eV,as shown by the transmission plus reflectance spectra, compatible with the projected estimate based on outer quantum efficiency. The photoelectric characteristics from solar cells improve as the sulfurization temperature rises. For an area of 0.16 cm^2,the solar cell produced by the Cu_2SnS_3 absorber stratum annealed by 550 °C achieves a 0.28% efficiency [37].

Kanai et al., (2015): Cu_2SnS_3 thin films have been characterised as the result of annealing after co-evaporation of Cu, Sn, and cracked sulphur. Now a quick thermal treating oven supplied by N_2 gas on air pressure, the as-deposited films by annealed at 570 °C for 5 minutes in the of attendance 100 mg of sulphurion lumps. After that, the CTS films were utilised such as absorber layers in solar cells, then their efficiency was measured for various Cu/S ncompositional rate . Films through a considerably Sn-rich composition had the largest grain size. The use of a CTS thin film in solar cells by a (Cu/Sn) rate of nearly 1.9 had the best performance. The voltage across the open circuit of cell by a Cu/Sn rate of 1.87 was 258 mV, the current density in a short circuit was 356mA/cm^2, the factor of fill was 0.467 plus power transformation efficiency was 4.29 % [38].

Liu et al., (2016): in this research demonstrates the use of small -cost metal stannate-founnded nanostructures as fast materials for great- fulfillment UV photodetectors. Thin-film devices embrance of amorphous $ZnSnO_3$ nanotubes and/or polycrystalline Zn_2SnO_4–SnO_2 nanoparticles by diverse optical plus electrical architectures were successfully produced using a durable, affordable, and scalable drop-casting approach. Thermal treatment from amorphous $ZnSnO_3$ nanocubes resulted in the formation of Zn_2SnO_4–SnO_2 heterojunction nanoparticles. Big-area, regular, and continuous film photodetectors by clear plus quick responses, with rise and decay durations smaller than 1.0 s, have been developed when subjected to UV irradiation 370 nm. When compared to their predecessors, these two stannate nanostructures have more benefits, for example ZnO, SnO_2, Zn_2SnO_4, ZnO–SnO_2 single nano structures or film photo sensors, containing photo-sensitivities that are extremely high ($S>10^2$ and $\sim10^3$ existed completed for ($ZnSnO_3$) and Zn_2SnO_4–SnO_2 photodetectors, respectively then excellent responsivite (as great as 0.5 A W^{-1} at 5.0 V bias of the Zn_2SnO_4–SnO_2 photo sensors) below short light intensity [39].

Dias and Krupanidhi (2016): Have successfully synthesized Cu_2SnS_3 (CTS) thin-film deposition employing a spin coating method. The films feature a tetragonal crystal structure, according to XRD. The film form and particle size were then determined using SEM. The crystal's various planes were examined using TEM. Its excellent absorption coefficient of 10^4 cm^{-1} and optimum band gap of 1.23 eV enable its use as photoactive material. The visible and infrared (IR) photoresponses were examined at various light intensities. At 3V applied bias, the current increased from a dark current of 0.31 A to 1.78 A at 1.05 suns and 8.7 A under 477.7 m W/cm^2 IR illumination intensity. At 1.05 lights, the responsivity, sensitivity, outer efficiency in quantum, Then it was revealed that specific detectivity exists. (10.93 mA/W, 5.74 and 2.47) %, plus 3.47× 10^{10}, respectively, while at 477.7 m W/cm^2 IR illumination, they were 16.32 mA/W, 27.16 and 2.53 percent, and 5.10× 10^{10} Jones, respectively. The transient photoresponse was measured using visible and infrared illumination [40].

Sreejith et al., (2016): CuZnS is a novel potential element for thin-film photovoltaics that is plentiful and ecologically kindly, according to the report. Copper and Zinc atom ratios may be changed to control electrical and optical characteristics, making it suitable for use as an absorber or window layer. This material's conductivity may be altered of n to p by changing the Cu/Zn rate. The current study shows that raising the Cu to Zn ratio in CuZnS improves the cell characteristics of the CuZnS/In_2S_3 hetero junction significantly. Current density rise of 5.4 mA/cm^2 to 10.7 mA/cm^2, improving transformation efficiency of 1% to 1.95%. Results are clear based by the enhancement from several band structures [41].

Kim et al., (2016): have reported that extremely crystallized CTS thin films by prepared via sputtering-based on deposition. Furthermore, the impact from various annealing temperatures by the crystallographic, electrical, Cu_2SnS_3 thin films were investigated for their optical characteristics. XRD from the (112), (220), and (312) planes reveal such the produced Cu_2SnS_3 thin films include a monoclinic structure. Extrapolating from external quantum efficiency (EQE) measurements, the direct bandgap energy of Cu_2SnS_3 thin film annealed at 580 °C is 1.03 eV. The CTS-based thin-film solar cells (TFSCs) are invented by a structure of Mo/CTS/CdS/i-ZnO/AZO/Al. 1.35% of initial power-transformation efficiency with a (28.3 mA/cm^2) of current density in a short circuit was obtained. An voltage in the open circuit. and the factor of fill were found to be 147.5 mV and 32% , respectively [42].

Becker et al., (2017): Reported a mono-crystalline CdTe/MgCdTe binary - CuZnS hole contact in a heterostructure solar cell an ITO electrode had been published. Other contact materials, such as a-Si:H or ZnTe, have been used in similar devices to achieve highet open-circuit voltages and low circuit current densities. Cu_x Zn_{1-x} S is a tunable material system that was synthesized by chemical bath deposition (a low-cost deposition process) and offered a variety of band gaps, conductivity, and band offsets. Devices with x = 15%, 25%, and 65% copper compositions have been created and analyzed, producing a top active-area power transformation efficiency of 12.9 %, an voltage in an open circuit of 956 mV, the factor of fill 63.5%, and a low current density in the circuit from 21.2 mA/cm^2 [43].

Xu et al., (2017): In this research. A thin coating of (CZS) for a solar cell was successfully prepared using a pyrolysis by spray preparation process. XRD, UV, SEM, and the J–V tester were used to study the impact of changing the spray temperature of the substrate on the structural, optical, compositional, morphological, and photovoltaic characteristics of the generated CZS film. Under ideal conditions, our unique CZS thin films include a perfect crystallinity phase with a band gap of 2.21 eV and transformation efficiency of 0.84 % , as evidenced by the results [44].

Asemi and M. Ghanaatshoar, (2018): In this work, a transparent conductive made an (oxide/mesoporous) Zn_2SnO_4.Thermal evaporation is used to place various types of metal oxide semiconductor thin films (such as SnO_2, TiO_2, and ZnO) on the FTO substrate to reduce charge recombination at the synthesized material interface and increase photovoltaic performance. The results show that, compared to SnO_2 and (ZnO), the TiO_2 thick layer is the best effective obstructive layer to suppressing recombination of charges and boosting the constructed devices current density in a short circuit and power conversion efficiency. Furthermore, the creation of an energy barrier at the FTO/Zn_2SnO_4 contact results in the formation of an energy barrier, The device with the TiO_2 blocking layer achieves With a current density of 7.36 mA/cm^2 in a short-circuit and a voltage in the open circuit of 664 mV, the highest power conversion efficiency is 3.02%. According to this study, Charge recombination at boundary is one of the major problems limiting the power conversion efficiency of dye-sensitized solar cells [45].

Wu et al., (2019): Using the sol-gel solution approach, they created monoclinic Cu_2SnS_3thin films. The influence of the Cu/Sn atomic ratio on structure and morphology have been investigated. The CTS films grew more compact when the Cu/Sn atomic ratio rise from 1.6 to 2.0, minor phases for example SnS faded away, then the grain size of the films reduced. The Cu/Sn ratio of 1.9 in the CTS film resulted in a monoclinic structure and homogenous morphology plus a band gap of 1.12 eV, resulting in a power transformation efficiency of 0.58%. Then, Cu_2SnS_3 (CTS) can be considered a possible thin-film solar-cell material [46].

Osorio - Rivera et al., (2020): The application of heterogeneous Cd_2SnO_4/ CdS/Cu_2O/Ag in solar cells was researched by the researcher. Chemical procedures were used to deposit the heterostructure on the glass substrate: (1) Sol-gel synthesis of Cd_2SnO_4 as TCO, (2) Chemical bath deposition of CdS as an n-layer, and (3) Cu_2O as the player via pyrolysis by spray . The Cd_2SnO_4 and CdS layers have thicknesses of 290 and 135 nanometers, respectively. Cu_2O (τ)

of various thicknesses was used to investigate the impact of this parameter on solar cell performance (135, 185, 220, 350, and 800 nm). Photovoltaic values at their best remained VOC = 346 mV, JSC = 1.57 mA/cm^2, FF = 33.4 and = 0.18 percent for = 220 nm. Gaps in the Cu_2O plus CdS bands. The current donating is mostly due to flaws in the Cu_2O lattice, which result in an energy level source inside the band gap [47].

Karimi et al., (2021): Using the co-precipitation approach, high-quality Zn_2SnO_4 nanoparticles were generated, and they were able to improve the degree of crystallization as well as a pure phase of the final nanopowders by varying pH, Temperatures of annealing plus concentrations of precursors. The porous layer was then modified with MgO and Al_2O_3 passivation layers, after which Zn_2SnO_4 crystalline nanoparticles by an average size of nearly 35 nm existed utilized as a porous layer. Controlling the solution concentration and spin coating operation speed enhanced the thickness of these barrier layers, which was critical in reducing recombination by significantly improving the showing of DSSCs. The electronic settings with the highest values were obtained for J_{SC} = 8.59 mA/cm^2, V_{OC} = 0.66 V, and FF = 0.51 for the MgO-treated device with a rotational speed of 4000 rpm, which exhibited a 40% increase in efficiency from 2.07% to 2.90 %as compared to the untreated sample. All of the treated samples showed a reduction in VOCs. Electrochemical resistance spectroscopy, The transport and recombination mechanisms were subsequently investigated using, voltage in open-circuit decay, and the dye loading procedure, which confirmed a higher transfer ratio and slower electron recombination in the greatest modified devices [48].

Deevi, and Reddy, (2021): Zinc Stannite Zn_2SnO_4 nanoparticles were synthesized using a solvent and heat technique, according to the study. XRD analysis reveals that the nanoparticles generated have a face-centered cubic spinel shape. According to TEM pictures, the produced Zn_2SnO_4 nanoparticles are roughly 20 nm in size. To prepare photoanodes for use in semi-transparent dye sensitized solar cells, a paste incorporating synthetic Zn_2SnO_4 nanoparticles was developed. Semi-transparent dye-sensitized solar cells based on dye adsorbed Zn_2SnO_4 photoanodes have a photoconversion efficiency of 0.86% [49].

1.10 Aim of the Work:

1-Synthsis of some different ternary metal oxides and sulfied Cd_2SnO_4 (CTO), Zn_2SnO_4 (ZTO), Cu_2SnS_3 (CTS), and CuZnS (CZS) thin films using different method (chemical spray pyrolysis, spin coating , sol-gel and drop-casting methods)

2-Study effect of substrates temperature on the structure ,Morphological ,Optical and electrical properties of prepared thin film.

3-Synthsis of Cd_2SnO_4 (CTO), Zn_2SnO_4 (ZTO), Cu_2SnS_3 (CTS), and CuZnS (CZS) nanoparticle by sol-gel method.

4-Applications of prepared thin films in photovoltaics applicable such as solar cell and photodetectors.

Chapter Two

Theoretical Part

2.1 Introduction

This chapter covers the fundamentals of solar cells, synthesis processes, and applications. It also defines photodetectors and describes how they work. Detectives and other important features are also discussed. Finally, the chapter includes theoretical equations for structural, electrical, and optical properties of thin films.

2.2 Nanomaterials

Nanotechnology has risen to the forefront of one of physics and other disciplines most significant and exciting topics, promising scientific revolutions that will soon affect the course of technology in a variety of domains. Nanomaterials are complex materials that range in size from 1 to 100 nanometers (nm) [50]. Nanoparticles provide unique potential because to their critical mechanical and physical properties, which might lead to new and exciting applications. In numerous facets of nanomaterial composition, significant progress has been made. The emphasis changed from synthesis to the development of wear- and corrosion-resistant functional structures and coatings. Materials have a wide range of properties based on the nanoparticles they contain. Compounds based on ceramic and metal nano-granules are far more durable than their larger-granule-based counterparts [51].

2.2.1 Classification of Nanomaterials

Consider the dimensionality of the nanoscale component with which the material is created, as this classification may be more meaningful in terms of the material's nanostructure [51, 52].

1. Zero-dimension (0- D)

In zero-dimensional (0-D) nanomaterials, all three dimensions of matter are present at the nanoscale; a great example is nanoparticles.

2. One-dimension (1- D)

One dimension of nanostructure in these nanostructures would be beyond the range of nanometers. for example (Nanowire and Nanotubes).

3. Two-dimensional (2- D)

This type of nanomaterial has two dimensions outside of the nanometer range. Coatings and thin multilayer films, as well as nanowalls and nanosheets, are examples of nanofilms.

4. Three-dimensional (3- D)

There are no dimensions at this nanoscale, but there are dimensions at the macroscale. Bulk materials are three-dimensional nanomaterials consisting of individual blocks on a nanometer scale (1–100 nm) or more. Figure 2.1 depicts nanomaterials of various forms and sizes.

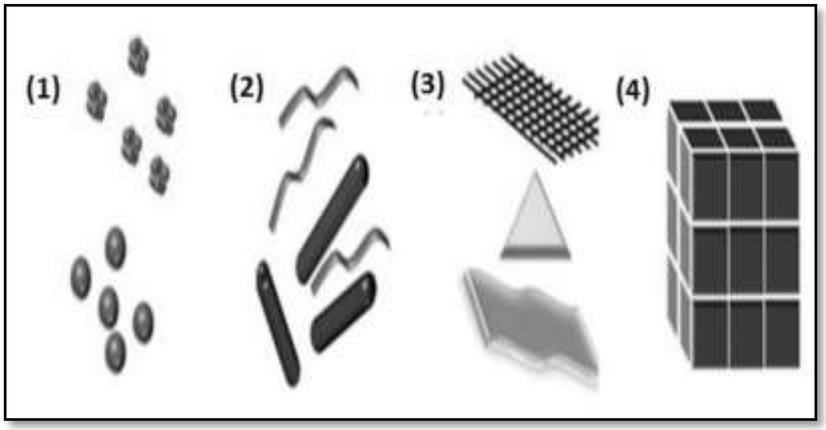

Figure 2.1. Schematic illustration classification of nanomaterials (1) 0-D spheres and clusters, (2) 1-D Nanofibers, Wires, and Rods (3) 2-D Films, Plates, and networks,s and (4) 3-D Nanomaterials [53].

2.3 Quantum Confinement Effect

Lehman and Gosele suggested a formation mechanism model [53] for quantum size structures. In this concept, these structures are thinned until they reach a diameter where size effects widen the effective band gap. With decreased dimensionality, these effects provide a thorough explanation of semiconductors' optical, electrical, and vibrational properties, as shown in figure 2.2 [54]. The absorption of a PSi material is highly influenced by quantum confinement (QC). There is also a widening band gap and a blue shift of the absorption edge [55]. PSi is home to a variety of luminous phenomena. From the UV to the IR, emission peaks have been discovered around various center wavelengths [56]. The origin of the illuminating phenomenon is thought to be quantum confinement in the skeleton's nano-size Si wires. The band gap grows when the feature size of such light-emitting parts diminishes with increasing porosity, causing luminescence peaks to shift in the spectra [57]. Since discovering its efficient visible photoluminescence at room temperature, PSi has gotten a lot of attention as a new optoelectronics material. To date, several experimental and theoretical investigations have been published in an attempt to determine the source of light emission by the PSi layer. Canham presented the first model of such events, in which visible emission results from electron-hole recombination between discrete energy levels inside quantum wells formed by bulk silicon areas separated by nanoscale silicon particles (nanocrystallites) [57]. A quantum-confined solid structure can be constructed in a number of different ways. Quantum well structures quantize charge carrier movement in one direction, quantum wire structures in two directions, and quantum dots in three directions [58]. The quantum confinement phenomenon in semiconductor nanoscale materials (quantum dots, wells, and wires) has recently gotten a lot of press because of its potential applications in optoelectronics [59]. The observed change in excitonic photoluminescence toward higher energies than bulk materials could be explained by the valance-conduction band gap widening as the size of a nano-object diminishes, increasing quantum efficiency [60]. According to quantum confinement, the energy gap of PSi can be estimated based on crystal size as follows [57]:

$$E_g^* = E_g + \frac{88.34}{L^{1.37}} \tag{2.1}$$

Where; $E_g^*$is the energy gap of PSi layer (eV), E_g is the energy gap of bulk silicon (eV), and L is the confinement diameter (nm).

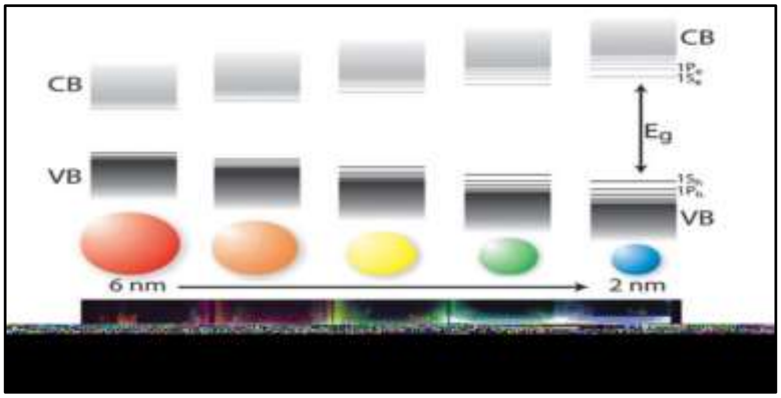

Figure 2.2. Schematic of the quantum confinement impact on the energy level structure of a semiconductor material [61].

2.4 The Semiconductor Materials

On the basis of conductivity, materials are divided into three categories: conductors, insulators, and semiconductors. Materials that fall between metals and insulators are called semiconductors. The resistance of metals is greater than the resistance of insulators. In 1833, Michael Faraday began researching semiconductor materials. He discovered that the resistance of silver sulfate is inversely proportional to its temperature, which affects electrical conductivity [62]. The two types of semiconductors are inorganic and organic semiconductors.

2.4.1 Inorganic Semiconductors

Inorganic semiconductor is any semiconductor with conductivities that alternate between metals and insulators. Inorganic semiconductors are divided into two categories: elemental semiconductor materials (group IV of the periodic table) and compound semiconductor materials. Compound semiconductor materials are made up of certain combinations of group III and group V elements, or group II and group VI elements. Some elemental semiconductor materials and compound semiconductor materials are shown in Table 2.1 [63].

Table 2.1. Some inorganic semiconductors [64].

Elemental Semiconductor	**Si (Silicon)**
	Ge (Germanium)
	AlP (Aluminum phosphide)
	GaAs (Gallium Arsenide)
	ZnO (Zinc Oxide)
	Tl_2SnTe (Thallium tin telluride)
	$BaTiO_3$ (Barium titanate)
	Cu_2ZnSnS_4 (Copper zinc tin sulfide)

2.4.2 Organic Semiconductors

In 1977, Heeger, Mac Diarmid, and Shirakawa discovered that the conductivity of aconjugated polymers may be increased up to 5 orders of magnitude for certain types of semiconductors. Molecular organic semiconductors and polymeric organic semiconductors are the two types of organic semiconductors [65]. Organic semiconductors are mostly carbon (C) and hydrogen (H) atoms. Small organic molecules can be utilized instead of polymer chains to create molecular organic semiconductors. Molecular organic semiconductors include aromatic hydrocarbon compounds such as tetrathiafulvalene, tetracyanoquinodimethane, and thallium (III) nitrate [66].

2.5 Hybrid Organic-Inorganic Semiconductors

Hybrid semiconductors usually refer to the materials that composed of different semiconductors: organic-inorganic semiconductors, where both of these semiconductors contribute to the charge transport and carrier concentration and have different band gaps [67]. The term heterojunction refers to the interaction of organic and inorganic semiconductors. The energy bands in the heterojunction area will have a discontinuity due to an abrupt junction in which the semiconductor transitions from a narrow band gap material to a broad band gap material. Materials made of organic and inorganic semiconductors with close work functions must be chosen to allow easy free charging.

2.6 Porosity of Porous Silicon

The porosity of porous silicon is its most essential feature (PSi). Porosity [68] describes the vacancy fraction within the PSi layer. Throughout the preparation process, the porosity of the silicon substrate is highly impacted by the wafer type, wafer resistance, HF concentration, etching time, and etching current density. When the current density rises or the HF concentration falls, it will continue to rise, and weight measurements will estimate the porosity. Weighting the silicon substrate before and after the etching procedure (m_1 & m_2) and after removing the porous silicon layer with molar NaOH can be used to assess the layer's porosity (m_3). The porosity can be calculated using the following equation [69]:

$$\gamma(\%) = \frac{m_1 - m_2}{m_1 - m_3} \qquad (2.1)$$

where γ is the porosity. According to the above formula, it is necessary to use the thickest sample possible.

2.7 Physical Properties of Thin Films

Depending on why thin films are created, they have varying physical quality. Because research in this area has been uneven, we will focus on thin film's structural, optical, and electrical properties.

2.7.1 Structural Properties

The study of thin-film structural properties is vital to establishing the nature and quality of the film, as well as the types of crystalline levels it contains and other factors. It also goes over the numerous outcomes related with differences in the physical properties of the films as a result of different preparation techniques, material types and quantities, and other variables. Some of the best well-known techniques for evaluating of X-ray diffraction is used to study the structure of bulk materials and thin films (XRD). Analyzing the diffraction shape can reveal the crystallization and inter planner spacing of the substance under investigation [70]. It was developed in 1913 by English physicists Sir W.H. Bragg and his son Sir W.L. Bragg to explain why crystal cleavage faces appear to reflect X-ray beams at certain angles of incidence (θ), where the variable (d) is the distance between atomic levels in a crystal and lambda (θ) is the wavelength of the incident X-ray beam (n) is an integer. Figure 2.3 depicts the interference between waves diffracted from two adjacent rows of atoms [70]. Other ramifications When X-rays diffract off a crystal lattice, they produce diffracted intensity peaks that meet the following criteria [71]:

1. The diffraction angle is equal to the incidence angle.
2. An integer number of wavelengths separates the two paths.

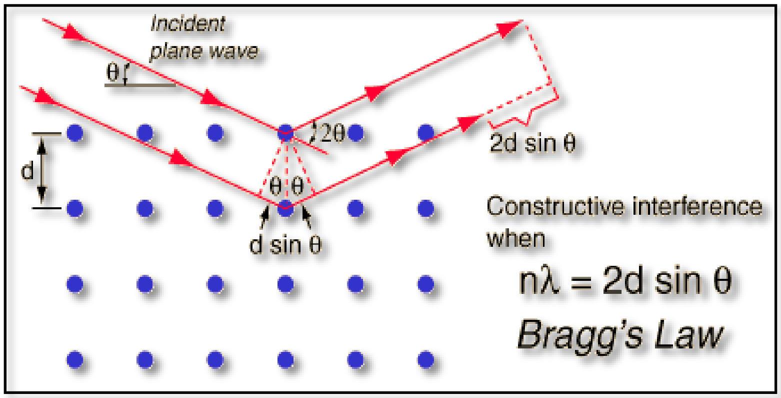

Figure 2.3. Interference between waves diffracted from two adjacent rows of atoms in a crystal [71].

The X-ray diffraction technique describes the crystallization and randomness of materials as follows [72]:-

1- X-ray diffraction shows several broad peaks in randomly-crystalline materials that do not show the reflection of a single crystal, as in Fig. 2.4a.

2- X-ray diffraction shows sharp reflections (single sharp peak) in monocrystalline materials, as in Fig. 2.4b.

3- X-ray diffraction shows various peaks at different angles for polycrystalline materials, as in Fig. 2.4c.

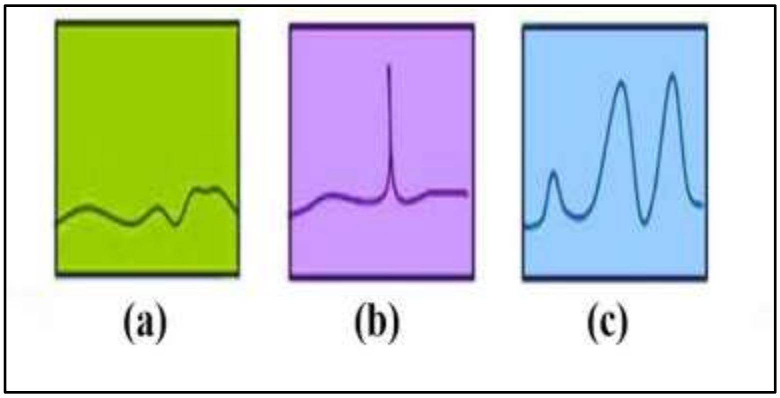

Figure 2.4. (XRD) of (a): Amorphous material,(b): Single crystalline material, and (c): Polycrystalline material [72].

Thin films structural properties can be used to investigate their crystallographic structure. X-ray diffraction is used to examine these quality. To calculate inter-planar spacing d using X-ray diffraction patterns, utilize Bragg's formula [73].

$$n\lambda = 2d\sin\theta \tag{2.3}$$

where *n* is a positive integer representing the order of diffraction, λ is the wavelength of the incident X-ray beam, *d* it is possible to calculate the inter planer distance and θ is the XRD peaks Bragg diffraction angle.

The structure for (Cd_2SnO_4 and Zn_2SnO_4) films is represented by the lattice constants for the (cubic) structure, which may be determined using equation [74].

$$\frac{1}{\mathrm{d}^2} = \frac{h^2 + k^2 + l^2}{a^2} \tag{2.4}$$

The structure for (Cu_2SnS_3) film is represented by the lattice constants for the (tetragonal) structure, which can be computed using the following equation [75]:

$$\frac{1}{d^2} = \frac{h^2 + k^2}{a^2} + \frac{l^2}{c^2} \tag{2.5}$$

The (hexagonal) structural lattice constants indicate the structure of the (CuZnS) film, which may be computed using the following equation [75]:

$$\frac{1}{d^2} = \frac{4}{3}\left[\frac{h^2 + hk + k^2}{a^2}\right] + \frac{l^2}{c^2} \tag{2.6}$$

where *h*, *k*, and *l* are the Miller indices.

By comparing d values obtained from X-ray diffraction patterns with d values obtained from ICDD (International Centre for Diffraction Data) cards for (Cd_2SnO_4, Zn_2SnO_4, Cu_2SnS_3, and CuZnS) and their films, the Miller indices and structure of (Cd_2SnO_4, Zn_2SnO_4, Cu_2SnS_3, and CuZnS) and their films can be recognized material. The preferred orientation's Full Width at Half Maximum FWHM (β) It is equal to the width of the line profile (in radian) at half of the highest intensity and can be measured. [76].

Shearer and Williamson-Hall methods are two different methods that were used to estimate the crystallite size.

1. Shearer method

Peak broadening can be used to calculate crystallite size using XRD [77]. Using the X-ray line broadening method, the particle size of a substance can be determined (Cd_2SnO_4, Zn_2SnO_4, Cu_2SnS_3, and CuZnS) with the Scherer equation [78]:

$$\mathrm{D} = \frac{\mathrm{K}\,\lambda}{\beta\ \cos\theta} \tag{2.7}$$

where D is the size of the crystallite, K is the shape factor (0.9), λ is the wavelength of the incident X-ray radiation (1.5406 Å for Cu Kα), β is the peak's total width at half maximum (in radians), then θ is the XRD peaks Bragg diffraction angle.

2. Williamson-Hall method

$S \approx \beta s/\tan\theta$ is a relationship between crystal defects and strain-induced peak broadening distortion. The Shearer equation has a 1/cosθ dependency, but not a tan reliance, like the induced strain [77]. The Shearer equation and $S \approx \beta s/\tan\theta$ [79] are combined to provide the following findings.

$$\beta_{hkl} = \beta_D + \beta_S \tag{2.8}$$

$$\beta_{hkl} = \left(\frac{K\lambda}{\mathrm{Dcos}\,\Theta}\right) + 4S\tan\theta \qquad (2.9)$$

S denotes the microstrain.

Equation rearranging (2.9) gives:

$$\beta_{hkl}\cos\theta = \left(\frac{K\lambda}{D}\right) + 4S\sin\theta \qquad (2.10)$$

If $\beta_{hkl}\cos\theta$ when the fitted line For the peaks, stays planned by detail to 4sin θ , the slope and y-intercept of the fitted line can be used to compute strain and crystallite size [79].

When thin films are created, micro strain is created. Stretching or compressing the lattice causes a variation in the lattice constants of the (Cubic, Tetragonal, and Hexagonal) structures from the JCPDS values. As a result, strain widening is caused by varying atom displacements relative to their reference lattice position.

The density of dislocations (δ) can be calculated using the below [79]:

$$\delta = 1/D^2 \qquad (line\ /m^2) \qquad (2.11)$$

To compute the number of crystallites, which will elucidate the nature of the prepared films. This relationship can also be used [80]:

$$N_o = t/D^3 \qquad (2.12)$$

where N_o is the number of crystallites and t is the thickness.

2.9 Atomic Force Microscopy (AFM) Measurements

The atomic force microscope (AFM) is part of the scanning probe microscope family, growing steadily since Binning and Quate [81], invented the scanning tunneling microscope. The forces influential between a fine tip and a sample are measured by the AFM. The cantilever tip is related to the allowed end and taken very close to the surface. The cantilever's positive or negative bending is caused by striking or repulsive forces coming of interactions between the tip and the surface.

The bending is detected using a laser beam reflected of the back side of the cantilever Figure (2-5) shows the mechanism of the atomic force microscope (AFM) device [82, 83].

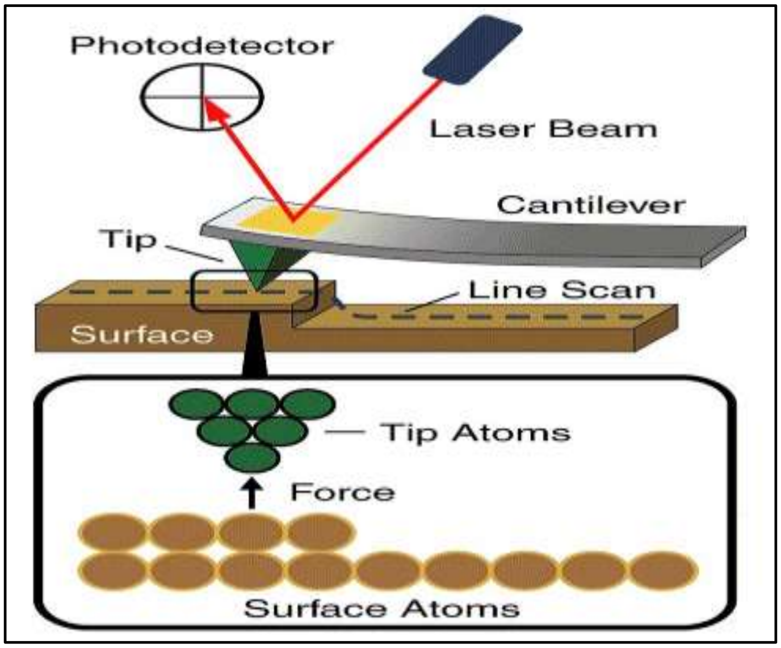

Figure 2.5. Schematic of the cantilever-tip assembly used in an AFM [84].

2.9 Field Emission-Scanning Electron Microscopy (FE-SEM)

The great magnification power, analytical ability, and high-quality images, make FE-SEM one of the devices that we cannot do without in scientific research, especially in nanotechnology. The field-emitting scanning electron microscope (FE-SEM) is utilized in a variety of applications, including investigating thin films' surface structures and examining the crystal structure of semiconductors, and microelectronic circuits. The mechanism of the (FE-SEM) device works by releasing electrons from their source by the (Electron Gun) and firing them in the form of flow of electrons that are directed by magnetic lenses on the sample to be examined and scanning its surface in three dimensions (3D) to produce three-dimensional images with all its details. (Cracks) or others (pinholes). When the electronic beam, which is controlled by the magnetic field, is scanned by using a variable potential difference to control the movement of the electron beam on the sample, it will interact with the surface of the sample and extract electrons from it specifically, as these electrons are detected(FE-SEM Detector) by attracting scattered electrons. Depending on the number of electrons that reach the detector, it will record a specific degree of illumination level on the screen, and by using (additional probes) the scattered electrons are detected by reflection from the surface of the sample, as well as (X-rays) emitted from the sample point by point and line by line. Thus, an image of the original sample is formed. The device must also be emptied of air when it is turned on. Figure 2.6 shows a diagram of the (FE-SEM) device [85].

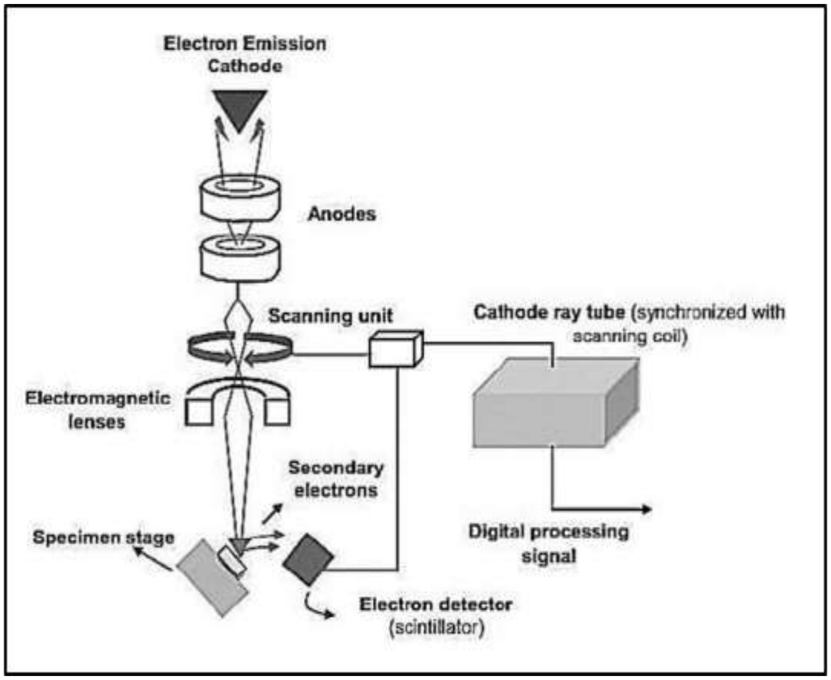

Figure 2.6. A schematic diagram of the FE-SEM parts [85].

2.10 Optical Properties of Crystalline Semiconductors

Studying a material's optical characteristics is fascinating for several reasons. To begin, the usage of optical materials in applications for example interference filters, optical fibers, and reflective coatings necessitates a detailed understanding of their optical properties constants over a broad wavelength range. Second, the optical of all materials are linked to their atomic structure, electronic band structure, and electrical properties.

2.10.1 Transmittance (T)

The transmittance is determined by the ratio of the intensity of the rays transmitting through the film (IT) to the intensity of the incident rays ($I_\circ$) (T)[86]:

$$T = I_T/I_o \tag{2.13}$$

2.10.2 Reflectance (R)

Reflected is calculated by dividing the intensity of the rays (IR) reflectance through the film by the intensity of the incident rays (I_o) (R)[87]:

$$R = I_R/I_o \tag{2.14}$$

R is proportional to the refractive index and extinction coefficient of the substance [86]:

$$R = (n-1)^2 + K_o^2 (n-1)^2 + K_o^2 \tag{2.15}$$

where R is the reflectance, n is the refractive index and $K_\circ$is the extinction coefficient.

2.10.3 Absorbance (A)

The ratio of a substance's absorbed light intensity (I_A) to the incoming light intensity (I_o) is known as absorbance [86]:

$$A = I_A / I_o \tag{2.16}$$

According to the rule of conservation of energy, the specta of reflectance, absorption, and transmission is equal to one [87, 88]:

$$R + A + T = 1 \tag{2.17}$$

The technique through which intrinsic semiconducting materials absorb light is known as fundamental absorption (FAP). Basic absorption is defined as a transition from one band to another or excitation of electrons of the valance band to the conduction band. Basic absorption, which appears as a quick rise in absorption, can be utilized to calculate the energy gap of a semiconductor [88]. When input photon energy equals forbidden gap energy (E_g), the fundamental absorption edge occurs, and the cutoff wavelength c is given by the ratio [89]:

$$\lambda_c(nm) = 1240/Eg(\text{eV}) \tag{2.18}$$

The fluctuation of the semiconductor's absorption coefficient as a function of wavelength is shown in Figure 2.7.

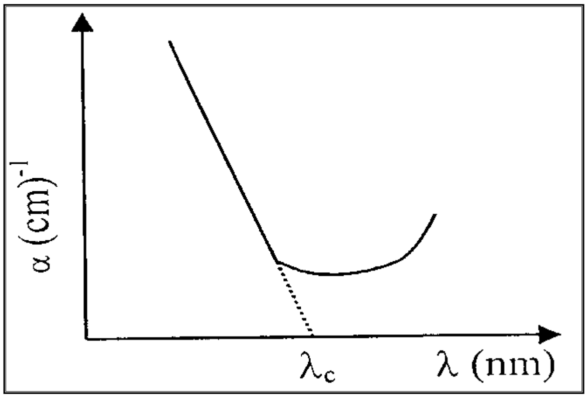

Figure 2.7. The crystal semiconductor's fundamental absorption edge [89].

2.11 The Fundamental Absorption Edge

The fundamental absorption edge can be defined as the rapid increasing in absorbance when absorbed energy radiation is almost equal to the band energy gap; therefore, the Fundamental Absorption Edge represents the least difference in the energy between the upper point in valance band and the lower point in conduction band [86,90].

2.12 Absorption Regions

Absorption regions are usually divided into three areas [86]:

A) High Absorption Region

This region shown in figure (2.8) at part (A), where the magnitude of absorption coefficient (α) is larger or equal to (10^4 cm^{-1}). This high absorption refers to electronic transitions from extended levels in valance bands to extended levels in conduction bands, as throughout this region, the forbidden energy gap (Eg) can be recognized. The absorption coefficient (α) in this location can be calculated using the following equation[90,91] .

$$\alpha h\nu = A'(h\nu - E_g)^r \qquad (2.19)$$

where $A'$is the types of transitions has an effect on the constant, $h\nu$ is photon energy in (eV) units, E_g is optical energy gap and r constant value and determined by the transition's type.

B) Exponential Region

This region is depicted in part (B) of figure 2.8, where the absorption coefficient (α) is approximately ($1cm^{-1}<\alpha<10^4cm^{-1}$) and refers to the transition between the extended level from the (V.B.) to the local level in the (C.B.) also from local levels in top of (V.B.) to the extended levels in the bottom of (C.B). The absorption ion coefficient in the region can be expressed according to Urbach relation [88]:

$$\alpha = \alpha_o \exp(h\nu/E_u) \qquad (2.20)$$

where E_u is Urbach energy for localized states.

C) Low Absorption Region

The absorption coefficient (α) is quite low in this region (approximately $1cm^{-1}$). Inner the forbidden energy gap (E_g), transitions amidst local states take place. which is illustrated in portion (A) of figure 2.8.

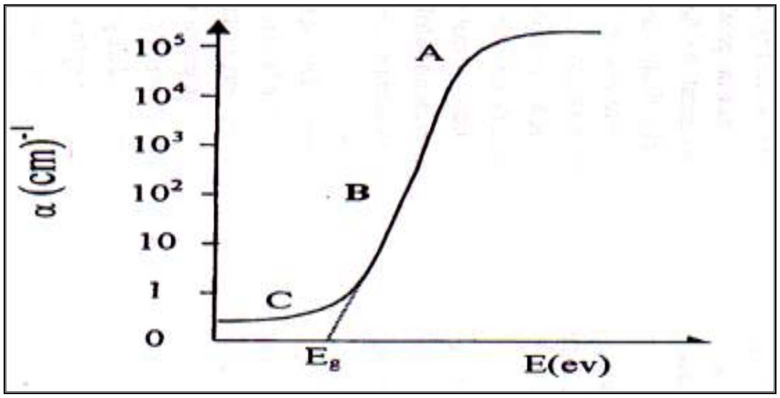

Figure 2.8. The absorption regions in semiconductors [89].

2.13 The Electronic Transitions

We can differentiate two types of electronic transitions in the study of optical qualities: direct and indirect, which are defined by the lower conduction band position point and the upper valance band position point [92].

2.13.1 Direct Transitions

In semiconductors, this transition occurs while (C.B. bottom)'s is exactly over the top of (V.B.), meaning that their wave vectors are equal, i.e. (ΔK=0). Absorption appeared in this state when $\left(h\nu = {E_g}^{opt}\right)$. The direct transfers are divided into two types[86]:

a) Direct Allowed Transition

As illustrated in figure 2.9.a, this transition occurs amid the upper points in the (V.B.) and the lowest points in the (C.B.).

b) Direct Forbidden Transitions

As seen in the figure, this transition happens between the near top points of (V.B.) and the near bottom points of (C.B.) (Fig.2.9.b). Equation (2-20) [87,93] gives the absorption coefficient for this transition type. For permissible direct transitions, r=1/2, whereas for forbidden direct transitions, r=3/2 [93]. The excited electron transition occurs vertically at a forbidden direct transition condition then of an neighboring region of allowable direct transition, i.e., of a region neighboring to the higher point of the valance band to points neighboring to the lesser point of the conduction band on the condition that the wave vector stays the similar, e.g. $(\Delta\vec{K} = 0)$ before and after transition, as depicted in figure 2.12.b. It's value noting that none of the double transitions is temperature-dependent [92].

2.13.2 Indirect Transitions

In these transitions, the bottom of (C.B.) in the (E-K) curve is not above the top of (V.B.), and the electron transits from (V.B.) to (C.B.) in a non-perpendicular manner, with the value of the electron's wave vector not being the same before and after the transition(ΔK≠0). This transition typically occurs with the help of a particle named "Phonon" aimed at the laws of energy conservation and momentum Indirect transitions are divided into two categories [76]:

c) Allowed Indirect Transitions

As illustrated in figure 2.9.c, these transitions occurred between the upper of (V.B.) and the lowest of (C.B.) in a distinct region (K-space).

d) Forbidden Indirect Transitions

As illustrated in figure 2.9.d, the prohibited indirect transition occurs between close points at the upper of (V.B.) and near locations at the lowest of (C.B.) with a change in the value of wave vector (($\Delta\vec{K}$) before and after the transition. The absorption coefficient for a transition with phonon absorption is given in[76,94]:

$$\alpha h\nu = B(h\nu - E_g \pm\ E_{ph.})^r \qquad (2.21)$$

where B is a constant and is affected by the parameters of the valence and conduction bands, as well as the temperature, $E_{ph.}$ energy of phonon, is (+) when phonon absorption and (-) when phonon emission, (r = 2) for the allowed indirect transition, and (r = 3) for the forbidden indirect transition.

Temperature affects secondary electron changes, as the rise as the temperature rises. It's worth noting that there are no phonons at low temperatures, so photon absorption is less likely. Phonon emission increases at high temperatures. Such transitions are distinguished by their existence in all energies in the conduction and valence bands, as long as the conservation of energy and momentum principles are followed [92].

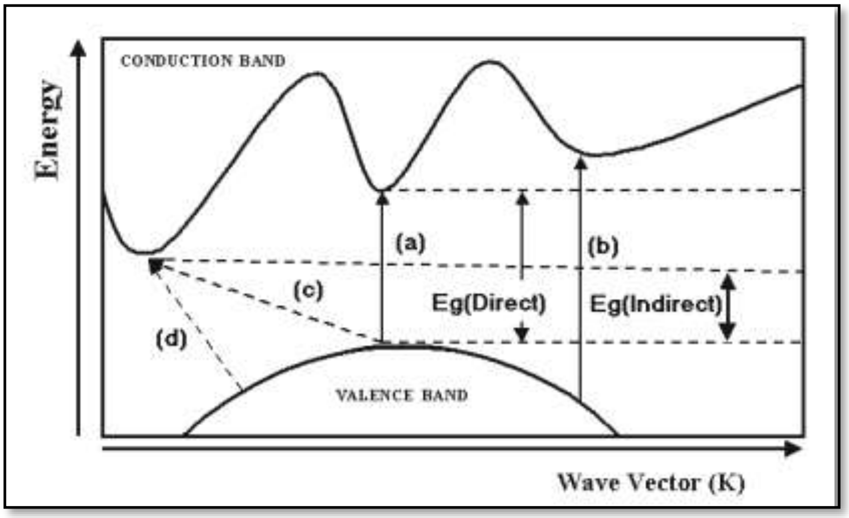

Figure 2.9. The transition types.

(a) allowed direct transition (c) allowed indirect transition
(b) forbidden direct transition (d) forbidden indirect transition [95].

2.14 Optical Energy Gap (E_g)

The energy difference between the top of the valence band and the bottom of the conduction band is referred to as the band gap. Electrons can jump from one frequency range to the next. The band gap energy is the smallest amount of energy required for an electron to go from the valence band to the conduction band. In the semiconductor and nanomaterial sectors, the band gap is critical. The energy band gap insulators are substantial (> 4 eV), whereas the band gap semiconductors are tiny (3 eV). The energy band gap reduces as the temperature rises in some semiconductors [96].

Tauc's plot, includes sketching a graph between $(\alpha h\nu)^2$and $(h\nu)$ in eV, creating a straight line, and then extrapolating this line to $(\alpha h\nu)^2 = 0$ to produce the direct bandgap of material [97], can be used to estimate the energy gap for allowed direct transition materials.

2.15 Optical Constants

2.15.1 Absorption Coefficient

In the direction of incident wave diffusion, the absorption coefficient is defined as a part decrease in the flow of incident rays energy relation to the space unit. Each semiconductor material has its absorption coefficient, which changes based on incident photon energy ($h\nu$) and semiconductor quality[98].

The photon will transfer if the incident photon energy is less than the energy gap, and the thin film transmittance is determined by the relationship [86] [99]:

$$T = (1 - R)^2 e^{-\alpha t} \tag{2.22}$$

The formula can be used to calculate the absorption coefficient from the absorbance [95]:

$$\alpha = (2.303) A/t \tag{2.23}$$

2.15.2 FTIR Spectra

Longer wavelength or low-frequency infrared spectroscopy can be utilized to detect various substances. This necessitates the use of a Fourier transform infrared (FTIR) spectrometer. The fact that molecules absorb specific frequencies typical of their structure, known as resonant frequencies, i.e. the absorbed radiation has the same frequency as the vibrant bond or cluster, is all that is required for spectroscopy. Energy is detected using the geometry of the molecular potential energy surfaces, the masses of the atoms, and the related vibronic coupling. No two compounds have the same infrared spectrum since each one is made up of a different combination of atoms. As a result, infrared spectroscopy can positively identify (analyze qualitatively) any type of material. In addition, the size of the peaks in the spectrum indicates how much material is there. Bulk and thin film, liquid, solid, pastes, powder, fiber, and new materials can all be examined using FTIR. When proper standards are used, FTIR study can be used for both quantitative (quantity) and qualitative (identification) material analysis. FTIR can be put to use to evaluate materials with a thickness of up to100 microns. FTIR can be accustomed evaluate materials by a diameter of above 11 millimetres then can measure in bulk or the top(1 micrometre) layer. Clean compound FTIR spectra are generally so distinct that they resemble a molecular "fingerprint" [98].

2.16 Electrical Properties

The electrical characteristics of crystalline and non-crystalline semiconductors differ due to their various electronic transitions. Crystalline materials, whose size and boundaries affect charge carrier movement, and the grain limits of semiconducting compounds differ from semiconducting elements in terms of charge carrier transfer due to grain size variation. The electrical conductivity of semiconductors depends mainly on temperature. It behaves opposite to the behavior of conductive materials, as its resistance decreases with increasing temperature, so it is characterized by having resistance with a negative thermal coefficient [100].

2.16.1 Hall Effect

The Hall Effect is the creation of a voltage difference (the Hall voltage) across an electrical conductor that is perpendicular to and transversal to an electric current. It was first discovered in 1879 by Edwin Hall.[101]. The ratio of the induced electric field to the product of the current density and the applied magnetic field is known as the Hall coefficient. It is a property of the conductors material, as its value is determined by the charge carriers' type, number, and quality The current is made up of several elements. Electrons travel in the reverse direction of the current I in classic electromagnetism (through convention "current"). illustrates a "hole flow" in theory). Because the voltage is applied in the reverse direction in several semiconductors, it looks that "holes" are real inflow. The Hall voltage V_H can be calculated for a simple metal with only one type of charge carrier (electrons) by applying the Lorentz force and observing that charges do not move in the y-axis direction in the steady-state condition because the magnetic force on both electron in the y-axis direction is cancelled by a y-axis electrical force due to the buildup of charges. The V_X expression is the current's drift velocity, which is considered to be zero at this point by convention. In the y-axis direction, the $V_X\ B_Z$ the expression is negative. By the right-hand rule, the $V_X\ B_Z$ the term is negative in the y-axis direction, as shown in figure 2.10 [102].

$$F = q[E + (V \times B)] \tag{2.24}$$

$0 = -E_y V_X B_Z$ where E_y is assigned in the y-axis direction, not with the arrow as seen in the illustration. Instead of holes, electrons pass across wires, so $V_X = -V_X$ and $q = q\ -$Also $E_y = -V_H/w$ Substituting these changes gives:

$$V_H = V \times B_Z w \tag{2.25}$$

$$I_X = nwt\ (-V_X) \tag{2.26}$$

(wt) is the cross-sectional area. The Hall voltage is obtained by solving for the wand plugging into the above:

$$V_H = \frac{I_X B_Z}{n_e t} \tag{2.27}$$

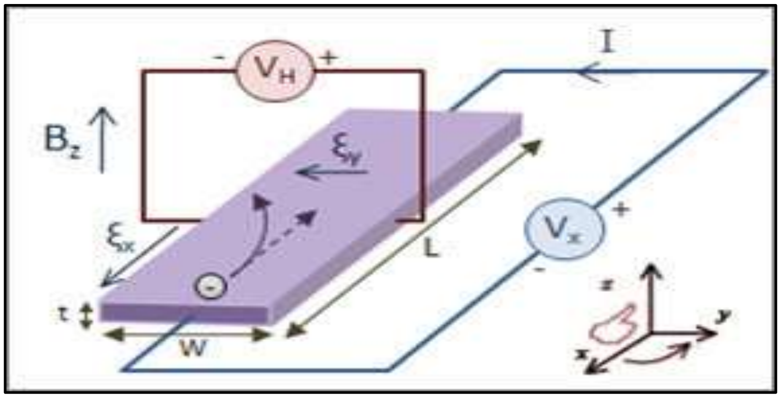

Figure 2.10. Hall Effect measurement setup for electrons [102].

If the charge build up had been positive (as it appears in some semiconductors), then the V_H assigned in the image would have been negative (positive charge would have built up on the left side). This is how you compute the Hall coefficient:

$$R_H = \frac{E_y}{j_X B_Z} \tag{2.28}$$

where j_X is the carrier electron current density and E_y is the induced electric field (I). This is converted to SI units as follows:

$$R_H = \frac{E_y}{j_X B_Z} = \frac{V_H t}{IB} = -\frac{1}{ne}\ for\ n - type\ or \frac{1}{nH} for\ p - type \tag{2.29}$$

From σ and R_H we may determine the Hall mobility

$$\mu_H = \sigma |R_H| \tag{2.30}$$

As a result of the scattering factor r, the Hall mobility is larger than the conductivity mobility. The drift (mobility at high temperatures is a trap) was thought to limit the forms mobility:

$$\mu_D = \mu_o A \exp(-\Delta E / K_B T) \tag{2.31}$$

where: μ_D/μ_o is 1/100 and DE hopping energy [103].

2.17 Heterojunctions

Although a heterojunction is the interface of two different materials, it is most usually used to refer to the intersection of two monocrystalline semiconductor materials in semiconductor research. Depending on the distances at wherein the transition from one, substance to another is completed close to the point of contact such heterojunctions can be classed as abrupt or graded. The transition happens over a few atomic distances (≤ 1μm)) in the former case, whereas it occurs at distances on the order of several diffusion lengths in the latter case. Another often utilized approach of marking the heterojunction is the kind of conductivity current on any side of the junction. whether the two semiconductors complex must like conductivity kinds, the junction is called isotype heterojunction; if they don't, it's called anisotype heterojunction. Gubanov was the first to think about these combinations, but heterojunction research did not begin until Kroemer [104] hypothesized that anisotype heterojunctions would have extremely high injection efficiencies relative to homojunction. Anderson, in 1960, invented the first isotype and anisotype heterojunction. In greater detail, he also went through the energy band organization around the semiconductor-to-semiconductor contact around the semiconductor-to-semiconductor contact. Other researchers have since presented many models for different types of heterojunctions, and their validity has been demonstrated by experiments[105].

2.17.1 Abrupt Anisotype Heterojunctions

Minority-carrier heterojunctions, such as n-p and p-n heterojunctions, are identical to n-p or p-n homojunction in that they are minority-carrier devices.

Unlike Shockley's [105] homojunction model, none of the many heterojunction models proposed by various researchers can account for almost all of the physical phenomena in such heterojunctions. This is demonstrated by the fact that the properties of the interface in heterojunctions differ significantly from one material to the next and are highly reliant on the method of fabrication. Existing models for anisotype heterojunctions can be thought of as an extension of the traditional homojunction concept. In this section, numerous workers hypothesized processes until charge- transporter transfer now abrupt anisotype heterojunctions are discussed in sequential order.

- *Tunneling model*

R. H. Rediker et al., [105] were the first who used the tunneling process toward characterize the current-voltage describe of an abrupt p-n heterojunction. To transition from n-type to p-type or vice versa, electrons must overcome or tunnel through the potential barrier in the n-type wide-bandgap material, according to Prices' calculations (Fig. 2.11). Whether this flow of electrons is due to thermal emission over the barrier or tunneling over the barrier under forward bias will be determined by the properties of the n-type material.

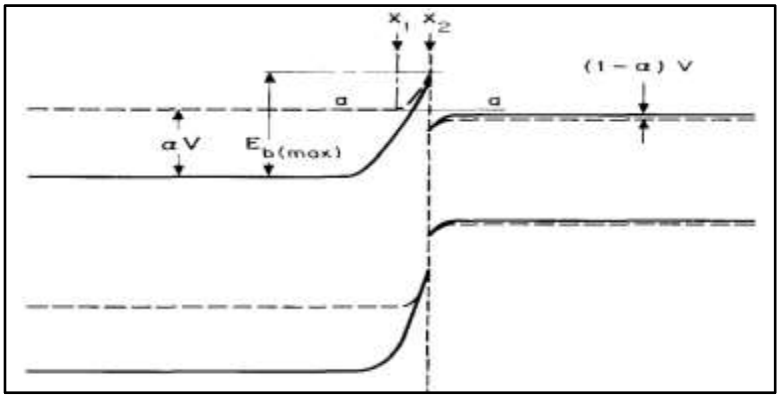

Figure 2.11. Schematic representation of the tunneling model based on an energy band diagram of Anderson [106].

$$\mathrm{p} = exp\left[-2\int_{x_1}^{x_2} 2(m_{n}^{*}\{E_b\ (x) - q\alpha V\}]^{\frac{1}{2}}\ \frac{\mathrm{dx}}{\hbar}\right] \tag{2.32}$$

where $E_b\ (x)$ is the height of the barrier at any point x above the bottom of the conduction band, αV is the proportion of the applied voltage V that is successful in elevating the wide-band gaps conduction band, m_{n}^{*} exists the real mass of electrons in an n-type material (assumed to be invariant), q is the electronic charge, $\hbar = h/2\pi$ and is the hole density. It is feasible to generate a variety of equation solutions by assuming the functional dependency of $E_b\ (x)$ on x. For the linear case (constant field $F_o$in the transition zone), the solution can be approximated.

$$\mathrm{p}_{\approx}\ exp\left[-\frac{4}{3}(m_{n}^{*})^{\frac{1}{2}}\frac{\{E_{b(max)}\}^{\frac{3}{2}}}{\hbar F_O}\right] exp\left[-2(m_{n}^{*})^{\frac{1}{2}}\frac{\{E_{b(max)}\}^{\frac{1}{2}}}{\hbar F_O}q\alpha V\right] \tag{2.33}$$

where $E_{b(max)}$ is the most significant height of the barrier with respect to the bottom of the conduction band with zero applied voltage.

The tunneling current multiples the tunneling probability (equation 2.33) by the incident electron flux. As a result, when tunneling through the barrier outnumbers thermal emission across the barrier in this scenario, the generic equation for current-voltage characteristics under forwarding bias is [106]:

$$I = I_s(T)\mathrm{e}^{\frac{V}{V_O}} \tag{2.34}$$

Where V_O is a fixed then $I_s(T)$ is a temperature-dependent function that is least rising. While Puroltit et al. didn't supply an term or clarification for $I_s(T)$, their experimental observations of the voltage and temperature dependence of frontward current and much extra anisotype heterojunctions, graphically exemplify in figure (2.12), specified that frontward current-voltage characteristics could be represented by equation (2.34) over the entire domain or over a specific applied voltage.

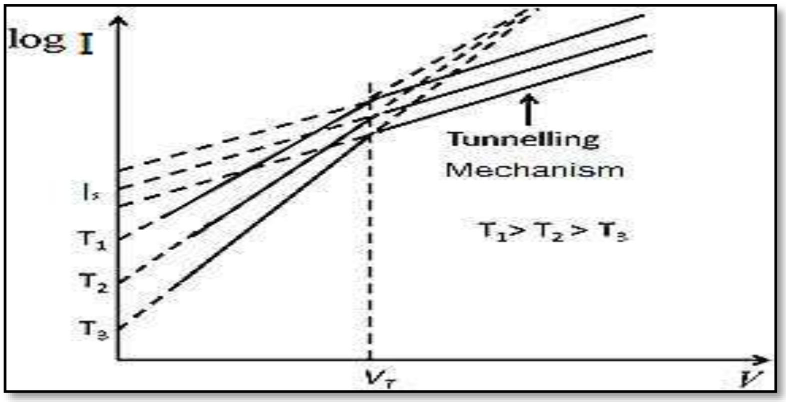

Figure 2.12. Typical experimentally observed log I vs, applied voltage, $V$for a p-n heterojunction at three different temperatures [104].

-Tunneling-recombination model

The parallels between tunneling currents in anisotype heterojunctions (equation 2.34) and excess current in an Esaki diode prompted Milnes and Feucht [107] to suggest a model based on band-to-band tunneling mixed with recombination processes, as shown in figure (2.13). Even though they included an n-p heterojunction in their study, the discussion is limited to a similar approach of an A p-n heterojunction for comparison's sake.

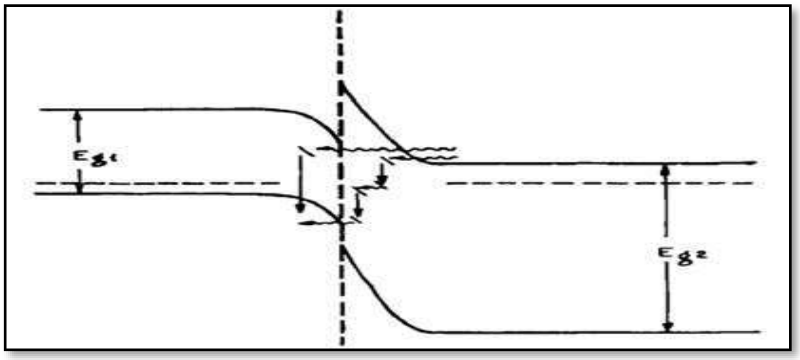

Figure 2.13. Schematic representation of the tunneling-recombination process [107].

(Energy band gap for a forward-biased abrupt p-n heterojunction)

The various processes involved in this model are schematically shown in figure (2.14). In this model, electrons tunnel from the conduction band of a wide-band gap material (n -type) into empty inter band states in a narrow-band gap material (p-type) and then recombine with holes, or holes tunnel from the (p- type) material into occupied states in the (n-type) material and then recombine with electrons. A forward current of the kind [108], occurs from tunneling that starts at the bottom of the conduction band or the top of the valence band.

$$I = B\mathrm{e}^{[-\alpha(V_D - V)]} \tag{2.35}$$

V_D is the diffusion voltage, V is the applied voltage, then B is dependent on the electrons active mass in the prohibited zone. Figure 2.18 shows the current-voltage properties from an abrupt p-n heterojunction.

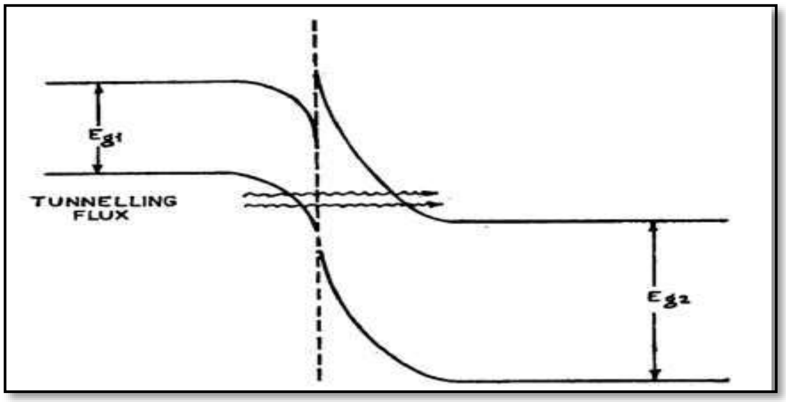

Figure 2.14. Energy band diagram for an abrupt p-n heterojunction, under reverse bias, indicating tunneling mechanism [107].

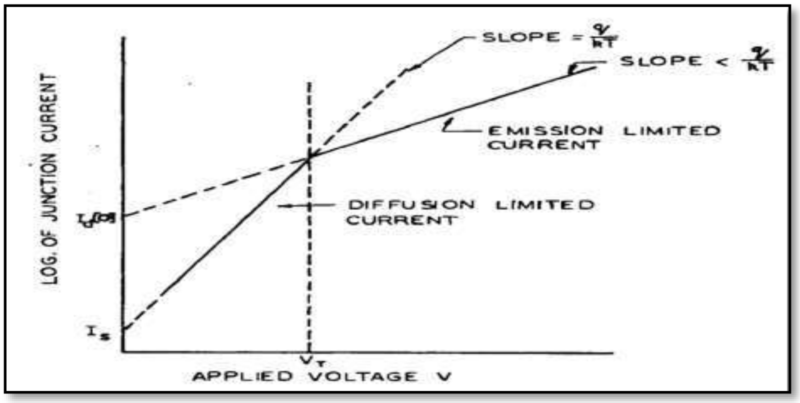

Figure 2.15. Semi logarithmic current-voltage characteristics for an abrupt p-n heterojunction [107].

2.18 Electrical Properties of Heterojunction

The electrical characteristics that characterize heterojunction are (current-voltage). In truth, these characteristics allow one to determine not only a heterojunction's band structure (i.e., the type of heterojunction and the built-in junction potential) but also the heterojunction's device usefulness because the manufacturing procedure and doping levels of the two semiconductors that make up a heterojunction are critical.

2.18.1 (I-V) Characteristics of Heterojunction

At a heterojunction's interface, the built-in junction potential and energy discontinuities in the conduction and valence band edges are examined and use to control the compact junction potential and energy cutout in the conduction and valence band edges. The polarity of the applied voltage has an impact on the results, these features might be classified as forward or reverse bias. The term forward bias refers to when the applied voltage has a polarity that lowers the built-in junction potential [109].

2.18.1.1 (I-V) Properties of Heterojunction in the Dark Condition

The properties of (current-voltage) revealed that depending on the polarities of the voltages, the electrical conductivity mechanisms are confidential equally a frontward or back bias happening the diode [105].

(I-V) Properties of Heterojunction in the Dark Condition (Forward Bias)

The (voltage-current) parameters of the p-n junction in the situation of front bias (i.e., the connection of the negative terminal (n) to the junction with the source's negative side, and the positive side (p) with the source's positive pole), as shown in figure 2.16. As the voltage rises, the current increases with it. There are numerous models that can be used to describe the current forward bias flow (model of propagation, emission, penetration, and recombination). The forward bias with bias voltages produces a curved form that may be divided into two zones [110].

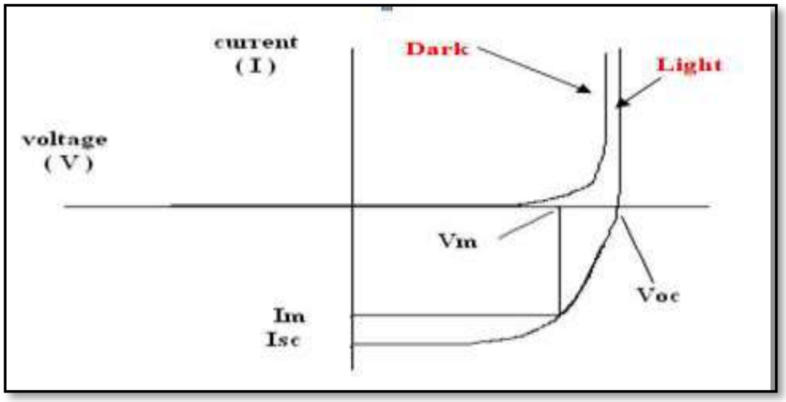

Figure 2.16. Current-voltage characteristics of an ideal anisotype heterojunction in the dark and under illumination [111].

i)- The low-voltage region (V<0.5V)

The I-V correlation is represented by the relationship (2.35) [106]:

$$I_f = I_s \left[e^{\left(\frac{qV}{n_f k_B T}\right)} - 1 \right] \text{were} (1 = \text{neglagted}) \;\; I_f = I_S \, e^{\left(\frac{qV}{n_f k_B \, T}\right)} \qquad (2.36)$$

where I_f is the forward current, q is the electron charge, T is the absolute temperature, I_s is the saturation current, V is the applied front bias voltages to detectors, k_B is Boltzmann constant, ($\frac{\mathrm{k_B\,T}}{q} = 0.0258$ volt), and n_f is the ideality factor parameter, which is related to the heterojunction's numerous physical properties and has a value between 0 and 1. (1 and 2).

ii)- Zone of large voltages:- In which the I-V correlation is described in the following relation [106]:

$$I_f \propto e^{(AV)} e^{(BV)} \tag{2.37}$$

Temperature and voltage do not affect the constants A and B. Because of the penetration current's dominance over the junction, the equation is proportionate (2.37). This equation applies to a material with a tiny p-type energy gap that has been recombined with a hole in the presence of forward bias and high voltages, i.e. the electron passes through a wide-gap n-type material's conduction band. Alternatively, in n-type material, the holes may recombine with the electrons by transitioning in the opposite direction [108].

❖ (I-V) Properties of Heterojunction in the Dark Condition (Reverse Bias)

The (voltage-current) parameters of the p-n junction are shown in Figure 2.20, (bias in the other direction). The characteristics of reverse bias can be separated into two groups in the case of reverse bias [106].

i)- The low reverse voltage

The reverse bias current (I_r) and the applied reverse voltages, i.e. ($I_r \alpha V$), will exhibit a direct correlation in the heterojunction.

ii)- The high reverse voltage

When m ≥ 1, are proportional to the relationship ($I_r \alpha V^m$), and these results are interpreted using the biases of the tunneling model [107]. A plus voltage is applied to the N-type material and a minus voltage is applied to the P-type material in the opposite Bias state. Plus voltage catch electrons far since the junction and towards the positive electrode in N-type materials. The holes in p-type material, on the other hand, are pulled across from the junction and towards the minus electrode. The depletion layer grows larger due to the absence of electrons and holes, offering a high impedance path that is virtually an insulator, and a high potential barrier is produced across the junction, preventing current from flowing through the semiconductor material [106].

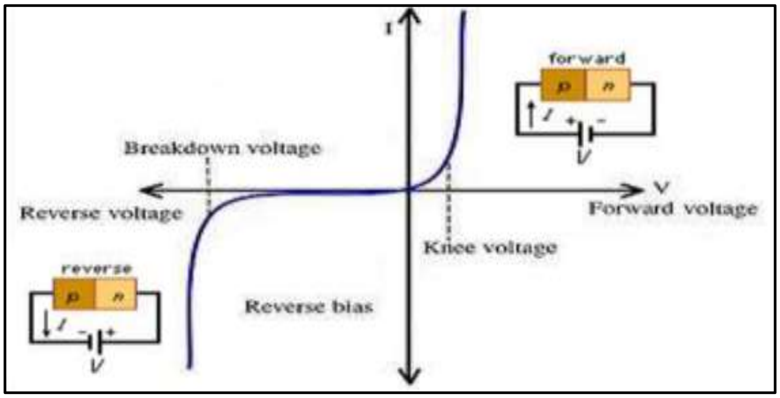

Figure 2.17. (I-V) characteristics of a p-n junction diode.

2.18.1.2. Characteristics of Heterojunction (I–V) Under Illumination

The optical properties of semiconductors in terms of photon energy ($h\upsilon$) and their link to the forbidden energy gap (E_g), When the wavelength is short, ($\lambda_{cut\ off}$) grows big(α ≥cm^{-1}), and the incident beam is absorbed exceptionally close to the surface; this is the process of optical absorption and how electron-hole pairs are produced in semiconductors, because of the high rate of recombination. This holds true for the optical properties of the heterojunction. Charge carriers are formed in the space charge area (depletion zone) when the heterojunction is lighted, resulting in the formation of a photocurrent (I_{ph}), which is characterized by the following relation [106]:

$$I_{Ph} = qAG_{Ph}(w + L_n + L_P) \quad (2.38)$$

where q is an electron charge, A heterojunction zone, w is the width of the depletion zone, $G_{Ph}$the rate of charge carrier generation is a function of the absorption coefficient, L_P , L_n electron and hole propagation lengths are measured sequentially. It has something to do with the qualities of the (I-V) of the heterojunction dark state. The (I-V) In the instance of lighting, the following relationship can be described [108]:

$$I_{Ph} = I_L - I_d \tag{2.39}$$

where I_d dark current (represents the contribution of all electrons and free holes transmitted under the influence of an external electric field) when the heterojunction is illuminated, I_L the total current in illumination state, Is saturation current and I_{Ph}photocurrent generated by incident radiation (representing the increase in the concentration of charge carriers) that the value of [E_{g1}>E_{g2}] Because photons drop on the obverse surface of the extensive-gap material Eg1, high-energy photons are absorbed in the material with a broad energy gap, while small-energy photons are run out done the extensive-gap solid and soak up by the tapered-gap solid. The effect of the window is the name given to this phenomenon. As a result, the asymmetric heterojunction (p-n) [108] has an adequate light response.

2.19 Solar Cells

Using photovoltaic technology, solar cells convert solar energy directly into electricity. It is based on two factors in general. Current generation from absorbed incoming photons and charge carrier loss via so-called recombination mechanisms [112]. The radiant power per unit area perpendicular to the suns direction but close to the earth-sun distance is essentially constant outside the earth's atmosphere. The strength of this radiation is referred to as the solar constant or air mass zero (AM0) radiation. In photovoltaic work, the solar constant is currently agreed to be 1.353 kW/m^2. A weighted average of measurements made by equipment mounted on balloons, high-altitude airplanes, and spacecraft was used to arrive at this value. Knowing the precise distribution of energy content in sunlight is crucial in their job [113], because different wavelengths of light induce varied responses in solar cells P-n junctions are used in traditional semiconductor solar cells. As shown in figure 2.18, a p-n junction is formed by two semiconductors with different predominant charge carriers and doping concentrations, an n-doped and a p-doped material [114].

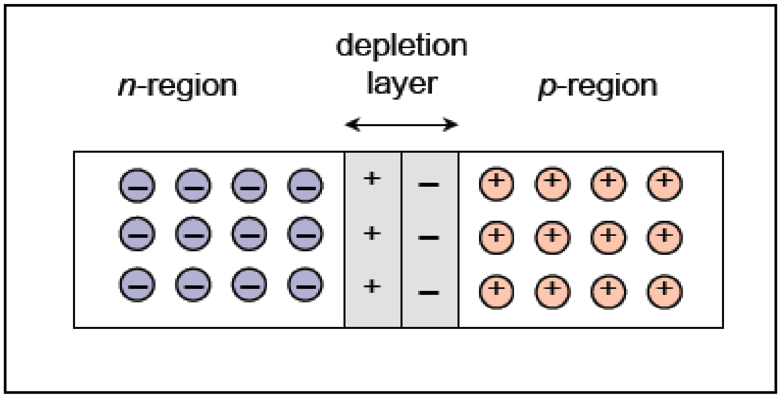

Figure 2.18. The p-n junction of solar cell [114].

The electrons diffuse from the n-type side to the p-type side. Similarly, holes flow by diffusion from the p-type side to the n-type side. If the electrons and holes were not charged, this diffusion process would continue until the concentration of electrons and holes on the two sides were the same, as happens if two gasses come into contact with each other. However, in a p-n junction, when the electrons and holes move to the other side of the junction, they leave behind exposed charges on dopant atom sites, which are fixed in the crystal lattice and are unable to move. On the n-type side, positive ion cores are exposed. On the p-type side, negative ion cores are exposed. An electric field forms between the positive ion cores in the n-type material and negative ion cores in the p-type material. This region is called the "depletion region" since the electric field quickly sweeps free carriers out, hence the region is depleted of free carriers. A "built in" potential due to electric field is formed at the junction [115, 116].

2.19.1 Photovoltaic (PV)

Photovoltaic has a long history dating back to the nineteenth century. In 1839, Henri Becquerel found that when two separate brass plates immersed in an electrolytes liquid were exposed with sunshine, they produced a continuous current. The notion of employing semiconductor material as a source to transform solar radiation into electricity was born from his theory [115, 117]. The photoelectric effect was discovered in the twentieth century by Albert Einstein and others [118]. The first silicon solar cell was produced by Chapin et al., and Bell laboratories, in 1954. The cell, which employed silicon(as raw material), had a 6 percent starting efficiency that was quickly increased to 10% [119]. Russell Ohl invented the silicon solar cell in 1941. Solar cell efficiency began to improve after his discovery [120]. Kallman and Pope also discovered the first photovoltaic effect in an organic crystal in 1959 [121]. Dewald's (1959, 1960) showed clear explanations of semiconductor electrochemistry principles laid the groundwork for rapid experimental advances in the 1960s, when many fundamental concepts were established, such as the relationship between the sign of the photo potential and the conductivity type of the electrode (Williams, 1960) [122]. The PV cell is the smallest component in photovoltaic system. It comprises semiconductors, which have electrons that are weakly bonded and occupy a region of energy known as the valence band. When a valence electron receives energy above a certain threshold, known as the band gap energy, the bonds are broken, and the electron is "free" for roam about in a new energy band known as the conduction band, where it can "conduct" electricity complete the material. For each negative-charged electron. A hole is generated when a matching mobile positive charge is created. The conduction band's free electrons are separated from those in the valence band by the band gap (measured in parts of electron volt or eV). Photons, which are light particles, have the energy to liberate the electron [111]. See the diagram 2.19.

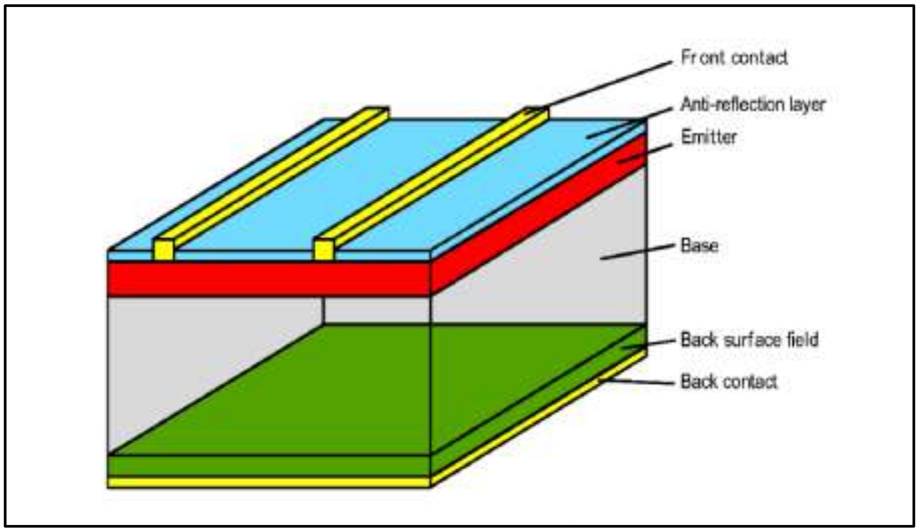

Figure 2.19. Structure of a PV cell[115].

Photons collide with valence electrons in a solar cell, shattering their connections and jumping to the conduction band (see Figure 2.20). Conduction-band electrons are caught and driven to an outside circuit via a specially built selective contact. When electrons work in an outside circuit, for example pushing water, spinning a fan, driving a sewing device motor, turning on a light bulb, or operating a computer, they lose energy. The passage of these electrons in the outside circuit and contacts is known as electric current. The energy threshold is slightly lower than the potential at which electrons are released into the surrounding environment[123].

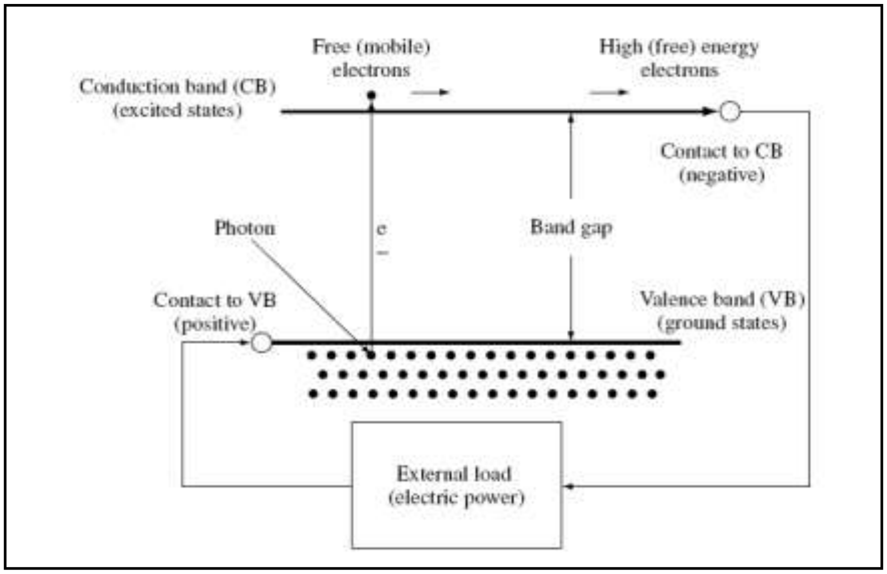

Figure 2.20. Schematic of a solar cell[137].

A typical PV system is made up of a large number of individual PV cells, typically (28-36), that are interconnected and encased into PV modules [124, 125], as shown in figure 2.21. They yield DC current, which is changed hooked on a further usable AC current through an inverter, an electronic device.

2.20 Generations of Solar Cells

Solar cells are classified into four generations, which are as follows:

- First Generation

First-generation solar cells are the most frequent technology used in commercial solar cell manufacture. These cells are made of single-layer p-n junction devices with a large area and are made from a crystalline silicon wafer. They have a broad spectrum of absorption and high carrier motilities, but they are costly to manufacture [126].

- Second Generation

Thin-film solar cell technologies of the second generation, ow-energy preparation methods such as vapor deposition and electroplating are employed [126]. Thin-film solar cells are less expensive, but their efficiency is lower [127].

- Third Generation

Third-generation photovoltaics are defined by Shockley and Queisser [125] as cell designs that exceed the 31 percent theoretical upper limit of a single junction solar cell. Third-generation PV technologies can overcome the fundamental limitations of photon to electron conversion in single-junction systems, resulting in higher efficiency and lower prices [128]. Third-generation photovoltaics differ significantly from semiconductor devices. Emerging devices include photo-electrochemical cells, polymer solar cells, and nano-crystal solar cells [129].

- Fourth Generation

When it comes to fourth-generation composite photovoltaic technology, polymers with nanoparticles can be combined to form a single multi-spectrum film. The thin multi-spectrum layers can then be stacked using polymer solar cells and multi-junction technology to improve the efficiency and cost of multi-spectrum solar cells [129].

2.21 Solar Cells Characterizations

The *J*-*V* curve with and without illumination is one of the most important characterization methods in defining the performance of a solar cell, as shown in figure 2.21. Solar cells ability to convert incident light into power. The photons energy is used to calculate the conversion of photon energy to electrical energy. Under lighting, externally applied voltage (*V*) as a function of electrical current

(I_s), short circuit current density, open-circuit voltage ,maximum voltage, maximum current, short circuit current ,fill factor ,and efficiency are among the major metrics that may be calculated from the *J*-*V* curve of a solar cell under illumination [130].

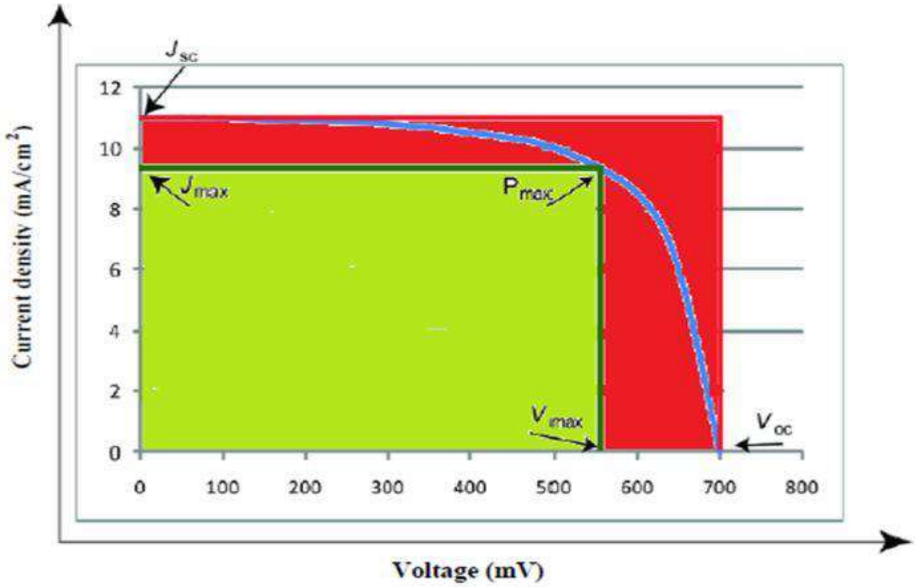

Figure 2.21. Typical current density-voltage characteristic of solar cell [126].

2.21.1 Short Circuit Current (I_{SC})

The short-circuit current, or I_{SC}, flows through the solar cell when the device's load resistance and output voltage are both zero. In absolute terms, it equals the number of photons transformed to hole-electron pairs [131]. The generation and collection of photogenerated carriers determine the short-circuit current. As a result, various factors influence it, including incident light spectrum, active layer absorption coefficient, and thickness, solar cell area, and collecting efficiency, which is determined by minority carrier lifespan [132].

2.21.2 Short Circuit Current Density (J_{sc})

Short circuit current density is used to measure a cell with a known surface area. The small circuit current density (J_{SC}) [133] is calculated by dividing the short circuit current by the lighted energetic of the cell. When the burden resistance and voltage are both zero, it is measured in the lighted cell. Because it is easier to compare devices with different energetic zones, current density (J) is frequently used instead of current (I). The J-V graph illustrates the current density in a short circuit (Figure 2.22). The J_{SC} can be calculated using the following equation [134]:

$$J_{SC} = I_{SC}/A) \tag{2.40}$$

where A is the active surface area of the cell and I_{SC} is the short circuit current.

2.21.3 Open-Circuit Voltage (V_{oc})

As demonstrated in figure 2.22, open-circuit voltage is the maximum voltage a solar cell may produce when the load has infinite resistance and the external current is zero. The V_{OC} parameter and the device configuration are determined by the absorbing materials optical band gap. Here is the formula for estimating the V_{OC} f a solar cell [135]:

$$V_{OC} = \frac{\grave{n}\, K_B T}{q} ln\left[\frac{I_{ph}}{I_O} + 1\right] \tag{2.41}$$

where ǹ is the diode ideality factor (1 for an ideal diode), K_B is Boltzmann constant, T is temperature, q is electron charge, I_{ph} is the light-generated current density and I_O is the current density at saturation.

2.21.4 Maximum Voltage (V_{max})

The maximum voltage, as shown in figure 2.22, is the voltage at which the PSC's output power peaks.

2.21.5 Maximum Current (I_{max})

The maximum current is the current at which the PSC output power is highest; it is determined by incident light intensity and the connection between material interfaces (shown in figure 2.22) [136].

2.21.6 Maximum Power (p_{max})

The solar cells' power output is determined by the product of voltage and current ($P= I \times V$), and the (I,V) combination for which (P) maximizes (p_{max}) is known as the maximum power point (MPP), as shown in Figure 2.22. The device's series and shunt resistances define its magnitude. The device's power output is enhanced by minimizing internal resistance with a low series resistance and a high shunt resistance [137]. The maximum value is p_{max}. As a result of the following formula:

$$P_{max} = J_{max} \times V_{max} \tag{2.42}$$

Where P_{max} is maximum power, V_{max} *is* the voltage at its highest power output and J_{max} is the maximum power point current density.

2.21.7 Fill Factor ($F.F$)

The fill factor, abbreviated as ($F.F$), is an important measure for determining the effectiveness of a cell. It determines how ideal the device. The $F.F$ is defined as the output of V_{OC} then J_{SC} (area inside the green square separated through area within the red square as shown in figure (2.22) divided by the highest power output per unit area. The $F.F$ of PSCs can be calculated using the following equation [130]:

$$F.F = \frac{J_{max}.V_{max}}{J_{SC}.V_{OC}}\ \frac{P_{max}}{J_{SC}.V_{OC}} \qquad (2.43)$$

When the cell's internal resistance is zero, the fill factor ranges from 0 to 1, with 1 being the appropriate *F.F* value. The *F.F.* is affected through series resistance since internal and shunt resistance [138].

2.21.8 Power Conversion Efficiency (η)

The relationship between maximum output power (p_{max}) and incident power is defined as the efficiency of a solar cell (P_{in}). The spectrum and intensity of incident sunlight, as well as the ambient temperature, determine the efficiency. A photovoltaic cell is a device that generates electricity from sunlight. The *J-V* curve can be used to calculate maximum efficiency. The next equation is used to compute the efficiency(η)[139]:

$$\eta(\%) = \frac{J_{max}V_{max}}{P_{in}} = \frac{P_{max}}{P_{in}}\ \frac{J_{SC}.V_{OC}\ FF}{P_{in}}\ \times 100\ \% \qquad (2.44)$$

2.22 The Equivalent Electrical Circuit of Solar Cell

The corresponding circuit for a solar cell is shown in Figure 2.22. A solar cell is made up of a diode and a current source, as well as two resistances: shunt resistance (R_{Sh}) and series resistance (RS).

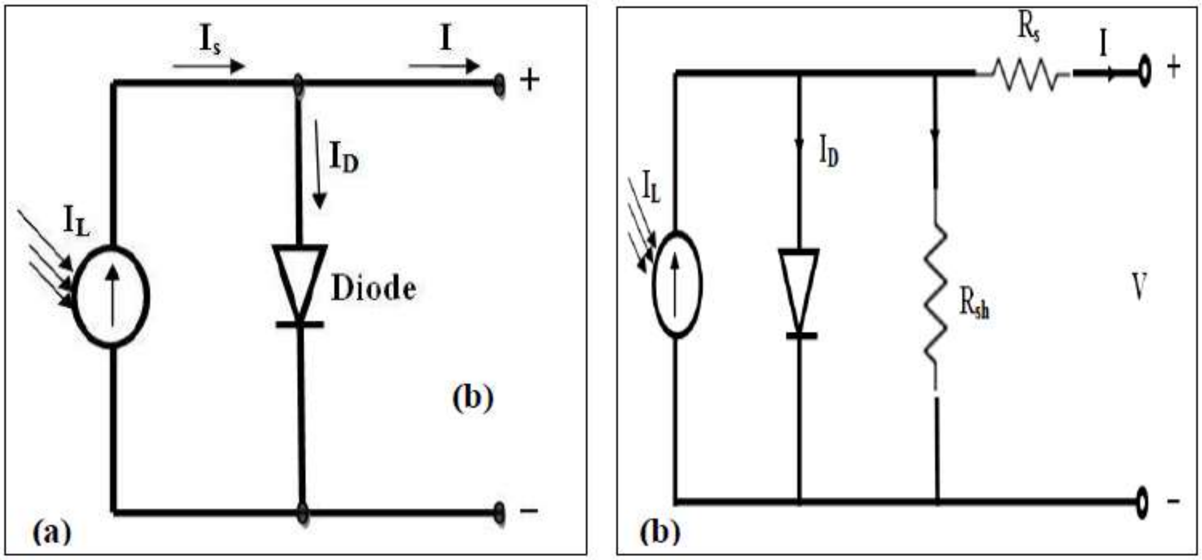

Figure 2.22. Equivalent electrical circuit of (a) Ideal and (b) Real solar cells[140].

Series resistance and shunt resistance are two characteristics that influence efficiency. Series resistance is began through the electric resistance from the various components in the cell to current flow and the contact resistance between the metal contact and the semiconductor. Manufacturing faults, on the other hand, cause shunt resistance [141]. Figure 2.23 shows how series and parallel resistances diminish the fill factor. The cell is ideal if (R_{Sh}) is infinitely large and (R_S) is zero[142, 143].

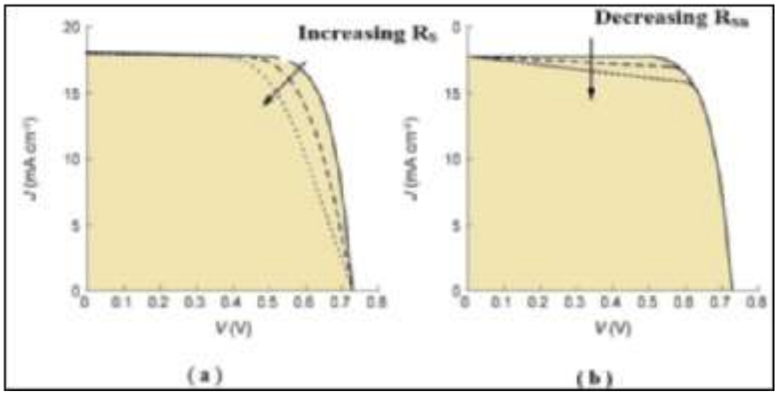

Figure 2.23. Effect of (a) increasing series and (b) reducing parallel resistances [143].

2.23 Photodetectors

An optical detector is a type of photovoltaic device that is built of semi-conductive materials. Absorbed electromagnetic radiation is transformed to output electric current, which is ordinarily proportionate to irradiance (the quantity of electromagnetic energy intensity), depending on the kind of detector how it works. Thermal detectors respond to changes in temperature produced by incoming IR radiation through physical and electrical qualities, while photon detectors generate infinite electrical carriers through photons and bound electrons.

- It is creating carriers that are proportionate to the incident light.
- By using a current-gain mechanism, carriers can be transported and/or multiplied (according to detector type).
- An output signal is generated due to current interaction in an external circuit.

2.23.1 Thermal detector

The thermal effect is utilized in these detectors because absorbed thermal radiation causes molecules to migrate, generating an increase in the energy-absorbing ambiance temperature, which causes physical changes in the detector. Thermal detectors, respond to all wavelengths in the same way (Fig. 2.24).

Thermal detectors offer a broad spectrum response and operate at room temperature. The following are the several types of thermal detectors:

- Thermoelectric Join Devices: (Thermocouple).
- Bulk equipment (Bolometer, Micro Bolometer, and Pyro electric).

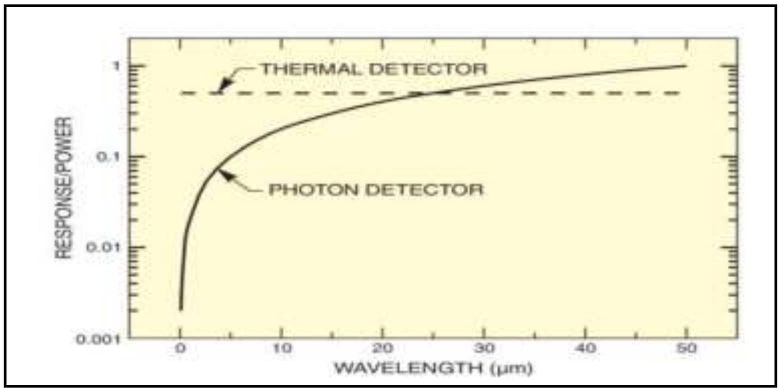

Figure 2.24. Relative spectral responsivities of perfect detectors.

2.23.2 Photon Detectors

The photoelectric effect is used in photon detectors. When light rays strike the detector, photons are absorbed, and electrons are moved over the energy gap to the conduction band by higher energy levels, creating charge carriers (electrons or holes) that increase conductivity or cause voltage differences. The detectors are defined by their spectral response within a particular wavelength range of 300 to 1000 nm, which is dependent on the energy gap and the semiconductor material properties of the detector [144].

1. Photoconductive Detectors

It's a semiconductor chip on both ends with ohmic connections. The electrical conductivity parameter impacts the outcome when exposed to visual radiation. If the input photon's energy is high enough, conduction electrons are formed as the electrons absorb it, increasing the conductivity. The detectors electrical conductivity will alter as the intensity of the incident radiation increases. The sole difference between this sort of detector and others is that it only works with an external electric field. There are two sorts of such detectors [145]:

- Intrinsic photoconductive detectors.
- Extrinsic photoconductive detectors.

2. Photovoltaic Detectors

The production of an internal electric field due to the transfer of carriers from high concentration areas to low concentration areas is required to develop an electric driving force in these light detectors. As a result, these reagents can operate in the presence or absence of an external electric field (i.e., without bias effort) [138]. A reverse bias is usually applied to these detectors. The electric field in the absorption zone is considerable at the reverse bias in order to increase detector qualities such as conductivity. (Table 2.2). Spectral range of wavelengths of electromagnetic radiation. When the reverse bias is present, the depletion zone (W) expands, reducing the heterojunction's range, reducing the time constant ($RC = \tau$), and finally causing a quick reaction. Photovoltaic detectors include heterojunction, Schottky, PIN, MOS, and MIS diodes [146]. The energy gap for both materials utilized in the photodetector determines the spectral range of these detector's operations. Table (2.2) shows the wavelength spectrum range within electromagnetic radiation [147].

Table 2.2. Spectral range of wavelengths of electromagnetic radiation.

Wavelength Range	Division Wave Name	Abbreviation
(200-400) nm	Ultraviolet	UV
(400-700) nm	Visible	VIS
(700-1000) nm	Near infrared	NIR

2.24 Photodetector parameters

The optical detector's essential performance characteristics are used to determine the detector's efficiency and suitability for practical applications.

2.24.1 Spectral response measurements

a- Responsivity R_λ

Responsivity is the ratio of produce electrical signs (current or voltage) to event radiation control, or the r.m.s sign voltage to the r.m.s rate of the event radiation control. The responsivity to monochromatic light for wavelength event is typically take by [148]:

$$R_\lambda = \frac{J_{ph}(\lambda)}{P_{inc}(\lambda)} \tag{2.45}$$

where $J_{ph}(\lambda)$ is the photocurrent density as a function of wavelength measured with photodetectors and $P_{inc}(\lambda)$ is the incident power density recorded with photodetectors. The responsivity is strongest in the wavelength range where the photon energy is somewhat higher than the band gap energy. It rapidly drops in the bandgap area, where absorption increases [149].

b- Photocurrent Gain (*G*)

For each photon absorber each second, the photocurrend gain *"G"* of a detectors is definite as the amount of charge transporters flux between the two detector contact electrodes each second [149]:

$$Gain = \frac{h.c}{e.\lambda} \times R(\lambda)100\ \% = \frac{1240}{\lambda\ \mathrm{nm}} \times R(\lambda)100\ \% \tag{2.46}$$

where h is the Planck constant, c is the speed of light, e is the electron charge, and λ is the wavelength .

2.24.2 Specific Detectivity (D)

One of the most essential detector qualities is detectivity (D), which is defined as the least capable of the incident optical signal that the detector can detect. It is determined by, as mentioned in the equation below (the temperature, the cut-off frequency, the incident wavelength, the detector area, the width of the frequency band, the voltage applied to the detector, and the detection noise) [150]:

$$D_\lambda = \frac{1}{NEP} = \frac{R_\lambda}{I_n} \tag{2.47}$$

The responsivity is R_λ, and the present noise is I_n. Detectivity (D) rises when NEP is low. NEP is measured in Watt units. The symbol for detectivity (D) will be replaced by $D*$ when 1 Watt of optical power is incident on a device with an optical area of 1 cm^2. The noise is measured with a bandwidth of 1 Hz (normalized detectivity). The $D*$ is a relationship that is used to compare detector types [149].

$$D^* = R_\lambda \frac{A^{1/2}\,\Delta f^{1/2}}{I_n} = (A\Delta f)^{1/2}.D_\lambda \tag{2.48}$$

$$I_n = \sqrt{2qI_d}\sqrt{\Delta f} \tag{2.48}$$

Where Δf denotes frequency bandwidth, A denotes effective detection area, q electron charge, R denotes spectral response, I_d is for dark current, and D^* is unaffected by the detectors size. The specific detectivity is measured in (cm.Hz$^{1/2}$ W^{-1}) units.

Chapter Three

Experimental part

3.1 Introduction

The procedures and apparatus used in this investigation, as well as the deposition parameters and solution preparation, are described in this chapter. It begins with chemical spray deposition, spin coating, and drop-casting, and then progresses to the cleaning of glass, quartz, and porous silicon substrates. Finally, characterization approaches to study the structural, surface morphological, optical, electrical, solar cell, and photodetector properties of the deposited films. The essential steps of the experimental work are depicted in Figure 3.1.

3.2 Raw Materials

Chemicals that were used to manufacture solar cells and photodetector are summarized in Table (3.1):

Table (3.1): Raw Materials

Materials	**Details**
Hydrofluoric acid HF	**Purity (99%), pancreas, Quimica (QP), Espana.**
Cd $(NO_3)_2.4H_2O$	**Molecular weight (308.47 g/mol), purity (99,99%), (Qualikems Fine Chem Pvt .Ltd India)**
Zn $(NO_3)_2.6H_2O$	**Molecular weight (297.47 g/mol), purity (98%), (Anmol chemicals. India)**
$SC(NH_2)_2$	**Molecular weight (76.11 g/mol), extra pure,(CDH. India).**
$SnCl_2$	**Molecular weight (189.62 g/mol), Purity (99%), (Sigma Aldrich Co.)**
$Cu_2Cl_2.2H_2O$	**Molecular weight (170.48 g/mol), purity (97%), (Junsei Chemical- Ltd Co., Japan).**

Related to table 3-1

$ZnCl_2$	**Molecular weight (136.29 g/mol), purity (97%), (Avon hem- Ltd Co. England)**
Aluminum (Al)	**Purity (99%), (Balzar Co.)**
Acetone (C_3H6O)	**(C_3H6O) Purity (99%), (VWR chemical)**
Ethanol (C_2H_5OH)	**Purity (99%), (Sigma Aldrich Co.)**
Silicon Wafer (Single Crystal), (n, p-type)	**5 Ω/cm^2, 500 µm, Bioanalyse, Turkey.**
2-Methoxy-ethanol ($CH_3O.CH_2.CH_2OH$)	**Molecular weight (76.10 g/mol), Purity (99%), (Chemical Limited Pool-England) BDH.**
Ethanolamine (C_2H_7NO)	**Molecular weight (61.08 g/mol), purity (98, 5%), (HIMEDIA Co.), India.**
Hydro Chloric acid HCI	**(57% of weight in water),(BDH-LTD Co.), Germany.**
citric acid $C_6H_8O_7.H_2O$	**Molecular weight (192.124g/mol), Company Alpha chemika.**
Ammonium Hydroxide NH_4OH	**Company SIGMA Aldrich (USA) concentration 25%.**
Mono-Ethanolamine (C_2H_7NO)	**Molecular weight (61.08 g/mol), purity (98%), company (HIMEDIA).**

3.3 Sample Preparation

3.3.1 Preparation of Solution

This study used different chemical techniques with various materials in the Nano factor of nanostructured thin films.

1- Dissolving cadmium nitrate Cd $(NO_3)_2.4H_2O$ at a concentration of (0.1M) as a source of cadmium ions and tin chloride at a concentration of (0.1M) ($SnCl_2$) as a source of tin ions in 100 ml of water produced the solution used to form the film of (Cd_2SnO_4). This solution was heated for 30 minutes on a magnetic stirrer, with a drop of (HCl) added to guarantee optimal solubility with water. The end result was a clear, transparent homogeneous solution.

2- Dissolving zinc nitrate $Zn(NO_3)_2.6H_2O$ at a concentration of (0.1M) as a source of zinc ions and tin chloride at a concentration of (0.1M) ($SnCl_2$) as a source of tin ions in 100 ml of water produced the solution used to form the film of (Zn_2SnO_4). This solution was heated for 30 minutes on a magnetic stirrer, with a drop of (HCl) added to guarantee optimal solubility with water. The end result was a clear, transparent homogeneous solution.

3- The solution used to prepare the thin film (Cu_2SnS_3) was made by dissolving aqueous copper chloride $Cu_2Cl_2.2H_2O$ at a concentration of (0.02M) as a source for copper ions and tin chloride at a concentration of (0.01M) ($SnCl_2$) as a source of tin ions and thiourea SC $(NH_2)_2$ at a concentration of (0.06M) as a source of sulfur ions with a final volume of 5 ml of 2-methoxy ethanol anhydrous The end result was a clear, yellow homogeneous solution as in the figure (3.2) .

4- The solution used to prepare the thin film (CuZnS) by dissolving aqueous copper chloride $Cu_2Cl_2.2H_2O$ at a concentration of (0.02M) as a source of copper ions and zinc chloride at a concentration of (0.02M) ($ZnCl_2$) as a source of zinc ions and thiourea $SC(NH_2)_2$ at a concentration of (0.04M) as a source of sulfur ions with final volume of 5 ml of 2-methoxy ethanol anhydrous The end result was a clear, grean homogeneous solution as in the figure (3.2). The account was done masses, and it is required to dissolve it to guarantee normalization needed through the following relationship [151] The masses of the materials to be solved corresponding to the concentration relationship (3 - 1) were calculated as shown in Table (3-2).:

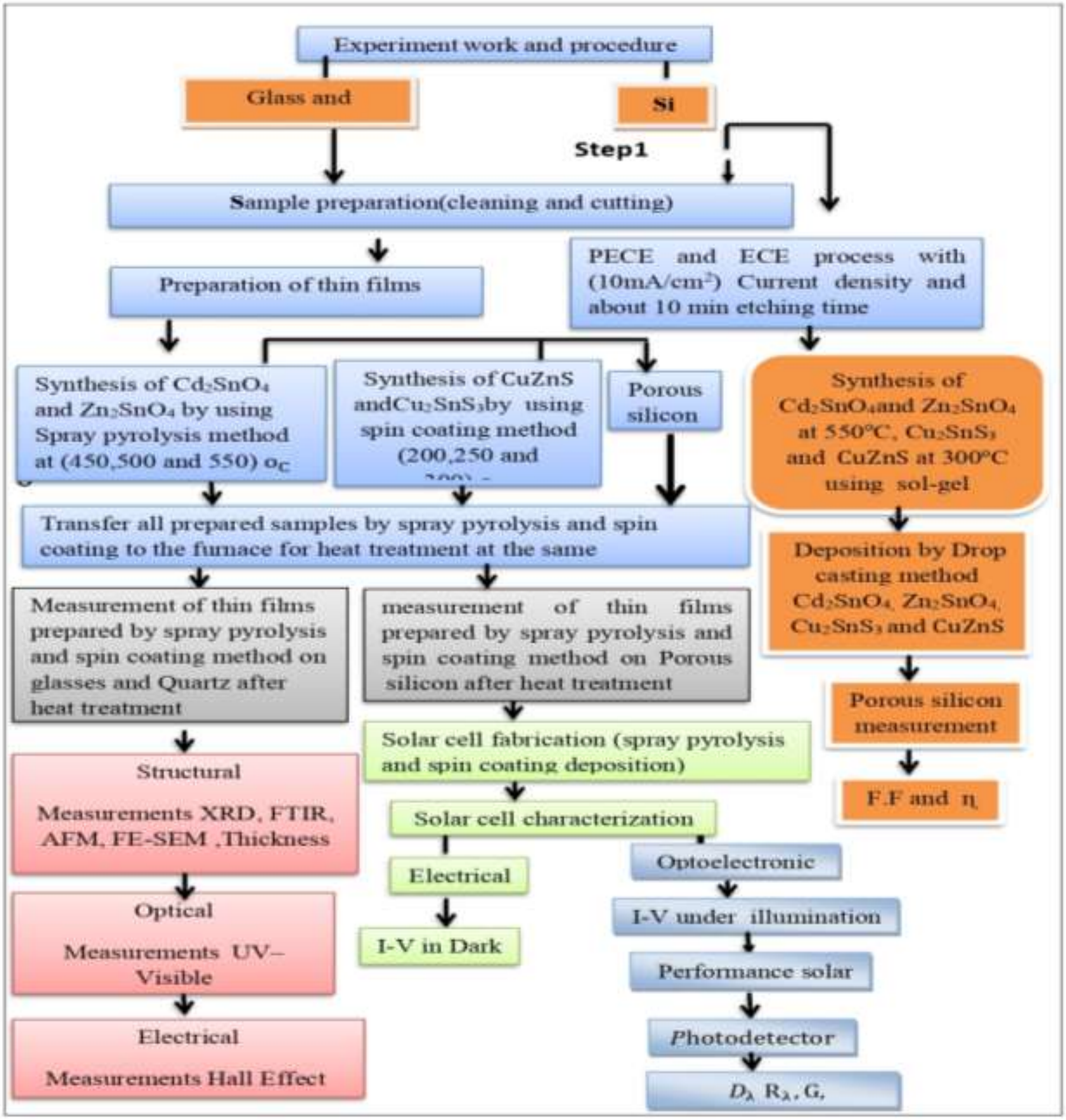

Figure 3.1. The schematic diagram of the experimental work.

$$eafM = (W_t/W_{Wt.}).(1000/V) \tag{3.1}$$

where M is the specific molar concentration (mol/L), W_t is the weight required to be dissolved (g), is $W_{Wt.}$ the molecular weight of the solute (g/ mol), and V the volume of dissolved solvent (ml).

Table 3.2. Masses of materials that make up the thin films (CTO,ZTO,CTS and CZS).

Thin Film	**$Cd(NO_3)_2.4H_2O$**	**$SnCl_2$**	
Cd_2SnO_4	3.087g	1.8962g	
Zn_2SnO_4	$Zn(NO_3)_2.6H2O$	$SnCl_2$	
	2.9747g	1.8962g	
Cu_2SnS_3	$Cu_2Cl_2.2H_2O$	$SnCl_2$	$SC (NH_2)_2$
	0.017042g	0.009481g	0.02283g
CuZnS	$Cu_2Cl_2._2H_2O$	$ZnCl_2$	$SC(NH_2)_2$
	0.017042g	0.0068145g	0.015222g

An electronic balance (Mettler AE-160) weighed the materials (10^{-4} g). Tables 3.2 (c, d) represent the weights of the prepared materials. It is dissolved in (5ml) of 2 – methoxy ethanol anhydrous, and the mixture is placed on a (magnetic stirrer) at (50 °C) for a period of time (10 min). Then, drop by drop, (0.05 ml) of mono-Ethanolamine is added to control the alkalinity of the solution and obtain complete solubility of the compounds; after 5 minutes on the magnetic stirrer at the same temperature, the solution is clear and free of residue. The pH was found to be identical (pH = 7). As demonstrated in fig. 3.2, the final color of the solutions washomogeneous.

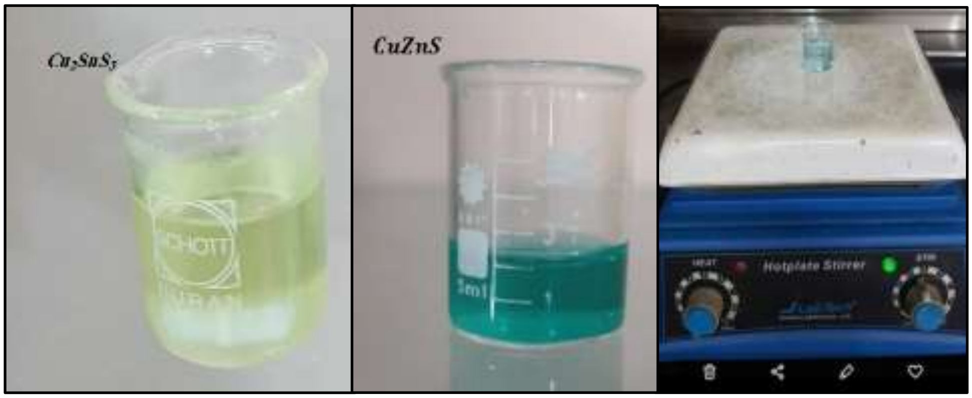

Figure 3.2. Steps of preparing a solution (Cu_2SnS_3 and CuZnS).

3.3.2 Substrate Preparation

a. Glass slides:

The substrate parameters are important because they have a big impact on the deposited films' qualities. The effectiveness with which the substrate is cleaned has a substantial effect on the adhesion quality of the deposited films. Glass was used to make the slides. To test the structural, optical, and electrical properties of thin films (China National Machinery) with dimensions (2.5 ×7.6 cm) was used as the glass substrate on which thin films were created. The glass slide was sliced (1.5×1) cm and thickness (0.1) cm. The processes outlined below can be used to specify cleaning methods [152]:

1- Before being submerged in distilled water for 10 minutes, the glass slides were cleaned with a washing solution to take out any oil or dirt that has developed taking place the substrate's surface.

2- The substrate were submerged in distilled water before being cleansed using an ultrasonic machine for 10 minutes (Bran sonic 220).

3- The substrate were rinsed for 10 minutes in high purity (C_2H_5OH) ethanol tank using the same ultrasonic instrument (99 %).

4- Wipe the slides with soft paper or use an electric drier to dry them.

b. (n-type and p-type) Silicon Substrates:

To eliminate impurities and residuals, the Si samples were washed with alcohol and an ultrasonic bath. The substrates were pit by HF (10%) for 5 minutes to remove the natural oxide. Electrochemical (EC) and photoelectrochemical (PE) methods were used to create thin homogeneous PSi layers of varying thicknesses taking place the forward surface of the material .

3.3.3 Fabrication of Porous Silicon

3.3.3.1 Electrodes Deposition

Prior using the anodization technique, the lowest electrode was plated by a thick aluminum layer., then the electrical characteristics were measured using ohmic contacts. It's made from high-purity aluminum wire vacuum-sealed (99.99 %). At a pressure of 10^{-5} Torr, the evaporation process began. A layer of 500 nm provided the most excellent conditions for good Ohmic contact.

3.3.3.2 The Electrochemical Etching Process

A P+ silicon wafer ($5/cm^2$, 500 µm) of (Bioanalyse, Turkey) by an orientation from(100) was employed as a substrate. To make porous silicon, electrochemical etching was used to modify the surface of a Si wafer. Before pouring a 1:1 mixture of HF (45%) and 100% ethanol into Teflon cells, clean Si was placed at the bottom (99.99 %). A gold ring was employed using current as an electrode densities from10 $mA.cm^{-2}$ within 10 minutes. After that, the porous silicon was bathed in distilled water and dried with nitrogen gas to generate an etched sample area of roughly (0.785 cm^2), as illustrated in figure 3.3. This work was carried out in the laboratories of the Physics Department, College of Science, Al-Mustansiriya University.

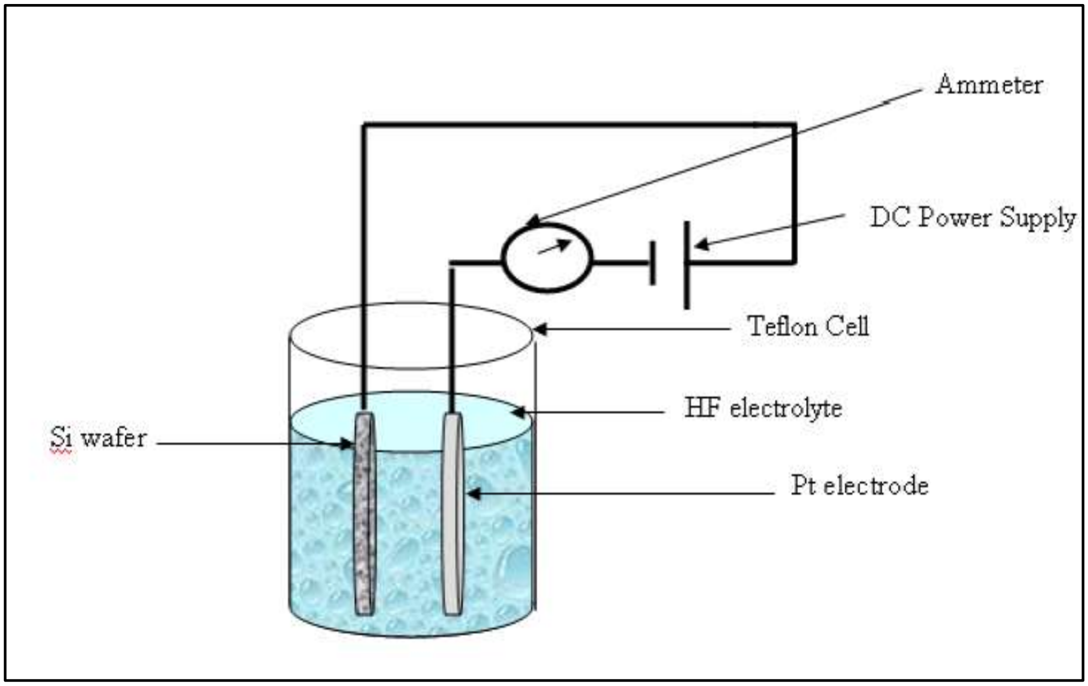

Figure 3.3. Schematic diagram of the electrochemical etching utilized in this study.

3.3.3.3 The Photo Electrochemical Etching (PEC) Process

When a sufficiently enough photon shines on the surface of an n-silicon substrate, holes can be photo-generated in bulk. To illuminate the surface of n-type substrates, a 30 mW diode laser (red-650nm) was used. A double-concave lens was used to achieve a 0.785cm^2 etched area. As seen in the illustration figure 3.4.

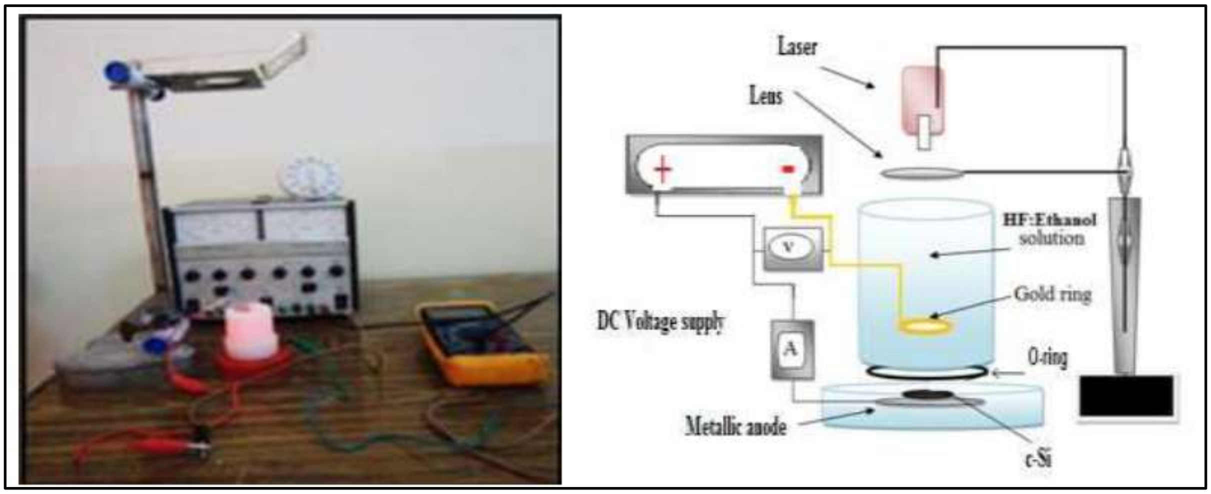

Figure 3.4. Schematic diagram of the PEC system.

3.4 Thin Film Deposition.

Different deposition techniques were applied to deposit Cd_2SnO_4, Zn_2SnO_4, Cu_2SnS_3, and CuZnS on glass and PSi at different temperatures. In the present study, the spin coating technique was used to deposition Cu_2SnS_3 and CuZnS layers Whereas, Cd_2SnO_4 and Zn_2SnO_4 thin films were deposited by Spray pyrolysis. The thickness of the film prepared in the study (300 ±10) nm was used for structure, optical, morphological, and electrical measurements and (1) μm to study the properties of solar cells and photodetectors.

3.5 Chemical Spray Pyrolysis System

Figure 3.5 depicts the spray pyrolysis system, which consisted of multiple assembled components to produce the required films. The elements are as follows:

3.5.1 Atomizer

Figure 3.5 shows how the spraying component is created locally out of normal glass. It is connected to the heater by vertically running metal support. The atomizer consists of a cylindrical tube that stores approximately (100 ml) of the aqueous solutions required to make thin film and is connected to a tap with a valve that regulates the flow of liquid to the capillary tube at the bottom of the film. The tap is 0.1 cm in diameter and 6 cm in length. This capillary tube is encased by a closed glass chamber at the top and an open bottom, both of which are designed to contain the capillary tube's aperture at the same level. This chamber has a side opening that allows gas to shoot out of the capillary tube's end. The spray is fashioned like a cone, with the tip at the end of the tube and the base descending to the heater's surface. The vertical distance between the capillary opening's end and the substrate is (31cm), and increasing it leads the liquid to be sprayed away from the substrate; if it's less than this value, the film will deform.

3.5.2 Electric Heater

The heater elevates the temperature to the required level for the reaction, ensuring that any changes in the film's crystal structure or physical properties are reflected in the film's crystal structure and physical properties. In this experiment, the required temperatures were (450, 500, and 550 ± 10 ° C), which were attained by connecting the heater to an (AC) power supply in the (250 volts) range.

3.5.3 Thermocouple

The thermocouple was of the type Ni Cr-Ni supplied by Phywe in Germany. It includes a thermal probe sensor directly attached to the heater's surface and the substrate's base and a digital temperature gauge that records any temperature changes.

3.6 The Effective Coefficients on the Film's Homogeneity

The homogeneity of prepared films is influenced by a number of factors, which should be considered during the preparation process:

3.6.1 Substrate Temperature

Because the temperature substrate influences the character of the chemical reaction, and thus the nature of the generating material after the reaction, it is one of the most important parameters that determine the homogeneity and dependence of created films and their quality. The temperature was (450,500, and 550 ^{o}C) during the spraying process to obtain remarkable homogeneity and uniformity in films.

3.6.2 Substrate Position

The substrate should be placed above the heater, and each area should be kept at the appropriate temperature and sprayed with the appropriate spraying solution.

3.6.3 Vertical Distance

It is the vertical distance from the end of atomizer tube to the heater surface. This distance must be neither high because the solution will be sputtering in this case, nor low so it concentrates on one spot. In this study, the best high used to get best homogeneous film was 31cm.

3.6.4 Spraying Rate

The atomizer valve was used to control the flow volume per minute of the solution, and the recommended flow rate was 1.65 ml/min.

3.6.5 Spraying Time

The solution should be sprayed for a brief time before ceasing to avoid cooling in the substrate and heater surfaces and crystalline formation. In the investigation, the spraying technique was constant for 5 seconds before being paused for 120 seconds.

3.6.6 Gas Pressure

To ensure that the solution sprays precisely and reaches the substrate surface as a spray rather than a droplet, the pressure the spraying must stay constant during the spraying procedure. 1.5×10^{-5} $N.m^{-2}$ is the applied pressure.

3.6.7 Deposition Process

The heater receives a current from the electrical power supply for about an hour until it reaches the required deposition temperature of 450 °C. To ensure access to 450 °C, glassy substrates and porous silicon were placed on the heater's surface for 15 minutes. The atomizer is positioned vertically at a distance of 31cm from the surfaces. The solution is then poured into the atomizer's cylindrical tube. The faucet's valve is then opened to let the solution flow as drops, and the gas is pumped at $1.5\times10^{-5}1.5\times10^{-5}$ $N.m^{-2}$ to convert the drops to the desired spray. The spraying procedure will run for 5 seconds and then halt for 120 seconds to ensure that the substrate temperature returns to normal. This process is repeated until the desired thickness is obtained. After spraying, the substrates are placed on the heating surface for 30 minutes to facilitate crystal development, then the power is switched off and the substrates are allowed to cool. This process is repeated in deposited thin films at 500 and 550 ºC, and samples are taken for heat treatment in an inside Korean oven (K&K, Korea) at (450,500, and 550 ^{o}C) temperatures. The deposition process is seen in figure 3.5.

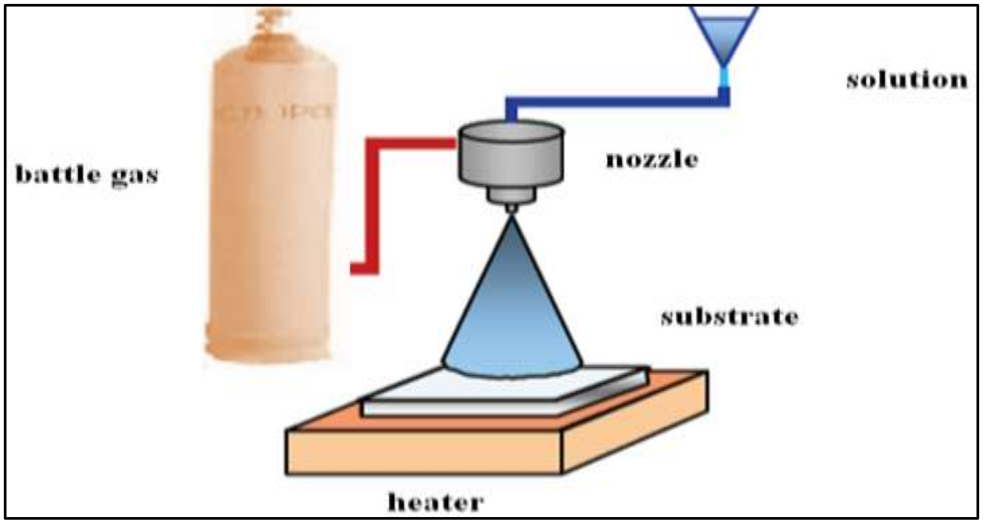

Figure 3.5. Spray pyrolysis deposition equipment.

3.7 Spin Coating Technique

The spin coating employed in this investigation was an (L2001A3, Ossila, UK) spin coater with an adjustable spin speed and time range of (100-6000) rpm and (1-1000) sec, respectively. The spin coating procedure is used to create uniform thin coatings with thicknesses ranging from micrometers to nanometers. Figure 3.6 shows the four steps of spin coating: deposition, spin-up, spin-off, and evaporation. The material is initially put on the turntable, then, while the evaporation process is taking place, it is spun up and down in succession. The applied solution is distributed on the spin coating via centrifugal force. As the spinning speed increases, the layer thins. The applied layer is then dried after this operation. Because of the fast rotation, identical evaporation of the solvent is achievable. The high volatile components of the solution are removed from the substrate by evaporation or simple drying, while the low volatile components of the solution remain on the substrate's surface [153].

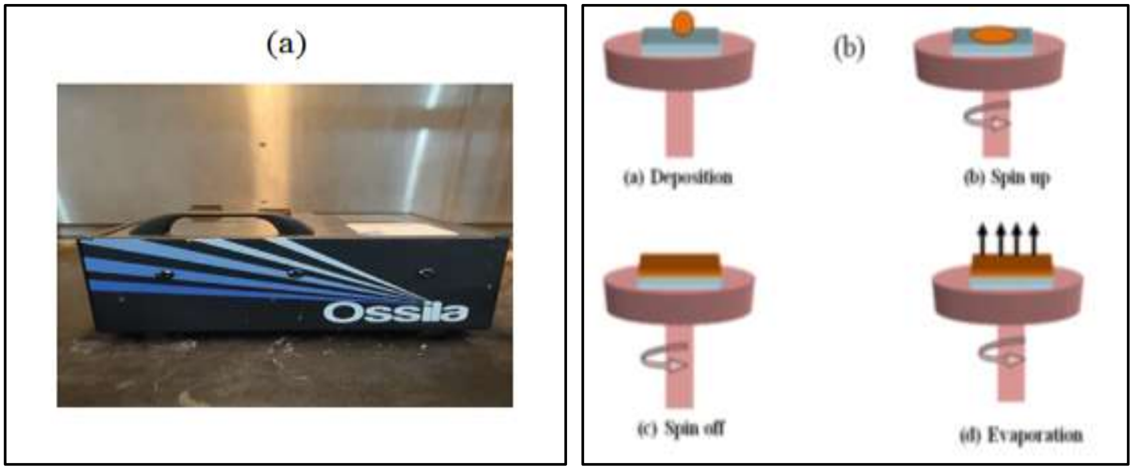

Figure 3.6. (a) A photograph of the spin coater instrument used and (b) spin coating steps on the substrate.

3.7.1 Factors that Influence Thin Film Preparation

When preparing thin films using the spin coating process, one of the essential contributing aspects to consider is:

1- The device should be balanced in terms of placement.
2- The location of the sample concerning the rotational center
3-Rotation time
4- Rotational velocity
5- The solution's concentration
6- The temperature at which the film is growing

3.7.2 Thin Films Deposition

The porous silicon base and glass prepared for deposition are placed on the spin device's bases. To get the best homogeneity film, consider its location in relation to the device's center of rotation. Because the centrifugal force and the continuity of movement towards the tangent are at the heart of the spin coating device's operation, the film distorts and loses its homogeneity if it is not properly centered with respect to the axis of rotation. The coating process begins by pouring the solution into the middle of the base with a liquid dropper until the entire surface is covered. Then it began spinning for a length of time, from rest to (2500 rpm) (30 sec). A portion of the solution volatilizes due to centrifugal forces, while part of it remains due to bonding forces between solution molecules and the glass base's surface. The glass substrate is then removed after the device has stopped. After dipping cotton ear cleaning sticks in ethanol solutions, it is cleaned from the bottom and sides and positioned on a (Hot Plate) at a constant temperature (135°C). The nucleation and growth process begins in the first layer of the thin film for a period of time to ensure that the film does not distort and dry at the proper temperature (10 mins). The base is lifted, left, cooled, and repeated, except for the heat source, where the temperature rises. Deposition the second layer of the film at different temperatures (200, 250, and 300 °C) and times (10minutes). Then lower the hot plate's temperature until it reaches room temperature, ensuring that the thin film is not distorted. Then the heat treatment process begins by placing samples inside an oven at temperatures of (200, 250and 300 ^{o}C) to eliminate organic residues (organic contamination) and undesirable elements (residues of solution components) to remove unwanted materials and produce a thin film (CTS, CZS).

3.7.3 Synthesis of Cd_2SnO_4, Zn_2SnO_4, Cu_2SnS_3 and CuZnS Nanoparticles by Sol-Gel Procedure

The sol-gel method is used in material science to make solid materials for small molecules. This chemical reaction creates a sol (colloidal solution) that develops into a diphasic gel-like structure with liquid and solid phases. Metal oxides and Sulfide are created using this method. It requires turning monomers into a colloidal solution (sol) that acts as a precursor for a discrete particle integrated network (or gel).

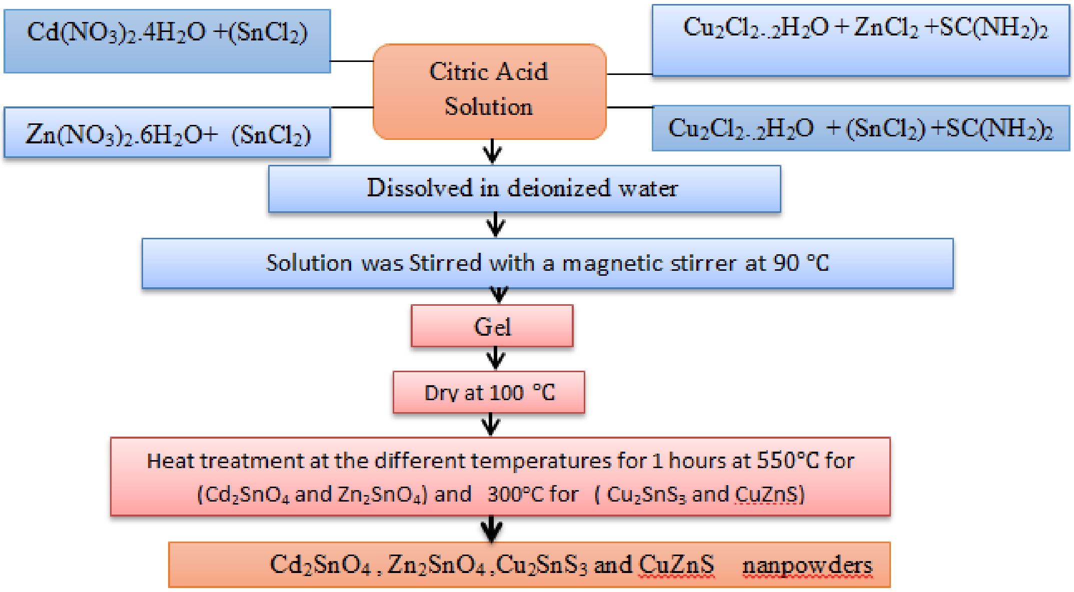

Figure 3.7. The diagram of the sol-gel method.

3.7.3.1 Calculating Weight of the Materials

Molar concentration or molarity is defined as the amount of solute per unit volume of solution or per unit volume available to the species and is most usually stated in units of moles of solute per liter of solution for use in broader applications. The weight of the substance is calculated using the Molarity rule from equation (3-1).

Table 3.3. Masses of materials that made up the thin films (Cd_2SnO_4, Zn_2SnO_4, Cu_2SnS_3 and CuZnS) by the Sol-Gel Method.

Thin film	**Requirement**			
Cd_2SnO_4	$Cd(NO_3)_2.4H_2O$	$SnCl_2$	$C_6H8O_7.H_2O$	
	3.08g	1.89g	0.96g	
Zn_2SnO_4	$Zn(NO3)2.6H_2O$	$SnCl_2$	$C_6H8O_7.H_2O$	
	2.90g	1.89g	0.96g	
Cu_2SnS_3	$Cu_2Cl_2.2H_2O$	$SnCl_2$	$Sc(NH_2)_2$	$C_6H8O_7.H2O$
	1.70g	1.89g	0.76g	0.96g
CuZnS	$Cu_2Cl_2.2H_2O$	$ZnCl_2$	$Sc(NH_2)_2$	$C_6H8O_7.H_2O$
	1.70g	1.36g	0.76g	0.96g

3.7.3.2 Preparation of Cd_2SnO_4, Zn_2SnO_4, Cu_2SnS_3 and CuZnS Nanoparticles by Sol-Gel method

1- In preparation of Cd_2SnO_4 thin films, the following solutions were used: 0.1M Cd $(NO_3)_2.4H_2O$ in 100 ml of the water, 0.05 citric acid $C_6H_8O_7.H_2O$ in 100 ml of the water and 0.1 M $SnCl_2$ dissolved in 100 ml of the water separately. After mixing is completed, all solutions are placed in one beaker.

2- In preparation of Zn_2SnO_4 thin films, the following solutions were used: 0.1M $Zn(NO_3)_2.6H_2O$ in 100 ml of the water, 0.05M citric acid $C_6H_8O_7.H_2O$ in 100 ml of the water and 0.1 M $SnCl_2$ dissolved in 100 ml of the water separately. After mixing is completed, all solutions are placed in one beaker.

3- In preparation of Cu_2SnS_3 thin films, the following solutions were used: 0.1 M $Cu_2Cl_2.2H_2O$ in 100 ml of the water, 0. 05 M citric acid $C_6H_8O_7.H_2O$ in 100 ml of the water, 0.1 M $SnCl_2$ melted in 100 ml of the water, and 0.1M $SC(NH_2)_2$

dissolved in 100 ml of the water separately. After mixing is completed, all solutions are placed in one beaker.

4- In preparation of Cu_2SnS_3 thin films, the following solutions were used:1M $Cu_2Cl_2.2H_2O$ in dissolved 100 ml of the water, 0.05 M citric acid $C_6H_8O_7.H_2O$ in 100 ml of the water,1 M $ZnCl_2$ dissolved in 100 ml of the water and 0.1M $Sc(NH_2)_2$ dissolved in 100 ml of the water separately. After mixing is completed, all solutions are placed in one beaker.

At 90 °C, the solution was agitated with a magnetic stirrer. Then, drop by drop, ammonium hydroxide (NH_4OH) was added to the mixture until it was transparent. The ammonium hydroxide (NH_4OH) was important for keeping the pH of the solution. The final pH of this transparent homogenous solution was (7). For around 4 hours, keep stirring until a gel develops. The gel was then left to burn at 100 °C. A light, Combustion produced fluffy matter, which was then processed further heat-treated for 1 hour at a temperature of 500 °C for Cd_2SnO_4 and Zn_2SnO_4 300 ^oC for Cu_2SnS_3 and CuZnS to obtain highly crystalline Cd_2SnO_4, Zn_2SnO_4, Cu_2SnS_3 and CuZnS nanoparticles as shown in Fig. 3.8 and 3.9.


(a) (b) (c)

Figure 3.8. The sol-gel steps technique for Cu_2SnS_3 thin film: (a) solution, (b) gel and (c) burn.

(a) (b) (c)

Figure 3.9. The sol-gel steps technique for Zn_2SnO_4 thin film: (a) solution, (b) gel and (c) burn.

3.7.3.3 Thin Film Deposition

After the oxides and sulfide were obtained by the sol-gel method, 0.6 g of each oxide was dissolved in 100 ml of de-ionized water; the solution was stirred by a magnetic stirrer for 30 min at 90 °C and then deposited by, using the Drop casting method has been deposit a Cd_2SnO_4, Zn_2SnO_4, Cu_2SnS_3 and CuZnS film on PSi samples.This technique is the most effective for forming diverse thin films because it allows for great productivity with a simple setup and no material waste.

3.8 Preparation of Contact Electrodes

The aluminum (Al) contact electrode was deposited on the final layer using a shadow mask, and it was employed an aluminum (Al) wire as a depositing electrode (99.9%) that was constant over the prepared films. Thermal evaporation was used to deposit the aluminum electrode using the Edward coating unit model (606) under the pressure of 10^{-5} mbar provided by rotary and diffusion pump, and thickness of 250 μm, with an area of 0.1 cm^2 on the (Cd_2SnO_4, Zn_2SnO_4, Cu_2SnS_3, and CuZnS) /PSi) layer as electrodes.

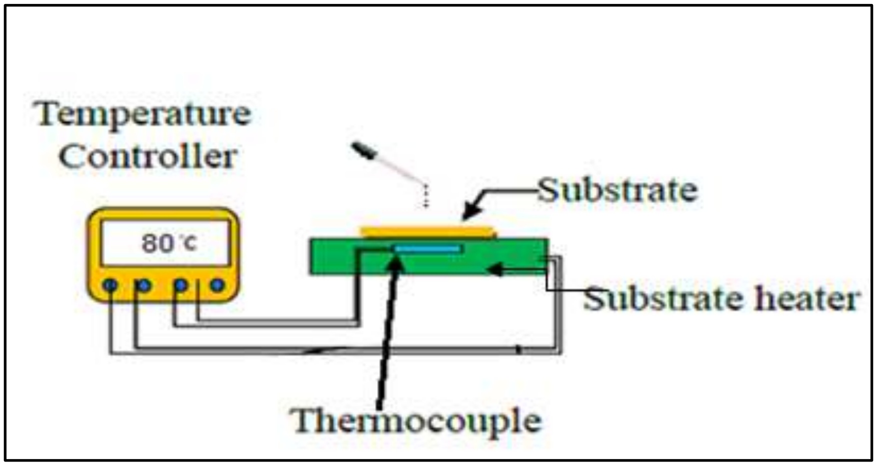

Figure 3.10. Schematic diagram drop-casting method experimental setup.

3.9 Heat treatment of Samples

In our current investigation, we used an electric furnace with a temperature range of up to (1200 °C) (forence). For one hour, the films Cd_2SnO_4 and Zn_2SnO_4 were heated to (450, 500, and 550°C), Cu_2SnS_3 and CuZnS were heated to (200, 250, and 300 °C),. The samples were left to cool for 24 hours before being removed to conduct the appropriate testing.

3.10 Masks Preparation

As illustrated in Figures 3.10 (a and b), suitable masks were created from aluminum foil with dimensions (width: 2 mm, spacing between electrodes: 2 mm) and then cleaned with distilled water and alcohol to make the shape of electrodes that were utilized for the measurements of hall effect.

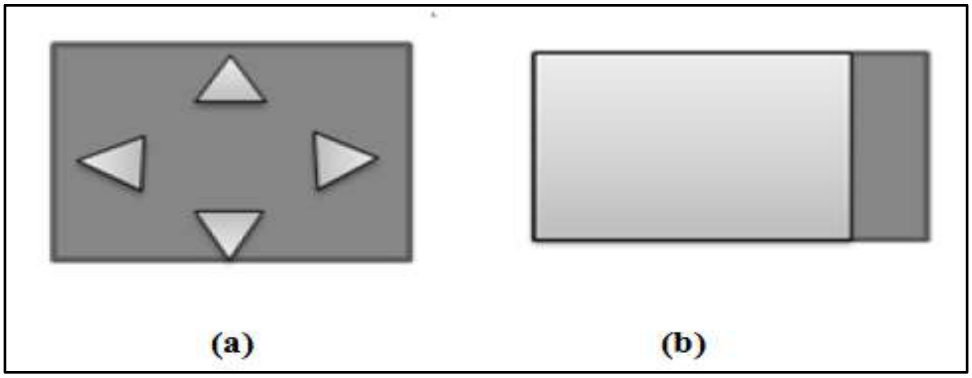

Figure 3.11. Mask for (a) Hall effect and (b) device.

3.11 Device Fabrication

3.11.1 Fabrication of Heterojunctions (Solar Cell and Photodetectors)

Figures 3.12 clarifies Thin films were deposited on porous Si wafers prepared by spray pyrolsis,spin coating and drop casting methods Cd_2SnO_4 /PSi/Si/Al, Zn_2SnO_4/Psi/Si/Al, Cu_2SnS_3/Psi/Si/ Al and CuZnS /PSi/Si/Al.

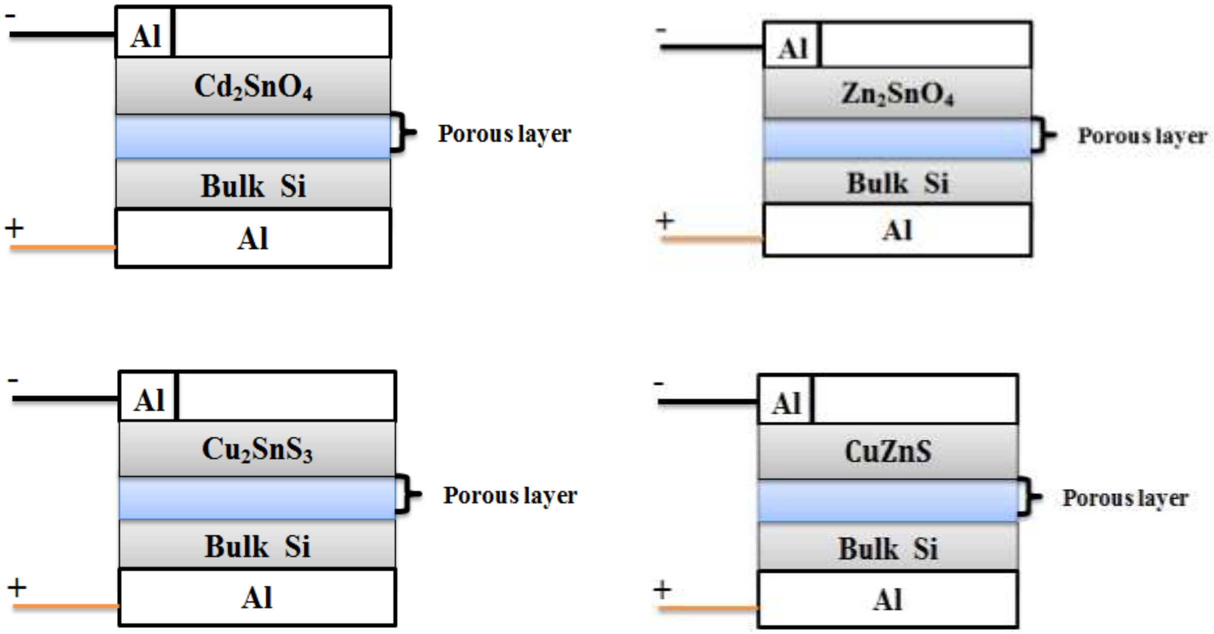

Figure 3.12. The basic structure of typical (Cd_2SnO_4, Zn_2SnO_4, Cu_2SnS_3 and CuZnS)/PSi/Si/ Al heterojunction.

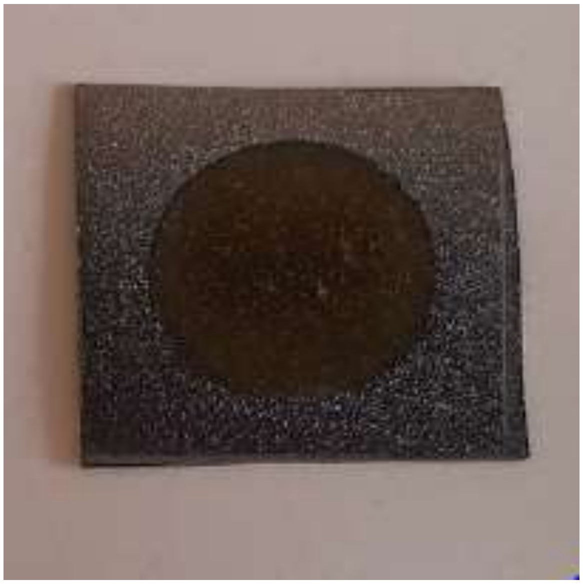

Figure 3.13. Porous silicon membrane.

3.12 Measurements

The following measurements were performed on Cd_2SnO_4, Zn_2SnO_4, Cu_2SnS_3, and CuZnS thin films prepared by spray pyrolysis and spin coating (XRD, AFM, FE-SEM, FTIR, UV and electrical properties).

3.12.1 The Thickness of the thin film

Thin-film thickness is an important factor in determining physical properties, and there are numerous ways for determining thin film thickness.

- **Gravimetric Method**

The thickness of thin films (t) can be measured in various ways. The gravimetric approach is one of the most appropriate and suitable methods. This method is based on the difference in substrate weight before and after film deposition. A Sartorius BP 3015 sensitive electronic balance was utilized. The relationship below can be used to compute thickness [155].

$$t = (\Delta m/\rho A) \tag{3.2}$$

Where $\Delta m = m_2 - m_1$the difference in mass between the glass substrate before and after deposition

m_1: the mass of the glass substrate before deposition (g).

m_2: The mass of the glass substrate after deposition (g).

A: area of the thin film (cm^2) , and ρ density of the thin-film material and density of the Cd_2SnO_4, Zn_2SnO_4, Cu_2SnS_3 and CuZnS are equal to (7.26 ,6.13,5.02 and 2.072 g/cm^3) respectively. Because this method has a ratio of error, other methods for measuring film thickness are more precise.

- **Cross Section**

An approach used for estimating the thickness of manufactured films that involves imaging the thin film's cross-section. During a check, it is the most accurate and reliable approach in this study (FE-SEM).

3.13 Characterization Techniques

3.13.1 Structural Measurement (X-Ray Diffraction)

The X-ray diffract meter model (XRD- Philips Xpert, The Netherlands) with the target type (Cu-Kα) and the single wavelength used ($\lambda_{Cu-K\alpha}$=1.54060 Å) available in Kashan University-Republic of Iran, as the diagnosis of the XR pattern and the locations of the peaks that appear on the X-ray images for a range of angles (2θ = 20 - 80) [76].

3.13.2 Field Emission Scanning Electron Microscopy (FE-SEM)

The cross-sectional images were taken with an (FE-SEM) device to measure the thickness of the prepared films using (ZEISS Sigma FE-SEMs, Germany) in the Central Research Laboratory of Mashhad University-Iran.

3.13.3 Atomic Force Microscope (AFM)

AFM is high-resolution technique used to determent the porosity, thickness, and topography of a sample surface. It generates photographs of the sample surface in two dimensions (2D) and three dimensions (3D). In this research, an atomic force microscope (AFM) available at the Central Research Laboratory-University of Mashhad, Republic of Iran, was used with specifications: TT-2, an advanced second-generation tablet microscope (Japan).

3.13.4 Fourier Transform Infrared Spectroscopy (FTIR)

The absorption band was recorded with wavenumbers (400-4000 cm^{-1}). In this research, a spectroscopic device (FTIR) model (IRAFFINITY-1CE) was manufactured by the Japanese company (SHIMADZU CORPORATION). Figure 3.17 was utilized, which is available in the College of Science – University of Diyala laboratory.

Figure 3.17. Fourier transform infrared spectroscopy system.

3.13.5 UV-Vis Spectroscopy

For optical measurements, including transmission and absorption spectra, a UV-Vis double beam spectrophotometer (Visible1800) built by (Shimadzu, Japanese Co.) was utilized. The absorbance of Cd_2SnO_4, Zn_2SnO_4, Cu_2SnS_3, and CuZnS thin films was measured over a spectral range of from nm (200 -1100 nm) . A blank sample of substrate is used as a reference in the measurement of optical transmittance. Figure 3.18 depicts the schematic diagram of UV-Vis spectroscopy. This measurement was made at the University of Diyala -College of Science as shown in Fig.(3-19) .

Figure 3.18. UV-Vis system.

3.13.6 Hall Effect Measurements

The electrical mobility, carrier concentration, resistivity, and type of carriers are all determined using the Hall Effect technique at different deposited temperatures thin films for Cd_2SnO_4, and Zn_2SnO_4 (450, 500, and 550 ºC), for Cu_2SnS_3 and CuZnS (200, 250 and 300 ºC). Hall Effect measurement has been done by (HMS-3000, VER 3.5) which is provided by the American company (ECOPIA) and is located in recent divisions in the Ministry of Science and Technology. The device is connected to a computer and comes with a special program that displays the most important parameters for the sample under investigation at room temperature, including the type of semiconductor, charge carrier mobility and concentration, resistance, electrical suspension, and information about other a parameter. Hall Measurement system using (0.55 Tesla) magnetic field as shown in Fig.(3-19).

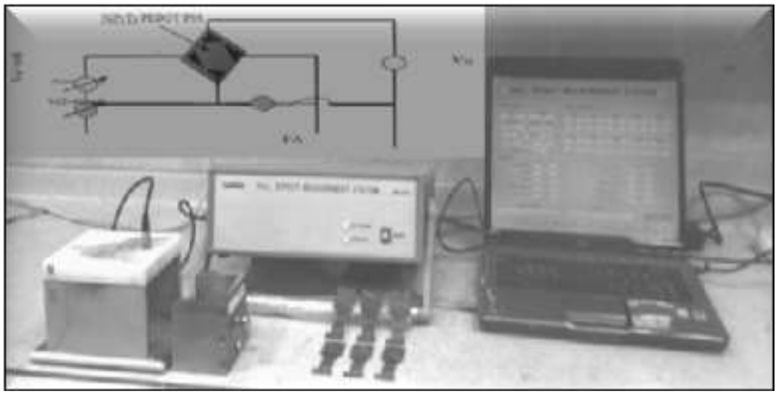

Figure 3.19. Hall effect measurement system.

Using thermal evaporation in a vacuum, four aluminum (ohmic contacts) are formed on the sample, which is then inserted in a four-point probe inside the device as shown in Fig.(3-20) . The carrier concentration (n_H), Hall mobility (μ_H) and conductivity (σ) are evaluated using equation 2.29 and 2.30, respectively .

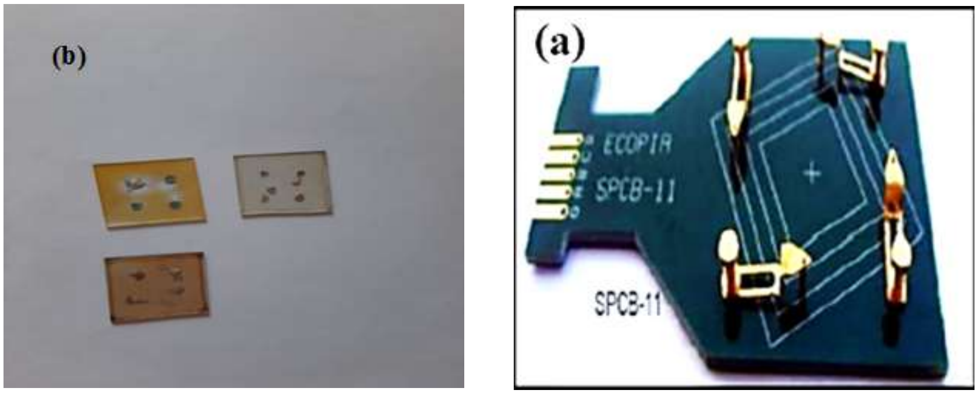

Figure 3.20. Image of the sample holder on which the samples are placed, (b) Image of the prepared samples.

3.14. Solar Cell Parameters

3.14.1 Open-Circuit Voltage Measurement

The value of open-circuit voltages (V_{oc}) reflects the quantity of voltages produced by the heterojunction in the absence of an external bias voltage on the heterojunction and is a function of incident light intensity was computed with an incident light power density of 100 mW/m^2. After determining the maximum values for both current and voltages (Im,Vm) and short circuit current (I_{sc}), open-circuit voltages (V_{oc}), and fill factor and conversion efficiency by drawing the relations between current and voltages, equations 2.43 and 2.44 were used to calculate fill factor ($F.F.$) respectively and conversion efficiency (percent) using a digital scale of type (Keithley 619 Digital Electrometer) and resistors box valued(1-100) m Ω.

3.14.2 Short-Circuit Current Measurement

The characteristics of (I-V) are measured in the dark and at room temperature by placing the samples inside a dark chamber and connecting to the electrical circuit, by measuring the dark current (I_d) and the bias voltage (V) at the front bias by connecting the n-type of the solar cell from the negative voltage from the power source and the p-type of the solar cell to the positive voltage from the power source using a two-channel digital scale from type (Digital electrometer Keithily-616, Tektronics CDM (250) multimeter, dual Farnel LT30/2 (0-10)Volt power supply Tektronics CDM (250) multimeter).

3.15 Electrical Properties of Heterojunction

3.15.1 (I-V) Characteristics Measurement in the Dark Condition

The current (I_d) is measured in one of the digital scale's channels, while the voltages (V) are monitored. By connecting the negative part of the sample from the positive voltage of the continuous power source, and the positive part of the sample from the negative voltage of the power source, the dark current and bias voltage (i.e. Reverse Bias) is measured. The study of these characteristics was conducted within the range of voltage bias (0-10) Volts, with a continuous power supply (D.C Power Supply) as the source (Dazheng: PS-303D) [155,134]. The circuit diagram for measuring current-voltage characteristics in the dark is shown in figure 3.21.

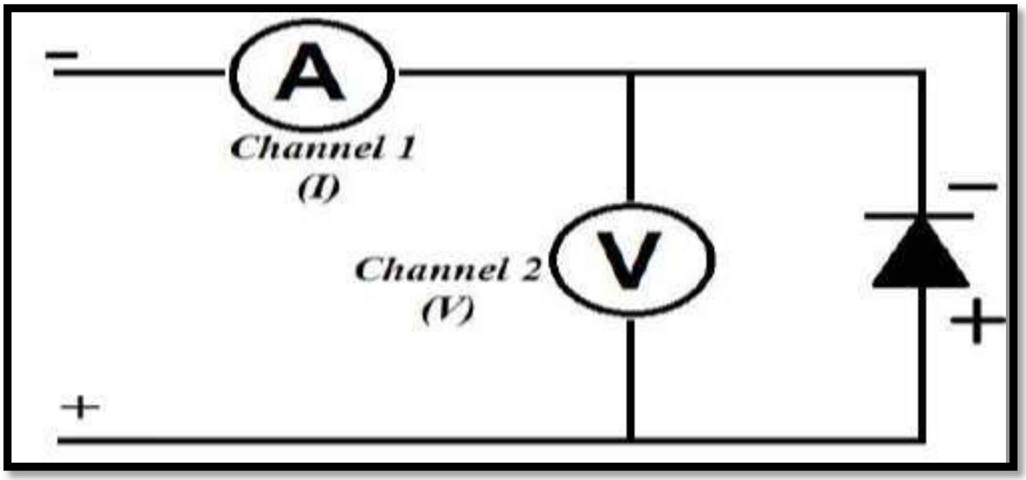

Figure 3.21. Ideal Circuit diagram used to measure current-voltage characteristics in the dark case.

3.15.2 (Current-Voltage) Characteristics Measurement under Illumination

As a function of the reverse bias, the photocurrent generated (I_{ph})) for the prepared solar cell was measured (V). The solar cell was exposed to white light from a halogen lamp (Halogen Lamp-(240V and 50 W) prepared by a company (Wotan-Germany) with a power density of (100mW/m^2), and it was determined that the reverse bias voltage applied to the solar cell is variable within the range (0-10) Volts by comparing the photocurrent values generated by solar cell illumination with the dark current values of the cell under the reverse voltage applied. The (UNI-Trend Group: Hong Kong) firm's type (UT136) digital ammeters and voltmeters were employed in the electrical circuit, and the incidence of radiative power on the heterojunction from the lamp was evaluated using an optical power gauge of type (LP1) from the business (Sanwa Electric Instrument Com-Tokyo).

3.16 Photodetector Properties Measurements

3.16 .1 Spectral Responsively (R_λ).

The spectral response (R_λ) amount for the specific wavelengths incident on the detector was estimated using the equation for the spectral response (R_λ) 2.45 as measured by the instrument (Double-beam UIR-210A spectrophotometer operated in wavelengths range (350-1000) nm. Figure 3.22 shows the equipment used to calculate the spectrum reaction of the manufactured photovoltaic detectors. This study was done in the laboratories of the Physics Department, College of Science, Al-Mustansiriya University.

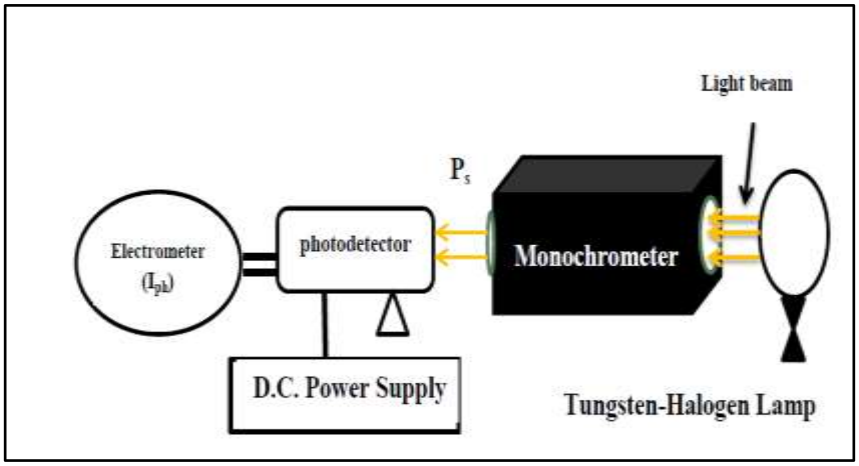

Figure 3.22. The system used to measure the spectral response of the prepared photovoltaic detectors.

3.16.2 Spectral Detectivity (D*)

The manufactured detector's spectral detectivity (D*) was estimated as a function of wavelength using the formula 2.48.

Chapter Four

Results and Discussion

4.1 Introduction

This chapter includes the results and the analysis of the experimental details measurements (structural, surface morphology, optical, electrical characteristics, solar cells, and photodetectors) that were prepared by spray pyrolysis and spin-coating technique the results and the analysis of the experimental details measurements (solar cells) prepared by drop-casting technique.

4.2 Structural Measurements

4.2.1 XRD Analysis of (Cd_2SnO_4) Thin Films Prepared by Spray Pyrolysis Technique

The X-ray diffraction (XRD patterns of Cd_2SnO_4 thin films at varied deposition temperatures (450, 500, and 550 °C) are shown in Figure 4.1. The pattern has diffraction peaks around (2θ~27.6351°, 32.0593°, 39.3630°, 56.3694°, 67.0209° and 68.4199 °) for Cd_2SnO_4 thin film deposited at 450 °C. The pattern exhibits diffraction peaks around (2θ~27.5824°, 32.0585°, 39.3447°, 56.3479°, 67.0499°, and 68.3645°) for the thin film deposited at (500 °C). Diffraction peaks around (2θ~27.4568°, 32.0295°, 39.3421°, 56.3509°, 66.9838°, and 68.1341°) were seen when thin film was deposited at (550 °C). the prepared thin films had the lattice parameters of a cubic spinel structure a=b=c= 8.9885, 8.9885, and 9.0448 Å, respectively, at varied deposition temperatures (450, 500, and 550 °C). All of the peak positions correspond to the (220), (311), (400), (440), (533), and (622) planes and they fully matched the standard pattern with card numbers # 80-1468 from the International Diffraction Data Center (ICDD). The strongest peak is found at 2θ ~32º, often known as the (311) plane. These findings are nearly identical to those published by Gnanamoorthy et al., [156]. The XRD pattern preferred the (311) orientation, which has a high intensity since heating increases the intensity of the planes, which improves the crystal structure [157]. These spectra were used to analyze diffraction angle (2θ), inter planer distance (d), full width at half maximum (FWHM), and phases recognized along the (hkl) planes are all structural factors., which are provided in table 4.1

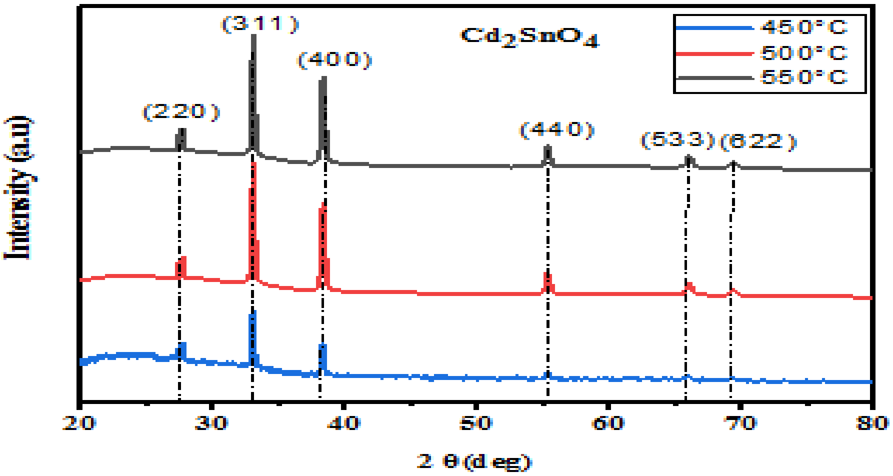

Figure 4.1. X-ray Diffraction of Cd_2SnO_4 thin films deposited at different substrate temperatures (450, 500 and 550 °C) prepared by spray pyrolysis.

Table 4.1. X-ray diffraction results of Cd_2SnO_4 thin films prepared by spray pyrolysis technique.

Thin film	Temperature °C	2 θ(deg)	d (Å)	(hkl)	FWHM (deg)
Cd_2SnO_4	**450**	**27.6351**	**3.1932**	**(220)**	**0.3382**
		32.0593	**2.71014**	**(311)**	**0.2852**
		39.3630	**2.34900**	**(400)**	**0.2460**
		56.3694	**1.66099**	**(240)**	**0.1968**
		67.0209	**1.41650**	**(533)**	**0.2460**
		68.4199	**1.35620**	**(622)**	**0.7200**
	500	**27.5824**	**3.1952**	**(220)**	**0.3322**
		32.0585	**2.71239**	**(311)**	**0.2460**
		39.3447	**2.34705**	**(400)**	**0.2460**
		39.3447	**1.41532**	**(240)**	**0.2952**
		67.0499	**1.41532**	**(533)**	**0.3936**
		68.3645	**1.35507**	**(622)**	**0.4800**
	550	**27.4586**	**3.1988**	**(220)**	**0.3243**
		32.0295	**2.71239**	**(311)**	**0.1968**
		39.3421	**2.34900**	**(400)**	**0.1968**
		56.3509	**1.66099**	**(240**	**0.2952**
		67.9838	**1.41650**	**(533)**	**0.7200**
		68.1341	**1.35589**	**(622)**	**0.6955**

4.2.2 XRD Analysis of (Zn_2SnO_4) Thin Films Prepared by Spray Pyrolysis Technique

Figure 4.2 shows the X-ray diffraction (XRD) patterns of Zn_2SnO_4 thin films prepared by spray pyrolysis at different substrate temperatures (450, 500, and 550 °C).The deposited films have a polycrystalline structure, which was achieved using the spray pyrolysis process. The pattern of Zn_2SnO_4 thin film deposited at 450 °C has five diffraction peaks around (2θ~29.6436°, 34.6851°, 36.4354°, 41.0518°, and 60.9610°) and corresponding to the (220), (311), (222), (400), and (440) planes of the (cubic spinel) structure of Zn_2SnO_4 as confirmed by standard data .Many peaks for hexagonal ZnO (2θ~31.9992°, 47.7467°, 56.6877°, and 62.2236°) and tetragonal SnO_2 (2θ~26.6052°, 37.6160°, and 51.4990°) can be seen in the XRD pattern .For Zn_2SnO_4 thin film deposited at (500°C),the pattern displays diffraction peaks at (2θ~29.6127°, 34.6109°, 36.4014°, 41.6458°, and 60.3810°) corresponding to (220), (311), (222), (400), and (440) of the (cubic) structure of Zn_2SnO_4, as determined by standard data. The XRD patterns for hexagonal ZnO (2θ~31.9132°, 47.6334°, 56.6224°, and 62.9797°) and tetragonal SnO_2 (2θ~26.6454°, 37.6365°, and 51.4442°) reveal the presence of numerous additional peaks .For Zn_2SnO_4 thin film deposition at (550 °C), the pattern displays diffraction peaks at (2θ~29.60365°, 34.3810°, 36.1929°, 41.3655°, and 60.3376°) corresponding to (220), (311), (222), (400), and (440) of the (cubic) structure of Zn_2SnO_4, as validated by standard data. In the XRD patterns for hexagonal ZnO (2θ~31.6749°, 47.367°, 56.3123°, and 62.645°) and tetragonal SnO_2 (2θ~26.6052°, 37.7240°, and 51.5903°), numerous additional peaks can be observed. The peaks in the XRD pattern are completely match to the standard pattern with the card number of the International Center of Diffraction Data (ICDD) (24-1470,96-210-4744 and 96-901-1663) Returns to Zn_2SnO_4, SnO_2 and ZnO Respectively, with the strongest peak occurring at 2θ~34° in the (311) plane. The increasing strength of the peaks as the temperature rises indicates that the crystallization of the film improves with increasing temperature [24]. This result is highly congruent with the result published by. Mohammed et al. [24]. Notably, the XRD pattern favored the (311), which has a strong intensity. Structure parameters such as diffraction angle (2θ), lattice spacing (d), full width at half maximum (FWHM), and phases identified with (hkl) planes were determined from these patterns and are displayed in Table 4.2.

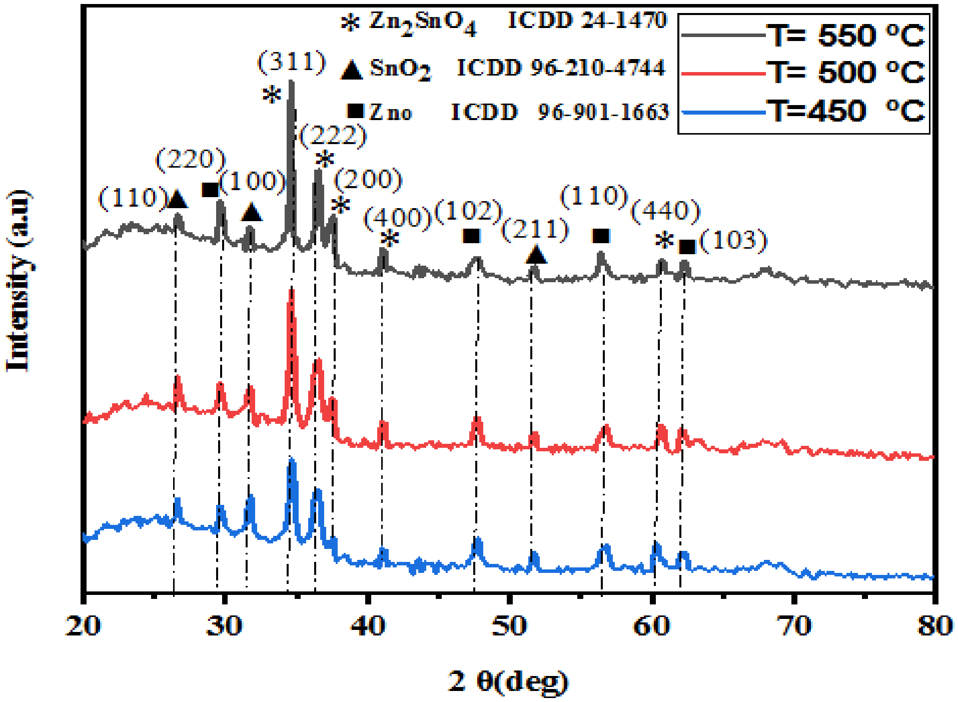

Figure 4.2. X-ray Diffraction of Zn_2SnO_4 thin films at different substrate temperatures (450, 500 and 550 °C) prepared by spray pyrolysis.

Table 4.2. X-ray diffraction results of Zn_2SnO_4 thin films prepared by spray pyrolysis technique.

Thin film	Temperature ^oC	2 Θ(deg)	d (Å)	(hkl)	FWHM (deg)
Zn_2SnO_4	450	26.6478	3.41794	(110)	0.61140
		29.6436	3.01116	(220)	0.70360
		31.9992	2.79468	(100)	0.70390
		34.6851	2.58417	(311)	0.75910
		36.4354	2.46395	(222)	0.74290
		37.6160	2.41279	(200)	0.51760
		41.0518	2.19690	(400)	0.76250
		47.7467	1.90331	(102)	0.80150
		51.4990	1.77310	(211)	0.73340
		56.6877	1.62250	(110)	0.89360
		60.9610	1.56525	(440)	1.68570
		62.2236	1.49078	(103)	00.5666
	500	26.6454	3.31806	(110)	0.54290
		29.6127	3.04327	(220)	0.70154
		31.9132	2.80202	(100)	0.67380
		34.6109	2.58954	(311)	0.70080
		36.4014	2.46617	(222)	0.71660
		37.6365	2.38808	(200)	0.46990
		41.6458	2.16639	(400)	0.73740
		47.6334	1.90757	(102)	1.00060
		51.4442	1.77486	(211)	0.66000
		56.6224	1.62421	(110)	0.70610
		60.3810	1.50921	(440)	1.07270
		62.9797	1.47469	(103)	0.67780
	550	26.6052	3.31127	(110)	0.51249
		29.60365	3.01325	(220)	0.70125
		31.6749	2.82740	(100)	0.4920
		34.3810	2.60969	(311)	0.3936
		36.1929	2.48606	(222)	0.3936
		37.7240	2.41279	(200)	0.40670
		41.3655	2.16731	(400)	0.66754
		47.367	1.91768	(102)	0.6853
		51.5903	1.77310	(211)	0.59286
		56.3123	1.63240	(110)	0.6074
		60.3376	1.51674	(440)	0.97690
		62.645	1.48175	(103)	0.6365

4.2.3 XRD Analysis of (Cu_2SnS_3) Thin Films Prepared by Spin Coating Technique

Figure 4.3 shows the X-ray diffraction (XRD) patterns of Cu_2SnS_3 thin films produced by spin coating at three deposition temperatures (200, 250, and 300 °C). Cu_2SnS_3 thin film deposited at 200 °C produces diffraction peaks around (2θ~28.5416°, 33.0402°, 47.4671°, and 56.3150°) corresponding to (112), (200), (220), and (312), respectively. The films are all tetragonal in structure with lattice parameters of a=b=5.4863 Å and c= 10.8944 Å. The pattern reveals diffraction peaks at (2θ~28.5354°, 33.1332°, 47.4792°, and 56.3157°) corresponding to (112), (200), (220), and (312) for Cu_2SnS_3 thin films deposited at (250 °C), and the films have a tetragonal structure" with lattice parameters a=b=5.4595 Å and c=10.8986 Å. For Cu_2SnS_3 thin film deposited at 300 °C, the pattern shows diffraction peaks around (2θ~28.5321°, 33.8201°, 47.4796°, and 56.3219°), which correspond to (112), (200), (220), and (312), and the films have a tetragonal structure with lattice parameters of a=b=5.4024 Å and c=10.814 Å. The XRD pattern peaks line up perfectly with the International Center of Diffraction Data (ICDD) card's standard pattern (01-089-4714). At 2θ~28.5°, which corresponds to the (112) plane, there is the highest peak. This result matches up very well with Dias et al. [40] found. Notably, the XRD pattern preferred the (112) orientation, which has a high intensity and shows that crystallization is most likely to happen along this plane [158]. From these patteren, structural parameters such as diffraction angle (2θ), lattice spacing (d), full width at half maximum (FWHM), and phases identified along the (hkl) planes were calculated and listed in Table 4.3.

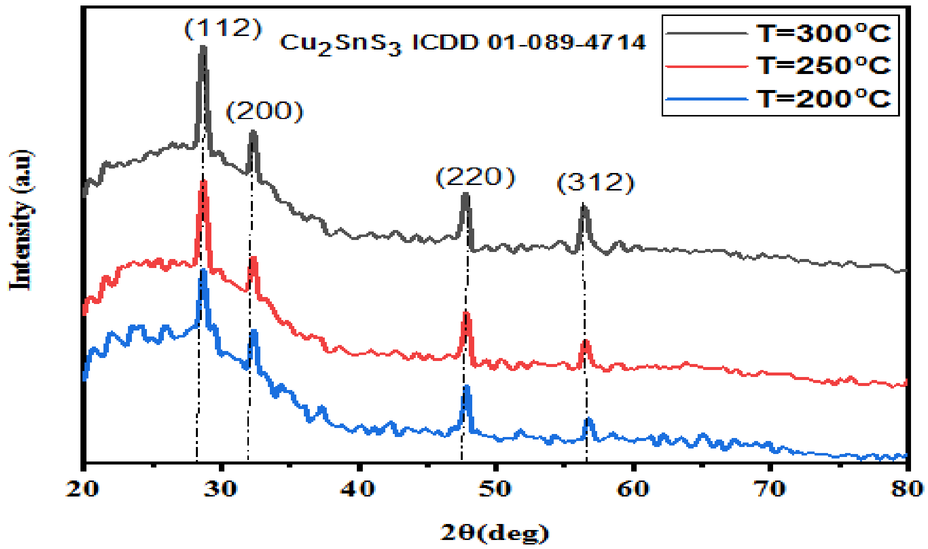

Figure 4.3. X-ray Diffraction of Cu_2SnS_3 thin films at different substrate temperatures (200, 250 and 300 °C) deposited and annealed.

Table 4.3. X-ray diffraction results of Cu_2SnS_3 thin films prepared by spin coating technique.

Thin film	Temperature °C	2 θ(deg)	d (Å)	(hkl)	FWHM (deg)
Cu_2SnS_3	200	28.5416	3.16352	(112)	0.57000
		33.0402	2.73473	(200)	0.45000
		47. 4671	1.94354	(220)	0.38000
		56.3150	1.63660	(312)	0.48000
	250	28.5354	3.15897	(112)	0.45000
		33.1332	2.72125	(200)	0.48000
		47.4792	1.93948	(220)	0.43000
		56.3157	1.63549	(312)	0.48000
	300	28.5321	3.12523	(112)	0.38000
		33.8210	2.71939	(200)	0.36000
		47.4796	1.91563	(220)	0.38000
		56.3219	1.63422	(312)	0.34000

4.2.4 XRD Analysis of (CuZnS) Thin Films Prepared by Spin Coating Technique

Figure 4.4 shows the X-ray diffraction (XRD) patterns of CuZnS thin film. Both CuS and ZnS thin films have peaks that are unique to them. The planes (100), (102), and (110), which belong to the hexagonal phase, show that CuS is in the hexagonal phase. A thin film of ZnS also has hexagonal phase planes (101) and (311). It is seen from the XRD patterns of the CuZnS thin films are polycrystalline with orientation along different planes and phases thin films of different deposition temperatures (200, 250, and 300°C), prepared by spin coating technique.For CuZnS thin film deposited at 200°C, the pattern shows diffraction peaks around (2θ~ 26.0891°, 28.5553°, 29.9234°, 46.1691°, and 57.1857°) corresponding to (100), (101), (102), (110), and (311), and the films have a hexagonal structure using the parameters of the lattice a=b=3.87 Å and c=5.60 Å. For making a thin film of CuZnS at 250 °C. The pattern contains diffraction peaks around it, as can be seen (2θ~26.2788°, 28.5752°, 29.4041°, 46.1196°, and 57.1357°), which correspond to (100), (101),(102), (110) and (311). All of the films have a hexagonal structure using the parameters of the lattice a=b=3.86 Å and c=5.64 Å. For CuZnS thin film deposition at 300 °C, the pattern shows diffraction peaks around (2θ~26.4086°, 28.6801°, 29.1619°, 46.6493°, and 57.3681°), which correspond to (100), (101), (102), (110), and (311), and the films have a hexagonal structure using the parameters of the lattice a=b=3.86 Å and c=5.61 Å. The XRD pattern's peaks line up perfectly with the standard pattern on the International Center of Diffraction Data (ICDD) card (80-0007& 06-0464). The highest point is at 2θ~29°, which corresponds to the (102) plane. This result fits very well with what. Gubari et al. [159] said their results were. Notably, the XRD pattern preferred the (102) plane, which has a high intensity and narrow peaks. This shows that the crystallinity of CZS nanoparticles [160]. From these patterns , structural parameters such as diffraction angle (2θ), lattice spacing (d), full width at half maximum (FWHM), and phases identified along the (hkl) planes were calculated and listed in Table 4.4.

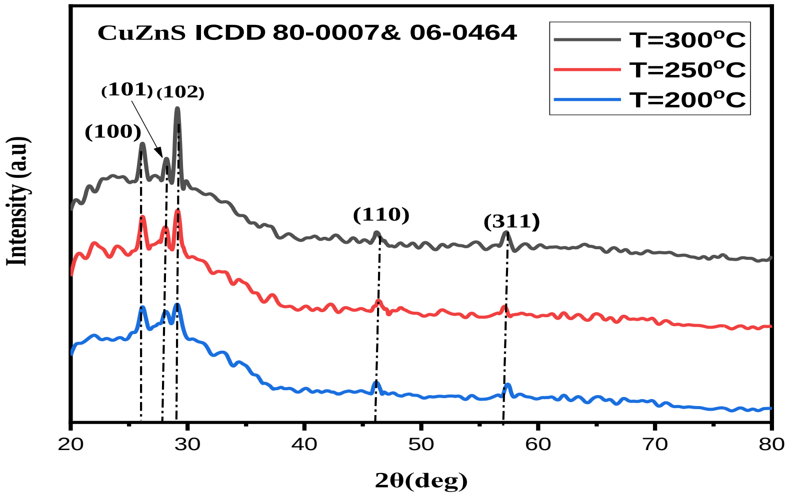

Figure 4.4. X-ray Diffraction of CuZnS thin films at different substrate temperatures (200, 250 and 300 ^{o}C) deposited and annealed.

Table 4.4. X-ray diffraction results of CuZnS thin films prepared by spin coating technique.

Thin film	Temperature ^{o}C	2 θ(deg)	d (Å)	(hkl)	FWHM (deg)
Cu Zn S	200	26.0891	3.36481	(100)	0.92000
		28.5553	3.17342	(101	0.57000
		29.9234	2.96784	(102	0.52000
		46.1196	1.95760	(110)	0.48000
		57.1857	1.59580	(311)	0.76000
	250	26.2788	3.35124	(100)	0.87300
		28.5752	3.17021	(101)	0.37000
		29.4041	2.98037	(102)	0.32000
		46.1691	1.95717	(110)	0.26000
		57.1357	1.59477	(311)	0.68000
	300	26.4086	3.36233	(100)	0.78000
		28.6801	3.16829	(101)	0.27000
		29.1619	2.98365	(102)	0.23000
		46.6493	1.95697	(110)	0.26000
		57.3681	1.593649	(311)	0.38000

4.2.5 XRD Analysis of Cd_2SnO_4 Thin Films Prepared by Drop Casting Technique

Figure 4.5 shows the X-ray diffraction (XRD) patterns of a thin Cd_2SnO_4 film that was made by drop-casting technique at a deposition temperature of 550 °C. The pattern has diffraction peaks at (2θ~27.5929°, 32.7340°, 33.0340°, 39.5103°, 48.4290°, 51.7779°, 66.0617°, and 67.3908°), which correspond to (220), (311), (222), (400), (422), (511), (533), and (622). The thin film have cubic structures with a=b=c= 9.3530 Å as their lattice parameters. The peaks in the XRD pattern are in the same positions as in the regular pattern with the card numbers #80-1468 from the International Center for Diffraction Data. At 2θ~32° which corresponds to the (311) plane, there is the strongest peak. This result is very similar to those reported by Dinesh et al. [161]. Notably, the (311) orientation, which has a high intensity, was the one that the XRD pattern preferred. Table 4.5 shows that the crystallite size of the thin film was calculated to be 13.4 nm. From these pattern , structural parameters such as diffraction angle (2θ), lattice spacing (d), full width at half maximum (FWHM), and phases identified along the (hkl) planes were calculated and listed in Table 4.5.

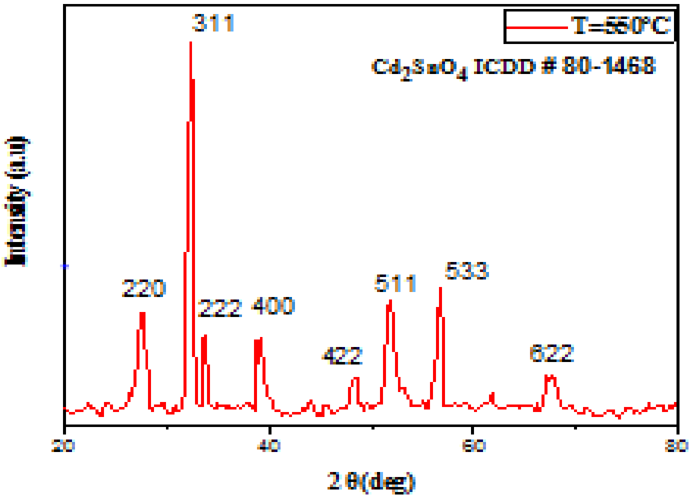

Figure 4.5. X-ray Diffraction of Cd_2SnO_4 thin films prepared by the drop-casting method that annealed at temperature (550 °C).

Table 4.5. X-ray diffraction results of Cd_2SnO_4 thin films prepped by drop-casting technique.

Thin film	Temperature (^oC)	2θ(deg)	(hkl)	d_{hkl} (Å)	FWHM (deg)	Crystallite Size (D) (nm)
Cd_2SnO_4	550	27.5929	(220)	5.19830	0. 8710	9.8
		32.7340	(311)	2.73361	0.64330	13.4
		33.0340	(222)	2.71223	0.79340	10.9
		39.5103	(400)	2.33583	0.80340	10.9
		48.4290	(422)	1.87808	1.12600	8.0
		51.4440	(511)	1.76420	1.03030	8.9
		66.0617	(533)	1.52689	0.87870	11.2
		67.3544	(622)	1.38848	1.51950	6.5

4.2.6 XRD Analysis of Zn_2SnO_4Thin Film Prepared by Drop Casting Technique

The X-ray diffraction (XRD) patterns of a Zn_2SnO_4 thin film at the temperature of 550°C degrees Celsius are displayed in figure 4.6. It was revealed that the films that were deposited had a polycrystalline structure. The Zn_2SnO_4 thin film pattern that was deposited at 550 °C displayed three diffraction peaks about (2θ~34.0479°, 36.3978°, and 60.5951°). These peaks correspond to (311), (222), and (440) of the (cubic spinel) structure of Zn_2SnO_4, which was confirmed by standard data. There are a lot of other peaks that have been found in the XRD pattern for the hexagonal ZnO of (2θ~31.9163°, 47.6839°, 56.7381°, and 62.0319°) and the tetragonal SnO_2 of (2θ~26.7331° and 51.9112°). The film has a cubic spinel structure with lattice parameters of a=8.6563 Å..The XRD pattern's peak positions are identical to the standard pattern associated with the card number from the International Center of Diffraction Data (ICDD) (24-1470,96-

210-4744 and 96-901-1663) Returns to Zn_2SnO_4, SnO_2 and ZnO Respectively . The most prominent peak appears at 2θ~34°, often known as the (311) plane. This result is in very good accord with the findings that were reported by Mohammed et al [24]. Notably, the (311) orientation, which has a high intensity, was the one that the XRD pattern preferred. Through calculations the crystallite size of the thin film has been determined to be 25 nm, according to the calculations. Diffraction angle, lattice spacing, FWHM, and phase identification long with (hkl) planes were analyzed from these patterns and reported in table 4.6 as structural characteristics.

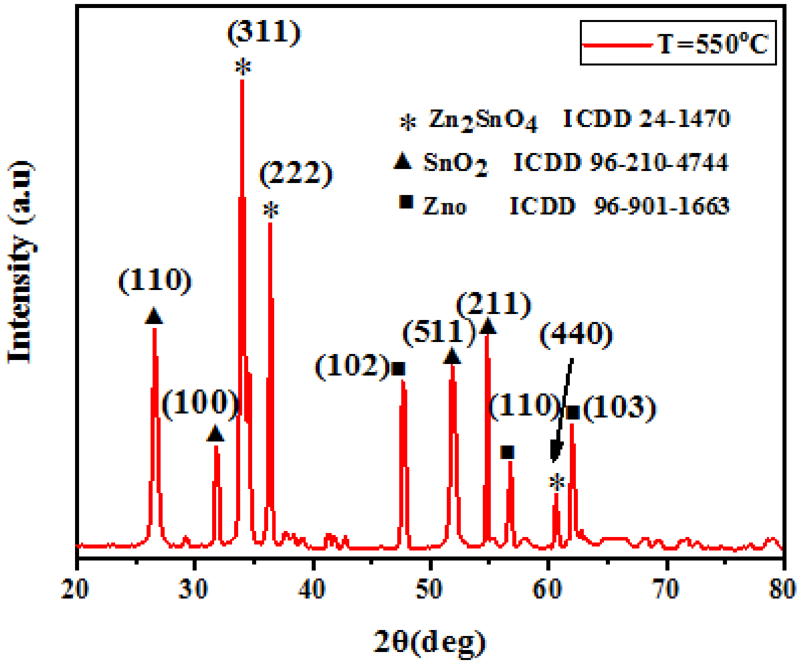

Figure 4.6. X-ray Diffraction of Zn_2SnO_4 thin films prepared by drop-casting method that annealed at temperature (550 °C).

Table 4.6. X-ray diffraction results of Zn_2SnO_4 thin films prepped by drop-casting technique.

Thin film	Temperature (^oC)	2θ(deg)	(hkl)	d_{hkl} (Å)	FWHM (deg)	Crystallite Size (D) (nm)
Zn_2SnO_4	550	26.7331	(110)	3.33204	0.50910	16.7
		31.9163	(100)	2.80175	0.48610	17.7
		34.0479	(311)	2.63106	0.34610	25.0
		36.3978	(222)	2.46641	0.46550	18.7
		47.6839	(102)	1.90567	0.46440	19.5
		51.9112	(211)	1.75998	0.49970	18.4
		54.8994	(511)	1.67104	0.51170	18.2
		56.7381	(110)	1.62118	0.46790	20.1
		60.5951	(440)	1.52689	0.42450	221.6
		62.0319	(103)	1.49532	0.50520	19.1

4.2.7 XRD Analysis of Cu_2SnS_3Thin film Prepared by Drop Casting Technique

Figure 4.7 displays the X-ray diffraction (XRD) patterns of Cu_2SnS_3 thin film that was created using drop coasting process and had its deposition temperature set at 300 $^{\circ}$C. Cu_2SnS_3 film deposited at a temperature of 300 ^{o}Cdiffraction peaks appear in the pattern at approximately(2θ~22.84427°, 32.0979°, 47.9101°,56.9611°, 58.6388°, 68.3560°, and 76.9837°, which correspond to the (111), (200), (220), (311), (222), (400), and (331) planes. The crystal structure of the film is cubic, and its lattice parameters are a=b=c=5.42 Å. This result is in very good agreement with the findings that Rahaman et al [162] published. The XRD pattern's peak positions are identical to the standard pattern associated with the card number from the International Center of Diffraction Data (ICDD) (89-2877). The most prominent peak can be found at a bearing of 2θ~28.4427°, referred to as the (111) plane. Particularly noteworthy is the fact that the XRD pattern favored the (111) orientation, which has a high intensity. It has been determined by calculations that the crystallite size of the thin film has been determined to be 26.7 nm, according to the calculations. Diffraction angle, lattice spacing, FWHM, and phase identification long with (hkl) planes were analyzed from these patterns and reported in table 4.7 as structural characteristics.

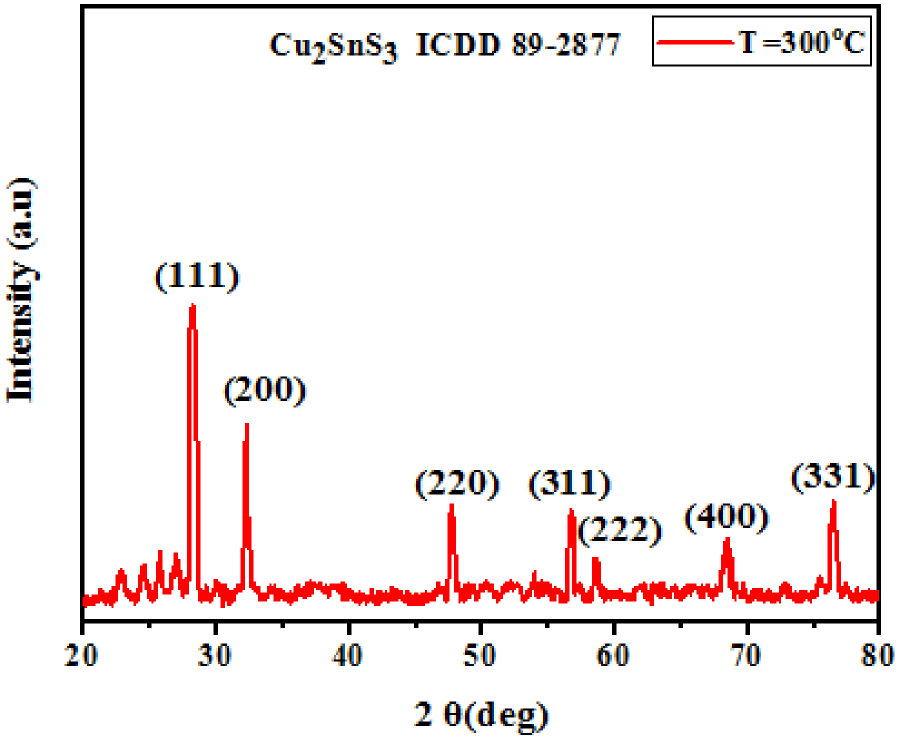

Figure 4.7. X-ray Diffraction of Cu_2SnS_3 thin films prepared by drop-casting method that annealed at a temperature (300 °C).

Table 4.7. X-ray diffraction results of Cu_2SnS_3 thin films prepped by drop-casting technique.

Thin film	Temperature (^oC)	2θ(deg)	(hkl)	d_{hkl} (Å)	FWHM (deg)	Crystallite Size (D) (nm)
Cu_2SnS_3	300	28.4427	(111)	3.13392	0.32000	26.7
		32.0979	(200)	2.78631	0.32230	26.7
		47.5285	(220)	1.91153	0.51810	17.5
		56.5841	(311)	1.62522	0.48070	19.6
		58.2820	(222)	1.57308	0.38800	24.4
		68.3560	(400)	1.36483	0.41790	24.0
		76.9837	(311)	1.23762	0.55390	19.1

4.2.8 XRD Analysis of CuZnS Thin Film Prepared by Drop Casting Technique

The X-ray diffraction (XRD) patterns of CuZnS thin film are shown in Figure 4.8. These patterns have characteristic peaks, just like the XRD patterns of CuS and ZnS thin films. Additionally, In the CZS XRD pattern, the cubic ZnS phase (ICDD No. 65-0309) is prominent, with the CuS phase accounting for the minor peaks (ICDD No. 89-2072) is predominant in the CZS XRD pattern, while the minor peaks are attributed to the CuS phase (ICDD No. 89-2072). The high-intensity peaks may be found by the 2θ values of 28.4622°, 47.7286°, and 56.3184°, which are indexed to their relevant planes of (111), (220), and (311). The CuZnS film is polycrystalline, as evidenced by the XRD patterns. CuZnS thin film deposition at 300°C exhibits diffraction peaks at (2θ~28.4622°, 32.2419°, 47.7286°, 56.3814°, 68.0317°, and 76.6493°) corresponding to (111), (200),(220),(331),(400), and (331), and the film is cubic crystal structure by lattice parameters a=b=c=5.46 Å. This result is in perfect agreement with

Sundaram et al. [160] findings. The strongest peak is found at 2θ~28.4622°, often known as the (111) plane. Particularly notable is the high-intensity (111) orientation preference in the XRD pattern. The crystallite size of the thin film has been determined to be 30.5 nm, according to the calculations. Diffraction angle, lattice spacing, FWHM, and phase identification long with (hkl) planes were analyzed from these patterns and reported in a table as structural characteristics 4.8.

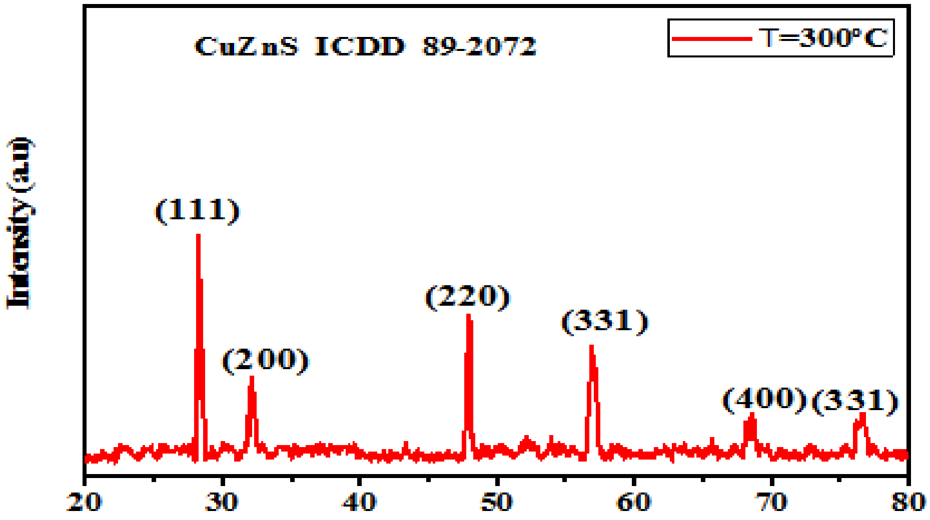

Figure 4.8. X-ray Diffraction of CuZnS thin films prepared by drop-casting method that annealed at a temperature (300 °C).

Table 4.8. X-ray diffraction results of CuZnS thin films prepped by drop-casting technique.

Thin film	Temperature (^oC)	2θ(deg)	(hkl)	d_{hkl} (Å)	FWHM (deg)	Crystallite Size (D) (nm)
CuZnS	**300**	**28.4622**	**(111)**	**3.15694**	**0.28000**	**30.5**
		32.8416	**(200)**	**2.72490**	**0.29670**	**29.1**
		47.9101	**(220)**	**1.89720**	**0.31820**	**28.5**
		56.9611	(311)	**1.61536**	**0.37650**	**25.0**
		68.2317	(400)	**1.37121**	**0.42860**	**23.3**
		76.6493	(331)	**1.24693**	**0.29000**	**34.9**

4.2.9 The XRD Crystallite Size (D)

The crystallite size of the thin films generated by spray pyrolysis and spin coating (Cd_2SnO_4, Zn_2SnO_4, Cu_2SnS_3, and CuZnS was determined using Scherer's formula (2.8). As indicated in Table 4.9, the best crystallite size for $Cd_2SnO_4$and Zn_2SnO_4 thin films formed at 550 ℃ is 42.01 and 21.13 nm, respectively. The larger crystallite size data indicate that the films crystallized better as the substrate temperature increased. Researcher [157], agree with this conclusion. As shown in Table 4.9, this improvement in crystal structure could be attributed to an increase in crystallite size as small crystallites join together in the planes as the substrate temperature rises. This result is consistent with the findings of other researcher [157]. The size of the crystallites grows larger as the temperature rises, and the largest grains form. Other parameters, such as lattice strain and dislocation density, decrease with temperature, ensuring better structural properties of the films annealed at high temperatures [163], and the better crystallite size for Cu_2SnS_3 and CuZnS deposited thin films at 300 ℃ equals to 21.58 and 35.70 nm, respectively, as illustrate in Table 4.9. The larger crystallite size data indicate that the films crystallized better as the temperature was raised. Researchers [158, 160] agree with this result. The W-H equation can be used to calculate the crystallite size (2.10) Figure 4.9 shows graphs for Cd_2SnO_4, Zn_2SnO_4, Cu_2Sns_3, and CuZnS thin films with (4sin θ) along the x-axis and (cos θ) along the y-axis. The crystallite size was calculated from the intercept of the linear fit, and the microstrain *S* was calculated from the fit's slope. Micro stresses are formed during the nanomaterial's formation and are raised as the lattice stretches or compresses. Varying atom displacements concerning their reference lattice positions induce micro strain [164]. The W-H plots for samples Cd_2SnO_4 and Zn_2SnO_4 thin films are shown in Figure 4.9, and the results are summarized in Table 4.9. Micro strain values that are positive for Cd_2SnO_4 and

Zn_2SnO_4thin films show that the lattice is stretching. W-H plots for Cu_2SnS_3 and CuZnS thin films are shown in Figure 4.10, and the findings are shown in Figure 4.9. Based on the data, Cu_2SnS_3 and CuZnS thin films have negative microstrain values. A negative slope from the graph indicates the subtle of compressive strain, slope corresponds to a tensile one [160,165]. The improvement in crystal size and reduction in compressive strain has been attributed to the increase in temperature [165].

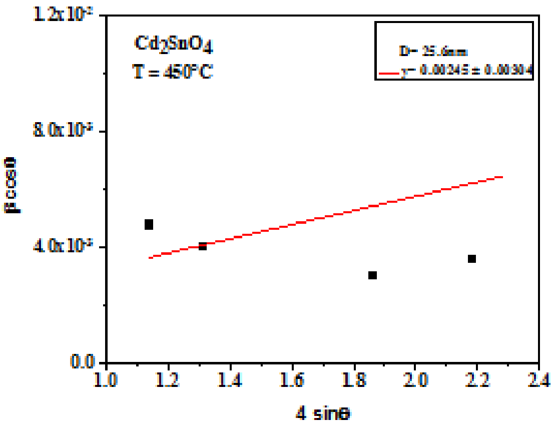

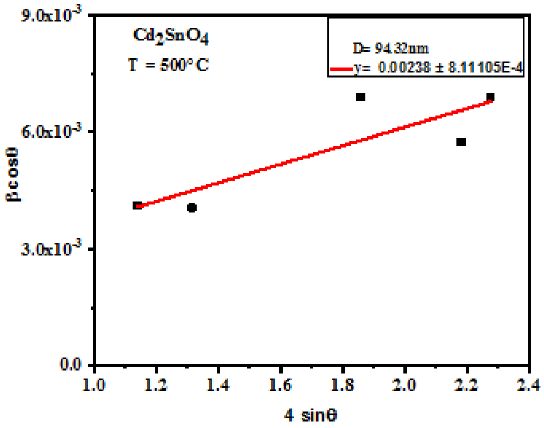

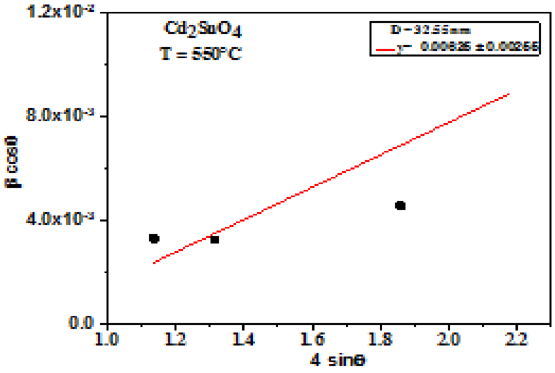

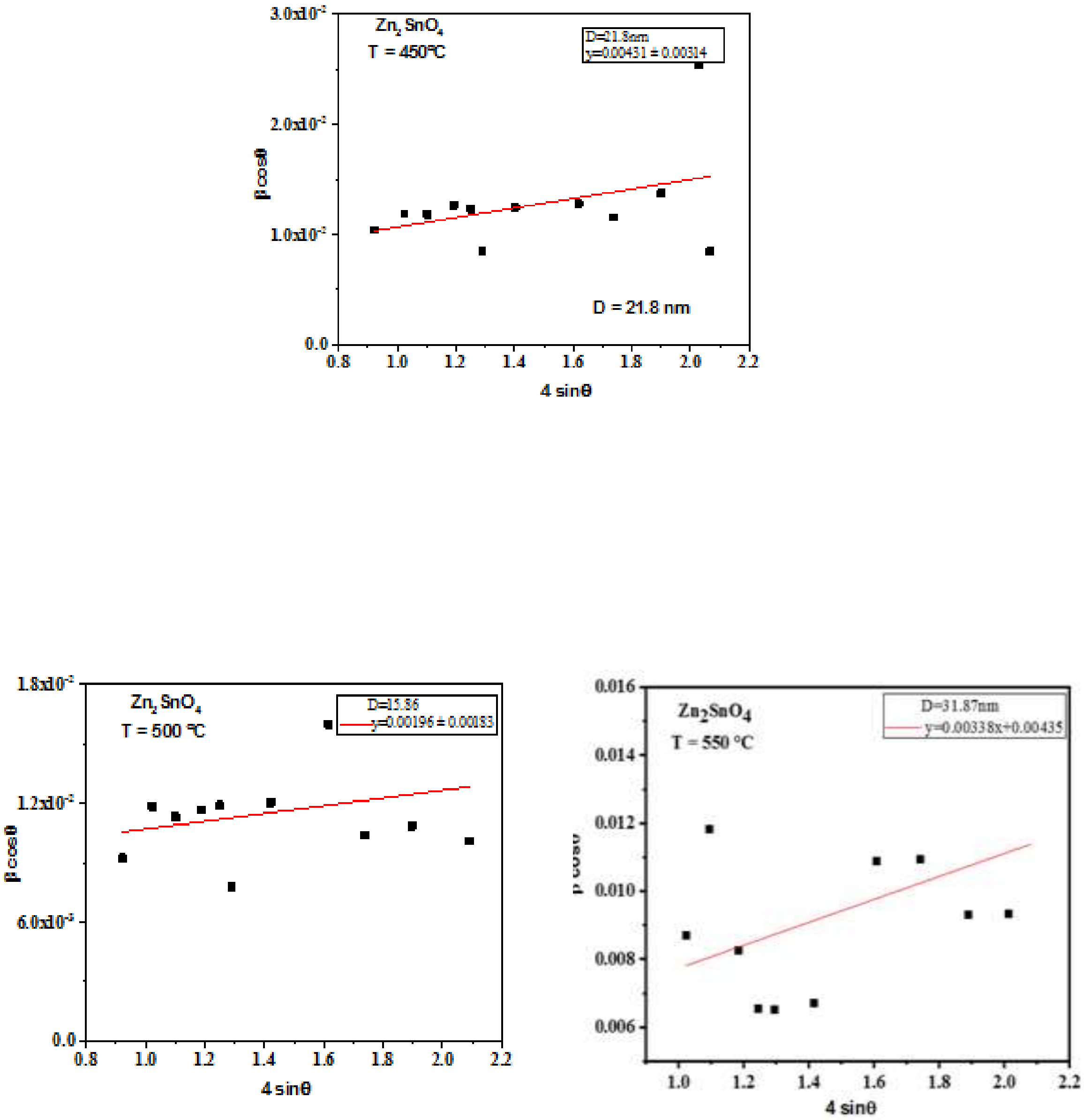

Figure 4.9. The W-H analysis of Cd_2SnO_4 Zn_2SnO_4 thin films at different substrate temperatures (450, 500 and 550 °C).

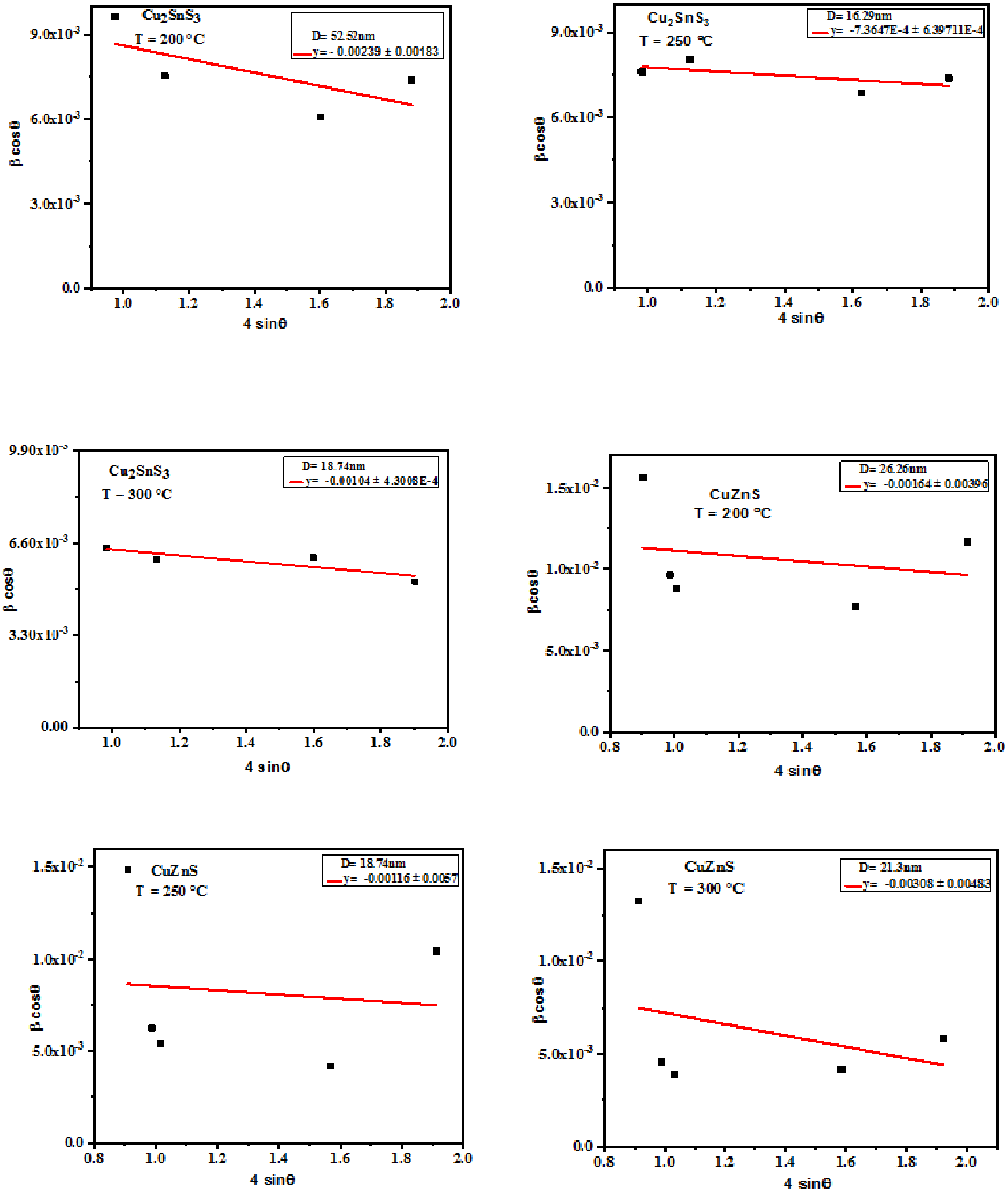

Figure 4.10. The W-H analysis of Cu_2SnS_3 and CuZnS thin films that were deposited on glass substrate and annealed at different substrate temperatures (200, 250 and 300 °C) prepared by spin coating method.

4.2.10 Dislocation Density (δ)

The number of faults in the crystal was measured by the dislocation density. According to equation (2.11), the density of dislocations is inversely proportional to the square of crystallite size. The dislocation density of thin films made by chemical spray pyrolysis and spin coating techniques (Cd_2SnO_4, Zn_2SnO_4, Cu_2SnS_3, and CuZnS) is low. For annealed films, the dislocation density can be seen at (0.564 and 2.240) cm^{-2} for the Cd_2SnO_4 and Zn_2SnO_4 thin films at 550 ℃ deposited temperature and for Cu_2SnS_3 and CuZnS crystallinity at 300 ℃ deposited temperature thin films (2.144 and 0.782). Table 4.9 illustrates this.

4.2.11 The Number of Crystallites (No)

Equation (2.12) can be used to measure the number of crystallites per unit area. Table 3.9 shows the number of crystallites calculated for (Cd_2SnO_4, Zn_2SnO_4, Cu_2SnS_3, and CuZnS) at various deposited temperatures.

Table 4.9. Structural parameters for (Cd_2SnO_4, Zn_2SnO_4, Cu_2SnS_3, and CuZnS) thin films prepared at different substrate temperatures spray pyrolysis and spin coating .

Sample	**T (^{o}C)**	**2 Θ (deg)**	**(hkl)**	**d_{hkl} (Å)**	**(FWM) (deg)**	**(D) nm**	**$\varepsilon \times 10^{-3}$**	**$\delta \times 10^{-3}$ $(nm)^{-2}$**	**N_o $(nm)^{-2}$**
Cd_2SnO_4	450	32.0593	(311)	2.71239	0.2852	30.2	1.195	1.096	0.010
	500	32.0585		2.71014	0.2460	35.1	1.031	0.811	0.007
	550	32.0295		2.71239	0.1968	43.8	0.825	0.521	0.004
Zn_2SnO_4	450	34.6851	(311)	2.58417	0.7591	11.4	3.160	7.694	0.220
	500	34.6109		2.58954	0.7008	12.4	2.918	6.503	0.173
	550	34.3810		2.60969	0.3936	22.0	1.639	2.066	0.030
Cu_2SnS_3	200	28.5321	(112)	2.85468	0.57000	15.0	2.411	4.44	0.101
	250	28.5354		2.84202	0.45000	19.0	1.903	2.77	0.049
	300	28.5416		2.82740	0.38000	22.5	1.607	1.975	0.029
Cu Zn S	200	29.9234	(102)	2.96784	0.52000	16.5	2.191	3.673	0.079
	250	29.4041		2.98037	0.32000	26.8	1.352	1.392	0.017
	300	29.1619		2.98365	0.23000	37.2	0.969	0.722	0.006

4.3 Fourier Transform Infrared Spectroscopy (FTIR)

Chemicals (chemical bonds), work environments (functional group), and compounds are all detected using infrared spectroscopy. The transmittance spectra of Cd_2SnO_4, Zn_2SnO_4, Cu_2SnS_3, and CuZnS thin films were studied using FTIR spectroscopy in the range of (400 - 4000) cm^{-1}. Figure 4.11 shows the FTIR specta of the Cd_2SnO_4nanomaterial at (450,500, and 550 ℃). Peaks at (464-571) cm^{-1} correspond to Cd-O vibrations, whereas another band (632-684) cm^{-1} relates to O-Sn-O symmetric stretching vibrations. Due to the O–O bands for Cd_2SnO_4 nanoparticles, a band in the range of (922-933) cm^{-1} may occur. The C–H stretching vibration mode is attributed to the peak at (2845-2977) cm^{-1}, whereas the wide peak about 3499 cm^{-1} is attributed to O–H stretching of surface adsorbed water [32, 166, 156].

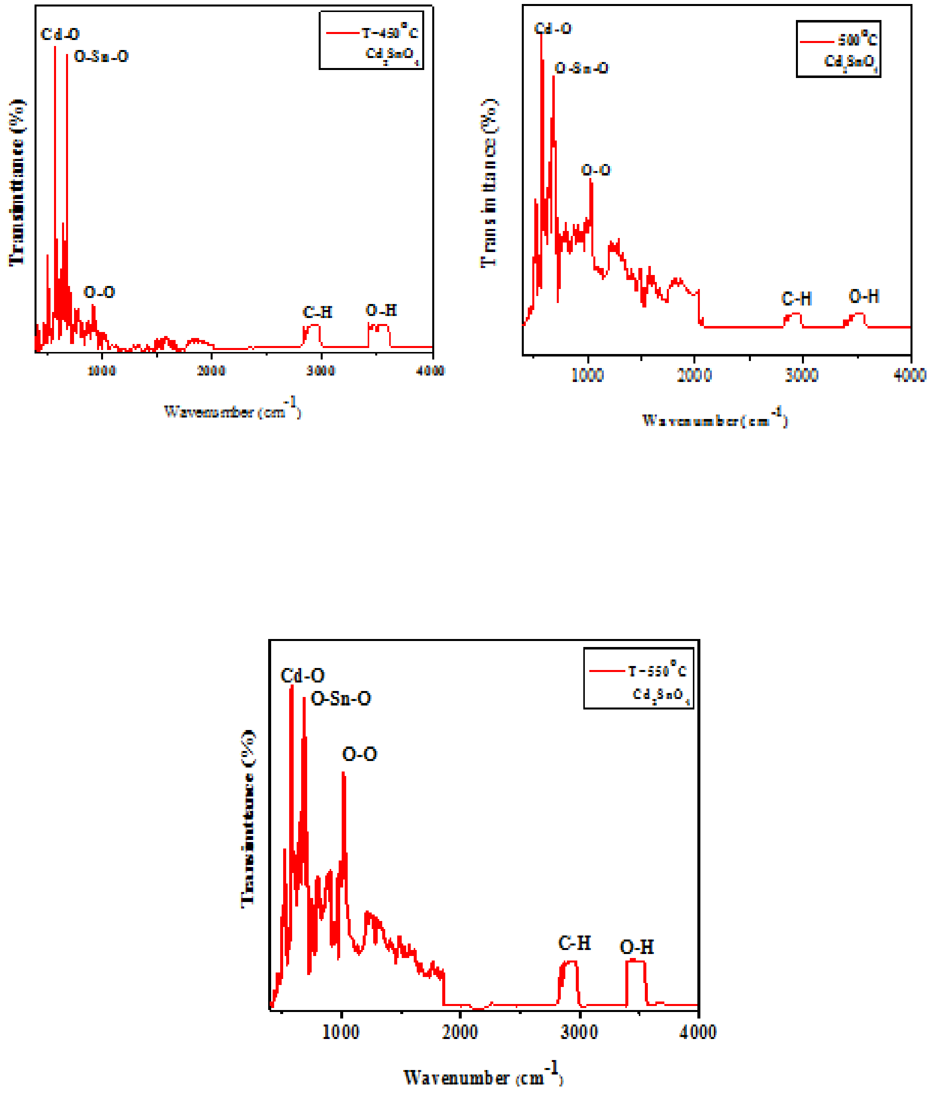

Figure 4.11. FTIR transmittance spectra of Cd_2SnO_4 thin film that was deposted on glasssubstrate at different substrate temperatures (450, 500. and 550 ^oC) prepared spray pyrolysis method.

Figure 4.12 depicts the spectra of Zn_2SnO_4 at three substrate temperatures (450, 500, and 550 °C). The absorption peak is detected at (522-590) cm^{-1} due to the symmetrical stretching vibration of ZnO and SnO_2 groups, and this band corresponds to the Sn-O-Zn bonding in ZnO. The peak at (2043-2052) cm^{-1} corresponds to the zinc potential bond in ZnO, whereas the peak at (1273-1288) cm^{-1} corresponds to the Sn–O stretching vibrations in ZnO. The absorption peaks at (2831-2895) cm^{-1} correspond to the C-H vibration mode, whereas the peak at 3482 cm-1 confirms the presence of hydrogen bonds[167, 168].

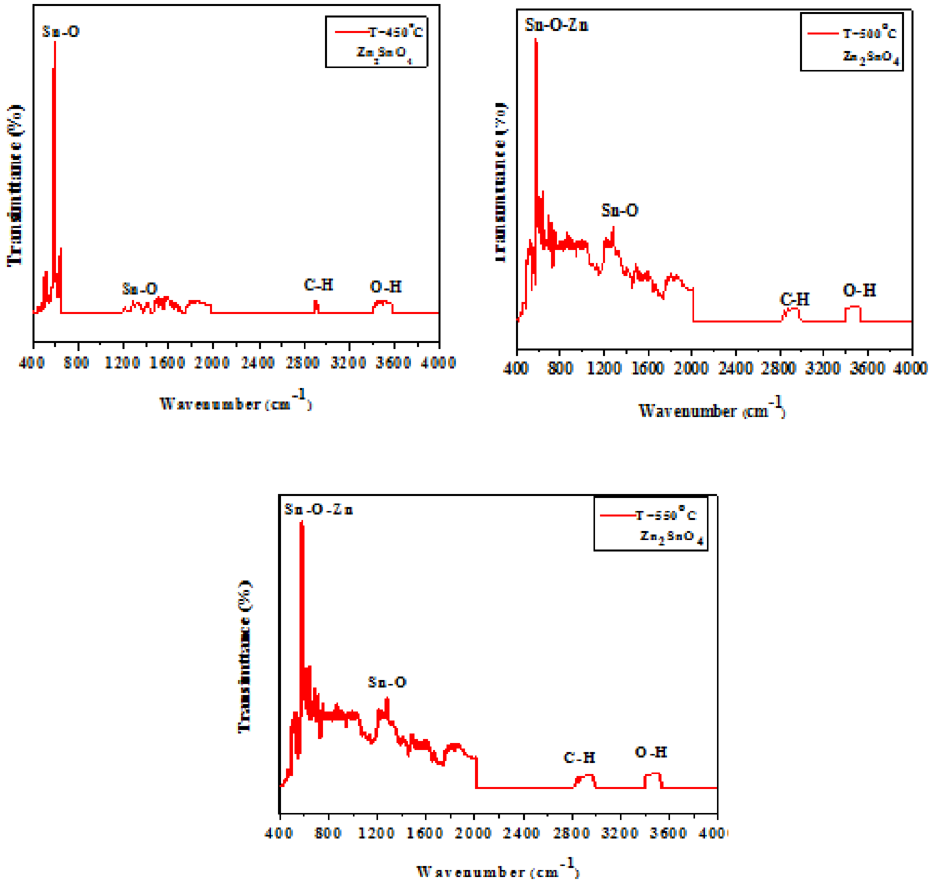

Figure 4.12. FTIR transmittance spectra of Zn_2SnO_4 thin film that was deposted on glass substtrate at different substrate temperatures (450, 500 and 550 ^oC) praered by spray by pyrolysis method.

Figure 4.13 displays a Cu_2SnS_3 thin film at temperatures of 200, 250, and 300 °C. There is a band that can be found at (443-450) cm^{-1} that has been attributed to Cu-O. The vibrational energies that can be observed in the range of (500-750) cm^{-1} have been attributed to Cu-S, Sn-S, and S-oxide bonds [169, 170]. There is a weak bond that is ascribed to the C- S bond that can be found in the region of (2221 - 2300) cm^{-1}. Additionally, additional bonds such as O-H vibrated in the region that ranged from(3338- 3350) cm^{-1} [169, 171] .

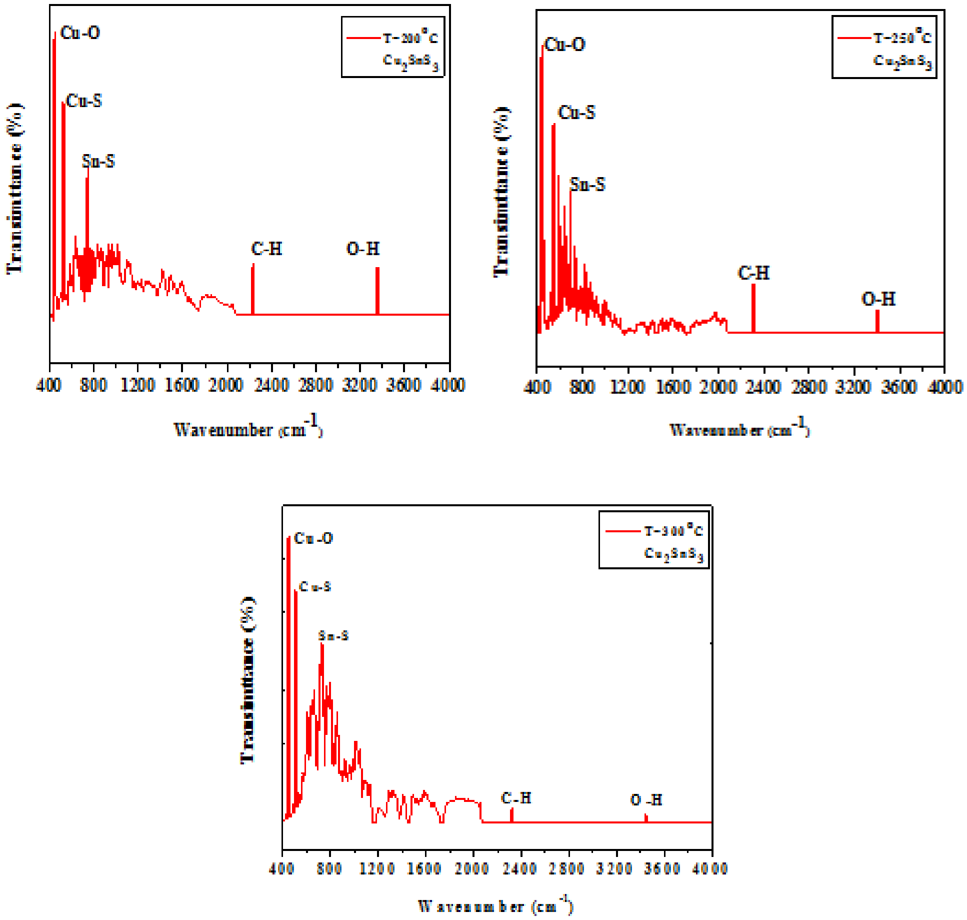

Figure 4.13. FTIR transmittance spectra of Cu_2SnS_3 thin film deposited on glass substrate and annealed at different temperatures (200, 250 and 300 ^{o}C) prepared by spin coating method .

The O-H stretching vibrations bond is responsible for a band at (3420-3433) cm^{-1}. The stretching vibration (C–H) demonstrated an expansion of the methoxy and methylene, resulting in absorption peaks in the range (2353-2366) cm^{-1}. The C=C stretching vibrations bond is responsible for the group peak at (1603-1620) cm^{-1} [172]. The interring C-C stretching band has been observed to be between 1467 and 1323 cm^{-1}, suggesting that the ring-opening reaction occurs partially at high temperatures. The band at (1103-1113) cm^{-1} in the spectra is mostly caused by C-O stretching in the secondary alcohol group of threonic acid and ascorbate ligands bound to the CuZnS surface [171]. The metal-S bond of CuZnS is ascribed to bands at 666 and 619 cm^{-1}.

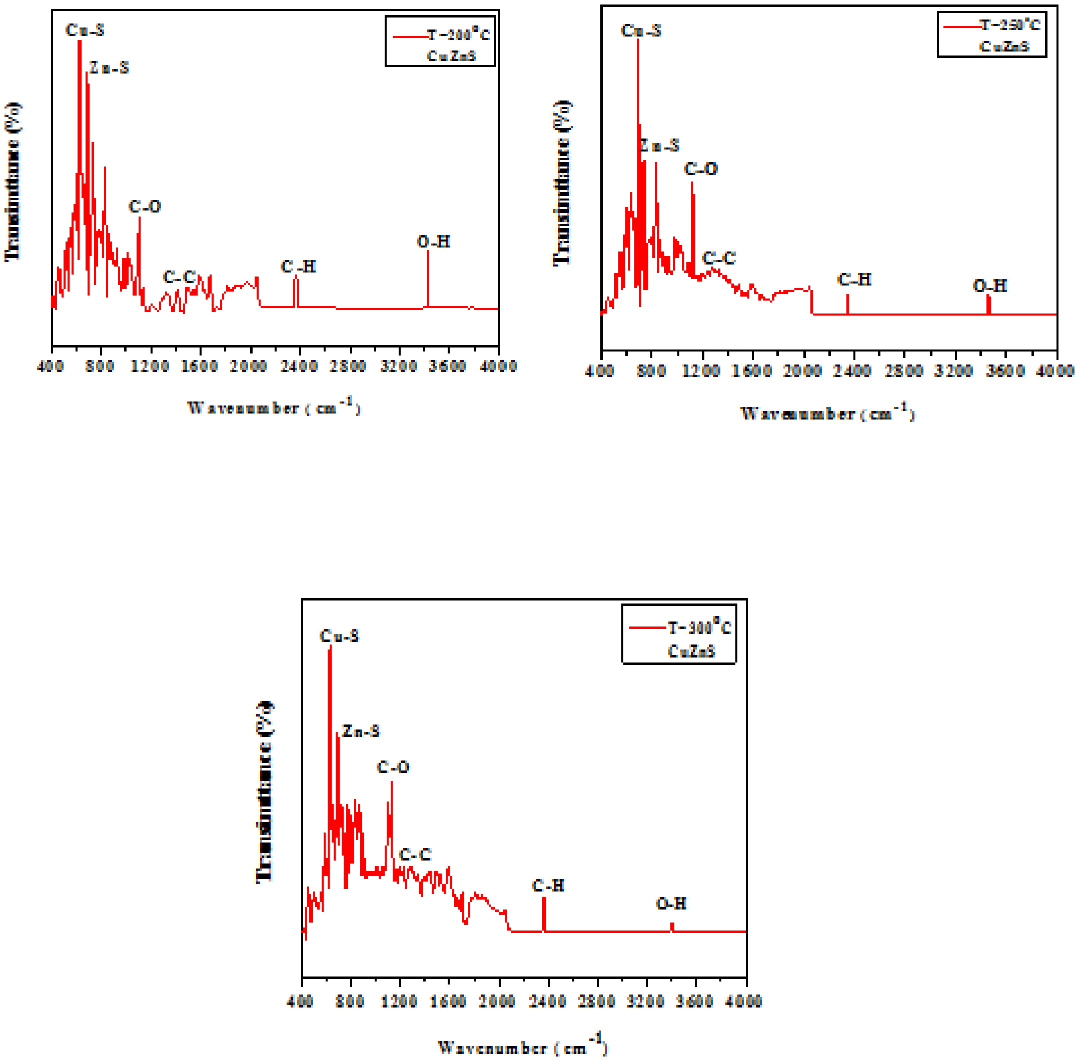

Figure 4.14. FTIR transmittance spectra of CuZnS thin film deposited on glass substrate and annealed at different temperatures (200, 250 and 300 °C) prepared by spin coating method.

4.4 Morphological Analysis

4.4.1 Atomic Force Microscopy (AFM)

The advanced second generation (AFM) with high imaging power was used to examine the surface topography of the prepared films at scan scales of 0.51×0.51 nm^2 for Cd_2SnO_4, Zn_2SnO_4, and 0.78×0.78 nm^2 for Cu_2SnS_3, CuZnS, and the amount of the influence of increasing the substrate temperature. The shape of the films Cd_2SnO_4 and Zn_2SnO_4 is shown in Figure 4.15. When the temperature rises, the morphology of thin films changes, revealing a higher number of grain sizes and a more homogenous distribution, indicating the film's crystalline structure. Grain growth occurs as a result of the heating, resulting in crystalline and excellent surface morphology. These results are supported by XRD properties.

The size of the particles and their molecular orientation vary as the temperature of the substrate rises. The average particle size increases as the substrate temperature rises, which could be due to bigger clusters formed by the coalescence of two or more grains, as well as a reduction or elimination of grain bounders [173]. Cu_2SnS_3 and CuZnS thin films have different morphologies (Figure 4.15). It is clear from the surface morphological variation of the deposited films that the surfaces were rough and compact, with no obvious cracks or holes. Because the grain size grows and the surface morphology becomes rougher as the drying temperature rises, there are many nucleation locations on the substrate and tiny crystallites are formed. These qualities are ideal for avoiding shunting issues in solar panels.

Large grain size is also preferred to limit recombination at grain borders and to involve carrier transit within the grain [174]. Table 4.10 estimates and lists the number of nucleation centers based on" particle size", "average roughness", then "root mean square" of the films. Cd_2SnO_4, Zn_2SnO_4, Cu_2SnS_3, then CuZnS thin films have particle sizes of 42.65, 17.87, 39.15, and 40.99 nm, respectively, which agrees with the results [19, 169, 174, 175]. Within the scanning region, the particles are evenly dispersed, with individual columnar grains extending upwards. For solar cells and photovoltaic applications, this surface property is critical [176, 177].

Table 4.10. AFM values of surface roughness, root mean square (RMS), and grain size of Cd_2SnO_4, Zn_2SnO_4, Cu_2SnS_3, and CuZnS thin films at different substrate temperatures.

Thin films	**Surface roughness average (nm)**	**Root mean square (nm)**	**Average grain size (nm)**
Cd_2SnO_4	5.129	6.368	21.98
	5.786	7.303	22.81
	8.544	10.58	42.65
Zn_2SnO_4	1.632	1.979	6.387
	1.969	2.416	12.22
	3.886	4.608	17.87
Cu_2SnS_3	5.869	7.411	21.42
	6.330	7.742	27.68
	15.56	17.71	39.15
CuZnS	4.782	5.749	15.49
	4.797	5.942	20.50
	8.394	10.447	40.99

Cd_2SnO_4

T=450 °C

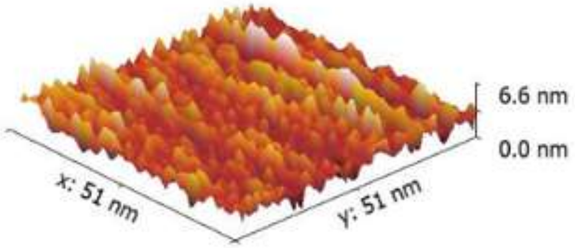

Cd_2SnO_4

T=500 °C

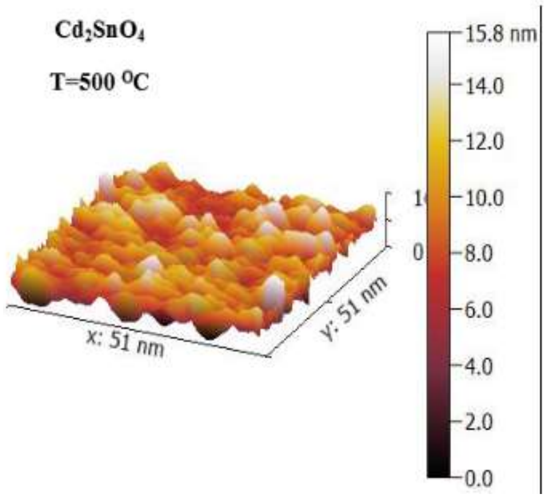

Cd_2SnO_4

T=550 °C

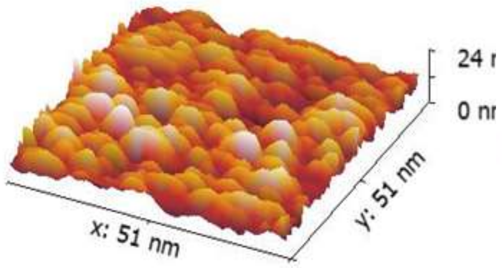

Zn_2SnO_4

T=500 °C

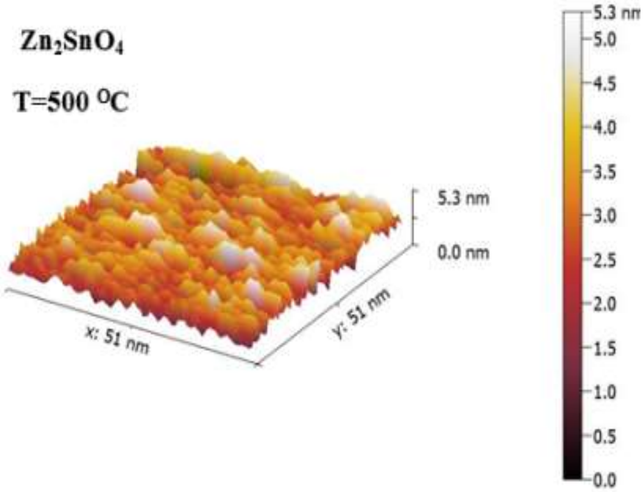

Zn_2SnO_4

T=450 °C

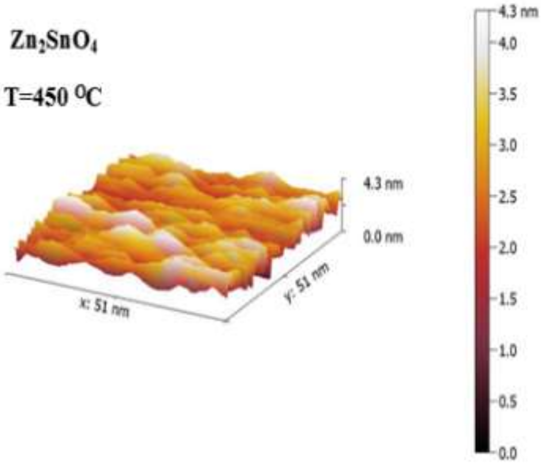

Zn_2SnO_4

T=550 °C

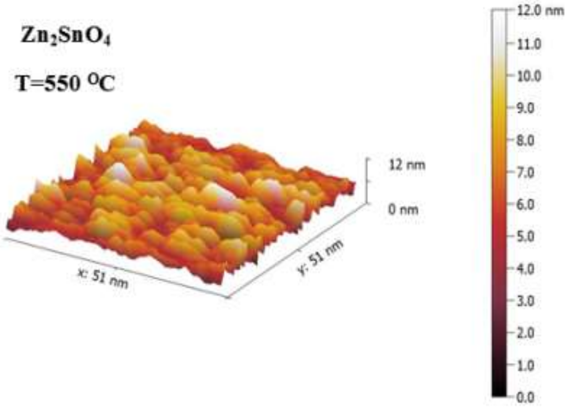

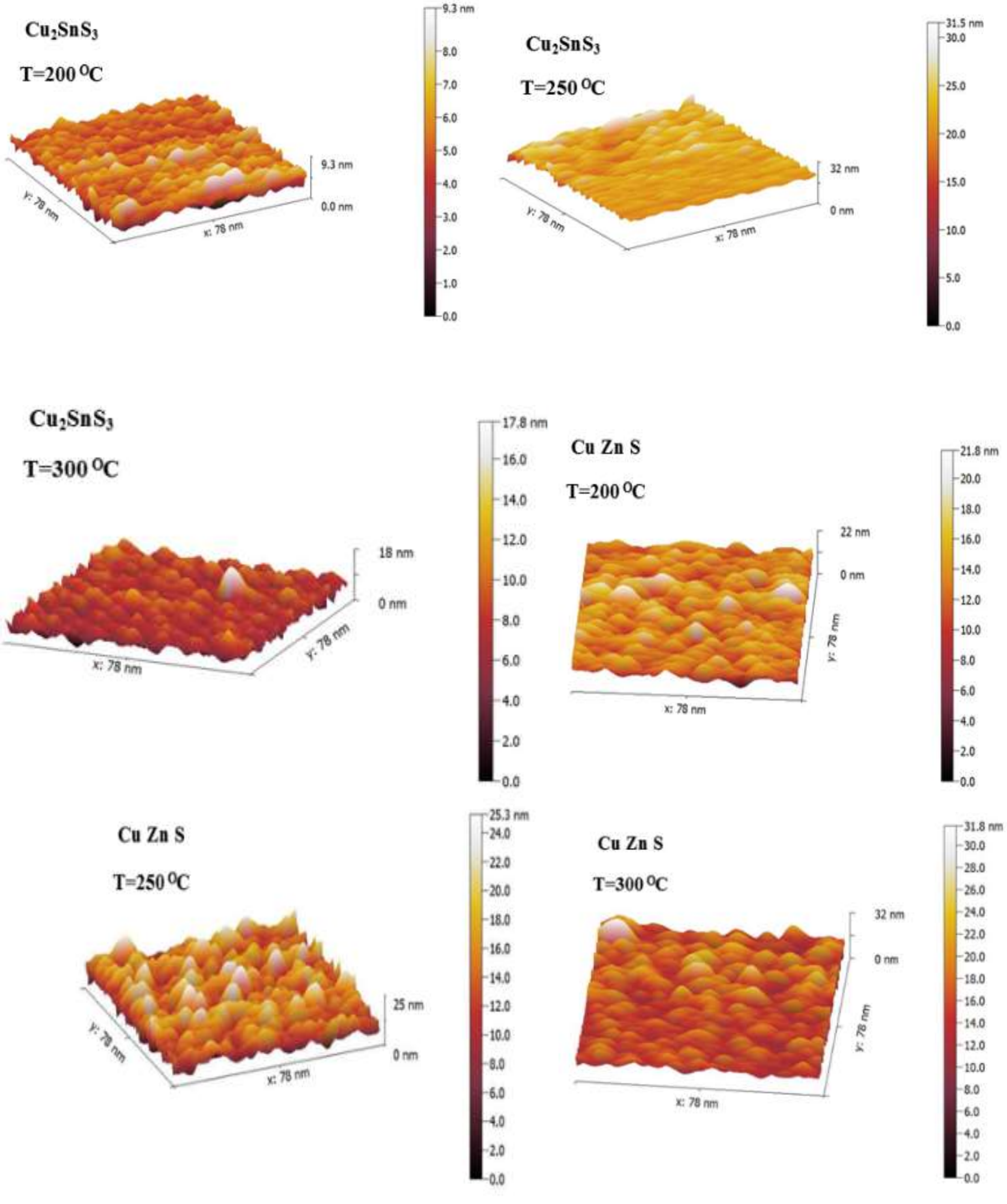

Figure 4.15. 3-D AFM images for Cd_2SnO_4, Zn_2SnO_4, Cu_2SnS_3 and CuZnS thin films deposited at different substrate temperatures.

Figure 4.16 illustrates granularity accumulation distribution charts for Cd_2SnO_4, Zn_2SnO_4, Cu_2SnS_3, and CuZnS thin films. The particle size distribution can be determined using the histogram.

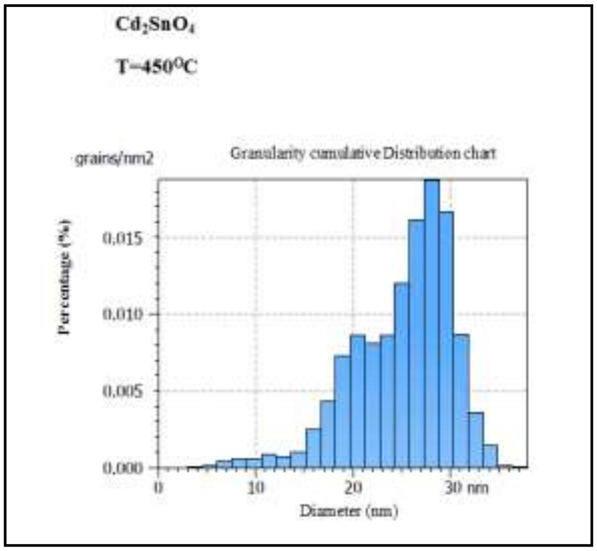

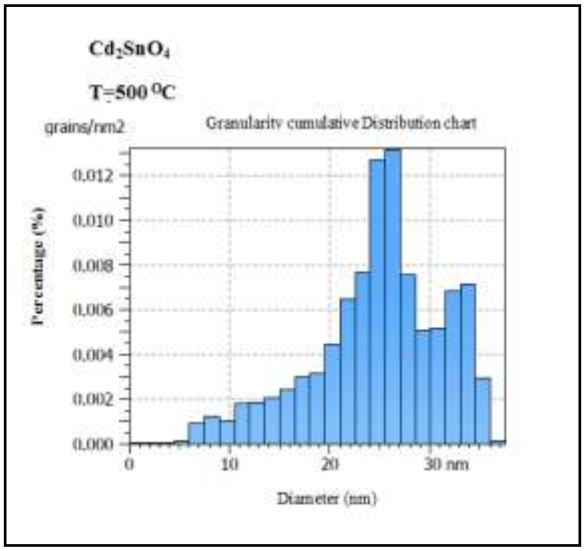

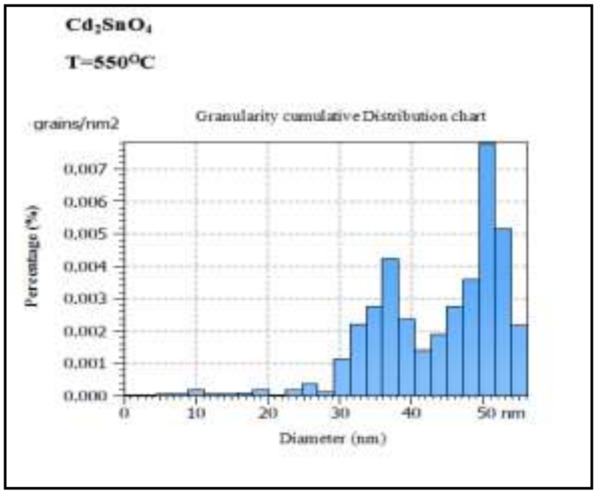

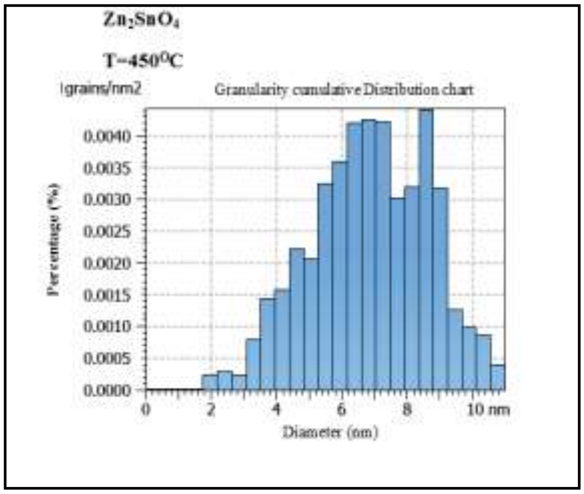

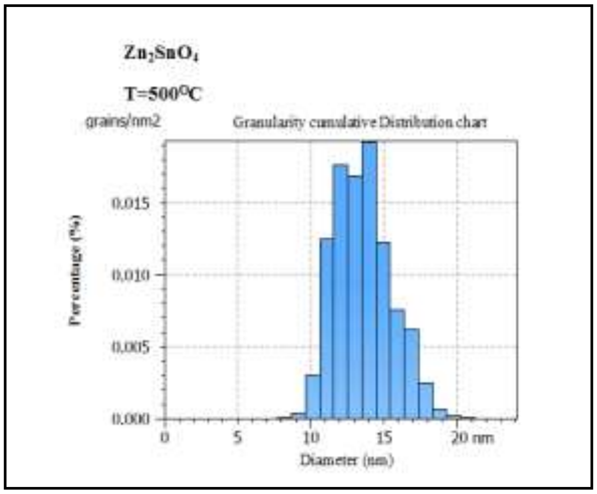

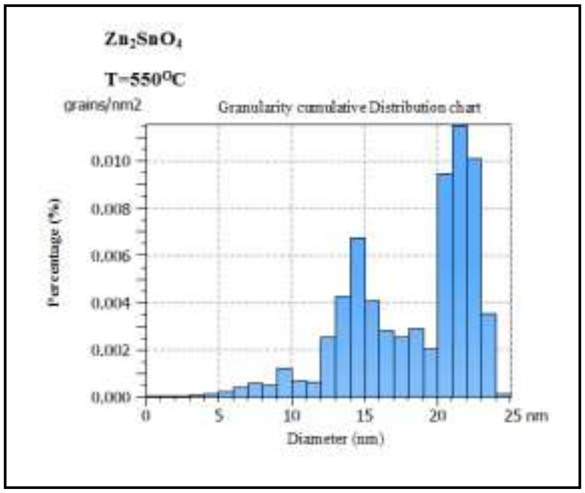

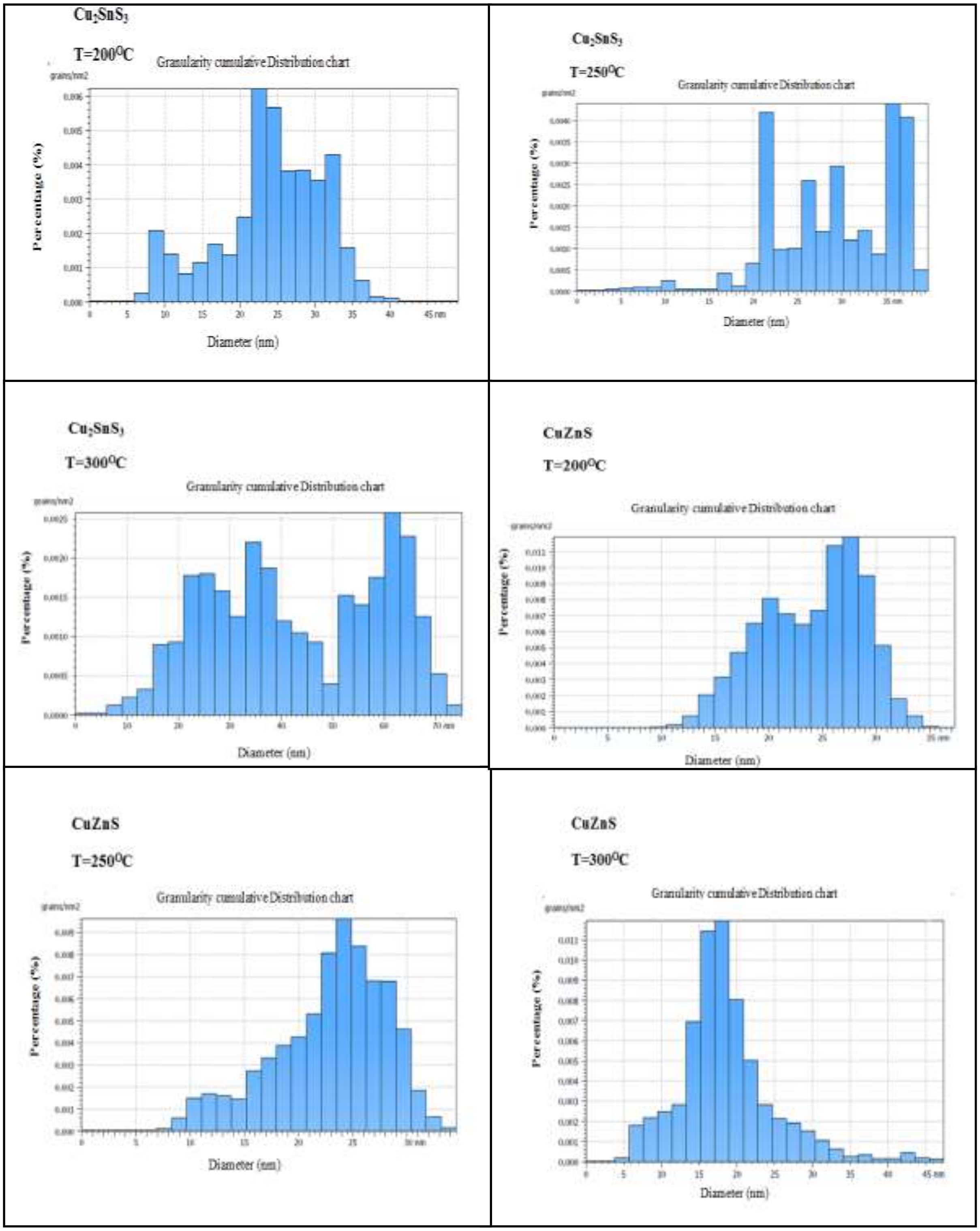

Figure 4.16. Granularity accumulation distribution charts of Cd_2SnO_4, Zn_2SnO_4, Cu_2SnS_3 and CuZnS thin films where deposited at different substrate temperatures prepared by spray pyrolysis and spin coating method .

4.4.2 Field Emission-Scanning Electron Microscopy (FE-SEM)

The FE-SEM device technology was used to investigate the surface morphology and microstructure features of the deposited thin films. It has a high ability to magnify and accurately photograph the surfaces of materials. Images of Cd_2SnO_4, Zn_2SnO_4, Cu_2SnS_3, and CuZnS films deposited at different temperatures are shown in Figures 4.17-(a-b) at magnification (50,100 KX). Image J software was used to analyze FE-SEM images of samples obtained to examine the surface of thin films and to calculate average particle size and determine the influence of increasing substrate temperature on the structure of prepared films, as shown in Table 4.11.

Figure 4.17 shows an image with the number of (100-200) grains taken to calculate the greatest (Max) and lowest (Min) grain sizes as well as the average grain size, as well as the size distribution chart and grain ratios. The maximum grain size was 123.62 nm for Cd_2SnO_4 films at 550 °C and 33.58 nm for Zn_2SnO_4 films, whereas the largest grain size was 100.29 nm for Cu_2SnS_3 at 300 °C and 157.95 nm for $CuZnS_3$ films. Both the XRD and AFM experiments concur well with these findings. Figures 4.17-a demonstrate the growth and distribution of Cd_2SnO_4 films at different temperatures (450, 500, and 550 ℃), as well as cross-sectional pictures. The surface structure of the thin film changed from spherical shapes at temperatures within the nano-scale range of 450 ℃ to Cauliflower granule shapes with increased temperature (500 and 550 ℃) without changing in thickness. Figures 3.17-b demonstrate the growth and distribution of Zn_2SnO_4 thin films at different temperatures (450, 500, and 550 ℃), as well as cross-sectional pictures. The surface structure of the thin film changed from spherical shapes at temperatures within the nano-scale range of 450 ℃ to small stone shapes with increased temperature (500 and 550 ℃) without a change in thickness. The average particle size of aggregated particles grows noticeably.

This result could be due to increased atom mobility as temperature rises, resulting in more effective recrystallization and grain development in the films, resulting in larger grains. This result is in excellent agreement with earlier research [24]. Figures 4.17-c illustrate the growth and distribution of Cu_2SnS_3 thin films at various temperatures (200, 250 and 300 ℃), as well as cross-sectional pictures. At varied substrate temperatures within the nano-scale range, the surface structure spherical forms of the thin film were seen with no change in thickness of the thin film. The size of the grains is expected to increase as the temperature rises. In addition, when temperatures rise, the gaps between grain boundaries widen. This result matched the findings of [38]. CuZnS films (Figures 4.17-d). At temperatures (200, 250, and 300 ℃) within the nano-scale range, the surface structure of the thin film matched a Cauli-Flower shape, with no change in thickness. The grain size of the Cd_2SnO_4, Zn_2SnO_4, Cu_2SnS_3, and CuZnS films increases as the substrate temperature rises, as seen in the grain distribution Diagram. The acquired results are nearly identical to the findings of the researchers [20, 29, 38].

Table 4.11. Values of smallest and largest particle size and average particle size of the prepared films Cd_2SnO_4,Zn_2SnO_4,Cu_2SnS_3 and CuZnS by spray pyrolysis and spin coating.

Sample	Temperature °C	Average size (nm)	Minimum Size (nm)	Maximum Size (nm)
Cd_2SnO_4	450	89.86	27.82	152.20
	500	112.17	33.71	190.52
	550	123.62	40.54	200.89
Zn_2SnO_4	450	22.14	11.13	36.74
	500	23.92	11.14	39.90
	550	33.58	8.21	60.82
Cu_2SnS_3	200	58.67	27.70	94.89
	250	74.66	40.85	125.16
	300	100.29	42.44	189.24
CuZnS	200	82.75	34.21	185.79
	250	108.50	33.42	230.88
	300	157.95	54.74	356.33

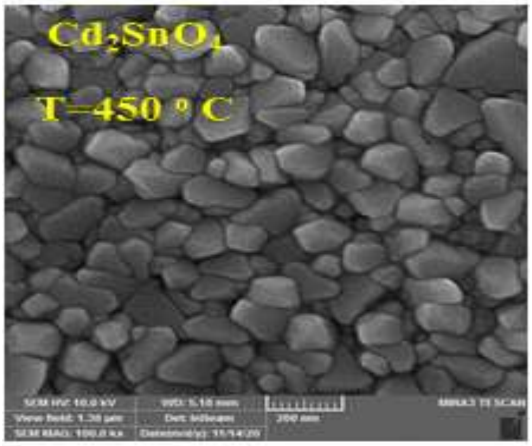
Cd_2SnO_4
T=450 ° C
SEM HV: 10.0 kV
WD: 5.18 mm
200 nm
MIRA3 TESCAN
View field: 1.38 μm
Det: InBeam
SEM MAG: 100.0 kx
Date(m/d/y): 11/14/20

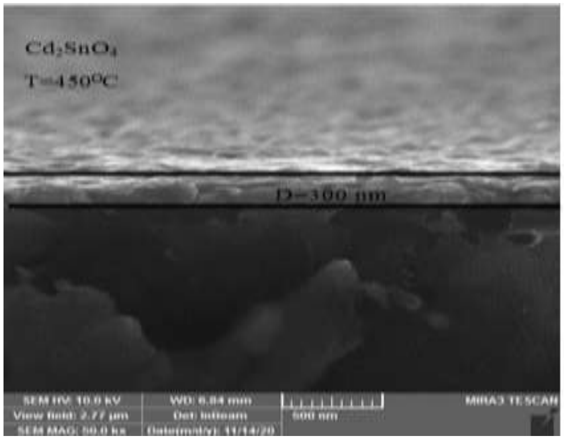
Cd_2SnO_4
T=450ºC
D=300 nm
SEM HV: 10.0 kV
WD: 6.84 mm
500 nm
MIRA3 TESCAN
View field: 2.77 μm
Det: InBeam
SEM MAG: 50.0 kx
Date(m/d/y): 11/14/20

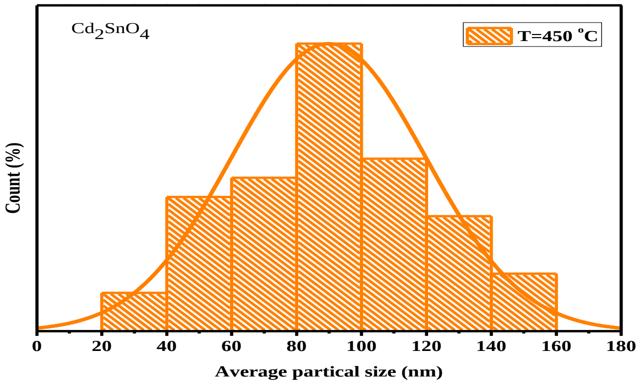
Cd_2SnO_4
T=450 °C
Count (%)
0
20
40
60
80
100
120
140
160
180
Average partical size (nm)

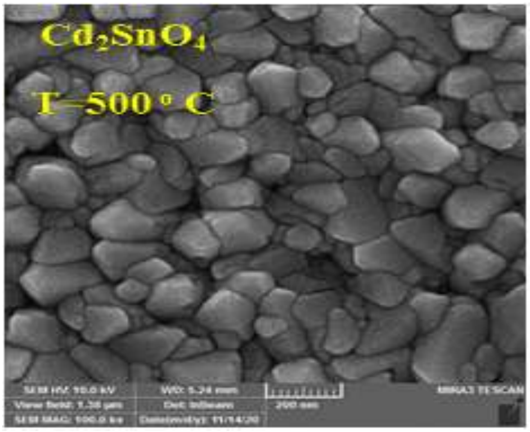
Cd_2SnO_4
T=500 ° C
SEM HV: 10.0 kV
WD: 5.24 mm
200 nm
MIRA3 TESCAN
View field: 1.38 μm
Det: InBeam
SEM MAG: 100.0 kx
Date(m/d/y): 11/14/20

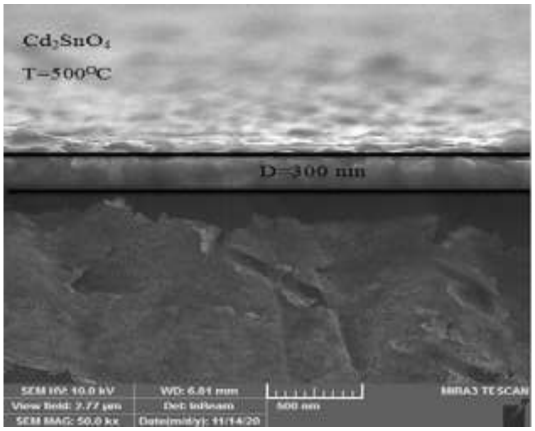
Cd_2SnO_4
T=500ºC
D=300 nm
SEM HV: 10.0 kV
WD: 6.81 mm
500 nm
MIRA3 TESCAN
View field: 2.77 μm
Det: InBeam
SEM MAG: 50.0 kx
Date(m/d/y): 11/14/20

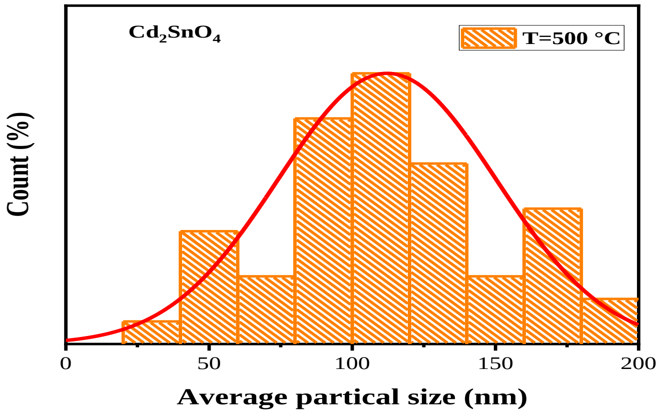
Cd_2SnO_4
T=500 °C
Count (%)
0
50
100
150
200
Average partical size (nm)

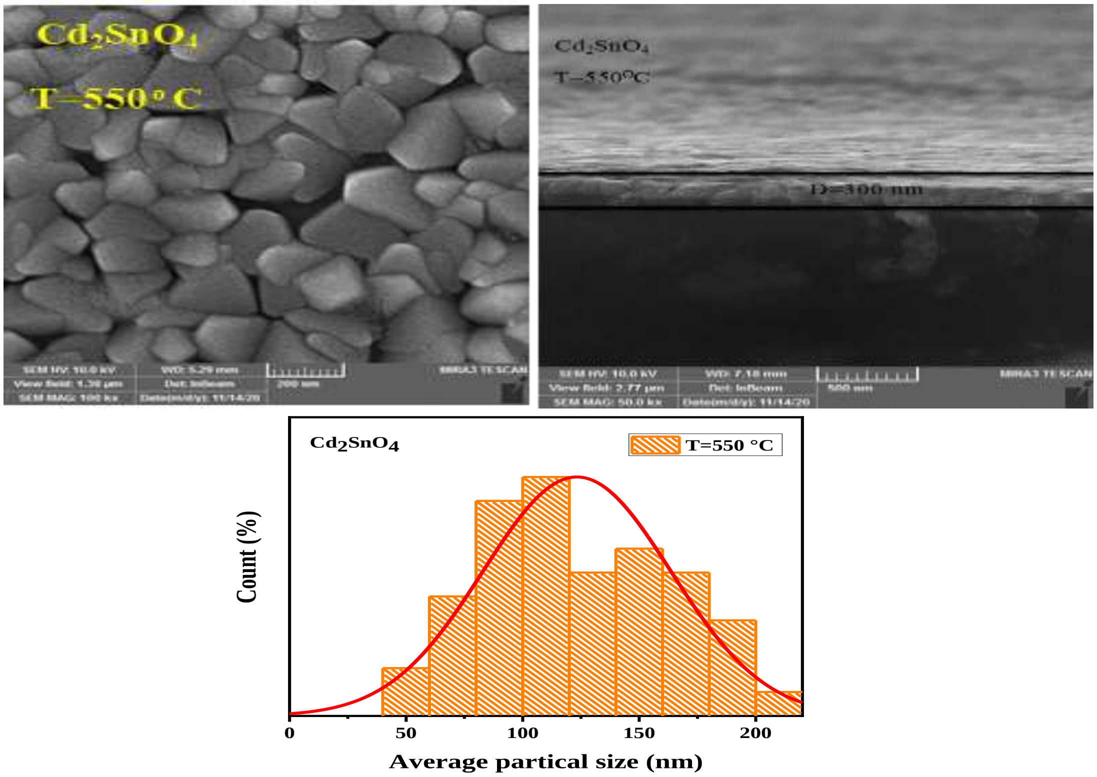

Figure 4.17-a. FE- SEM picture of $Cd_2SnO_4$with (cross-section) and planner volumetric distributions.

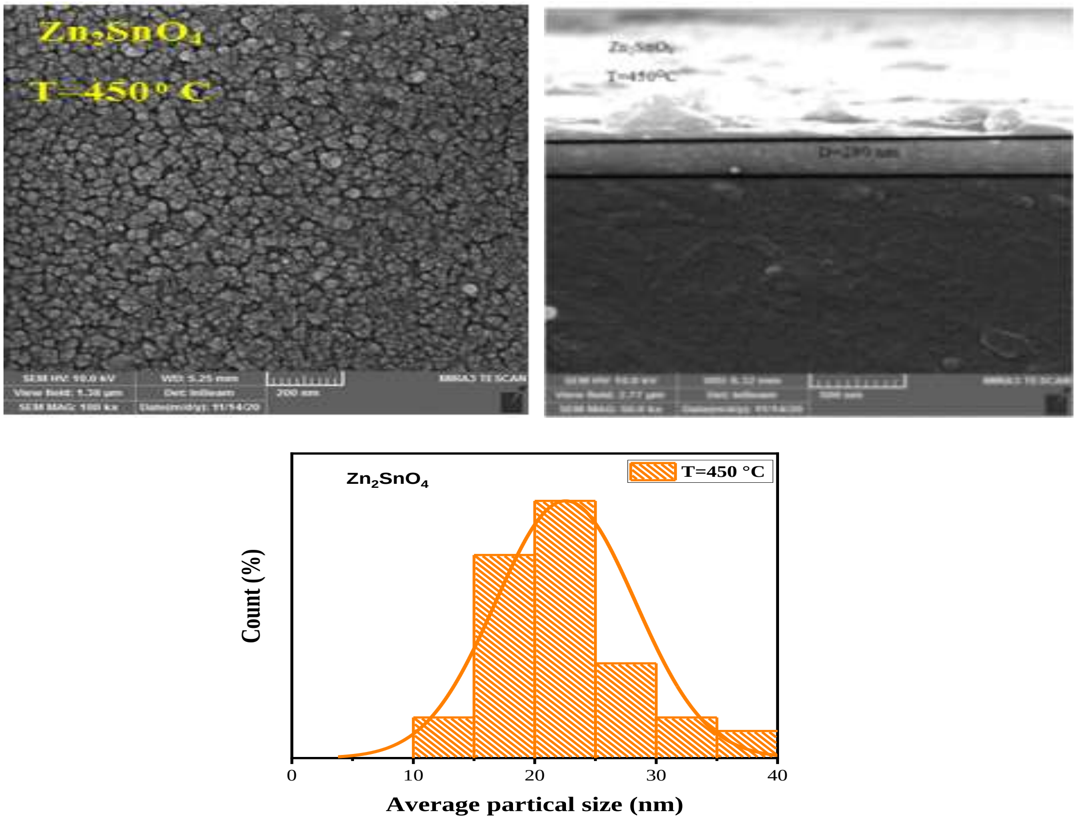

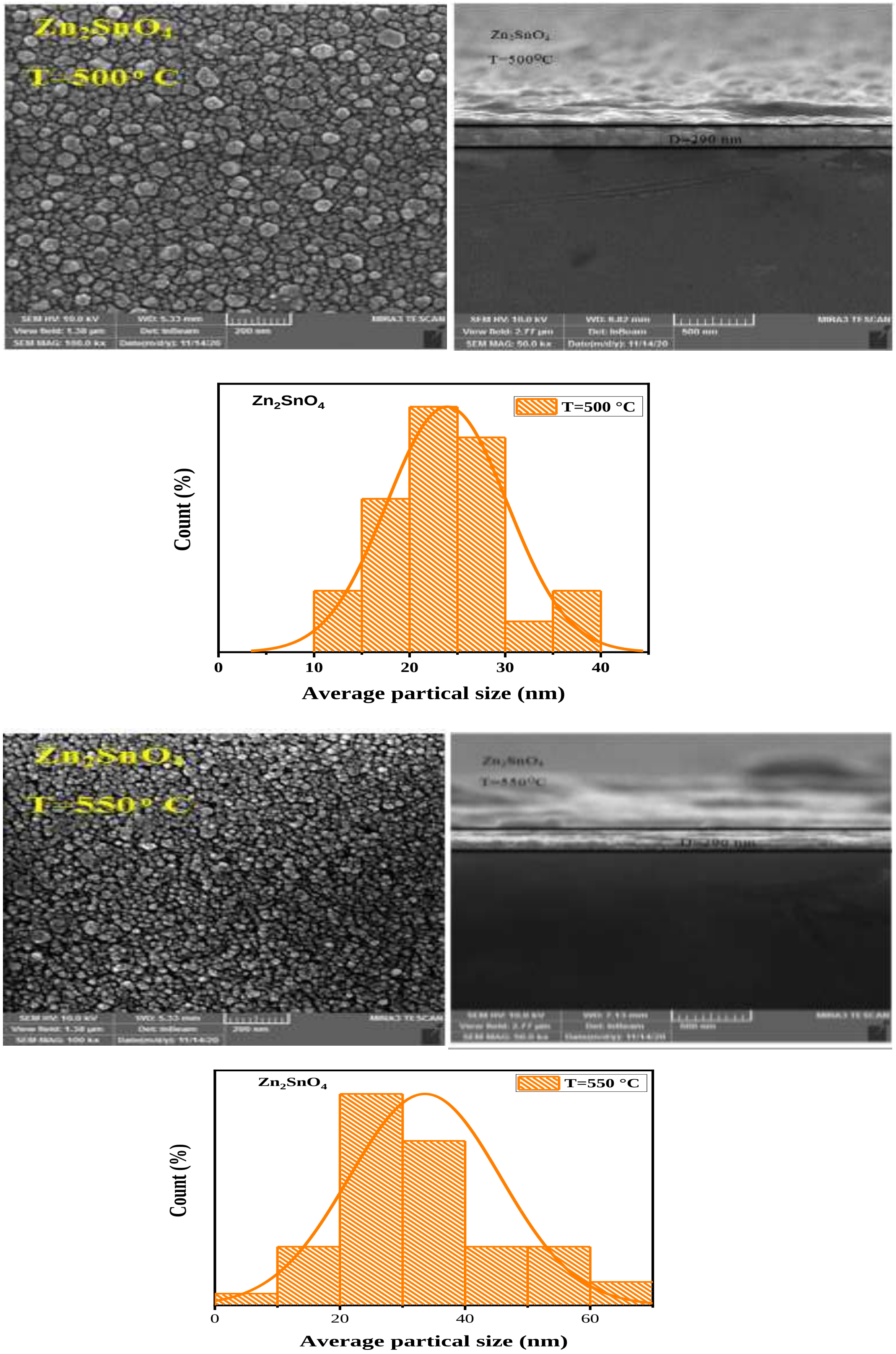

Figure 4.17-b. FE- SEM picture of Zn_2SnO_4 with (cross-section) and planner volumetric distributions.

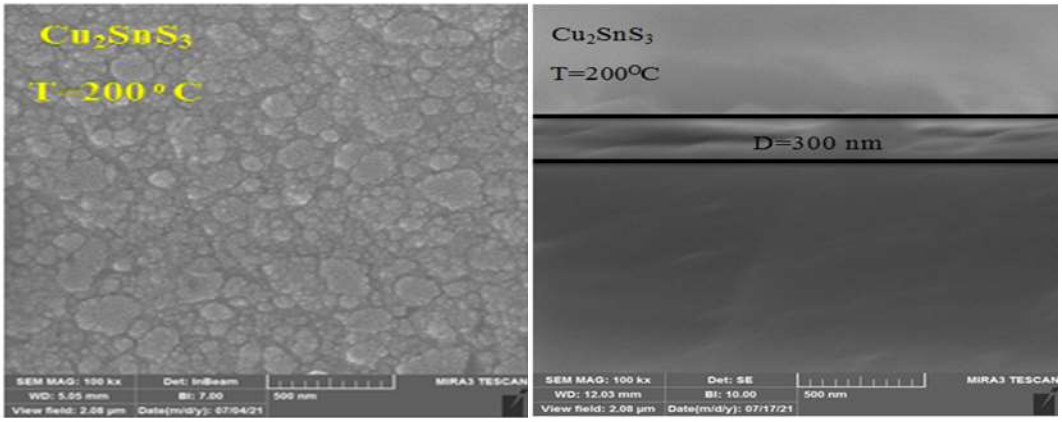
Cu_2SnS_3
T=200 ° C
SEM MAG: 100 kx
WD: 5.05 mm
View field: 2.08 µm
Det: InBeam
BI: 7.00
Date(m/d/y): 07/04/21
500 nm
MIRA3 TESCAN
Cu_2SnS_3
T=200°C
D=300 nm
SEM MAG: 100 kx
WD: 12.03 mm
View field: 2.08 µm
Det: SE
BI: 10.00
Date(m/d/y): 07/17/21
500 nm
MIRA3 TESCAN

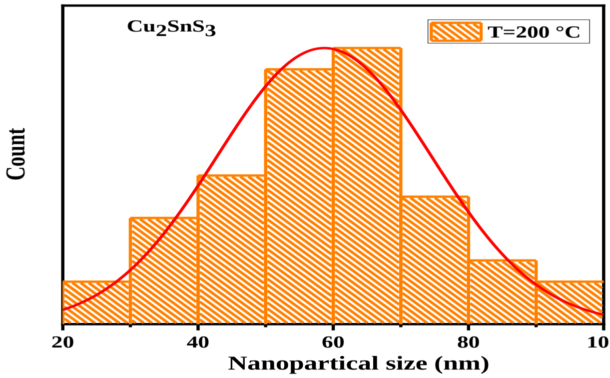
Cu_2SnS_3
T=200 °C
Count
20
40
60
80
100
Nanopartical size (nm)

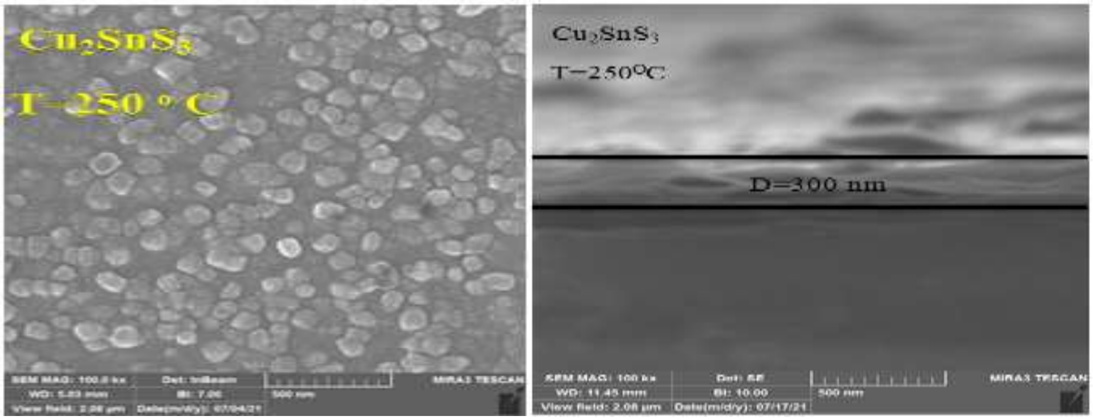
Cu_2SnS_3
T=250 ° C
SEM MAG: 100.0 kx
WD: 5.03 mm
View field: 2.08 µm
Det: InBeam
BI: 7.00
Date(m/d/y): 07/04/21
500 nm
MIRA3 TESCAN
Cu_2SnS_3
T=250°C
D=300 nm
SEM MAG: 100 kx
WD: 11.45 mm
View field: 2.08 µm
Det: SE
BI: 10.00
Date(m/d/y): 07/17/21
500 nm
MIRA3 TESCAN

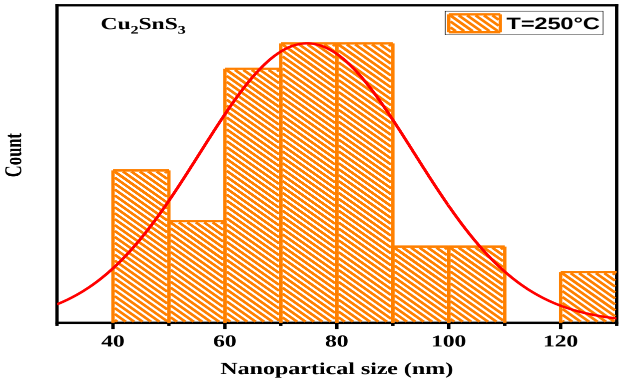
Cu_2SnS_3
T=250°C
Count
40
60
80
100
120
Nanopartical size (nm)

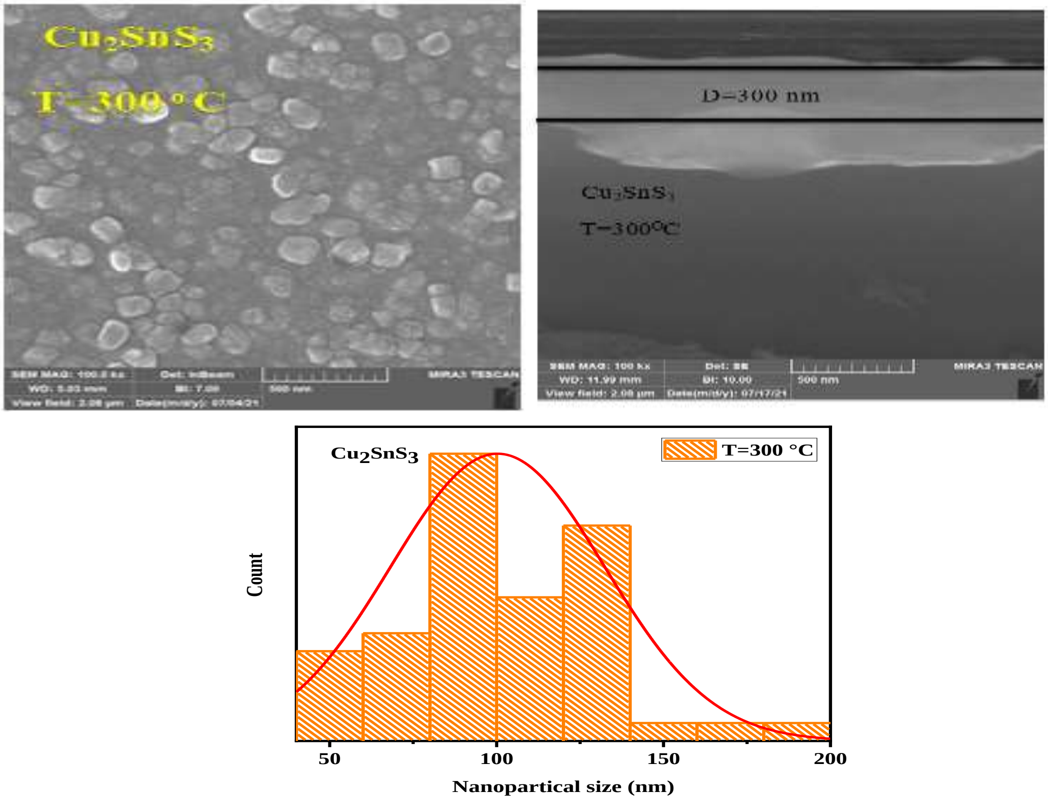

Figure 4.17-c. FE- SEM picture of Cu_2SnS_3 with (cross-section) and planner volumetric distribution.

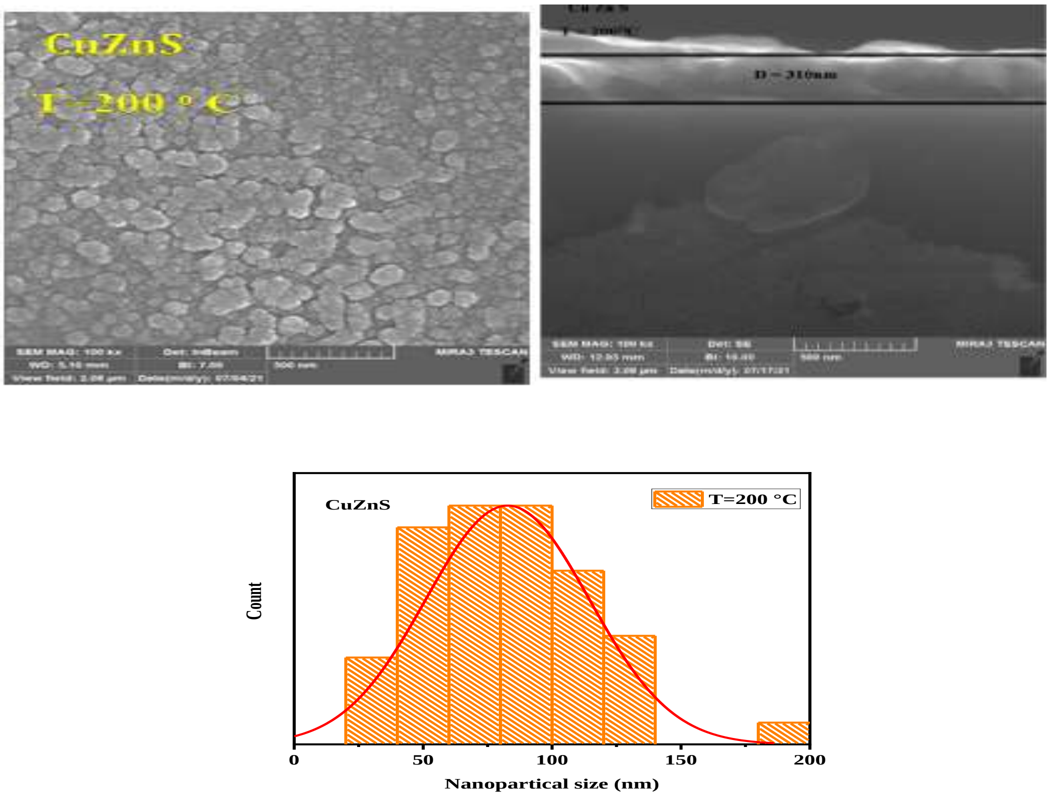

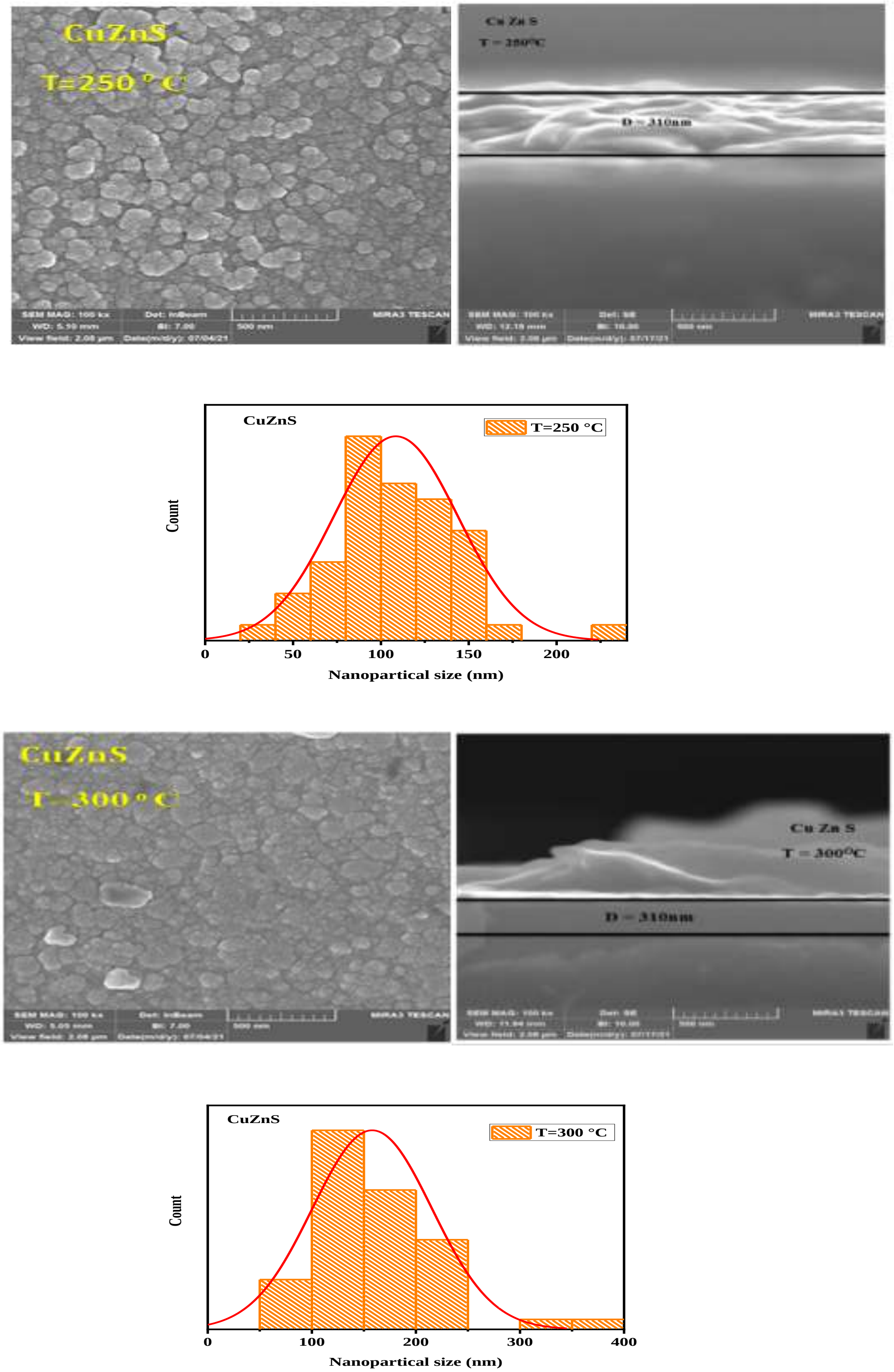

Figure 4.17-d. FE- SEM picture of CuZnS with (cross-section) and planner volumetric distributions.

4.5 Optical Properties of Thin Films

Optical properties of (Cd_2SnO_4 and Zn_2SnO_4) thin films deposited on glass substrates at (450, 500, and 550) ℃ for 1 hour and heat-treated at (450,500, and 550 ℃) and (Cu_2SnS_3 and CuZnS) thin films deposited at (200, 250, and 300) ℃ for 1 hour and heat-treated at (200, 250, and 200) ℃ have been investigated using UV-visible spectroscopy . The optical measurement results include transmittance and absorbance relationships for (Cd_2SnO_4, Zn_2SnO_4, Cu_2SnS_3, and CuZnS) thin films, as well as the computation of optical parameters such as absorption coefficient and optical energy gap.

4.5.1 Absorbance (A)

Figure 4.18-(a and b) illustrates the fluctuation in absorbance as a function of wavelength in the range (300-900) nm for Cd_2SnO_4 and Zn_2SnO_4 thin films, respectively. It can be seen that when the deposition temperature rises, the amount of absorption reduces with the increase of Temperatures due to the crystallization of the film structure by increasing The grain size, and slightly, the absorption edge shifts to a smaller wavelength (higher photon energy) . Donor levels (i.e. localized states) fade and disappear within the forbidden energy gap and conduction band. This causes a rise in the value of *Eg*. In the near UV-visible light region, a strong photo absorption at 330 nm for Cd_2SnO_4 at (450,500, and 550 °C) and Zn_2SnO_4 355 nm at 450 °C, 351 nm at 500 °C, and 347 nm at 550 °C Other research [24, 157] have found similar results. Figure 4.18-(c-d) shows that the absorbance spectrum of Cu_2SnS_3 and CuZnS thin films increases as the substrate temperature rises, revealing clear absorption edges. Indicates that increasing the substrate temperature process could improve the crystallinity of CTS and CZS [178, 160]. The improvement of crystallization results in an increase in the absorbance values of the films, which may be due to an increase

in the size of the fine grains with increasing temperature, a decrease in grain boundaries, dislocation density, and Micro-Strain values. As a result, increasing grain size results in less border scattering and fewer defects [160]. This is supported by FE-SEM images, AFM, and XRD measurements.

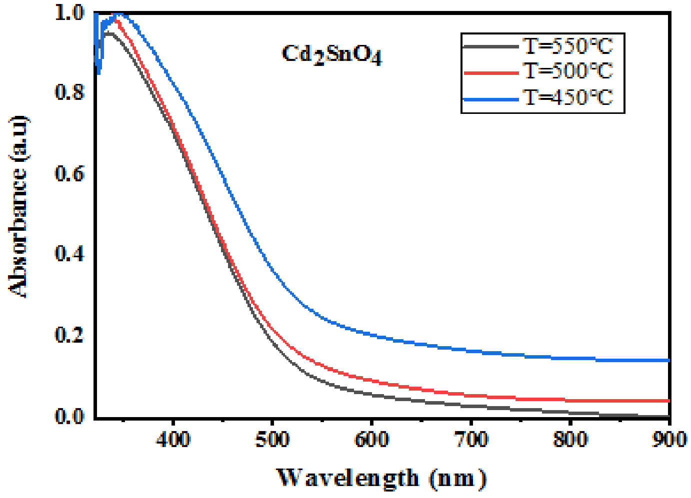

Figure 4.18-a. The absorbance of Cd_2SnO_4 thin films wear deposited prepared by spray pyrolysis method at different substrates temperatures (450, 500, and 550 °C).

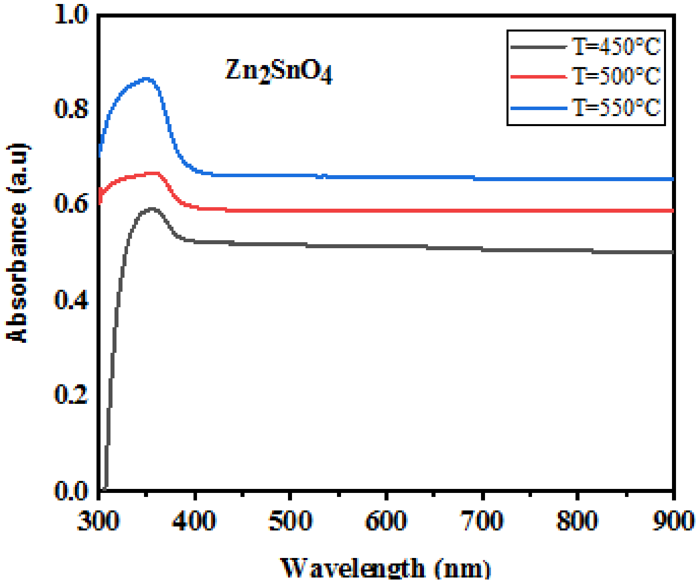

Figure 4.18-b. The absorbance of Zn_2SnO_4 thin films wear deposited prepared by spray pyrolysis method at different substrates temperatures (450, 500 and 550 °C).

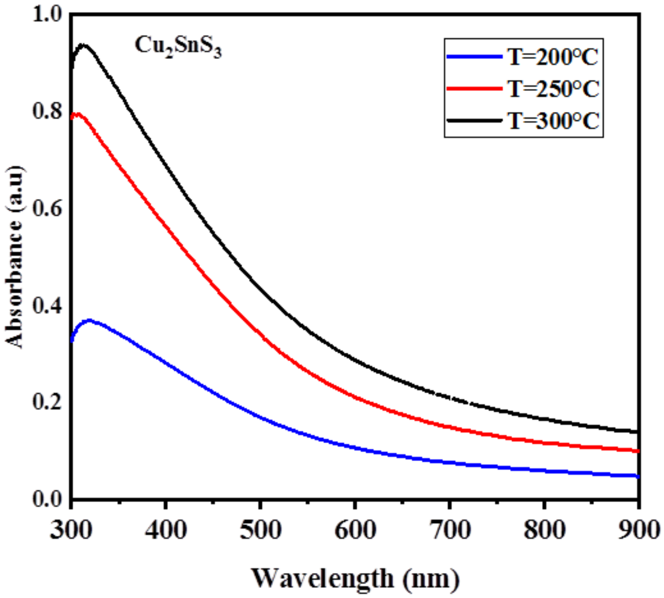

Figure 4.18-c. The absorbance of Cu_2SnS_3thin films wear deposited and annealed prepared by spin coating method at different substrates temperatures (200, 250 and 300 °C).

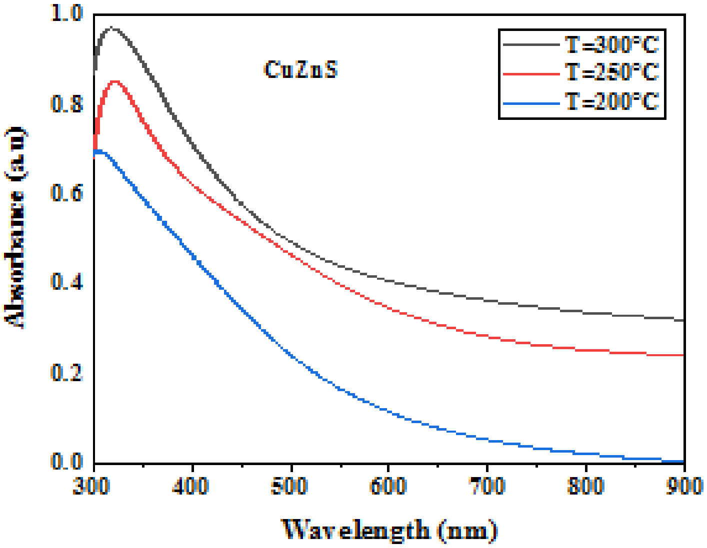

Figure 4.18-d. The absorbance of CuZnSthin films wear deposited and annealed prepared by spin coating method at different substrates temperature (200, 250 and 300 °C).

4.5.2 Transmittance (T)

The transmittance spectra curves of Cd_2SnO_4 and Zn_2SnO_4 thin films at wavelength range of 300-900 nm are shown in Figures 4.19- (a and b). The deposited films (Cd_2SnO_4) have visible and near-infrared transmission spectra. The image shows how rising substrate temperature affects the optical properties of the film. In the visible region, the average optical transmittance (550 to 900) nm for the deposited film at a temperature of 450 °C is 92.7 %, which decreases to 90.6 % after deposition at a temperature of 500 °C, and 85.7 % at a temperature of 550 °C. Increasing the substrate temperature also reduced the maximum optical transmittance from 96.3 % (660 nm) to 93.2 % (650 nm) and 88.8 % at a temperature of 550 °C (625 nm).

Increased substrate temperature led to shifts in the fundamental optical absorption edge toward the UV from 520 to 400 nm for 450 ℃ , because of an increase in free carrier concentration. As a result of the lower transmission in the UV–Vis near IR region [178, 179], the effect of free carrier absorption in the heat-treated material is apparent. The cadmium stannate, which has good transmittance through the visible range and strong reflectivity in the nearby IR region [180], is one of the possible choices for solar cell application [28]. The transmission spectra for ZTO samples were shown in Figure 4.19-b for Zn_2SnO_4 thin films. In the visible region of the spectrum, all of the samples show good transparency. The average transmission for 450 ℃ at wavelength 400 nm is 85 %, for 500 ℃ at wavelength 380 nm is 68 %, and for 550 ℃ at wavelength 360 nm is 55% . In the case of ZTO these high transparency values were reached. It noteworthy for its use in optoelectronic devices [28]. Figures 4.19-(c,d) shows the transmittance spectra curves for Cu_2SnS_3 and CuZnS thin films in the wavelength range of 300-900 nm. The transmittance spectrum decreases in the visible region because of the larger grains that have developed on the surface [160, 163].

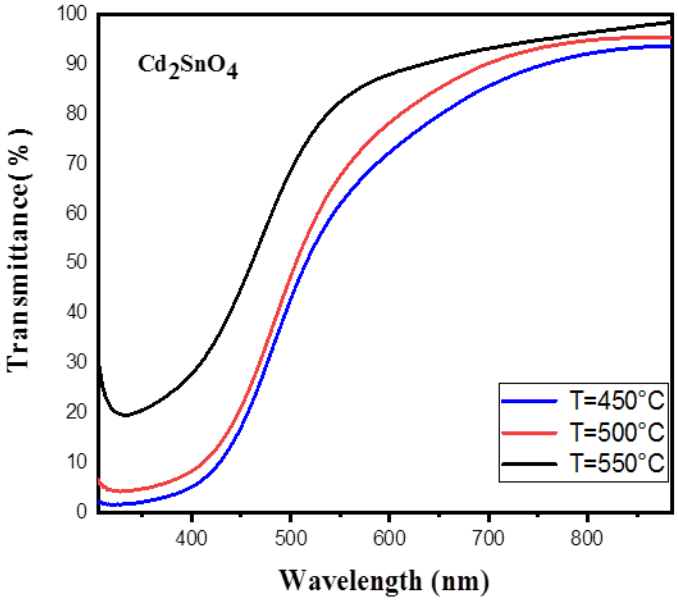

Figure 4.19-a. The transmittance spectra of deposited (Cd_2SnO_4) thin film as a function of wavelength at different substrate temperatures (450, 500. and 550 °C).

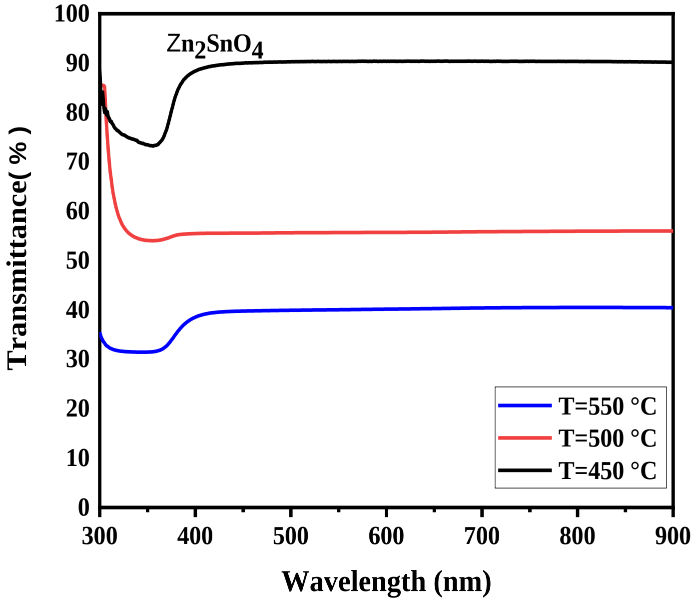

Figure 4.19-b. The transmittance spectra of deposited (Zn_2SnO_4) thin film as a function of wavelength at different substrate temperatures (450, 500 and 550 °C).

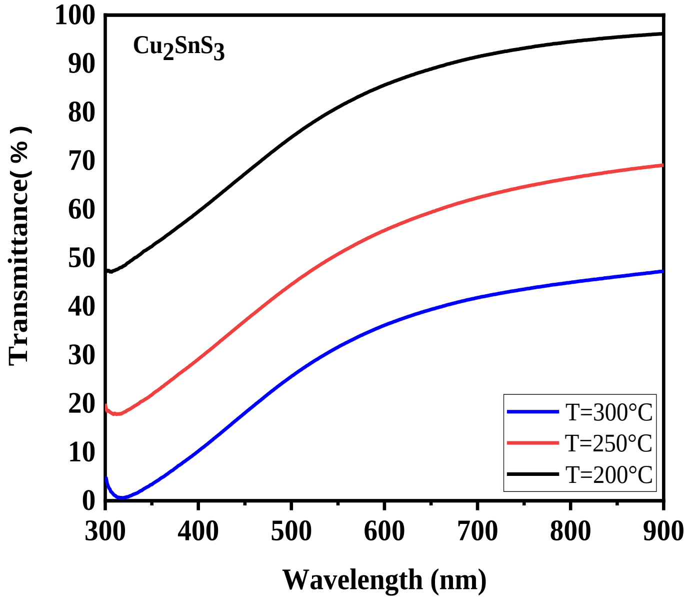

Figure 4.19-c. The transmittance spectra of deposited (Cu_2SnS_3) thin film as a function of wavelength at different substrate temperatures (200, 250 and 300 °C).

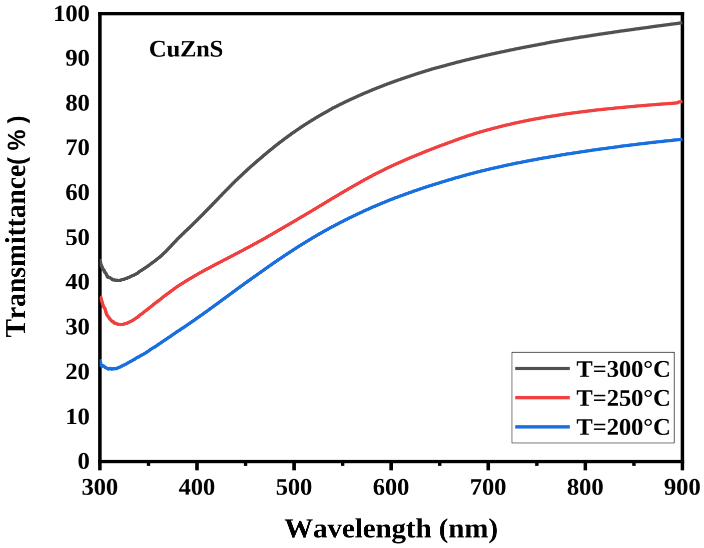

Figure 4.19-d. The transmittance spectra of deposited (CuZnS) thin film as a function of wavelength at different substrate temperatures (200, 250. and 300 °C).

4.5.3 Absorption Coefficient (α)

The absorption coefficient (α) is a measurement of a material's ability to absorb light. Using the absorption spectrum data, the absorption coefficients (α) for Cd_2SnO_4, Zn_2SnO_4, Cu_2SnS_3, and CuZnS are calculated using equation (2-20). Figure 4.20-(a, b) shows that the α-values for Cd_2SnO_4 increase to ($\alpha > 10^4$) cm^{-1} and Zn_2SnO_4 increase to ($\alpha > 10^5$) cm^{-1}, showing that a direct electronic transition occurs in these locations. Furthermore, we found that the α-value of Cd_2SnO_4 and Zn_2SnO_4 films has a high absorption coefficient in the short wavelength region (high energies). On the other hand, the value falls as the substrate temperature rises due to an increase in the energy gap E_g. The values of (α) are nearly identical to those reported by [24, 144]. Figure 4.20(c, d) shows that the Cu_2SnS_3 and CuZnS films have a high absorption coefficient ($\alpha > 10^4$) cm^{-1} and that the absorption coefficient increases as the substrate temperature rises, which could be attributed to the film's increased crystallinity [160].

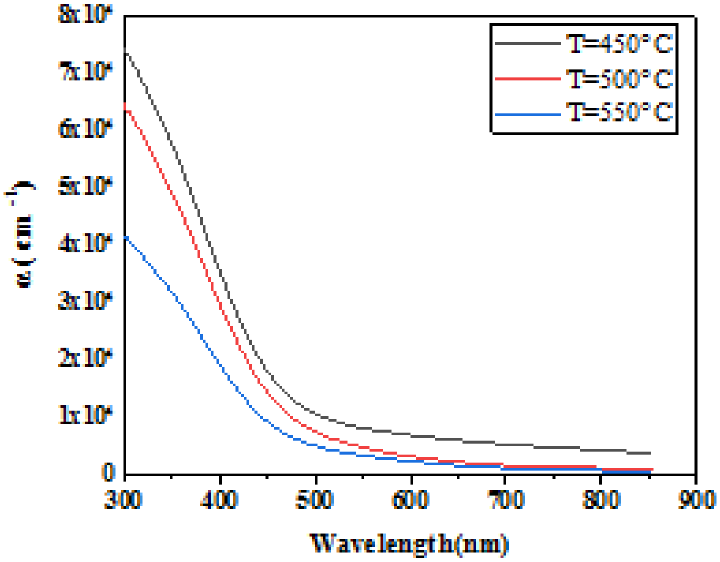

Figure 4.20-a. The absorption coefficient for deposited Cd_2SnO_4 thin film as a function of wavelength at different substrate temperatures (450, 500 and 550 °C).

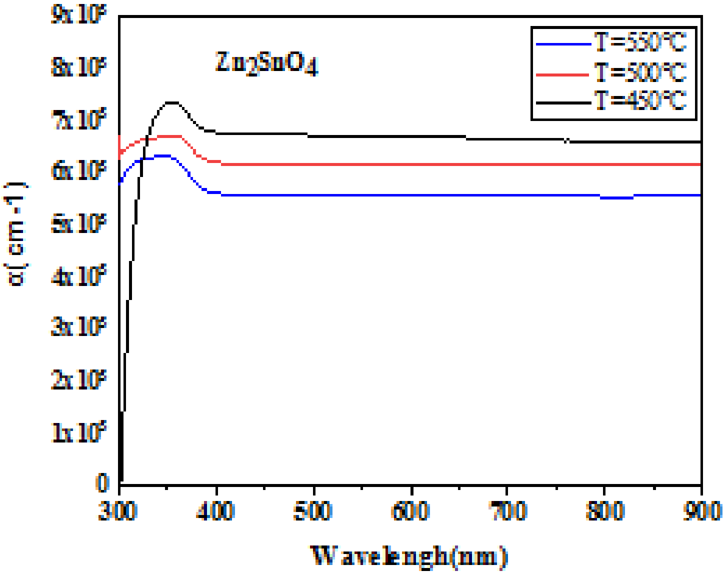

Figure 4.20-b. The absorption coefficient for deposited Zn_2SnO_4 thin film as a function of wavelength at different substrate temperatures (450, 500 and 550 °C).

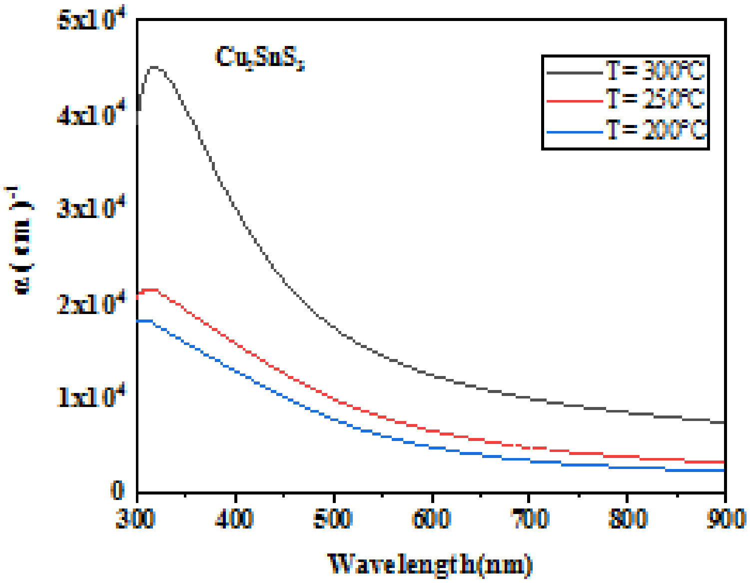

Figure 4.20-c. The absorption coefficient for deposited Cu_2SnS_3 thin film as a function of wavelength at different substrate temperatures (200, 250 and 300 °C).

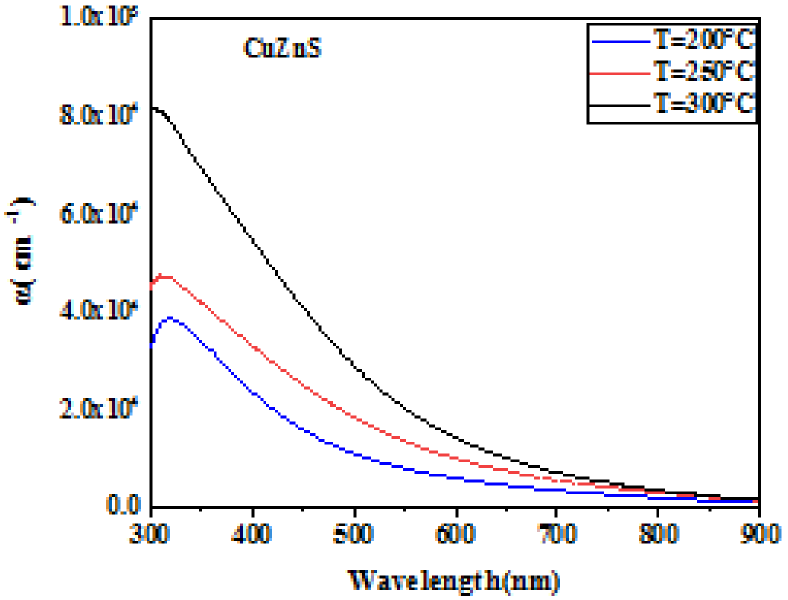

Figure 4.20-d. The absorption coefficient for deposited CZS thin film as a function of wavelength at different substrate temperatures (200, 250 and 300 °C).

4.5.4 Optical Energy Gap (E_g)

In general, the energy gap values are influenced by the crystal structure of samples, as well as the crystal lattice's structure and distribution of atoms, which is influenced through crystal regularity. The plot $(\alpha h\nu)^2$ vs. hν, is shown in Figures 4.21-(a-d). Using the absorption coefficient values (Tauc's equation) and assuming a direct transition between the valance and conduction bands of r = 1/2. Equation (2-11) was used to calculate the energy gap (*Eg*). The energy band gap for Cd_2SnO_4 thin films increased from 2.5 eV at 450 ℃ to 2.69 eV at 500 ℃ and 2.75 eV at 550 ℃ as shown in table 4.12 while the energy gap for Zn_2SnO_4 thin films increased from 3.20 eV at 450 ℃ to 3.25 eV at 500 ℃ and 3.30 eV at 550 ℃ as shown in table 4.12. This is related to the decrease in the number of grain boundaries and the increase in grain size. As a result of reduced absorption, an increase in *Eg* may improve crystal structures, resulting in a reduction in defects (tail state) in the forbidden gap, resulting in an increase in *Eg*. Researchers have given approximative estimates for absorption coefficients [24, 157]. The energy band gap for Cu_2SnS_3 and CuZnS thin films reduces when the substrate temperature rises, as seen in figures. as shown in table 4.12 . The band gap of Cu_2SnS_3 decreases from 2 eV to 1.86 eV and 1.65 eV, respectively. The improvement in crystallinity earlier reported by U. Chalapathi et al [182] may have contributed to the decrease in the band gap. The energy band gap for Cu_2SnS_3 and CuZnS thin films reduces when the substrate temperature rises, as seen in figures 4.21-c and 4.21-d. The band gap for Cu_2SnS_3 decreased from 2 eV to 1.86 eV and 1.65 eV, respectively. This phenomenon applies to photovoltaics application [165]. The band gap for CuZnS thin films decreased from 2.25 eV to 1.94 eV and 1.80 eV after increasing the substrate temperature. Due to an increase in crystallinity as seen in the XRD pattern, and it was discovered that increasing the copper concentration reduced the band gap value of CZS nanoparticles, as Sundaram et al. previously reported [162].

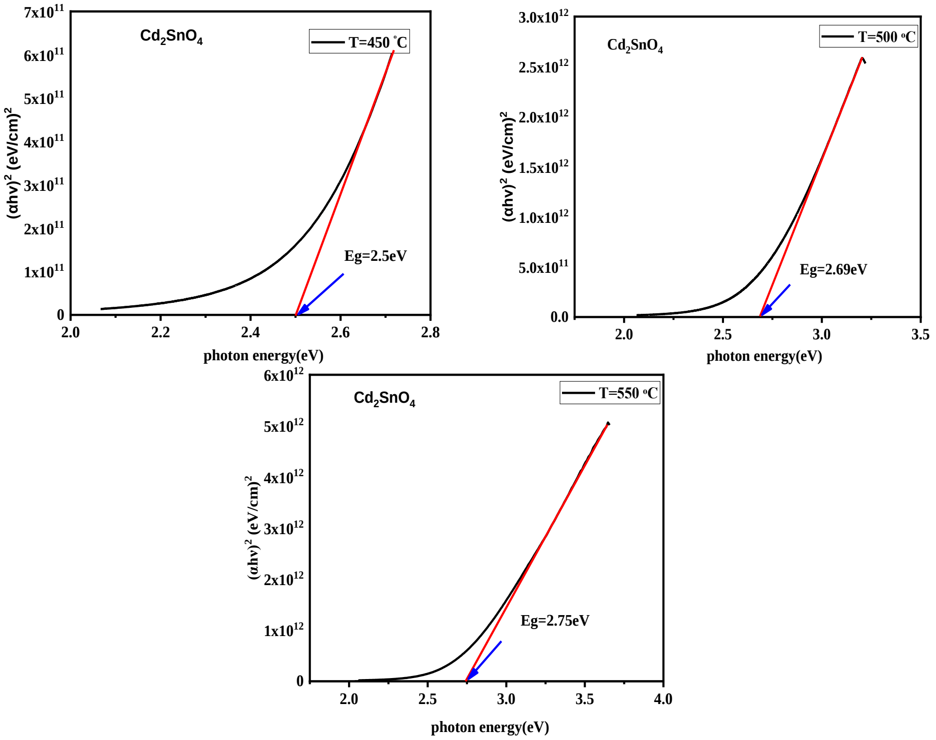

Figure 4.21-a. $(\alpha h\nu)^2$ as a function of photon energy of Cd_2SnO_4 films prepared at different substrates temperatures at (450, 500 and 550°C).

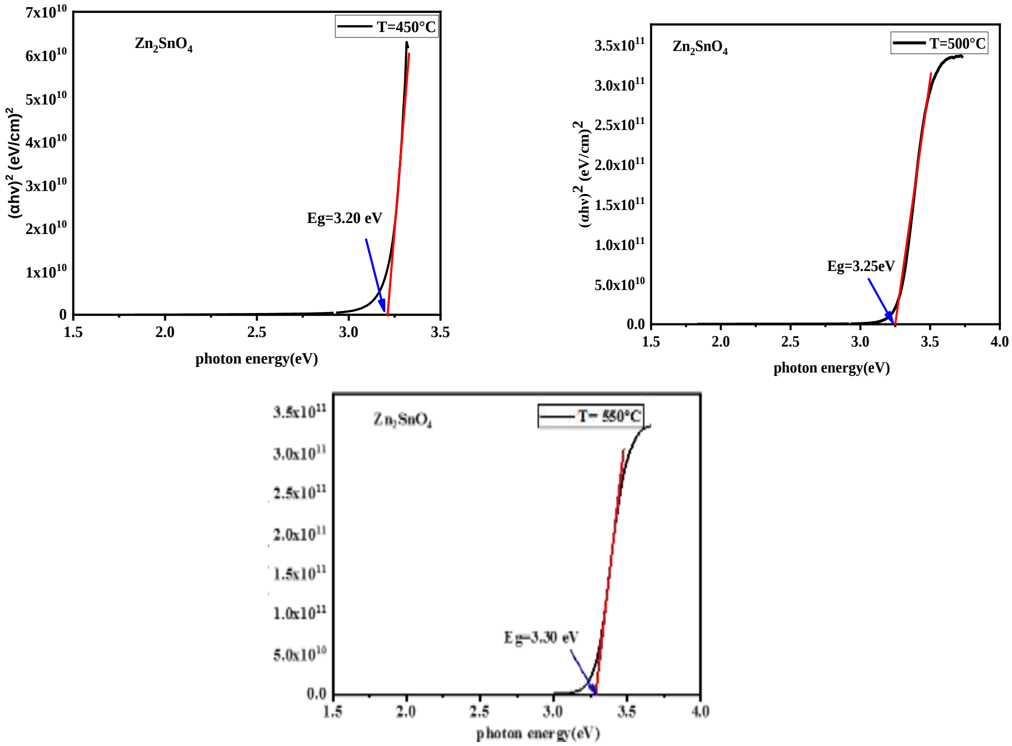

Figure 4.21-b. $(\alpha h\nu)^2$ as a function of photon energy of Zn_2SnO_4 films prepared at different substrates temperatures a (450, 500 and 550°C).

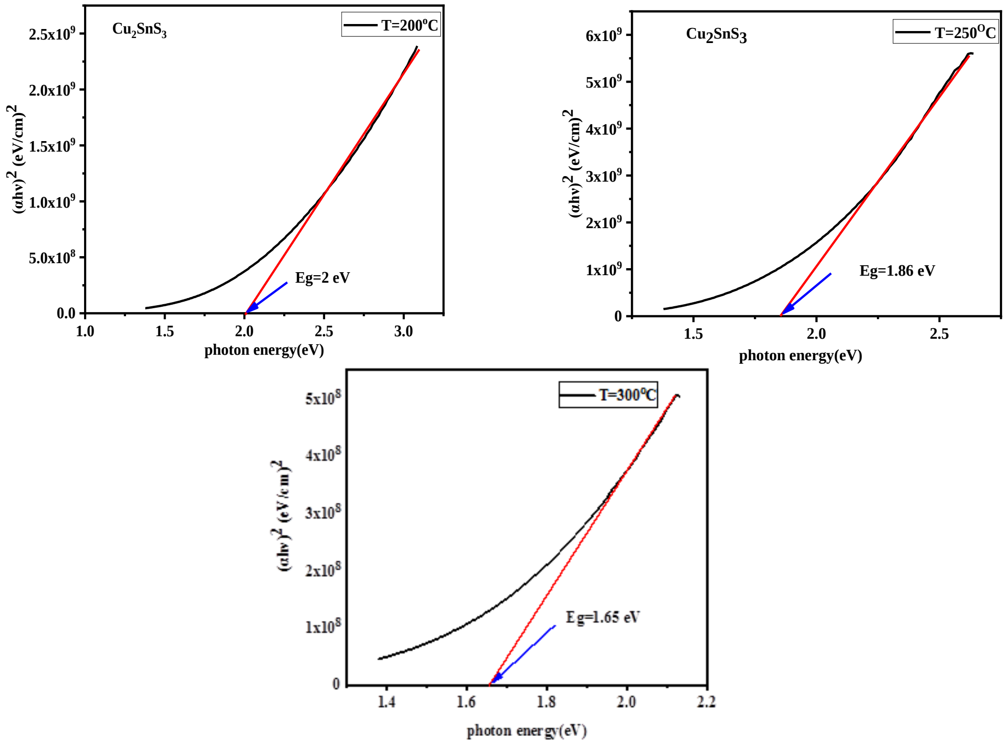

Figure 4.21-c. $(\alpha h\nu)^2$: as a function of energy photon for nanostructure Cu_2SnS_3 thin films were deposited at different substrate temperatures (200,250 and 300 °C).

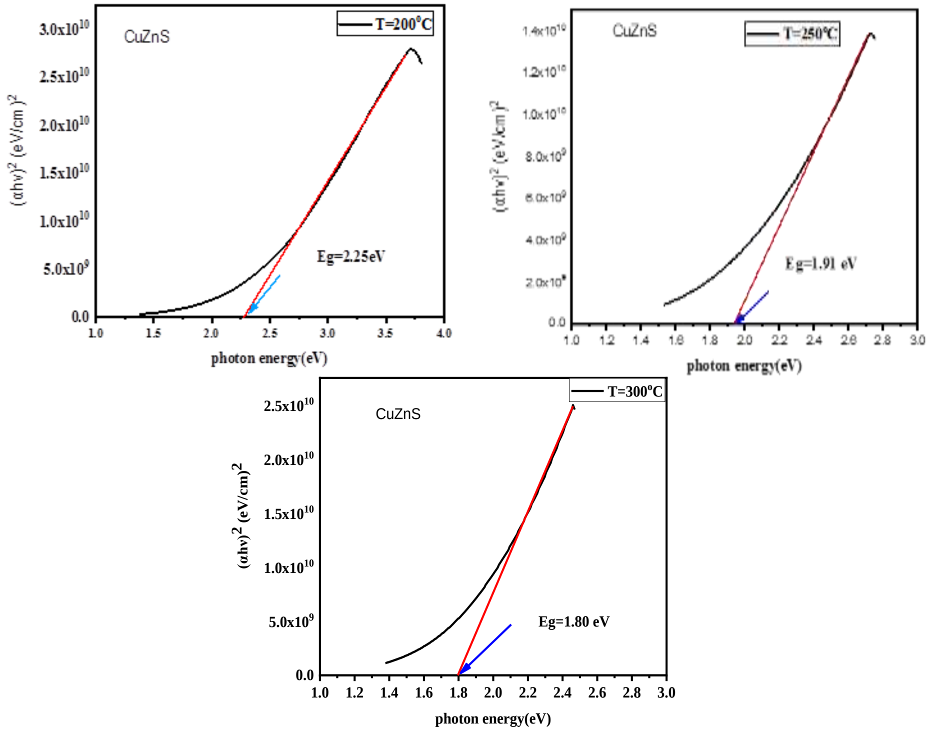

Figure 4.21-d. $(\alpha h\nu)^2$ as a function of energy photon for nanostructure CuZnS thin films were deposited at different substrate temperatures (200,250 and 300 °C).

Table 4.12. Values band gap of Cd_2SnO_4,Zn_2SnO_4,Cu_2SnS_3 and CuZnS at different temperature.

Thin film	**Temperature °C**	Energy Gap E_g **(eV)**
Cd_2SnO_4	450	2.5
	500	2.69
	550	2.75
Zn_2SnO_4	450	3.20
	500	3.25
	550	3.30
Cu_2SnS_3	200	2
	250	1.86
	300	1.65
CuZnS	200	2.25
	250	1.94
	300	1.80

4.6 Hall Effect

Hall measurements of Cd_2SnO_4, Zn_2SnO_4, Cu_2SnS_3, and CuZnS thin films grown on glass substrates at varying substrate temperatures (450, 500, and 550 ℃) were used to estimate carrier concentration, resistivity, mobility, and conductivity. As shown in Table 4.13 the results from the negative sign of the Hall coefficient show that the type of charge carriers is (n-type) based on eq (2-29). (That is, the majority of charge carriers are electrons), and the positive value of the Hall coefficient indicates that the type of charge carriers is (p-type) according to eq (2-29). (That is, the holes make up the majority of the charge carriers). Hall measurements shown. Both Cd_2SnO_4 and Zn_2SnO_4 semiconductor films consist of an n-type defect, and the conductivity of the films.

The presence of adsorbed oxygen in films traps certain electrons, resulting in a rise in resistivity. By creating oxygen vacancies, increasing the substrate temperature can help to minimize the influence of electron traps formed during film deposition. As a result, all of the films were treated at different temperatures (450, 500, and 550 °C) to improve the electrical conductivity of the thin films. The increase in carrier concentration can explain the decrease in resistivity as the substrate temperature rises [20].

Because all Cu_2SnS_3 thin films have a greater carrier concentration, varying mobility, and low resistivity, CTS thin films could be a promising absorber layer material for thin-film solar cells [181]. The p-type semiconducting nature of CuZnS films increased grain size, which decreased grain density, and hence scattering at grain borders should be reduced, according to Hall findings. As a result, resistivity values are reduced and conductivity is increased. Furthermore, copper-rich phases have high copper vacancies, which could explain the increase in carrier concentration for the samples at temperatures of 200, 250, and 300 ℃, making them suitable for optoelectronic devices [166].

Table 4.13. Hall effect measurement result Cd_2SnO_4, Zn_2SnO_4, Cu_2SnS_3 and CuZnS thin films at different substrate temperature.

Thin film	**Temperature (^oC)**	**Carrier Concentration $(cm)^{-3}$**	**Hall Coefficient R_H (cm^3/C)**	**Conductivity σ $(\Omega.\ cm)^{-1}$**	**Resistivity ρ (Ω. cm)**	**Mobility μ (cm^2/Vs)**	**Type**
Cd_2SnO_4	**450**	**5.774×10^{10}**	**-1.081×10^{8}**	**9.880×10^{-6}**	**$1.012 \times 10^{+3}$**	**1.068×10^{3}**	**n**
	500	**9.102×10^{11}**	**-6.858×10^{6}**	**7.750×10^{-2}**	**1.290×10^{1}**	**5.315×10^{5}**	**n**
	550	**2.545×10^{12}**	**-2.453×10^{6}**	**3.997×10^{-4}**	**2.502×10^{3}**	**9.804×10^{2}**	**n**
Zn_2SnO_4	**450**	**1.803×10^{10}**	**-3.461×10^{8}**	**4.336×10^{-6}**	**2.306×10^{5}**	**1.501×10^{3}**	**n**
	500	**6.468×10^{10}**	**-9.651×10^{7}**	**7.319×10^{-5}**	**1.366×10^{4}**	**7.064×10^{3}**	**n**
	550	**2.911×10^{12}**	**-2.144×10^{6}**	**7.936×10^{-3}**	**1.260×10^{2}**	**1.702×10^{4}**	**n**
Cu_2SnS_3	**200**	**1.415×10^{11}**	**4.410×10^{7}**	**3.133×10^{-7}**	**3.192×10^{6}**	**1.382×10^{1}**	**p**
	250	**7.494×10^{11}**	**8.329×10^{6}**	**4.111×10^{-6}**	**2.433×10^{5}**	**3.424×10^{1}**	**p**
	300	**1.231×10^{23}**	**5.071×10^{-5}**	**1.001×10^{6}**	**9.987×10^{-7}**	**5.078×10^{1}**	**p**
CuZnS	**200**	**2.442×10^{11}**	**2.556×10^{7}**	**9.916×10^{-6}**	**$1.008 \times 10^{+5}$**	**2.535×10^{2}**	**p**
	250	**5.522×10^{11}**	**1.130×10^{7}**	**1.117×10^{-5}**	**8.950×10^{-4}**	**1.263×10^{2}**	**p**
	300	**5.252×10^{18}**	**1.189**	**1.843×10^{3}**	**5.426×10^{-4}**	**2.191×10^{3}**	**p**

4.7 Properties of Cd_2SnO_4, Zn_2SnO_4, Cu_2SnS_3, and CuZnS/PSi Solar Cell by Spray Pyrolysis and Spin Coating Technique.

It is important to study the electrical and photoelectrical properties of the PSi layer because it could be used in many technological applications, like detectors, solar cells and sensors . The I-V characteristics, photovoltaic characteristics, and related electrical parameters such as fill factor, solar cell efficiency, and charge carrier transport mechanisms in Cd_2SnO_4/PSi/Si/Al,Zn_2SnO_4/PSi/Si/Al,Cu_2SnS_3/ PSi/Si/Al, and CuZnS/PSi/Si/Al heterojunctions are dependent on the structural properties of the PSi. The PSi layers (PSLS) were prepared for n and p-type silicon at a current density of 10 mA/cm^2 and an etching time of 10minutes.

These heterojunction's solar cell and photodetector characteristics have been investigated. They were deposited on various substrates in this study, including (n, p) porous silicon wafers.

4.7.1 (I-V) Characteristics of Heterojunction in the Dark Condition

The heterojunction's current and voltage relationship Cd_2SnO_4/PSi/p-Si/Al , Zn_2SnO_4/PSi/p-Si/Al, Cu_2SnS_3/PSi/n-Si/Al, and CuZnS/PSi/n-Si/Al forward bias and reverse bias at a voltage applied from (1-10V) are shown in Figures 4.22 - 4.25. Because of the low resistance, the current passing by the heterojunction grows with increasing applied voltage in the forward bias case, while no current passes through the heterojunction in the reverse bias situation (high resistance).The current general behavior with voltages in the forward and reverse bias is a common feature of heterogeneous heterojunctions [182, 183]. In the case for forward bias, based on these numbers, the current going by the heterojunction rises with increasing applied voltage. This current is called recombination current and only occurs at low voltages. This is produced when an electron falls from the conduction band into the valence band, into a hole. The second region at high voltage represents the region of diffusion or bending region, which depends on the series resistance. The bias voltage can deliver electrons with sufficient energy in this region to penetrate the barrier between the two sides of the junction. The second region is when the applied voltage increases, the current accelerates and rises with the applied voltage, and is called the drift current [126,184].

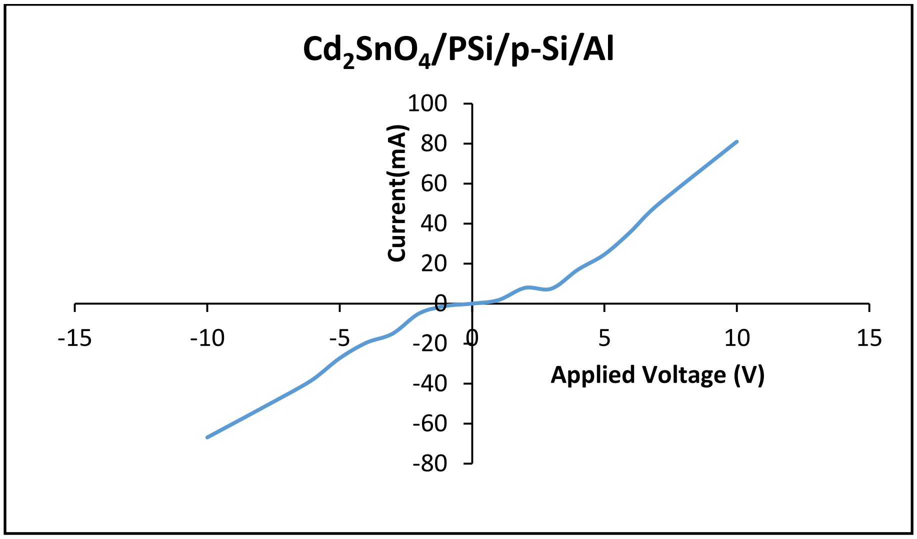

Figure 4.22. I-V Characteristics in the dark for both reverse and forward bias of Cd_2SnO4/PSi/p-Si/Al at 550°C.

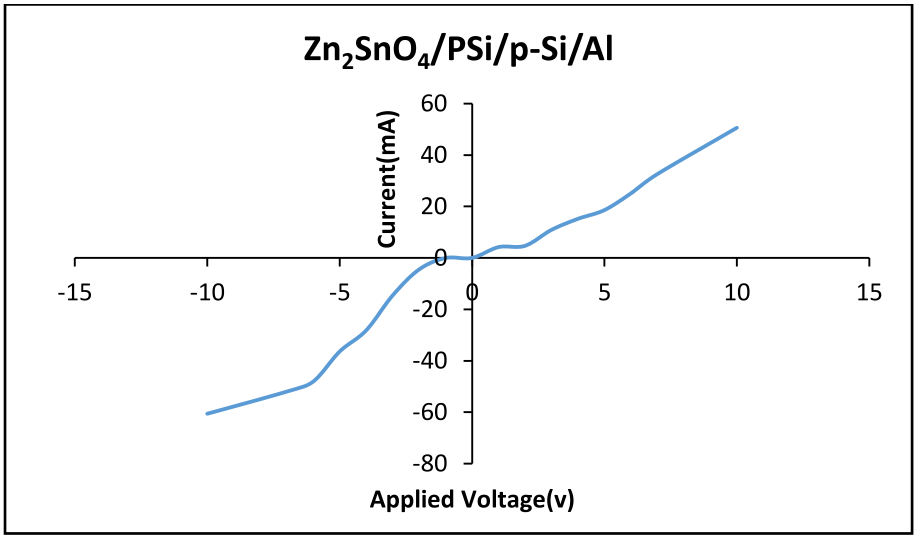

Figure 4.23. I-V Characteristics in the dark for both reverse and forward bias of Zn_2SnO_4 /PSi/p-Si/Al at 550°C.

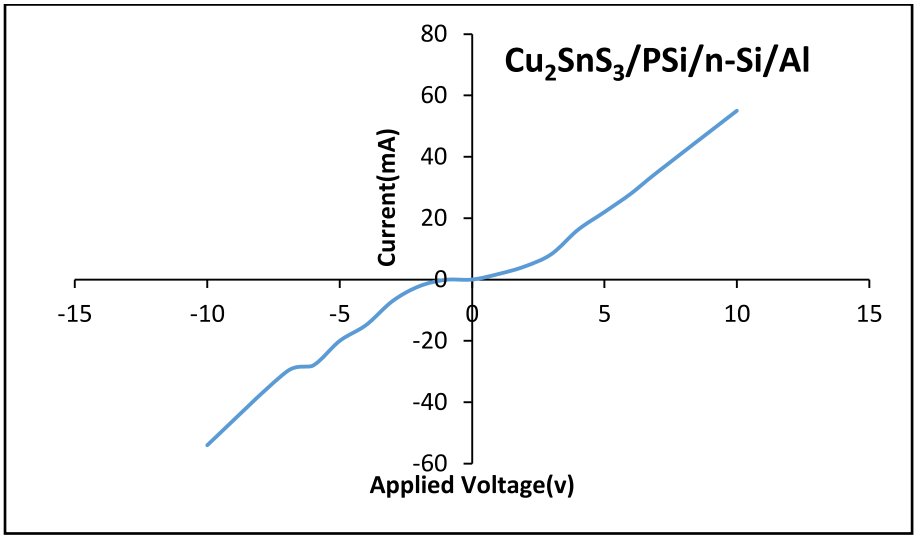

Figure 4.24. I-V Characteristics in the dark for both reverse and forward bias of Cu_2SnS_3/ PSi /n-Si/ Al at 300^{o}C.

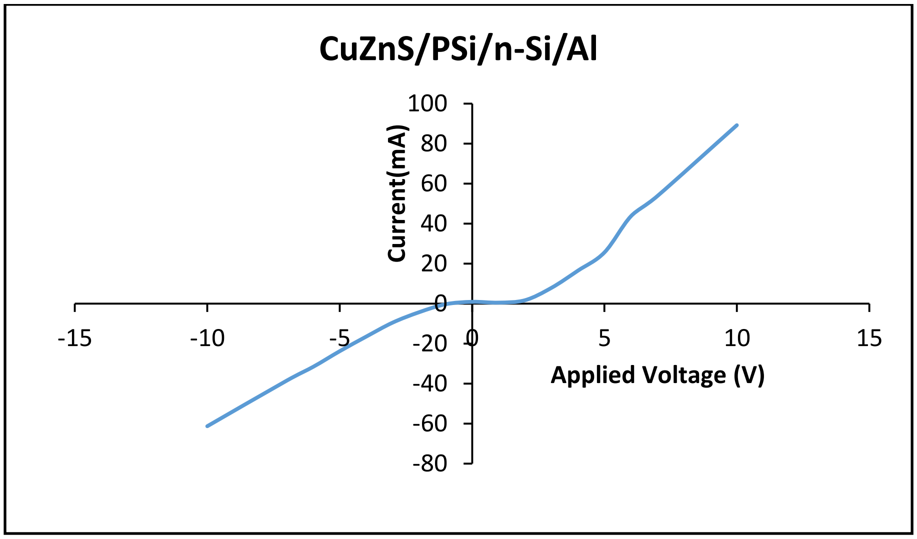

Figure 4.25. I-V Characteristics in the dark for both reverse and forward bias of CuZnS/PSi /n-Si/Al at 300^{o}C.

4.7.2 (I-V) Characteristics Under Illumination (Photocurrent)

Figures (4.26–4.29) depict (I-V) characteristics in the dark and light, creating photocurrent under a tungsten lamp illumination (100 mWm^{-2}). Note that the effective area of the cell (0.785 cm^2) is used for PSi. It is evident that the optical current (I_{ph}) increases when both the applied voltage and the intensity of the incident light are raised, leading to an increase in the number of charge carriers and the width of the depletion region, which in turn enhances electron absorption and generation. It is noticed that the illuminated current value is larger than that of the current value in the dark case, that the current, in this case, is not dependent on the voltage but due to photons incident on the heterojunction where the mobility of charge carriers (Electrons) is larger and thus increasing current.

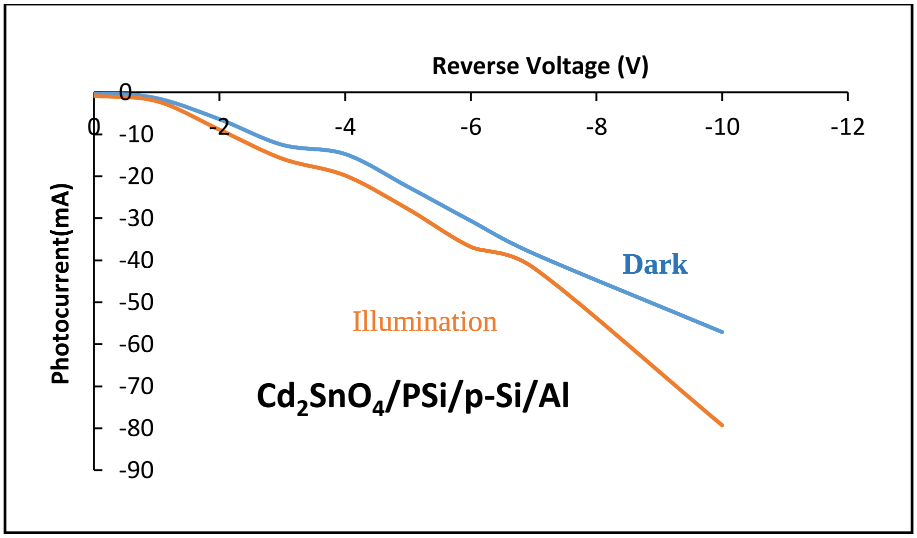

Figure 4.26. I-V Characteristics in the dark and under a light in the case of reverse bias of Cd$_2$SnO$_4$/PSi/p-Si/ Al.

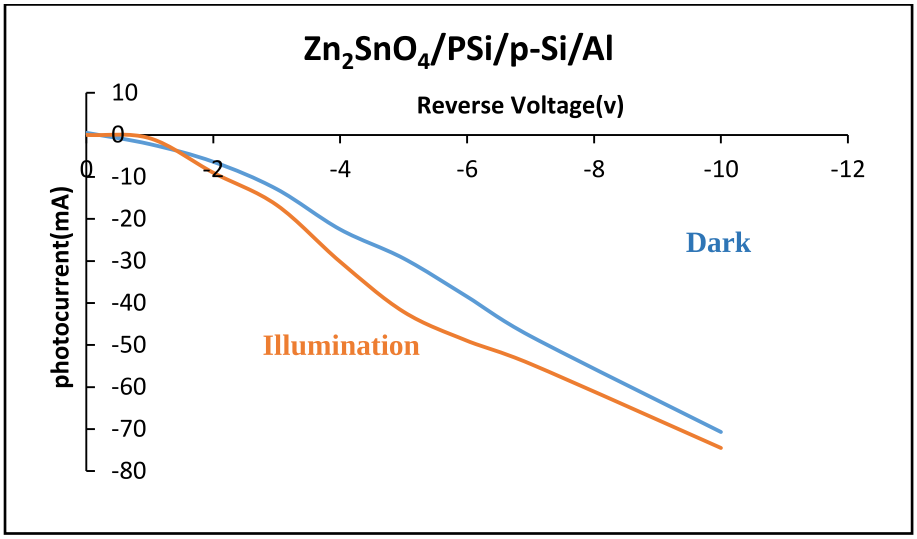

Figure 4.27. I-V Characteristics in the dark and under a light in the case of reverse bias of Zn_2SnO_4/PSi/p-Si/ Al.

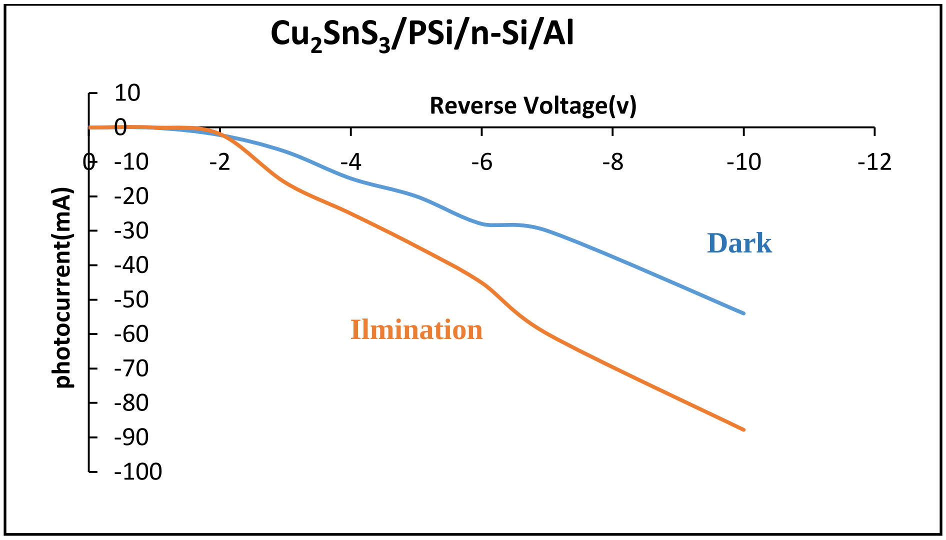

Figure 4.28. I-V Characteristics in the dark and under a light in the case of reverse bias of Cu_2SnS_3/PSi/n-Si/ Al.

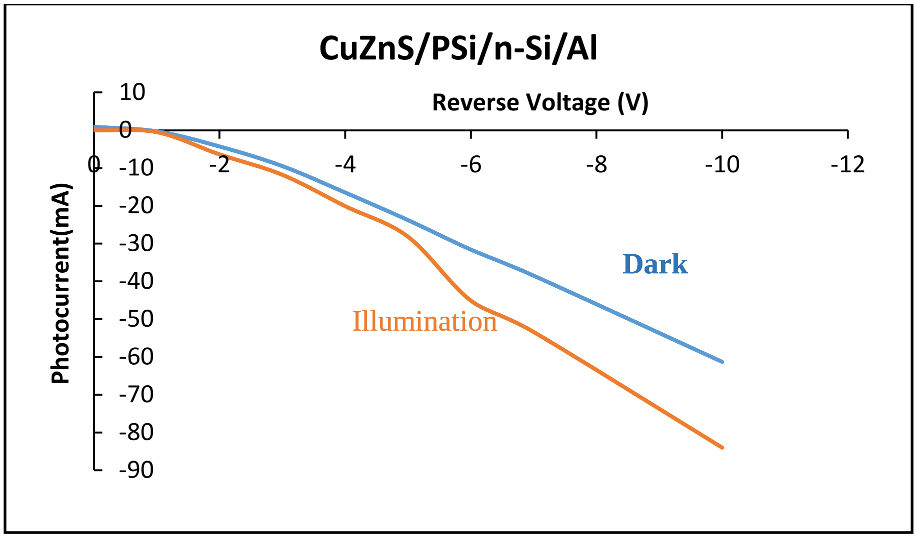

Figure 4.29. I-V Characteristics in the dark and under a light in the case of reverse bias of CuZnS/ PSi/n-Si/ Al.

4.7.3 Short Circuit Current (I_{sc})and Open Circuit Voltag(V_{oc})Measurments

The (I-V) curves of the heterojunction bonding generated by spray pyrolysis and spin coating are shown in Figures (4.30-4.33).The fill factor (*F.F*) and efficiency of photoelectric conversion (η) were determined using the formulas (2.43) and (2.44),respectively, based on the (I-V) curve. The photovoltaic properties of constructed solar cells, as well as the J-V characteristics of the heterojunction for substrates (PSi),are listed in table 4.14. The estimated properties of a solar cell are shown in table 4.14.(I-V) parameters of Cd_2SnO_4/PSi/p-Si/Al, Zn_2SnO_4/PSi/p-Si/Al, Cu_2SnS_3/PSi/n-Si/Al and CuZnS/PSi /n-Si/Al heterojunction parameters at different temperatures. The highest efficiency was obtained in heterojunction CuZnS /PSi/n-Si/Al and its value was (4.7 %).Due to the presence of CuS and ZnS, where CuS is more prominent in the XRD plot. A very attractive feature of the material is the properties of the films (both optical and electrical). The dominance of CuS decreases the band gap making the material a good absorber whereas the presence of ZnS allows high-energy photons to pass through, By increasing Cu concentration, which leads to a decrease in resistivity [33, 160].

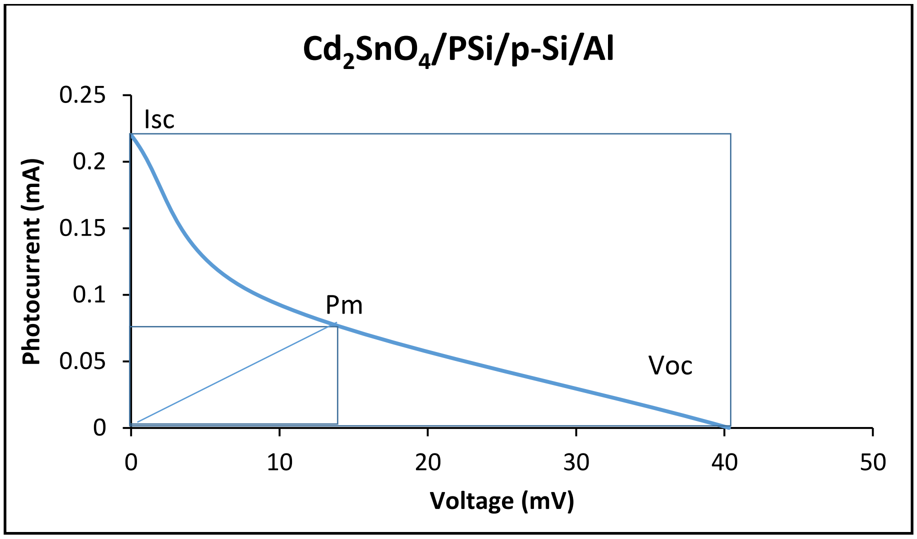

Figure 4.30. I-V Curve of a solar cell (SC) of Cd_2SnO_4/PSi/p-Si/Al.

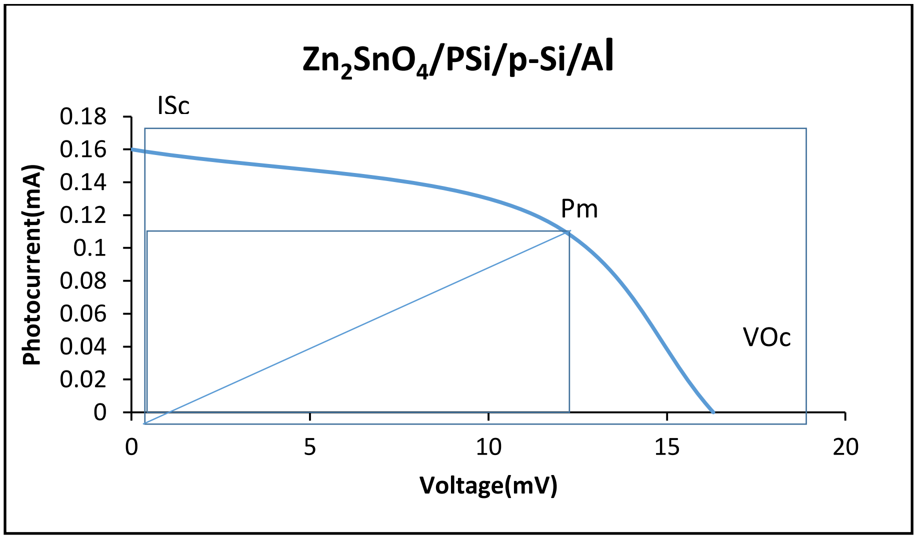

Figure 4.31. I-V Curve of a solar cell (SC) of Zn_2SnO_4/PSi/p-Si/ Al.

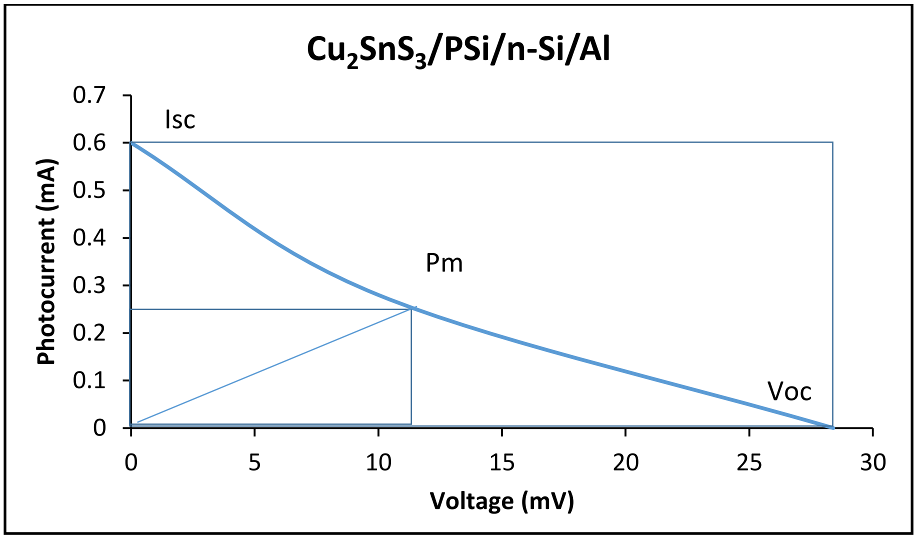

Figure 4.32. I-V Curve of a solar cell (SC) of Cu_2SnS_3/PSi/n-Si/Al.

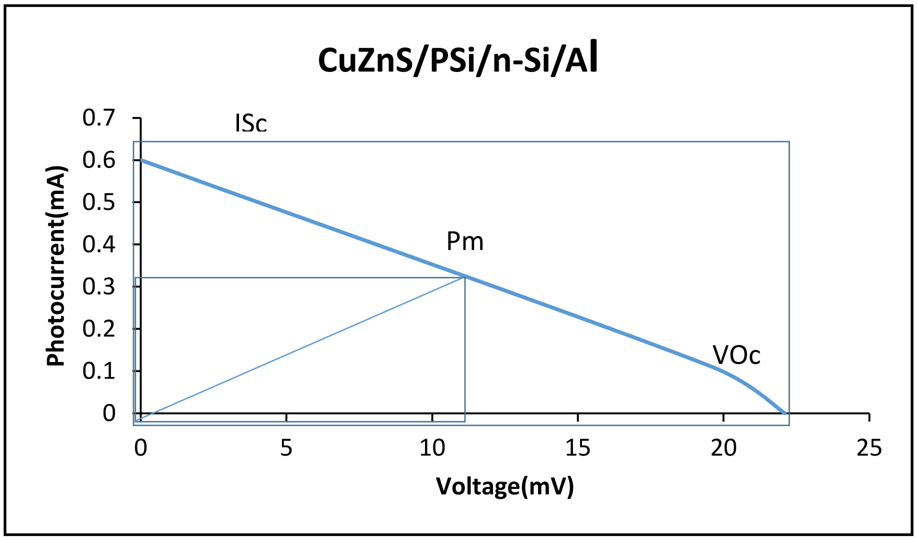

Figure 4.33. I-V Curve of a solar cell (SC) of CuZnS/PSi/n-Si/Al.

Table 4.14. Short-circuit current density, open-circuit voltage, filling factor and efficiency of prepared heterojunctions by spray pyrolysis and spin coating technique.

Solar cell	V_{OC} (mV)	J_{SC} (mA/cm^2) ×10^{-2}	V_m (mV)	Jm (mA/cm^2) ×10^{-2}	η%	F.F%
Cd_2SnO_4/Psi/Si/Al	40.3	0.28	14	0.089	1.24	0.11
Zn_2SnO_4/Psi/Si/A	16.3	0.19	11	0.14	1.54	0.50
Cu_2SnS_3/Psi/Si/Al	28	0.76	11	0.34	3.74	0.176
CuZnS/Psi/Si/Al	22.1	0.73	12	0.39	4.7	0.29

The (I-V) curves of the heterogeneous bonding prepared by the drop-casting technique are shown in Figures (4.34-4.37). The fill factor ($F.F$) and photoelectric conversion efficiency (η) were determined using the formulas (2.43) and J_{max}, V_{max} (2.44), respectively, based on the (J-V) curve. The heterojunction J-V characteristics for substrates (psi) and the photovoltaic properties of produced solar cells are given in Table (4.15). Table 4.15 displays the calculated solar cell parameters.(I-V) heterojunction parameters of Cd_2SnO_4 /PSi/p-Si/Al, Zn_2SnO_4/PSi/p-Si/Al, Cu_2SnS_3/PSi/n-Si/Al and CuZnS /PSi/n-Si/Al at various temperatures. We observe that the efficiency of all samples increased, indicating that the deposition method affected improving the efficiency of the solar cell. The sample with the highest efficiency was Cu_2SnS_3/PSi/n-Si /Al, with a value of 7.8 %; this may be a result of changing the phase of the thin film, as well as the sedimentation method, which plays a role in improving the efficiency of the cell [42].

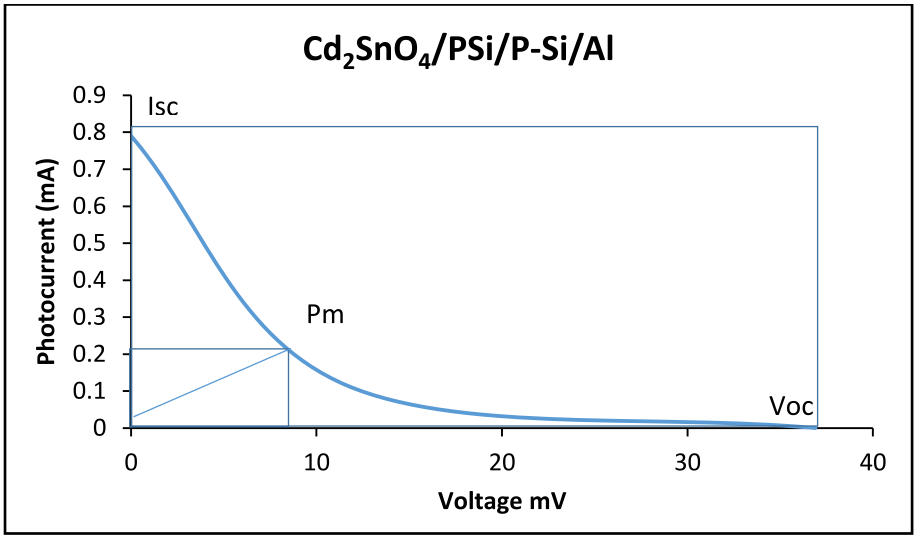

Figure 4.34. I-V Curve of a solar cell (SC) of Cd_2SnO_4/PSi/p -Si/Al.

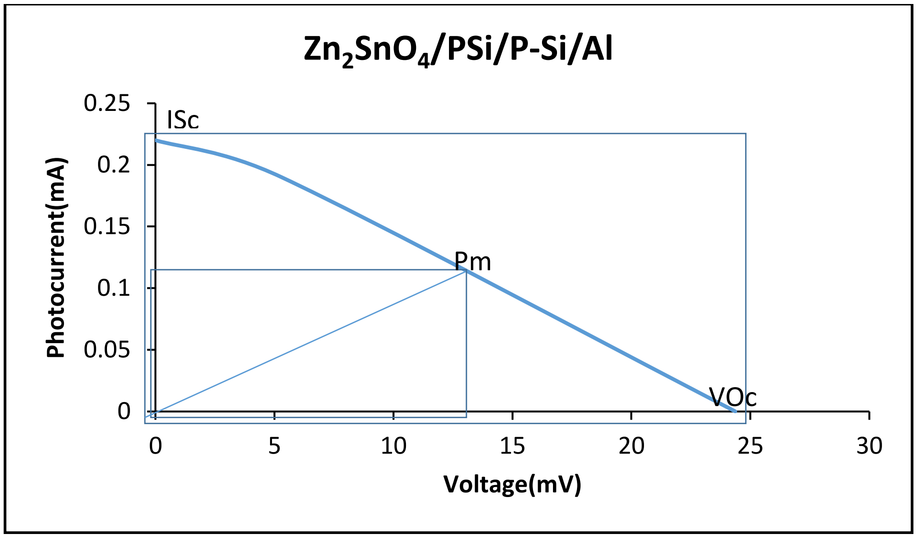

Figure 4.35. I-V Curve of a solar cell (SC) of Zn_2SnO_4/ PSi/p -Si/ Al.

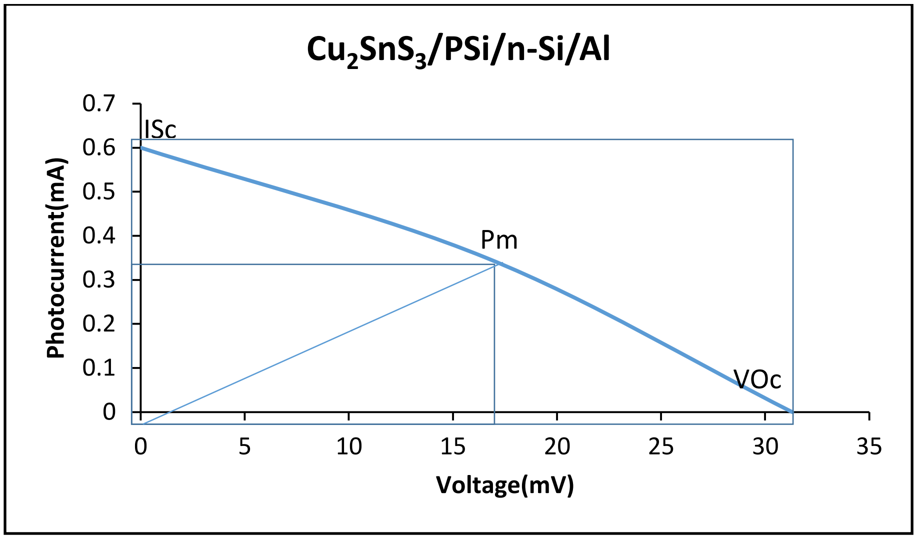

Figure 4.36. I-V Curve of a solar cell (SC) of Cu_2SnS_3/ PSi/n-Si/Al.

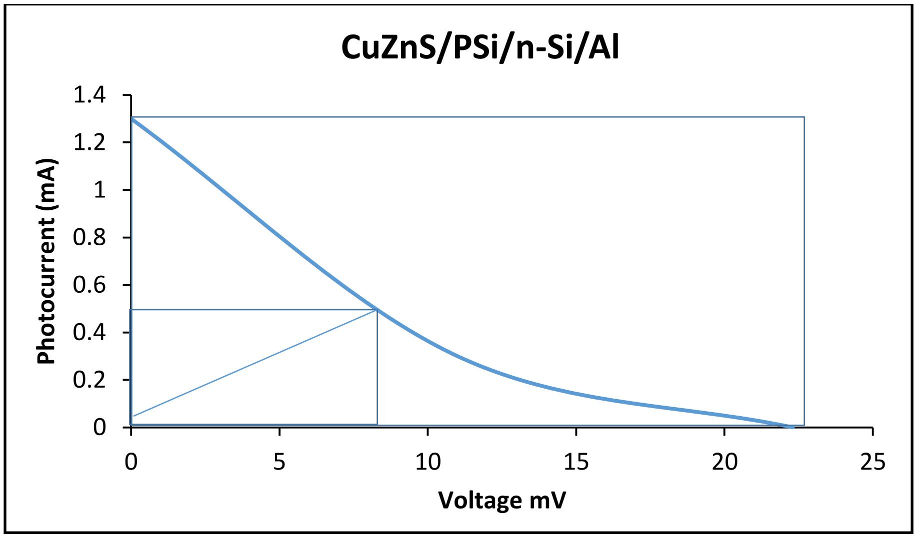

Figure 4.37. I-V Curve of a solar cell (SC) of CuZnS/ PSi/n-Si/Al.

Table 4.15. Short-circuit current density, open-circuit voltage, filling factor, and efficiency of prepared heterojunctions by drop-casting technique.

Solar cell	V_{OC} (mV)	J_{SC} (mA/cm^2) × 10^{-2}	V_m (mV)	J_m (mA/cm^2) × 10^{-2}	η %	$F.F$ %
Cd_2SnO_4 /PSi /p-Si/Al	36.9	1	8.5	0.26	2.27	0.0615
Zn_2SnO_4/PSi/p-Si/Al	24.37	0.28	14	0.15	2.11	0.31
Cu_2SnS_3/PSi/n-Si/Al	31.3	0.76	17.5	0.44	7.8	0.33
CuZnS/PSi/n-Si/Al	22.3	1.6	8	0.64	5.1	0.143

4.8 Detector Performance Parameters Measurement

In applications involving photodetectors and photovoltaic detectors, photovoltaic properties such as spectral responsivity, gain, and spectral detectivity are much crucial.

4.8.1 Spectral Responsivity (R_λ)

Figures(4.38-4.41) depict the spectrum response characteristics of heterojunction detectors at various temperatures within the range (400-900 nm) when biased with a voltage (3V). The response is determined using equation (2-45). The spectral responsivity curve of (Cd_2SnO_4/ PSi/p-Si/Al) and (Zn_2SnO_4 / PSi/p-Si/Al). (Figure 4.38 and 4.39) comprises double peaks of responsivity ; the elementary peak at a wavelength of (450±15) nm which corresponds to approximately the cutoff wavelength of Cd_2SnO_4 and Zn_2SnO_4. The second peak is positioned at (85±50) nm due to the silicon absorption edge [185]. (Short wavelengths) entails a significant increase in responsivity, which is related to the high absorption coefficient. This results in a lower absorption depth and a faster recombination process compared to any other region within the material; this is known as the probability of carrier concentration, which increases with the departure from the surface region responsivity ($R\lambda$) was expected to be 0.48 A/W for (Cd_2SnO_4/ PSi/p-Si/Al), and 0.084 A/W for (Zn_2SnO_4/ PSi/p-Si/Al). These results concur with those of Yan Zhao et al. [35].

The spectral responsivity curve (Cu_2SnS_3 /n-PSi /Si/Al) and (CuZnS/ PSi/n-Si/Al) is depicted in Figures 4.40 and 4.41. The initial heterojunction (CuZnS/ PSi/n-Si/Al) consists of one peak at a wavelength of (800±10) nm which responsivity (R_λ) was to be (0.57-0.60A/W), while the second heterojunction (Cu_2SnS_3 /PSi /n-Si/Al) the maximum responsivity (R_λ) was to be (0.30-0.35A/W) at wavelength 900nm.

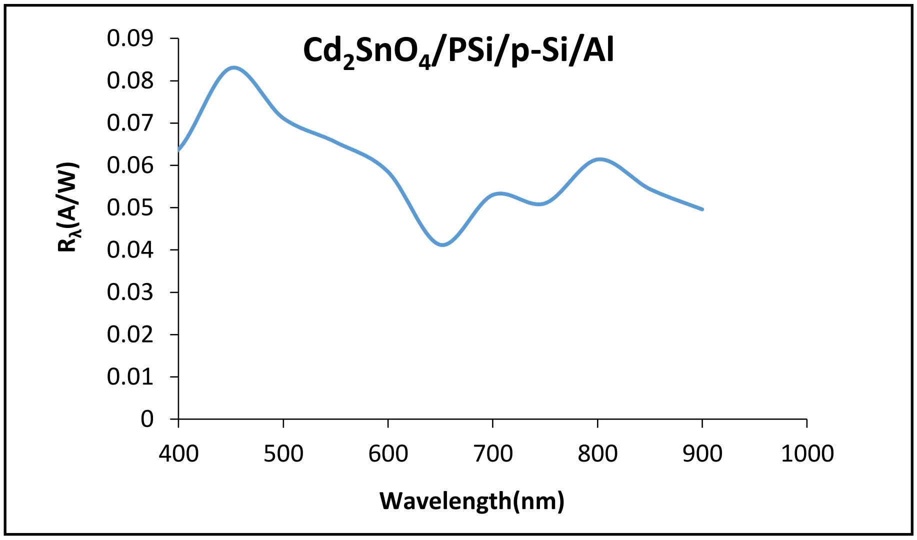

Figure 4.38. The variation of spectral responsivity with wavelength for Cd_2SnO_4 /PSi/p-Si/Al.

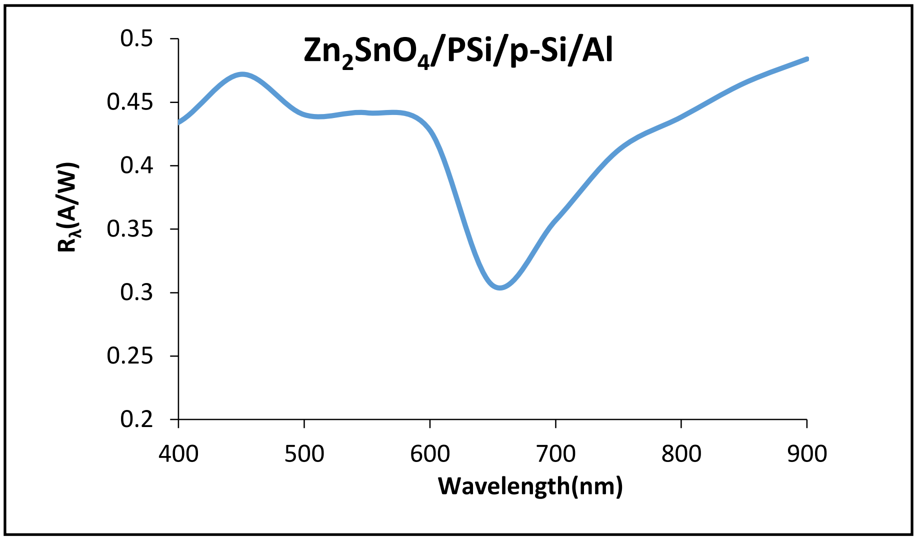

Figure 4.39. The variation of spectral responsivity with wavelength for Zn_2SnO_4/PSi /p-Si/ Al.

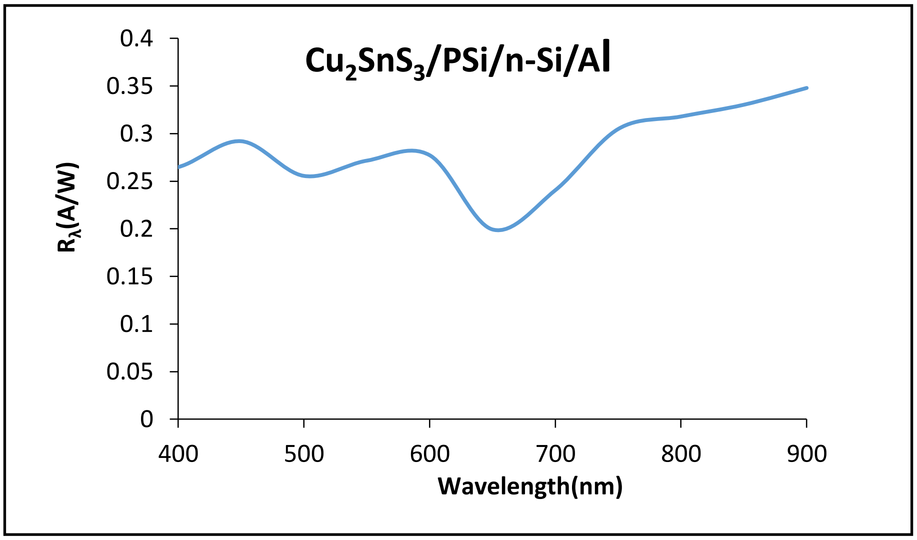

Figure 4.40. The variation of spectral responsivity with wavelength for Cu_2SnS_3/ PSi /n-Si/Al.

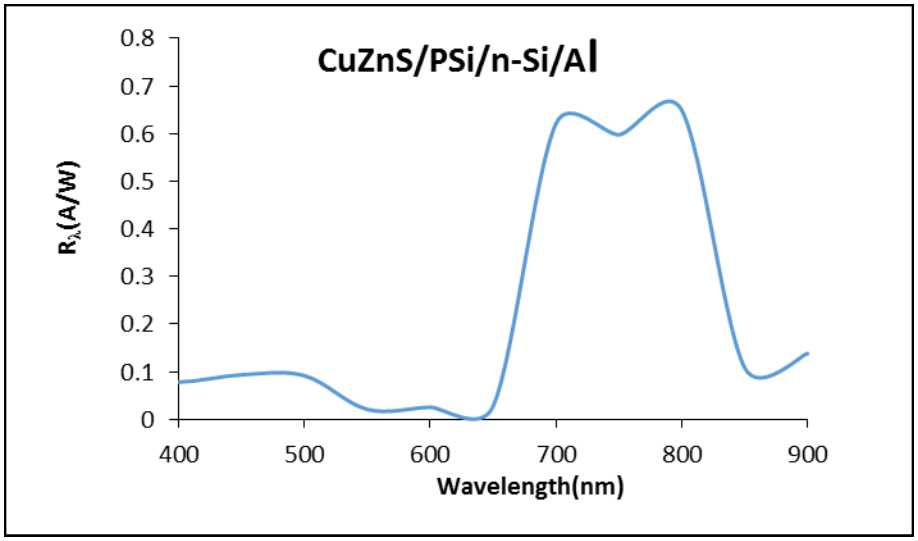

Figure 4.41. The variation of spectral responsivity with wavelength for and CuZnS / PSi/n-Si/Al.

4.8.2 Photocurrent Gain (*G*)

We determined the Photocurrent Gain (*G*) for Cd_2SnO_4, Zn_2SnO_4, Cu_2SnS_3, and CuZnS thin films at varying temperatures using equation (4.46), as depicted in Figure 4.42-45. The Cd_2SnO_4, Zn_2SnO_4, Cu_2SnS_3, and CuZnS thin film devices exhibit corresponding (*G*) values of 23,134, 0.26, and 82 % in the UV-Vis- IR range. As depicted in Figure 4.43 and Table 4.16, the Gain. The results indicate that UV-Vis light is particularly responsive to Zn_2SnO_4 thin-film devices. Due to its wide direct band gap of 3.3 eV with high internal UV photoconductivity gain due to the surface-enhanced electron-hole separation efficiency [35].

.

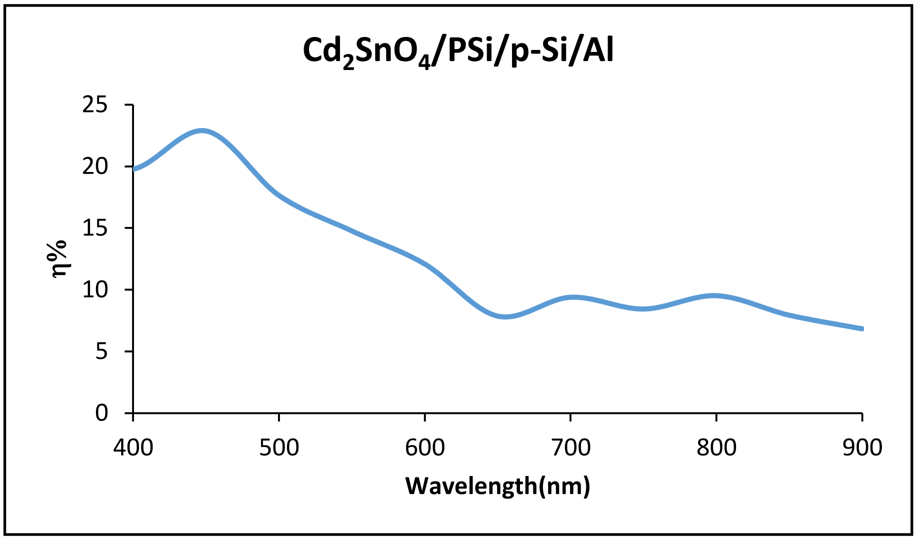

Figure 4.42. The variation of photocurrent Gain (G) with wavelength for Cd_2SnO_4 / PSi/p-Si/Al.

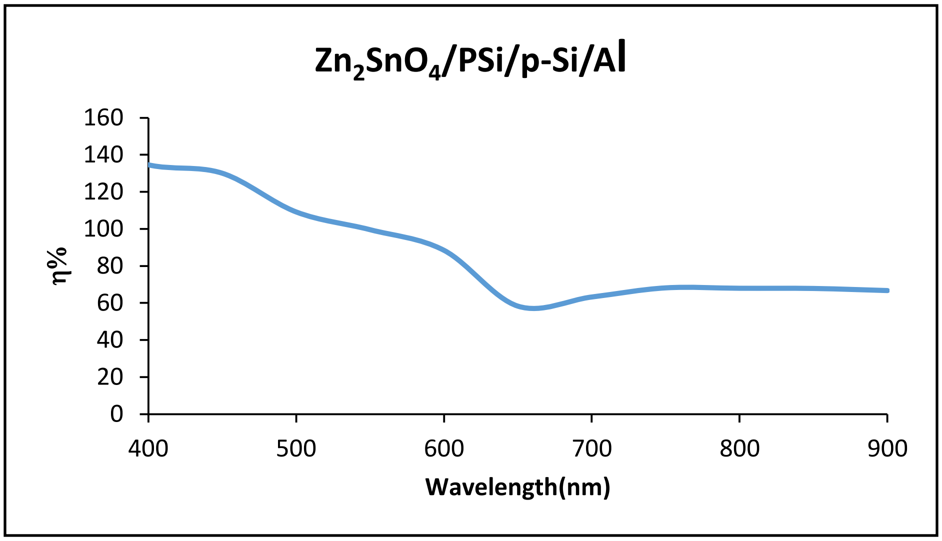

Figure 4.43. The variation of photocurrent Gain (G) with wavelength for Zn_2SnO_4 /PSi/p-Si/Al.

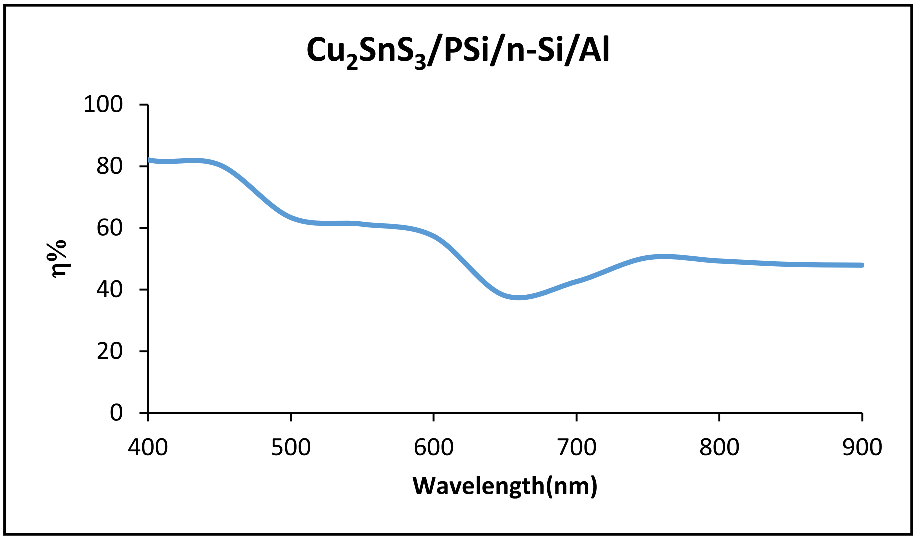

Figure 4.44. The variation of photocurrent Gain (G) with wavelength for Cu_2SnS_3 /PSi/n-Si/Al.

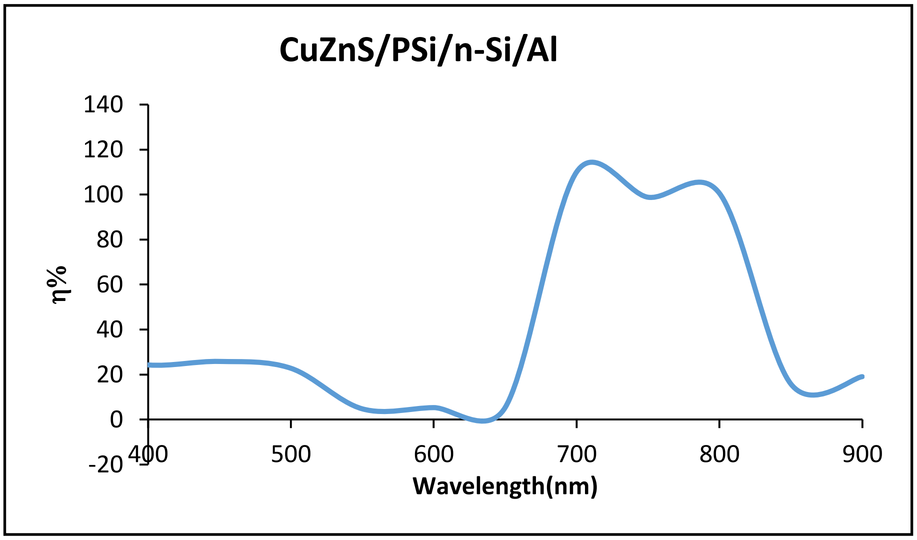

Figure 4.45. The variation of photocurrent Gain (G) with wavelength for CuZnS/PSi/n-Si/Al.

4.8.3 Specific Detectivity (*D**)

The specific detectivity of a photodetector is one of the most important qualities since it represents the minimum detectable power; as a result, the detector's performance is determined by this number, which dictates the detector's efficiency and ideal application region (Wavelength). Noise from surrounding radiation, Johnson-noise, noise created by the random motion of electrons and holes, transit time, and noise variety all influence the value of the particular detectivity. Figures 4.46-4.49 show how this works, the wavelength-dependent specific detectivity of manufactured photodetectors As the value of the particular detectivity is reliant on the spectral response according to the equation, we can observe that the curve behaves similarly to that of the spectral response (2.48 and 2.49). The direct relationship between detectivity and sensitivity may be seen in the graphs. As indicated in table 4.16, the specific detectivity is greater than (10^{10}cm $Hz^{1/2}$ W^{-1}); thus, this heterojunction is operational. From the Figures, the detectivity for heterojunctions varied between 1.18×10^{12}cm $Hz^{1/2}W^{-1}$ at wavelength (45±15) nm, with the greatest *D** determined to be 1.18×10^{12}cm $Hz^{1/2}W^{-1}$ at (450±15) nm for Cd_2SnO_4/PSi/p-Si/Al, and 6.7×10^{12}cm $Hz^{1/2}W^{-1}$ at the wavelength (45±5) nm, and the extreme *D** create to be 6.7×10^{12} cm $Hz^{1/2}.W^{-1}$ at (45±15) nm for Zn_2SnO_4/PSi/n-Si/Al photodetector.The detectivity for heterojunctions ranged between 9.2×10^{12}cm $Hz^{1/2}.W^{-1}$ at wavelength (80±10) nm and the maximum *D** was found to be 9.2×10^{12} cm $Hz^{1/2}.W^{-1}$ at (900nm) for CuZnS/Si and detectivity for heterojunctions ranged between 4.9×10^{12}cm $Hz^{1/2}.W^{-1}$ at a wavelength (900nm) and the maximum *D** found to be 4.9×10^{12}cm $Hz^{1/2}.W^{-1}$ for Cu_2SnS_3/PSi/n-Si/Al.

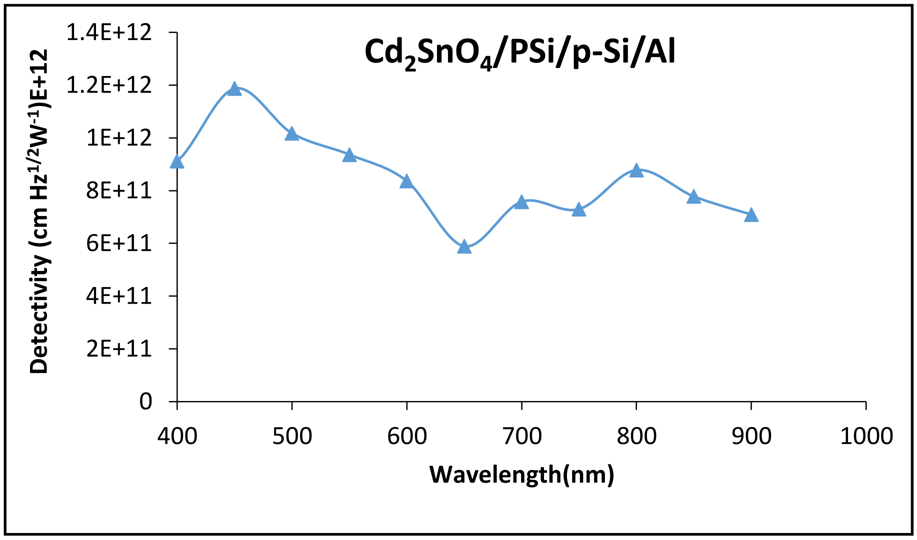

Figure 4.46. The variation of spectral detectivity with wavelength for Cd_2SnO_4/ PSi/p-Si/Al.

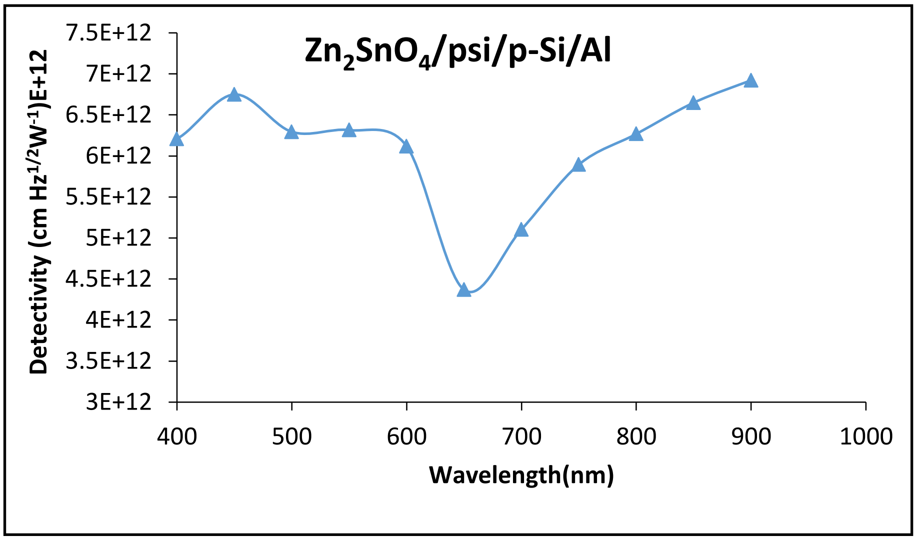

Figure 4.47. The variation of spectral detectivity with wavelength for Zn_2SnO_4/ PSi/p-Si/ Al.

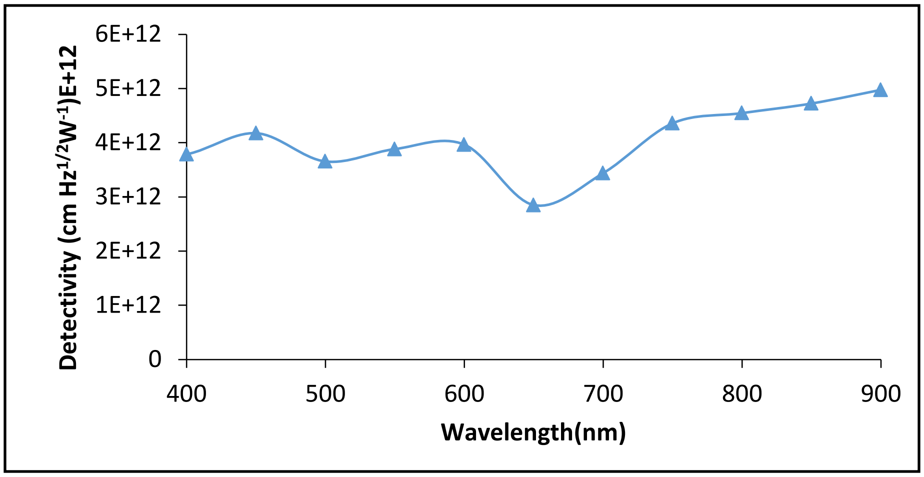

Figure 4.48. The variation of spectral detectivity with wavelength for Cu_2SnS_3/PSi/n-Si/Al.

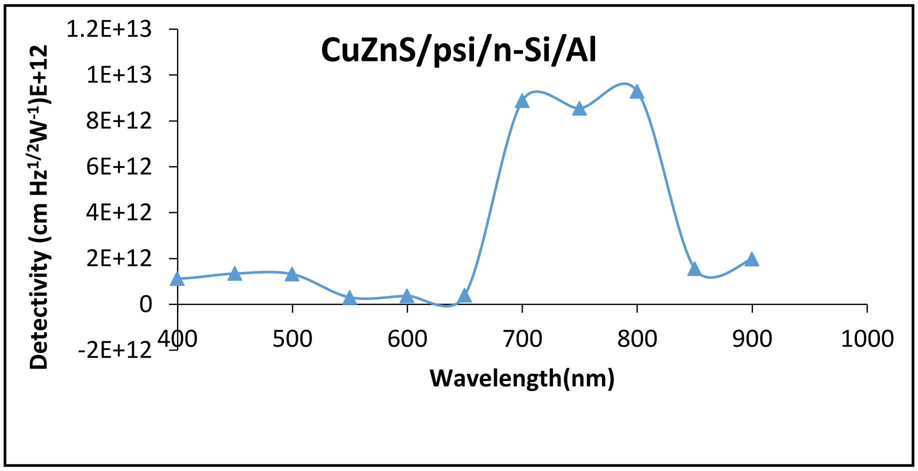

Figure 4.49. The variation of spectral detectivity with wavelength for CuZnS/PSi/n-Si/Al.

Table 4.16. Spectral Response, Gain, and Specific Detectivity values for prepared heterojunctions.

Sample	R_λ(A/W)	Gain	Detectivity (D_λ) ×10^{12} cm $Hz^{1/2}.W^{-1}$
Cd_2SnO_4/PSi/p-Si/Al	0.48	23	1.18
Zn_2SnO_4/PSi/p-Si/Al	0.084	134	6.7
Cu_2SnS_3/PSi/n-Si/Al	0.35	82	4.9
CuZnS/PSi/n-Si/Al	0.60	0.26	9.2

4.9 Conclusions

1.The results of X-ray diffraction measurements showed that films Cd_2SnO_4 and Zn_2SnO_4 prepared by spray pyrolysis method at temperature(450,500 and 550^{o}C) possess a polycrystalline structure of cubic (spinel)and in the dominant and preferred growth direction (311), whereas the films prepared by spin coating Cu_2SnS_3 are polycrystalline with a tetragonal structure and a hexagonal structure of CuZnS at temperature (200,250 and 300^{o}C),The results of X-ray diffraction measurements showed that films of , prepared by the sol-gel method possess a cubic structure (spinel) for Cd_2SnO_4 and Zn_2SnO_4 and cubic structure for Cu_2SnS_3 and CuZnS ,and that an increase in substrate temperature increased the crystal size ,according to the FTIR spectra, it has clearly confirmed the appearance of the broad O-H peaks. The presence of the nanostructures of the prepared thin films was confirmed by (XRD, AFM, FE-SEM) techniques.

2. AFM analyzes showed that the values of particle size, surface roughness and RMS can be controlled by controlling the temperature.

3. The results of field-emitting scanning electron microscopy (FE-SEM) showed that Cd_2SnO_4 films have spherical structure at temperature (450 ^{o}C) and change to Cauliflower-like shapes at (500, 550 ^{o}C) .while showed that Zn_2SnO_4 films have spherical structure at temperature (450 ^{o}C) and change to small stone at (500,550 ^{o}C),at all temperature Cu_2SnS_3 thin films have shape spherical at(200,250 and300^{o}C) also CuZnS thin films thin films have cauliflower-like shapes at(200,250 and 300^{o}C). The Cross Sectional FE-SEM images also showed that the thickness of the thin films was not affected by the temperature change.

4. The results of the optical tests showed that the values of transmittance, absorbance and direct optical energy gap can be controlled by changing the temperature of the films.

5. The results of the Hall effect measurements showed that the type of charge carriers is (n-type) for Cd_2SnO_4 and Zn_2SnO_4 films and (p-type) for Cu_2SnS_3 and CuZnS films.

6.This study showed that effectively Cd_2SnO_4, Zn_2SnO_4, Cu_2SnS_3, and CuZnS thin films can synthesized method chemical spry pyrolysis and the spin coating technique, respectively. The films were then deposited with a thickness of approximately 1 μm on PSi. The Cd_2SnO_4, Zn_2SnO_4, Cu_2SnS_3, and CuZnS thin films were additionally prepared using the sol-gel technique and deposited on PSi with a thickness of approximately 1μm using the drop-casting technique. From the obtained results, the following conclusions are drawn:

7.Incorporation of nanoparticles (Cd_2SnO_4, Zn_2SnO_4, $Cu_2SnS_{3,}$ and CuZnS) on porous silicon (PSi) improves the parameters of solar cell characteristics and the efficiency of solar cells, resulting in an appropriate heterojunction efficiency of (CuZnS)/ n-PSi for solar cells. 4.07 % via the spin coating technique at 300 °C.

8. The drop-casting technique enhanced the efficiency of solar cells, with the greatest value being 7.80 % for Cu_2SnS_3/n-PSi. This indicates that the strategy contributed to the increased efficiency of the solar cell.

9. The heterojunctions Zn_2SnO_4/p-PSi and Cd_2SnO_4/p-PSi are applicable for UV photodetector applications.

10. The heterojunctions Zn_2SnO_4/p-PSi and Cd_2SnO_4/p-PSi are applicable for IR photodetector applications.

Future Works

According to the findings of this study, the following additional research is recommended:

1. Manufacture of porous silicon solar cells through the manufacture of Cd_2SnO_4 and Zn_2SnO_4 using spin coating technique, and comparison the resulting cells with spray pyrolysis technique.
2. Study the effect of doping mixing (Cu_2SnS_3) with another semiconductor, such as ($ZnCl_2$,NaF, etc.), to synthesize the heterojunction and its use in porous silicon solar cells.
3. Developing porous silicon solar cells using the drop-casting technique and a Zn_2SnO_4/ CuZnS/PSi/Al multijunction preparation.

References

[1] F. D. Mirjan and M. A. Ammer ALshareefi, “Polyvinyl alcohol (PVA) rhodam B(Excellent Medicinal Applications asBiocompatibility and Biodegradable): study the optical properties”, Indian Journal of Forensic Medicine and Toxicology, Vol. 13, no. 2, pp.307-312, 2019.

[2] J.Fowlie, “Electronic and structural properties of $LaNiO_3$-based heterostructures”, Springer, 2019.

[3] S. S. Najm, “Effect of additive of copper nanoparticles on the electrical properties of polyvinyl-alcohol films”, Journal of Applied Physics,: Proceedings, 2021.

[4] J. Szczyrbowski and A. Czapla, “Optical absorption in DC sputtered InAs films”, Thin Solid Films, Vol. 46, no. 2, pp. 127-137, 1977.

[5] F. Coppola, R. Greco and G. Ragosta,“Isotactic polypropylene/EPDM blends: Effect of testing temperature and rubber content on fracture”, Journal of materials science, Vol. 21, no. 5, pp. 1775-1785, 1986.

[6] M. P. Soriaga, J. Stickney, L. A. Bottomley and Y.-G. Kim, “Thin Films: Preparation, Characterization, Applications: Preparation, Characterization, Applications”, Springer Science & Business Media, 2002.

[7] K. Chopra, “Thin Film Phenomena”, McGraw-Hill New York, Vol. 19692, pp.196, 1969.

[8] C. Rao, S. Vivekchand, K. Biswas and A. Govindaraj, “Synthesis of inorganic nanomaterials”, Dalton Transactions, no. 34, pp. 3728-3749, 2007.

[9] K. Bange, “Colouration of tungsten oxide films: a model for optically active coatings”, Solar energy materials and solar cells, Vol. 58, no. 1, pp. 1, 1999.

[10] K.T. Ramakrishna Reddy and R.B.V. Chalapathy, “Structural Properties of $CuGa_xIn_{1-x}Se_2$ Thin films deposited by spray pyrolysis”, Crystal Research and Technology: Journal of Experimental and Industrial Crystallography, Vol. 34, no. 1, pp. 127-132, 1999.

[11] D. Todorovsky, R. Todorovska, N. Petrova, M. Uzunova-Bujnova, M .Milanova,S. Anastasova, E. Kashchieva and S. Groudeva-Zotova, “Spray-pyrolysis, deep-and spin-coating deposition of thin films and their characterization”, Journal of the University of Chemical Technology and Metallurgy, Vol. 41, no. 1, pp. 93-96, 2006.

[12] J.C. Viguie and J. Spitz, “Chemical vapor deposition at low temperatures”, J. electrochem. Soc, Vol. 122, no. 4, pp. 585-588, 1975.

[13] I. A. Mahmood, M. M. Farhan and N. T. Mohammed, “Spray pyrolysis of Low Carbon Steel by Polymer Matrix Composite”, Al-

Nahrain Journal for Engineering Sciences, Vol. 18, no. 2, pp. 273-283, 2015.

[14] L.A. Isac, A. Duta, A. Kriza, I.A. Enesca and M. Nanu, “The growth of CuS thin films by spray pyrolysis”, Journal of the physics,Vol.61, no.1, pp. 096, 2017.

[15] K.-m. Lin and P. Tsai, “Growth mechanism and characterization of ZnO: Al multi-layered thin films by sol–gel technique”, Thin Solid Films, Vol. 515, no. 24, pp. 8601-8604, 2007.

[16] Sahu, B. Parija and S. Panigrahi, “Fundamental understanding and modeling of spin coating process: A review”, Indian Journal of Physics, Vol. 83, no. 4, pp. 493 N -502, 2009.

[17] R. Mamazza Jr, D. L. Morel and C. S. Ferekides, “Transparent conducting oxide thin films of Cd_2SnO_4 prepared by RF magnetron co-sputtering of the constituent binary oxides”, Thin solid films, Vol. 484, no. 1-2, pp. 26-33, 2005.

[18] K. Jeyadheepan, M. Thamilselvan, K. Kim, J. Yi and C.Sanjeeviraja, “Optoelectronic properties of RF magnetron sputtered cadmium tin oxide (Cd_2SnO_4) thin films for CdS/CdTe thin film solar cell applications”, Journal of Alloys and Compounds, Vol. 620, pp. 185-191, 2015.

[19] S. M. Shaban, B. S. Mahdi and R. M. S. Al-Haddad, “Investigation of the Dielectric Behavior and AC Conductivity of Cd_2SnO_4 Compound”, Al-Mustansiriyah Journal of Science, Vol. 22, no. 1, 2011.

[20] R. Kumaravel, V. Krishnakumar, V. Gokulakrishnan, K.Ramamurthi and K. Jeganathan, “Effect of annealing on the electrical, optical and structural properties of cadmium stannate thin films prepared by spray pyrolysis technique”, Thin Solid Films, Vol. 518 , no. 8, pp. 2271-2274, 2010.

[21] A. M. Al-Baradi, M. El-Nahass, M. Abd El-Raheem, A. Atta and A. Hassanien, “Effect of gamma irradiation on structural and optical properties of Cd_2SnO_4 thin films deposited by DC sputtering technique”, Radiation physics and chemistry, Vol. 103, pp. 227-233, 2014.

[22] X. Fu, X. Wang, J. Long, Z. Ding, T. Yan, G. Zhang, Z. Zhang, H. Lin and X. Fu, “Hydrothermal synthesis, characterization, and photocatalytic properties of Zn_2SnO_4”, Journal of Solid State Chemistry ,Vol. 182, no. 3, pp. 517-524, 2009.

[23] L. Wang, X. Zhang, X. Liao and W. Yang, “A simple method to synthesize single-crystalline Zn_2SnO_4 (ZTO) nanowires and their photoluminescence properties”, Nanotechnology, Vol. 16, no. 12, pp. 2928, 2005.

[24] S. J .Mohammed, K. A. Aadim and M. M. Ameen, “Effect of Annealing on Some Properties of Zn_2SnO_4 Thin Films Prepared by PLD Technique”, kirkuk university journal for scientific studies, Vol. 13, no. 4, pp. 94-112, 2018.

[25] T.E. Mitchell, L.W. Hobbs, A.H. Heuer, J. Castaing ,J. Cadoz and J. Philibert, “Overview No. 6: Interaction between point defects and dislocations in oxides”, Acta Metallurgica, Vol. 27, no. 11, pp. 1677-1691, 1979.

[26] P.A, Fernandes, P.M.P. Slam and A. Da Cunha, “A study of ternary $Cu2_SnS_3$ and Cu_3SnS_4 thin films prepared by sulfurizing stacked metal precursors”, Journal of Physics D: Applied Physics, Vol. 43, no. 21, pp. 215403, 2010.

[27] V. R. M. Reddy, M. R. Pallavolu, P. R. Guddeti, S. Gedi, K. K. Y. B. Reddy, B. Pejjai, W. K. Kim, T. R. R. Kotte and C. Park, “Review on Cu_2SnS_3, Cu_3SnS_4, and Cu_4SnS_4 thin films and their photovoltaic performance”, Journal of Industrial and Engineering Chemistry, Vol. 76, pp. 39-74, 2019.

[28] M. He, J. Kim, M.P. Suryawanshi, A.C. Lokhande, M. Gang, U.V. Ghorpade, D. S. Lee and J. H. Kim, “Influence of sulfurization temperature on photovoltaic properties of Ge alloyed Cu_2SnS_3 (CTGS) thin film solar cells”, Solar Energy Materials and Solar Cells, Vol. 174, pp. 94-101, 2018.

[29] M. A. Yıldırım, “The effect of copper concentration on structural, optical and dielectric properties of $Cu_xZn_{1-x}S$ thin films”, Optics Communications, Vol. 285, no. 6, pp. 1215-1220, 2012.

[30] M. A. Yildirim, A. Ates, and A. Astam, “Annealing and light effect on structural, optical and electrical properties of CuS, CuZnS and ZnS thin films grown by the SILAR method”, Physica E: Low-dimensional Systems and Nanostructures, Vol. 41, no. 8, pp. 1365-1372, 2009.

[31] A. Ates, M. A. Yıldırım, M. Kundakcı and A. Astam, “Annealing and light effect on optical and electrical properties of ZnS thin films grown with the SILAR method”, Materials Science in Semiconductor Processing, Vol. 10, no. 6, pp. 281-286, 2007.

[32] D. Tiwari, T. K. Chaudhuri, T. Shripathi, U. Deshpande and R. Rawat, “Non-toxic, earth-abundant 2% efficient Cu_2SnS_3 solar cell based on tetragonal films direct-coated from single metal-organic precursor solution”, Solar Energy Materials and Solar Cells, Vol. 113, pp. 165-170, 2013.

[33] M. S. Sreejith, D . R. Deepu, C. S. Kartha, K. Rajeevkumar and K. P . Vijayakumar, “Tuning the properties of sprayed CuZnS films for fabrication of solar cell”, Applied Physics Letters, Vol. 105, no. 20, pp. 202107, 2014.

[34] C. J. D. Godines, C.G.T. Castanedo, R. C. Pérez, G. T. Delgado and O. Z. Ángel, “Transparent conductive thin films of Cd_2SnO_4 obtained by the sol–gel technique and their use in a solar cell made with CdTe”, Solar energy materials and solar cells, Vol. 128, pp. 150-155, 2014.

[35] Y. Zhao, L. Hu, H. Liu, M. Liao, X. Fang and L. Wu, “Band gap tunable Zn_2SnO_4 nanocubes through thermal effect and their outstanding ultraviolet light photoresponse”, Scientific reports, Vol. 4, no. 1, pp. 1-7, 2014.

[36] A. Kanai, H. Araki, A. Takeuchi and H. Katagiri, “Annealing temperature dependence of photovoltaic properties of solar cells containing Cu_2SnS_3 thin films produced by co-evaporation”, physica status solidi (b), Vol. 252, no. 6, pp. 1239-1243, 2015.

[37] Y. Dong, J. He, L. Sun, Y. Chen, P. Yang and J. Chu, “Effect of sulfurization temperature on properties of Cu_2SnS_3 thin films and solar cells prepared by sulfurization of stacked metallic precursors”, Materials Science in Semiconductor Processing, Vol. 38, pp. 171-176, 2015.

[38] A. Kanai, K. Toyonaga, K. Chino, H. Katagiri and H. Araki, “Fabrication of Cu_2SnS_3 thin-film solar cells with power conversion efficiency of over 4%”, Japanese Journal of Applied Physics, Vol. 54, no. 8S1, pp. 08KC06, 2015.

[39] C. Liu, A. Piyadasa, M. Piech, S. Dardona, Z. Ren and P.-X. Gao, “Tunable UV response and high performance of zinc stannate nanoparticle film photodetectors”, Journal of Materials Chemistry C, Vol. 4, no. 25, pp. 6176-6184, 2016.

[40] S. Dias and S. B. Krupanidhi, “Solution processed Cu_2SnS_3 thin films for visible and infrared photodetector applications ”, AIP Advances, Vol. 6, no. 2, pp. 025217, 2016.

[41] M. Sreejith, D. R. Deepu, C. SudhaKartha, K. P. Rajeevkumar and K. Vijayakumar, “Improvement of sprayed CuZnS/In_2S_3 solar cell efficiency by making multiple band gap nature more prominent”, Journal of Renewable and Sustainable Energy, Vol. 8, no. 2, pp. 023502, 2016.

[42] I. Y. Kim, J. Y. Lee, U. V. Ghorpade, M. Suryawanshi, D. S. Lee and J. H. Kim, “Influence of annealing temperature on the properties and solar cell performance of Cu_2SnS_3 (CTS) thin film prepared using sputtering method”, Journal of Alloys and Compounds, Vol. 688, pp. 12-17, 2016.

[43] J. J. Becker, X. Xu, R. Woods-Robinson, C. M. Campbell, M. Lassise, J. Ager and Y.-H. Zhang, “CuZnS hole contacts on monocrystalline CdTe solar cells”, pp. 3410-3412, 2017 .

[44] X. Xu, Q. Chen, H. Yuan, N. Yi, J. Chen, X. Zhu, Y. Yamaguchi and X. Dou, “Facile preparation of novel Cu–Zn–S film by spray pyrolysis”, Journal of Materials Science: Materials in Electronics, Vol. 28, no. 23, pp. 18085-18089, 2017.

[45] M. Asemi and M. Ghanaatshoar, “Minimizing the charge recombination rate at the FTO/Zn_2SnO_4 interface by metal oxide semiconductors in DSSCs”, Journal of materials science, Vol. 53, no. 10, pp. 7551-7561, 2018.

[46] J. Wu, C. Gao, L. Han, S. Shen, M. Jia, L. Wang, L. Jiang and F. Liu, “The effect of different Cu/Sn ratios on the properties of monoclinic Cu_2SnS_3 thin films and solar cells fabricated by the sol–gel method”, Journal of Materials Science: Materials in Electronics, Vol. 30, no. 5, pp. 4378- 4384, 2019.

[47] D. Osorio-Rivera, G. Torres-Delgado, R. Castanedo-Pérez, J. Márquez-Marín and O. Zelaya-Ángel, “Cd_2SnO_4/CdS/Cu_2O/Ag solar cell obtained by chemical techniques”, Materials Research Bulletin, Vol. 122, pp. 110669, 2020.

[48] V. Karimi,M .Asemi and M. Ghanaatshoar, “Improving photovoltaic properties of ZTO-based DSSCs using surface modification of Zn_2SnO_4 nanoparticles prepared by co-precipitation method”, Materials Science in Semiconductor Processing, Vol. 127, pp. 105664, 2021.

[49] K .Deevi and V. S. R. I. Reddy, “Zn_2SnO_4 as electron transport material for semi-transparent dye sensitized solar cells”, Materials Letters, Vol. 283, pp. 128848, 2021.

[50] T. Pradeep, “understanding nanoscience and nanotechnology”, McGraw-Hill Education, 2007.

[51] J. Jeevanandam, A. Barhoum, Y. S. Chan, A. Dufresne and M. K. Danquah, “Review on nanoparticles and nanostructured materials: history, sources, toxicity and regulations”, Beilstein journal of nanotechnology, Vol. 9, no. 1, pp. 1050-1074, 2018.

[52] H. H. M. Darweesh, “Nanomaterials: Classification and Properties-Part I”, J Nanosci, Vol. 1, no. 1, pp. 1-11, 2018.

[53] V. Lehmann and U. Gösele, “Porous silicon formation: A quantum wire effect”, Applied Physics Letters, Vol. 58, no. 8, pp. 856-858, 1991.

[54] W. R. Saleh, S. Y. Al-Dabagh, M. A. Al-Azzawi, G. S. Muhammed and M. Suhail, “Far Infrared Photoconductive Detector Based on Multi-Wall Carbon Nanotubes”, International Journal of Application or Innovation in Engineering & Management ,Vol.4, no.1, 2015.

[55] L. Canham, “Handbook of porous silicon”, Springer International Publishing Berlin, Germany:, 2014.

[56] S. Svechnikov, E. Kaganovich and E. Manoilov, “Photosensitive porous silicon based structures”, Semiconductor Physics Quantum Electronics & Optoelectronics, 1998.

[57] A.G Cullis, L. T. Canham and P.D.J. Calcott, “The structural and luminescence properties of porous silicon”, Journal of applied physics, Vol. 82, no. 3, pp. 909-965, 1997.

[58] J. Torres, F. Castillejo and J. Alfonso, “Influence of the current density and resistivity on the optical properties of p-type porous silicon thin films fabricated by the electrochemical anodizing method”, Brazilian journal of physics, Vol. 36, no. 3B, pp. 1021-1024, 2006.

[59] T. Van Buuren, T. Tiedje, J.P. Dahn and B.M. Way, “Photoelectron spectroscopy measurements of the band gap in porous silicon”, Applied physics letters, Vol. 63, no. 21, pp. 2911-2913, 1993.

[60] X. Zhang, “Morphology and formation mechanisms of porous silicon”, Journal of the Electrochemical Society, Vol. 151, no. 1, pp. C69, 2003.

[61] C. de Mello Donegá, “Synthesis and properties of colloidal heteronanocrystals”, Chemical Society Reviews, Vol. 40, no. 3, pp. 1512-1546, 2011.

[62] T. Jenkins, “A brief history of... semiconductors”, Physics education, Vol. 40, no. 5, pp. 430, 2005.

[63] Y.-J. Lin, C.-L. Tsai and B.-C. Huang, “Discrepancy in mobility extracted from transfer and output characteristics of organic thin film transistors”, Applied Physics Letters, Vol. 97, no. 20, pp. 203509, 2010.

[64] T. Menke, “Molecular Doping of Organic Semiconductors: A Conductivity and Seebeck Study”, Dresden, Technische Universität Dresden, Diss, 2013.

[65] F. Qi, “Computational molecular design of polyhedral oligomeric silsesquioxane based organic-inorganic hybrid semiconductors”, University of Michigan, 2011.

[66] F. Yakuphanoglu, M. Aydin, N. Arsu and M. Sekerci, “A small-molecule organic semiconductor”, Semiconductors, Vol. 38, no. 4, pp. 468-471, 2004.

[67] C.-H. Chen and I. Shih,“Hybrid organic on inorganic semiconductor heterojunction”, Journal of Materials Science: Materials in Electronics, Vol. 17, no. 12, pp. 1047-1053, 2006.

[68] S.-J. Young, L.-W. Ji, S.-J. Chang and Y.-K. Su, “ZnO metal–semiconductor–metal ultraviolet sensors with various contact electrodes”, Journal of crystal growth, Vol. 293, no. 1, pp. 43-47, 2006.

[69] K. Behzad, W. M. M. Yunus, Z. A. Talib, A. Zakaria and A. Bahrami, “Effect of preparation parameters on physical, thermal and optical properties of n-type porous silicon”, Int. J. Electrochem. Sci, Vol. 7, pp. 8266-8275, 2012.

[70] S. R. Elliott, “Physics of amorphous materials”, Longman Group, Longman House, Burnt Mill, Harlow, Essex CM 202 JE, England, 1983.

[71] B. E. Warren, “X-ray Diffraction”, Courier Corporation, 1990.

[72] B. Mattes and L. Kazmerski, “Polycrystalline and Amorphous thin films and devices”, Material Science Series, 1980.

[73] R. James, “X-Ray Diffraction”, 2014.

[74] H. P. Klug, L. E. Alexander and X.-R. D. Procedures, “For Polycrystalline and Amorphous Materials”, John Willey, 1974.

[75] J. Talegaonkar, and D.R.Patil, “Ammonia gas sensing performance of polyaniline-SnO_2”, Int J Eng Res Technol, Vol. 5, no. 10, pp. 296-303, 2016.

[76] C. Kittel, “Introduction to solid state physics”, American Journal of Physics, Vol. 35, no. 6, pp. 547-548, 1967.

[77] R. Karimzadeh and N. Mansour, “The effect of concentration on the thermo-optical properties of colloidal silver nanoparticles”, Optics & Laser Technology, Vol. 42, no. 5, pp. 783-789, 2010.

[78] D. Haridasand V. Gupta, “Enhanced response characteristics of SnO_2 thin film based sensors loaded with Pd clusters for methane detection”, Sensors and Actuators B: Chemical, vol. 166, pp. 156-164, 2012.

[79] Y. Prabhu, K. V. Rao, V. S. S. Kumar and B. S. Kumari, “X-ray analysis of Fe doped ZnO nanoparticles by Williamson-Hall and size-strain plot methods”, Int. J. Eng. Adv. Technol, Vol. 2, pp. 268-274, 2013.

[80] A. Moses Ezhil Raj, L.C.Nehru, M. Jayachandran and C. Sanjeeviraja, “Spray pyrolysis deposition and characterization of highly (100) oriented magnesium oxide thin films”, Crystal Research and Technology: Journal of Experimental and Industrial Crystallography, vol. 42, no. 9, pp. 867-875, 2007.

[81] G. Binnig, C. F. Quate and C. Gerber, “Atomic force microscope”, Physical review letters, Vol. 56, no. 9, pp. 930, 1986.

[82] N. Yao and Z. L. Wang,“Handbook of microscopy for nanotechnology”, Springer, 2005.

[83] R .Garcıa and R. Perez, “Dynamic atomic force microscopy methods”, Surface science reports, Vol. 47, no. 6-8, pp. 197-301, 2002.

[84] Z. Dong,“Design, fabrication, testing of CNT based ISFET and characterization of nano/bio materials using AFM”, University of Arkansas, 2012.

[85] P. Jeeju and S. Jayalekshmi, “Investigations on some technologically important polymer nanocomposite films and semi crystalline Polypyrrole films”, Cochin University of Science and Technology, 2012.

[86] J. I. Pankove, “Optical processes in semiconductors Prentice-Hall”, New Jersey, Vol. 92, pp. 36, 1971.

[87] L. L. Kazmerski,“Electrical properties of polycrystalline semiconductor thin films”, Polycrystalline and amorphous thin films and devices, pp. 59-133, 1980.

[88] S. Schorr, “Structural aspects of adamantine like multinary chalcogenides”, Thin Solid Films, Vol. 515, no. 15, pp. 5985-5991, 2007.

[89] C. F. Klingshirn, “Semiconductor optics”, Springer Science & Business Media, 2012.

[90] S. Adachi, “Handbook on physical properties of semiconductors”, Springer Science and Business Media, 2004.

[91] C. Jacoboni, “Theory of electron transport in semiconductors a pathway from elementary physics to nonequilibrium Green functions”, Springer Science & Business Media, 2010.

[92] N. F .Mott and E. A. Davis, “Electronic processes in non-crystalline materials”, Oxford university press, 2012.

[93] B. Voutou, E.-C. Stefanaki and K. Giannakopoulos, “Electron microscopy: The basics”, Physics of Advanced Materials Winter School, Vol.1, no.11, 2008 .

[94] M. A. Habeeb and A. H. Abbas, “Effect of High Density Polyethylene (HDPE) on Structural and Optical Properties of (PP/PMMA) Blends”, International Letters of Chemistry, Physics and Astronomy, Vol. 60, pp. 95, 2015.

[95] J. Bardeen, F. Blatt and L. Hall, “Photoconductivity conference”, Wiley, New York, Vol. 195623, pp. 146, 1956.

[96] M. R. Hoffmann, S. T. Martin, W. Choi and D. W. Bahnemann, “Environmental applications of semiconductor photocatalysis”, Chemical reviews, Vol. 95, no. 1 , pp. 69-96, 1995.

[97] J. Tauc, “Amorphous and liquid semiconductors”, Springer Science & Business Media, 2012.

[98] S. Jain, M. Willander and R. Van Overstraeten, “Compound semiconductors strained layers and devices”, Springer Science & Business Media, 2013.

[99] G. Arrhenius, “X-ray diffraction procedures for polycrystalline and amorphous materials ”, ACS Publications, 1955.

[100] S. M. Sze, Y. Li and K. K. Ng, “ Physics of semiconductor devices”, John wiley & sons, 2021.

[101] I. Duran, M. Hron, J. Stockel, L. Viererbl, R. Vsolak, V. Cerva, I. Bolshakova, R.Holyaka and G. Vayakis, “Stability of the Hall sensors performance under neutron irradiation”, 2004.

[102] E. Lage, “Forças em campos magnéticos”, Revista de Ciência Elementar, Vol. 9, no. 1, 2021.

[103] R. A. Yotter and D. M. Wilson, “A review of photodetectors for sensing light-emitting reporters in biological systems”, IEEE Sensors Journal,Vol. 3, no. 3, pp. 288-303, 2003.

[104] S. Jain, “Solid state physics laboratory”, Journal of Physics Education, Vol. 2, no. 1, pp. 1-4, 1974.

[105] J.-P. Colinge and C. A. Colinge, “Physics of semiconductor devices”, Springer Science & Business Media, 2005.

[106] R. Rediker, S. Stopek and J. Ward, “Interface-alloy epitaxial heterojunctions”, Solid-State Electronics, Vol. 7, no. 8, pp. 621-622, 1964.

[107] A. G. Milnes, “Heterojunctions and metal semiconductor junctions”, Elsevier, 2012.

[108] H. S. Nalwa, “Handbook of surfaces and interfaces of materials ”, five-volume set: Elsevier, 2001.

[109] A. C. R. Series , “ PERSPECTIVES IN CONDENSED MATTER PHYSICS ”, Springer,1988.

[110] P. Paufler, “SR Elliott. Physics of amorphous materials. Longman Group Ltd., London, New York, 1984. Pp X+ 386. Price:£ 25.00. ISBN 0–582–44636–8 ”, Wiley Online Library, 1985.

[111] I. H. Khudayer, “Study of physical and optoelectronic properties of $CuInSe_2$/Si heterojunction solar cells”, Energy Procedia, Vol. 119, pp. 507-517, 2017.

[112] K. Mangersnes, “Back-contacted back-junction silicon solar cells”, 2011.

[113] M. A. Green, “Solar cells: operating principles, technology and system applications”, Englewood Cliffs, 1982.

[114] S. Wenger, “Strategies to Optimizing Dye-Sensitized Solar Cells”, EPFL, 2010.

[115] A. Goetzberger and V. U. Hoffmann,“Photovoltaic solar energy generation”, Springer Science & Business Media, 2005.

[116] A. McEvoy, L. Castaner and T. Markvart, “Solar cells: materials, manufacture and operation”, Academic Press, 2012.

[117] L. M. Fraas and L. D. Partain, “Solar cells and their applications”, John Wiley & Sons,Vol.217, 2010.

[118] M. A. Malik, O. Kiyani, A. Srinivasan and S. Makarov, “Alternative solar cells and their implications”, An Interactive Qualifying Project, Worcester Polytechnic Institute, MA, 2010.

[119] K. Fredin, “Studies of charge transport processes in dye-sensitized solar cells”, KTH, 2007.

[120] D. Mahesh and J. Rajesh, “TiO_2 microstructure, fabrication of thin film solar cells and introduction to dye sensitized solar cells”, Research Journal of Recent Sciences, Vol. 2, pp. 25-29, 2012.

[121] T. L. Benanti and D. Venkataraman, “Organic solar cells: An overview focusing on active layer morphology”, Photosynthesis research, Vol. 87, no. 1, pp. 73-81, 2006.

[122] M. D. Archer, A. J. Nozik, X. Ai and J. Benson-smith, “Nanostructured and photoelectrochemical systems for solar photon conversion”, World Scientific, Vol.3, 2008.

[123] A. Luque and S. Hegedus, “Handbook of photovoltaic science and engineering”, John Wiley & Sons, 2011.

[124] M.Pagliaro, R. Ciriminna and G. Palmisano, “Flexible solar cells”, ChemSusChem: Chemistry & Sustainability Energy & Materials, Vol. 1, no. 11, pp. 880-891, 2008.

[125] U. Desideri, F. Zepparelli, V. Morettini and E. Garroni, “Comparative analysis of concentrating solar power and photovoltaic technologies: Technical and environmental evaluations”, Applied energy, Vol. 102, pp. 765-784, 2013.

[126] A. A. Assi and W. R. Saleh, “Conductive polymer dye sensitive solar cell (DSSC) for improving the efficiency”, Ph. D. Thesis, University of Baghdad, 2014.

[127] V. Fthenakis, “Sustainability metrics for extending thin-film photovoltaics to terawatt levels”, MRS bulletin, Vol. 37, no. 4, pp. 425-430, 2012.

[128] A. Arya, M. Yaghoubi and K. Jafarpur, “A more realistic performance evaluation of solar convertors: the need for exergic spectral analysis of radiative heat transfer”, International Journal of Exergy, Vol. 33, no. 1, pp. 114-128, 2020.

[129] L. Wagner, “Overview of the solar industry‖”, Mora, Associated, 2007.

[130] A. K. Ali, N. A. Bakr and S. M. Jassim, “Fabrication of Dye Sensitized Solar Cell and Efficiency Enhancement by Using N719 and Z907 Dyes Mixture”, Journal of Photonic Materials and Technology, Vol. 2, no. 3, pp. 20-24, 2016.

[131] Z. Guo, J. S. Manser, Y. Wan, P. V. Kamat and L. Huang, “Spatial and temporal imaging of long-range charge transport in perovskite thin films by ultrafast microscopy”, Nature communications, Vol. 6, no. 1, pp. 1-8, 2015.

[132] S. I. Hossain, “Performance and stability of perovskite solar cells”, Iowa State University, 2018.

[133] H. Cheema, A. Islam, L. Han and A. El-Shafei, “Monodentate pyrazole as a replacement of labile NCS for Ru (II) photosensitizers: Minimum electron injection free energy for dye-sensitized solar cells”, Dyes and Pigments, Vol. 120, pp. 93-98, 2015.

[134] M. K. Nazeeruddin, P. Pechy ,T. Renouard, S. M. Zakeeruddin, R. Humphry- Baker, P. Comte, P. Liska, L. Cevey, E. Costa and V. Shklover, “Engineering of efficient panchromatic sensitizers for nanocrystalline TiO_2-based solar cells”, Journal of the American Chemical Society, Vol. 123 , no. 8, pp. 1613-1624, 2001.

[135] D. Black, “Fabrication of hybrid inorganic and organic photovoltaic cells”, 2011.

[136] E. Schönhofer, “Dye sensitized solar cells: from liquid electrolytes to solid state hole transport materials”, University_of_Basel, 2015.

[137] K. Emery, “Measurement and characterization of solar cells and modules”, Handbook of photovoltaic science and engineering, pp. 797-840, 2010.

[138] A. Rogalski, “ Infrared detectors”, CRC press, 2000.

[139] B. A. Gregg, “Dye-Sensitized Solar Cells”, Semiconductor Photochemistry And Photophysics/Volume Ten, Vol. 10, pp. 51, 2003.

[140] S. B. Lee, C. Pathak, V. Ramadesigan, W. Gao and V. R. Subramanian, “Direct, efficient, and real-time simulation of physics-based battery models for stand-alone pv-battery microgrids”, Journal of The Electrochemical Society, Vol. 164, no. 11, pp. E3026, 2017.

[141] L. C. Hirst and N. J. Ekins-Daukes, “Fundamental losses in solar cells”, Progress in Photovoltaics: Research and Applications, Vol. 19, no. 3, pp. 286 -293,2011.

[142] Y. Chergui, N. Nehaoua and D. Mekki, “Comparative study of dye-sensitized solar cell based on ZnO and TiO_2 nanostructures”, Solar Cells-Dye-Sensitized Devices, 2011.

[143] S. Roy, S. Das, C. K. Ghosh and C. K. Sarkar, “Solar Photovoltaic: From Materials to System”, Nanotechnology: Synthesis to Applications, pp. 197-218, 2017.

[144] D. A. Neamen, “Semiconductor physics and devices”, basic principles, McGraw-hill, 2003.

[145] H. Hartnagel, R. Katilius and A. Matulionis, “Microwave noise in semiconductor devices”, John Wiley & Sons, 2001.

[146] Y. H. Ogata, “Characterization of porous silicon by infrared spectroscopy”, Handbook of Porous Silicon, Springer, pp. 473-480, 2014.

[147] K. H. Rzayg, H. H. Ahmed and H. H. Ali, “Effect of Fe Doping on Structural and Electrical Properties of CdO Thin Films Prepared by Chemical Bath Deposition Technique”, Journal of University of Babylon for Pure and Applied Sciences, Vol. 27, no. 6, pp. 378-385, 2019.

[148] J.-M. Liu, “Photonic devices”, Cambridge University Press, 2009.

[149] I. Bahl, “Fundamentals of RF and microwave transistor amplifiers”, John Wiley & Sons, 2009.

[150] A. Abd, “Quantum Dots CdSe/PSi/Si Photodetector”, Ph. D. thesis, University of Al-Mustansiriyah, 2015.

[151] G. Busch and H. Schade,“Lectures on Solid State Physics”, International Series in Natural.Philosophy: Elsevier,Vol.79, 2013.

[152] J. T. Ballinger and G. J. Shugar, “Chemical technicians' ready reference handbook”, McGraw-Hill Education, 2011.

[153] B. Yilbas, A. Al-Sharafi and H. Ali , “Self-cleaning of surfaces and water droplet mobility”, Elsevier, 2019.

[154] D. Dubal, S. Patil, A. Jagadale and C. Lokhande, “ Two step novel chemical synthesis of polypyrrole nanoplates for supercapacitor application”, Journal of Alloys and Compounds, Vol. 509, no. 32, pp. 8183-8188, 2011.

[155] S. Zhang, X. Yang, Y. Numataa and L. Han, “ Highly efficient dye-sensitized solar cells: progress and future challenges ”, Energy Environmental Science, Vol. 4, pp. 60-62, 2011.

[156] G.Gnanamoorthy, T. Dhanasekaran, A. Padmanaban, S. P. Kumar, S. Munusamy, A. Stephen and V. Narayanan, “Photocatalytic activity and optical properties of Cd_2SnO_4 nanospheres”, Materials Today: Proceedings, Vol. 5, no. 2, pp. 8956-8960, 2018.

[157] E. M. Nasir, S. Iqbal and M. Alias, “Characterization of cadmium tin oxide thin films as a window layer for solar cell”, International Journal of Application or Innovation in Engineering &Management (IJAIEM), Vol. 2, no. 9, pp. 189-194, 2013.

[158] T. S. Reddy, R. Amiruddin and M. S. Kumar, “Deposition and characterization of Cu_2SnS_3 thin films by co-evaporation for photovoltaic application”, Solar Energy Materials and Solar Cells, Vol. 143, pp. 128-134, 2015.

[159] G. M. Gubari, N. P .Huse, A. S. Dive and R. Sharma, “ Synthesis and characterization of structural, morphological and photosensor properties of $Cu_{0.1}Zn_{0.9}S$ thin film prepared by a facile chemical method ”, In AIP Conference Proceedings ,Vol. 1953, no. 1, p. 100014, 2018.

[160] S. K. Sundaram, S. Subramanian, V. Panneerselvam and S. T. Salammal, “Temperature-dependent phase transition of CuZnS thin films and its effects on morphological, optical and electrical properties”, Thin Solid Films, Vol. 733, pp. 138810, 2021.

[161] S. Dinesh, M. Anandan, V.K. Premkumar, S. Barathan, G. Sivakumar and N. Anandhan, “Photocatalytic and electrochemical performance of hydrothermally synthesized cubic Cd_2SnO_4 nanoparticles”, Materials Science and Engineering: B, Vol. 214, pp. 37-45, 2016.

[162] S. Rahaman, Y. M. G. Shenoy, V. N. Krishna, S. Shekhar and H. Shaik,“Effect of annealing on the properties of Cu_2SnS_3 thin films using spin coating”, In AIP Conference Proceedings ,Vol.2105, no.1, p. 020001, 2019.

[163] I. Arora and P. Kumar, “Effect of annealing temperature on structure-property correlations in Zn_2SnO_4 nanostructured films for optoelectronics”, Materials Research Express, Vol. 7, no. 3, pp. 035023, 2020.

[164] R. H. Bari, S. B. Patil and A. R. Bari, “Synthesis, Characterization and Gas Sensing Performance Of Sol-Gel Prepared Nanocrystalline Sno_2 Thin Films”, International journal on smart sensing and intelligent systems, Vol. 7, no. 2, 2017.

[165] B. Patel, R. K. Pati, I. Mukhopadhyay and A. Ray, “Effect of vacuum and sulphur annealing on the structural properties of spray deposited Cu_2SnS_3 thin films”, Vacuum, Vol. 158, pp. 263-270, 2018.

[166] A. Aldwayyan, F. Al-Jekhedab, M. Al-Noaimi, B. Hammouti, T. Hadda, M. Suleiman and I. Warad, “Synthesis and characterization of CdO nanoparticles starting from organometalic dmphen-CdI_2 complex”, Int. J. Electrochem. Sci, Vol. 8, no. 8, pp. 10514-10506 , 2013.

[167] J. E. Jeronsia, L. A. Joseph, M. M. Jaculine, P. A. Vinosha and S. J. Das, “Hydrothermal synthesis of zinc stannate nanoparticles for antibacterial applications”, Journal of Taibah University for Science, Vol. 10, no. 4, pp. 601-606, 2016.

[168] M. Fakhrzad, A. Navidpour, M. Tahari and S. Abbasi, “Synthesis of Zn_2SnO_4 nanoparticles used for photocatalytic purposes”, Materials Research Express, Vol. 6, no. 9, pp. 095037, 2019.

[169] Z. L. Hadi, M. S. Essa and B. T. Chiad, “Ternary Cu_2SnS_3 thin films deposited by fully controlled system of spray pyrolysis”, Journal of physics,Vol.1234, no.1, p. 012041, 2019.

[170] P. N. P. Jeya Helan, K. Mohanraj, S. Thanikaikarasan, T. Mahalingam, G. Sivakumar and P. Sebastian, “Ethylenediamine Processed Cu_2SnS_3 Nano Particles via Mild Solution Route”,

Journal of New Materials for Electrochemical Systems, Vol. 19, no. 1, 2016.

[171] X.-F. Sun, R. Sun, P. Fowler and M. S. Baird, “Extraction and characterization of original lignin and hemicelluloses from wheat straw”, Journal of Agricultural and Food Chemistry, Vol. 53, no. 4, pp. 860-870, 2005.

[172] C.-Y. Chen, X.-Q. Zhao, H.-W. Yen, S.-H. Ho, C.-L. Cheng, D.-J. Lee, F.-W. Bai and J.-S. Chang, “Microalgae-based carbohydrates for biofuel production”, Biochemical Engineering Journal, Vol. 78, pp. 1-10, 2013.

[173] T. J. Coutts, D. L. Young, X. Li, W. Mulligan and X. Wu, “Search for improved transparent conducting oxides: A fundamental investigation of CdO, Cd_2SnO_4, and Zn_2SnO_4”, Journal of Vacuum Science & Technology A: Vacuum, Surfaces, and Films, Vol. 18, no. 6, pp. 2646-2660, 2000.

[174] C. Chen, M. Nasrallah and H. Anderson, “Synthesis and characterization of (CeO_2) 0.8 (SmO1. 5) 0.2 thin films from polymeric precursors”, Journal of the Electrochemical Society, Vol. 140, no ,12 .pp. 3555, 1993.

[175] E. Elangovan and K. Ramamurthi, “Micro-cubes with Porous Architecture: Synthesis and Gas-Sensing”, J. of Optoelectronics and Advanced Materials, Vol. 5, no. 1, pp. 45-54, 2003.

[176] S. Rabaoui, H. Dahman, S. Dekhil, K. Omri, A .Alyamani and L. El Mir, “Effect of drying temperature on the structural and optical characteristics of Cu_2SnS_3 thin films synthesized by simple spin coating technique”, Journal of Materials Science: Materials in Electronics, Vol. 26, no. 11, pp. 8588-8594, 2015.

[177] H. Dahman and L. El Mir, “Cu_2SnS_3 thin films deposited by spin coating route: a promise candidate for low cost, safe and flexible solar cells”, Journal of Materials Science: Materials in Electronics, Vol. 26, no. 8, pp. 6032-6039, 2015.

[178] Q. Chen, X. Dou, Y. Ni, S. Cheng and S. Zhuang, “Study and enhance the photovoltaic properties of narrow-bandgap Cu_2SnS_3 solar cell by p–n junction interface modification”, Journal of colloid and interface science, Vol. 376, no. 1, pp. 327-330, 2012.

[179] C. Cardile, M. Bowden, A. Koplick and R. Buckley, “Enhanced IR reflectance of cadmium stannate films prepared by DIP coating”, Thin solid films, Vol. 186, no. 1, pp. L11-L14, 1990.

[180] A. Nozik, “Optical and electrical properties of Cd_2SnO_4: a defect semiconductor”, Physical Review B, Vol. 6, no. 2, pp. 453, 1972.

[181] U. Chalapathi, Y. Jayasree, S. Uthanna and V. Sundara Raja, “Effect of annealing temperature on the properties of spray

deposited Cu_2SnS_3 thin films", physica status solidi (a) ,Vol. 210, no. 11, pp. 2384-2390, 2013.

[182] D. Dimova-Malinovska, J. M. Marshall and A. Vaseashta, "Nanostructured and advanced materials for applications in sensor, optoelectronic and photovoltaic technology", Springer,Vol.204, 2005.

[183] B. Bensahel, L. T. Canham and S. Ossicini, "Optical properties of low dimensional silicon structures", Springer Science & Business Media, 2012.

[184] H. P. Klug and L. E. Alexander, "X-ray diffraction procedures: for polycrystalline and amorphous materials", 1974.

[185] A. Patterson, "X-Ray Diffraction Procedures for Polycrystalline and Amorphous Materials", Journal of the American Chemical Society, Vol. 77, no. 7, pp. 2030-2031, 1955.

Published and Accepted Research Articles

- **Layth A. Saleh and Ziad T. Khodair** " *Influence of Deposition Temperatures on the Structural and Optical Properties of Zn_2SnO_4 (ZTO) Thin Films*", **NeuroQuantology , Vol. 20, No. 4, (2022) , DOINumber:10.14704/nq.22022.20.4.NQ22107.**

- **Layth A. Saleh and Ziad T. Khodair** " *Study the Structural and Optical Properties of Cd_2SnO_4 (CTO)Thin Films as a Function of DepositionTemperature*"**,MaterialsToday:Proceedings,Vol.57,No.2, pp.492-497,(2022) , doi.org/10.1016/j.matpr.2022.01.389.**

الخلاصة

في هذه الدراسة تم ترسيب الأغشية الرقيقة للمواد المحضرة (Cd_2SnO_4 و Zn_2SnO_4) بطريقة الانحلال الحراري في درجات حرارة (450,500 and550 ^{o}C)، وتم ترسيب اغشية رقيقة اخرى للمواد المحضرة (Cu_2SnS_3 و CuZnS) بطريقة الطلاء البرمي عند درجات حرارة(200,250 and 300^{o}C) وكذلك تم تحضير اغشية اخرى للمواد (Cd_2SnO_4 و Zn_2SnO_4) في درجة حرارة (550 ^{o}C) والمواد (Cu_2SnS_3 و CuZnS) في درجة حرارة (300 ^{o}C) بطريقة السائل الهلامي (سول-جل).

تمت دراسة الخواص التركيبية والبصرية والكهربائية (تأثيرهول) للأغشية الرقيقة المحضرة. أظهرت نتائج حيود الأشعة السينية (XRD) أن الأغشية التي تم تحظيرها بطريقة الانحلال الحراري Cd_2SnO_4 و Zn_2SnO_4 متعددة التبلور ذات تركيب مكعب (سبنيل) بينما الأغشية التي تم تحظيرها بواسطة الطلاء البرمي Cu_2SnS_3 متعدد البلورات مع تركيب رباعي و التركيب السداسي ل CuZnS وأن الزيادة في درجة حرارة الركيزة تزيد من حجم البلورة .كذلك تم قياس الحجم البلوري باستخدام صيغة شرر ل (Cd_2SnO_4, Zn_2SnO_4, and Cu_2SnS_3 CuZnS) ووجد انها تساوي (43.8 nm, 22.0 nm, 22.5 nm و37.2 nm) على التوالي. كما أظهرت نتائج حيود الأشعة السينية (XRD) أن جميع أغشية Cd_2SnO_4, Zn_2SnO_4, Cu_2SnS_3 and CuZnS المحضرة بطريقة (سول –جل) هي متعددة التبلور ذات تركيب مكعب. و لها حجم بلوري يبلغ (13.4 nm, 25.0 nm, 26 .7 nm و 30 .5 nm) على التوالي . وفقًا لأطياف (FTIR) فإنها أكدت تشكيل المواد المصنعة وكذلك ظهور قمم اهتزاز واسعة (O-H) عن طريق التبخير الحراري وطلاء البرمي. تم تأكيد وجود الهياكل النانوية للأغشية الرقيقة المحضرة بتقنيات (XRD، AFM، FE-SEM) ، حيث أظهرت نتائج قياسات مجهر القوة الذرية (AFM) تأثير واضح في قيم حجم الحبيبات وخشونة السطح و الجذر التربيعي لمتوسط الخشونة مع الركيزة المتغيرة مع درجة الحرارة للأغشية المحضرة عن طريق الانحلال الحراري والطلاء البرمي. تمت دراسة الخواص البصرية من خلال تسجيل الامتصاصية والنفاذية الطيفية ضمن مدى الطول الموجي (300-900 نانومتر).حيث أظهرت النتائج انخفاضًا في امتصاص الأغشية للضوء الساقط مع زيادة قيم النفاذية و زيادة الطول الموجي للأغشية الرقيقة Cd_2SnO_4 و Zn_2SnO_4. أظهرت النتائج أيضًا زيادة في قيم معامل الامتصاص مع زيادة درجة حرارة الركيزة زيادة في امتصاص الأغشية للضوء الساقط مع انخفاض قيم النفاذية و زيادة الطول الموجي لـ Cu_2SnS_3 و CuZnS و أظهرت ان قيم فجوة الطاقة تزداد مع زيادة درجة حرارة الركيزة للأغشية المحضرة بطريقة الانحلال الحراري Cd_2SnO_4 وZn_2SnO_4 وكانت قيم فجوة الطاقة لها2.75 eV و3.30 eVعند درجة حرارة 550 ^{o}C على التوالي. كذلك تم قياس فجوة الطاقة لكل من لكل من Cu_2SnS_3 و CuZnS وجد انها تساوي 1.65eVو 1.80eV على التوالي عند درجة حرارة 300 ^{o}C والمحضرة بطريقة الطلاء البرمي.

كذلك أظهرت نتائج تأثير هول أيضًا أن زيادة درجة حرارة الركيزة تساهم بشكل عام في تحسين الخواص الكهربائية لجميع الاغشية، وأن أعلى موصلية كهربائية كانت لـ Cu_2SnS_3 حيث بلغت $1.001x10^{6}$ $(\Omega.cm)^{-1}$ يقابلها زيادة تركيز حاملات الشحنة 1.231×10^{23} cm^{-3} ،

الخلاصة

وانخفاض المقاومة الكهربائية (9.987×10^{-7} Ωcm) . في هذه الدراسة ، تم استخدام النقش الكهروكيميائي لرقائق السيليكون من النوع (p and n-types) لتحضير نوع (p and n-types) من السيليكون المسامي بكثافة تيار تنميش ($10\ mA/cm^2$) ولمدة (10min). أخيرًا ،تم ترسيب Cd_2SnO_4 و Zn_2SnO_4 على السيليكون المسامي باستخدام طريقة الانحلال الحراري و (CuZnS and Cu_2SnS_3) المترسبة على السيليكون المسامي باستخدام طريقة الطلاء البرمي .و (Cd_2SnO_4، Zn_2SnO_4، CuZnS and Cu_2SnS_3) المترسبة على السيليكون المسامي بطريقة الصب بالقطرة بسمك (1µm),ثم ترسيب الألمنيوم كقطب كهربي موصل على الوجه الخلفي لخلية السيليكون باستخدام تقنية الانحلال الحراري. بعد ذلك تم فحص خصائص الخلية الشمسية والكاشف الضوئي. تم قياس خصائص منحنيات كثافة التيار الكهروضوئي (I-V) للخلايا الشمسية المصنعة تحت الضوء الشمسي المحاكي ($100mW/m^2$) ، تم حساب المعلمات بما في ذلك (فولتية الدائرة المفتوحة V_{OC}), (تيار الدائرة المغلقة I_{SC}),(عامل الملا FF ٪) و(كفاءة الخلية الشمسية η %). تم الحصول على أعلى كفاءة من خلال الطلاء البرمي وكانت قيمته (4.7٪) للوصلات غير المتجانسة (CuZnS)/ PSi / n-Si / Al) وأظهرت النتائج أن طريقة الصب بالقطرة لعبت دورًا رئيسيًا في زيادة أداء الخلية الشمسية. تم الحصول على أعلى كفاءة وقيمتها (7.80٪) للترابطات غير المتجانسة (Cu_2SnS_3) / PSi / n-Si / Al). أظهرت قياسات الاستجابة الطيفية لأجهزة الكشف الضوئية المعدة أنها عملت ضمن النطاق nm (900-400) ، وهي أعلى قيمة استجابة طيفية للوصلات غير المتجانسة يمكن استخدام (CuZnS)/ PSi / n-Si / Al) لتطبيقات جهاز الكشف الضوئي ضمن الأشعة القريبة من المنطقة تحت الحمراء و الطيف المرئي ، حيث تكون الاستجابة الطيفية (Rλ) والكشف النوعي (D *) لأجهزة الكاشفات الضوئية CuZnS / PSi / n-Si / Al حوالي (0.60 A / W) و ($9.2x10^{12}\ cm\ Hz^{1/2}\ W^{-1}$) على التوالي ، عند nm (λ ~ 450).

جمهورية العراق

وزارة التعليم العالي والبحث العلمي

جامعة ديالى- كلية العلوم- قسم الفيزياء

تحضير بعض التراكيب النانوية لأغشية أكاسيد المعادن الثلاثية والكبريتيدات الرقيقة للتطبيقات الكهروضوئية

اطروحة مقدمة إلى

مجلس كلية العلوم - جامعة ديالى

وهي جزء من متطلبات نيل درجة الدكتوراه فلسفة

في الفيزياء

من قبل

ليث علي صالح

بكالوريوس تربية فيزياء 2003

ماجستير علوم فيزياء 2016

أشراف

أ .د . زياد طارق خضير

1444 هـ **2022م**